NTNU – Trondheim
Norwegian University of
Science and Technology

Aluminum structures exposed to blast loading

Tore Andre Hustad
Andreas Lyngtveit Lindland

Department of Structural Engineering
Faculty of Engineering Science and Technology
NTNU- Norwegian University of Science and Technology

MASTER THESIS 2014

SUBJECT AREA:	DATE:	NO. OF PAGES:
Computational Mechanics	10 June 2014	16 + 178 + 97

TITLE:

Aluminum structures exposed to blast loading

Aluminiumskonstruksjoner utsatt for eksplosjonslast

BY:

Tore André Hustad
Andreas Lyngtveit Lindland

SUMMARY:
Design of blast resistance in structures is an important aspect in modern society. Plated structures are used in a lot of constructions that can be especially vulnerable to explosions. This includes e.g. protective, offshore or automotive structures. The main objective in this study was to investigate the response of thin plates made of the aluminum alloy 1050A-H14, as well as to evaluate the available computational methods.

Material tensile tests were performed in order to determine a material model. The material model was created through inverse modeling by the help of the computer code EUROPLEXUS.

Airblast experiments were performed by using composition C4 in experiments performed at Østøya in Horten. The experiments were performed in collaboration with the Norwegian Defence Estates Agency (NDEA). Experiments were performed on stiff calibration plates in order to measure the pressure from the explosions, as well as on aluminum plates in order to determine the structural response.

Analytical and numerical computations were performed in order to evaluate them compared to the experimental results. Numerical simulations were performed with both a Lagrangian and an embedded FSI approach.

The analytical approach underestimated the displacements. However, the results indicated that the analytical calculations could have given better results at lower deformations.

The Lagrangian approach overestimated the displacements. Additional simulations indicate that this could be due to overestimation of the load by the AIRB approach in EUROPLEXUS.

The embedded FSI approach underestimated the displacements. The simulations performed indicate that the description of the load is fairly accurate, but that the displacements were underestimated due to the use of elements that were too large.

RESPONSIBLE TEACHER: Professor Tore Børvik

SUPERVISOR(S): Professor Tore Børvik and Ph.D. Candidate Vegard Aune

CARRIED OUT AT: SIMLab, Department of Structural Engineering, NTNU

Institutt for konstruksjonsteknikk
Fakultet for ingeniørvitenskap og teknologi
NTNU- Norges teknisk- naturvitenskapelige universitet

MASTEROPPGAVE 2014

FAGOMRÅDE:	DATO:	ANTALL SIDER:
Beregningsmekanikk	10. juni 2014	16 + 178 + 97

TITTEL:

Aluminiumskonstruksjoner utsatt for eksplosjonslast

Aluminum structures exposed to blast loading

UTFØRT AV:

Tore André Hustad
Andreas Lyngtveit Lindland

SAMMENDRAG:
Dimensjonering mot eksplosjonslast er en viktig faktor i det moderne samfunn. Plater blir benyttet i mange konstruksjoner som kan være spesielt utsatt for eksplosjoner. Dette inkluderer f.eks. beskyttende konstruksjoner, offshore konstruksjoner eller i bilindustrien. Hovedmålet med dette studiet var å undersøke responsen fra tynne plater, laget av aluminiumslegeringen 1050A-H14. I tillegg skulle tilgjengelige beregningsmetoder vurderes.

Strekktester ble utført med materialet for å etablere en materialmodell. Denne modellen ble etablert ved hjelp av inversmodellering i elementprogrammet EUROPLEXUS.

Eksplosjonsforsøkene ble utført ved å detonere C4-ladninger i eksperimenter utført på Østøya i Horten. Forsøkene ble utført i samarbeid med Forsvarbygg. Forsøkene ble utført på stive kalibrasjonsplater for å måle trykket fra eksplosjonene. I tillegg ble det utført forsøk på aluminimiumsplater for å undersøke deformasjonen.

Analytiske og numeriske beregninger ble utført for å sammenligne med de eksperimentelle resultatene. Numeriske simuleringer ble utført gjennom en Lagrange-analyse, og gjennom simuleringer som tar hensyn til interaksjon mellom fluid og konstruksjon.

Den analytiske tilnærmingen underestimerte deformasjonene. Imidlertid indikerte resultatene at de analytiske metodene kunne gitt bedre resultater ved mindre deformasjoner.

Lagrange-analysene overestimerte deformasjonene. Simuleringene tyder på at dette kan skyldes overestimering av belastningen ved bruk AIRB-tilnærmingen i EUROPLEXUS.

Analysene som tok hensyn til interakson mellom fluid og konstruksjon, underestimerte forskyvningen. Simuleringene indikerer at lasten er beskrevet forholdsvis nøyaktig, men at forskyvningene muligens ble underestimert grunnet bruk av for store elementer.

FAGLÆRER: Professor Tore Børvik

VEILEDER(E): Professor Tore Børvik og Ph.D.-kandidat Vegard Aune

UTFØRT VED: SIMLab, Institutt for konstruksjonsteknikk, NTNU.

Department of Structural Engineering
FACULTY OF ENGINEERING SCIENCE AND TECHNOLOGY
NTNU – Norwegian University of Science and Technology

MASTER'S THESIS 2014

for

Tore A. Hustad and Andreas Lyngtveit Lindland

Aluminum structures exposed to blast loading

1. INTRODUCTION

Design and validation of blast resistant structures are important for the modern society to protect and secure its citizens. Plated structures are commonly used in applications including protective, offshore, automotive and aerospace structures, just to name a few. During the last decades aluminum has become increasingly more desirable for structural applications, particularly due to its relatively high strength to weight ratio and high formability. As a consequence, it is necessary to predict the structural response of aluminum plates exposed to blast loading. Today's protective design of blast resistant structures are based on the a priori specification of the pressure history acting on the structure, and does not account for the interaction of shock loading and structural response. However, since the response of these structures are typically highly nonlinear (both in geometric and material behavior), this may not be an adequate approach as it may result in an unphysical structural response. In reality, the characteristics of the pressure acting on the structure are a function of the structural response, and may therefore be significantly influenced by the displacement of the structure. In this study, the basic idea is to investigate the structural response of aluminum plates exposed to blast loading, and evaluate the available computational methods in terms of robustness and effectiveness.

2. OBJECTIVES

The research project has three main objectives: (1) characterize the material properties of the aluminum alloy 1050A-H14, (2) investigate experimentally the loading on and the blast resistance of a 400x400x0.8 mm aluminum plate, (3) employ and evaluate the analytical and numerical computational methods available for the design of such plates.

3. A SHORT DESCRIPTION OF THE RESEARCH PROJECT

The main topics in the research project will be as follows;

1. A study of current literature: The blast load phenomenon, blast load design, finite element (FE) theory, fluid-structure interaction (FSI) and suitable material models.
2. Material experiments: Uniaxial tension tests are performed at SIMLab (NTNU), and the data is used to identify material properties in a constitutive relation.
3. Component tests: The dynamic response of the aluminum plates is studied experimentally, in collaboration with the Norwegian Defence Estates Agency (NDEA), at Østøya by the end of the first quarter of 2014. Free air explosions will be generated using the explosive C4. Several series of blast tests are performed on plates to determine the loading, the dynamic response and possible FSI effects.
4. Numerical analyses: Non-linear FE numerical simulations of the experiments at Østøya are to be performed. The numerical techniques employed should contain a Lagrangian approach, as well as an approach that accounts for FSI.
5. Validation and documentation: The numerical results are compared to the experimental findings.

Supervisors: Tore Børvik and Vegard Aune (NTNU)

The thesis must be written according to current requirements and submitted to Department of Structural Engineering, NTNU, no later than June 10th, 2014.

NTNU, January 14th, 2014

Tore Børvik
Main supervisor/Professor

Acknowledgements

This master's thesis is written at Structural Impact Laboratory (SIMLab) at the Norwegian University of Science and Technology (NTNU). Some of the experimental work has been performed in collaboration with the Norwegian Defence Estates Agency (NDEA). During the work with this thesis, we have been supervised by Professor Tore Børvik at SIMLab, who is also representing the NDEA, and by Ph.D. Candidate Vegard Aune at SIMLab.

Through these 20 weeks of working with this thesis, we have gained a lot of experiences and knowledge. This include insight and understanding of the challenges and opportunities related to the research of materials exposed to blast loading. Even though this have been demanding – and at times very hectic – we have truly enjoyed it.

Several people have contributed with valuable help and guidance in this work. First we would like to express special thanks to our supervisors Professor Tore Børvik and Ph.D. Candidate Vegard Aune, for weekly guidance and assistance when needed. Their comments and advices have undoubtedly contributed to increased understanding and motivation for the work related to this thesis.

We would like to thank senior engineer Trond Auestad (SIMLab) and staff engineer Tore Wisth (NTNU) for assistance with the experiments both at Gløshaugen, NTNU and Østøya, Horten. We also owe Mr. Knut Ove Hauge from NDEA, thanks related to the experiments carried out at Østøya.

Ph.D. Egil Fagerholt from SIMLab deserves a lot of credit for giving us technical support, related to DIC analysis. We are deeply grateful for his helpfulness. In addition, we would like to thank scientific researcher Dr. Torodd Berstad (NTNU) for software assistance.

We will also address a word of thanks to our fellow student Solveig Heggelund for assistance and constructive discussions, both related to the experiments and the writing of our thesis.

Trondheim, 10 June 2014

Tore André Hustad   Andreas Lyngtveit Lindland

ii

Abstract

Design of blast resistance in structures is an important aspect in modern society. Plated structures are used in a lot of constructions that can be especially vulnerable to explosions. This includes e.g. protective, offshore or automotive structures. The main objective in this study was to investigate the response of thin plates made of the aluminum alloy 1050A-H14, as well as to evaluate the available computational methods.

Material tensile tests were performed in order to determine a material model. The material model was created through inverse modeling by the help of the computer code EUROPLEXUS.

Airblast experiments were performed by using composition C4 in experiments performed at Østøya in Horten. The experiments were performed in collaboration with the Norwegian Defence Estates Agency (NDEA). Experiments were performed on stiff calibration plates in order to measure the pressure from the explosions, as well as on aluminum plates in order to determine the structural response.

Analytical and numerical computations were performed in order to evaluate them compared to the experimental results. Numerical simulations were performed with both a Lagrangian and an embedded FSI approach.

The analytical approach underestimated the displacements. However, the results indicated that the analytical calculations could have given better results at lower deformations.

The Lagrangian approach overestimated the displacements. Additional simulations indicate that this could be due to overestimation of the load by the AIRB approach in EUROPLEXUS.

The embedded FSI approach underestimated the displacements. The simulations performed indicate that the description of the load is fairly accurate, but that the displacements were underestimated due to the use of elements that were too large.

Contents

Nomenclature

Acronyms

ALE	Arbitrary Lagrangian-Eulerian
CCFV	Cell-Centered Finite Volumes
CPU	Central Processing Unit
DIC	Digital Image Correlation
EoS	Equation of State
FE	Finite Element
FEA	Finite Element Analysis
FSI	Fluid-structure interactions
FV	Finite Volume
HE	High Explosives
JWL	Jones-Wilkins-Lee
LE	Low Explosives
MDOF	Multi-Degree-of-Freedom
MPP	Massively Parallel Processing
NCFV	Node-Centered Finite Volumes
PDEs	Partial Differential Equations
SDOF	Single-Degree-of-Freedom
SIMLab	Structural Impact Laboratory
SPH	Smoothed Particle Hydrodynamics

Greek Letters

α	Johnson's dimensionless damage number
α	The linear thermal expansion coefficient

α, β	Rayleigh proportional damping coefficients
α_0	Johnson's damage number in terms of impulse
α_{bal}	Dimensional scaling factor
β	Geometrical number for quadrangular plates
$\boldsymbol{\chi}$	Referential or ALE coordinates
$\hat{\boldsymbol{\Omega}}$	Reference domain in ALE formulations
$\hat{\boldsymbol{\phi}}$	Mapping function in ALE formulations
$\hat{\boldsymbol{\sigma}}, \hat{\sigma}_{ij}$	The corotational Cauchy stress
$\boldsymbol{\phi}$	Mapping function
$\boldsymbol{\psi}$	Mapping function related to ALE formulations
$\boldsymbol{\sigma}'$	Deviatoric stress tensor
$\boldsymbol{\sigma}^{\nabla J}$	The Jauman rate of the Cauchy stress
χ	Taylor-Quinney coefficient
δ	The mid-point deflection of a quadrangular plate
γ	Heat capacity ratio of a given gas
Γ_0, Γ	Boundary of initial and current configuration Ω_0
λ	Aspect ratio for quadrangular plates
∇	Spatial gradient operator
ν	Poisson's ratio
Ω_0, Ω	Initial and current configuration of a body
ω_i	Eigenfrequency of mode j
ω_{max}	Maximum eigenfrequency
ϕ	Modified damage number
ϕ_q	Damage number for quadrangular plates
ψ	Geometrical damage number
ρ	Density of detonation products
ρ	Material density
ρ_0	Density of air at ambient pressure
ρ_0	Density of uncompressed air
ρ_0, ρ	Original and current density

ρ_{bal}	Density of gas, used for modelling in EUROPLEXUS
ρ_e	Density of explosives
ρ_f	Flow density
ρ_{sol}	Density of the explosive in solid state
ρ_s	Air density behind wavefront
σ	The Cauchy stress or true stress
σ_0	Yield stress
σ_d	The damage stress
σ_{eq}	Equivalent stress
θ	Temperature
ε^p	Plastic strain
ξ	Damping ratio in mode j

Latin Letters

$\hat{\boldsymbol{a}}$	Mesh acceleration in ALE formulations
$\hat{\boldsymbol{D}}$	The corotational rate-of-deformation
$\hat{\boldsymbol{u}}, \hat{u}$	Mesh displacement in ALE formulations
$\hat{\boldsymbol{v}}, \hat{v}$	Mesh velocity in ALE formulations
$\boldsymbol{a}$	Nodal acceleration vector
$\boldsymbol{B}$	Matrix of shape functions derivatives
$\boldsymbol{b}$	Force per unit mass
$\boldsymbol{C}^{\sigma J}$	The material tangent moduli
$\boldsymbol{D}$	The rate-of-deformation tensor, symmetric part of $\boldsymbol{L}$
$\boldsymbol{D}^e, \boldsymbol{D}^t, \boldsymbol{D}^p$	Elastic, thermal and plastic part of the rate-of-deformation tensor, $\boldsymbol{D}$
$\boldsymbol{E}$	The Green strain
$\boldsymbol{F}$	The deformation gradient
$\boldsymbol{F}^{ext}, \boldsymbol{F}^{int}$	External and internal force vector
$\boldsymbol{I}$	2nd order unit tensor
$\boldsymbol{L}$	The velocity gradient
$\boldsymbol{M}$	Lumped mass matrix

$\boldsymbol{P}$	The nominal stress tensor
$\boldsymbol{R}$	The rotation matrix
$\boldsymbol{S}$	The second Piola-Kirchhoff (PK2) stress tensor
$\boldsymbol{u}$	Displacement field
$\boldsymbol{v}$	Velocity field
$\boldsymbol{W}$	The spin, skew-symmetric part of $\boldsymbol{L}$
$\boldsymbol{X}$	Material (Lagrangian) coordinates
$\boldsymbol{x}$	Spatial (Eulerian) coordinates
$\dot{\boldsymbol{u}}$	Velocity of a material point
$\dot{p}$	Equivalent plastic strain rate
$\dot{p}_0$	The reference strain rate
$\dot{T}$	The time derivative of the temperature
$\hat{v}_i$	Mesh velocity in ALE formulations
A	Area of quadrangular plate
A	Cross-sectional area
A, B, n, m	Material parameters in the von Mises yield function
A, B, R_1, R_2, ω	Coefficients in JWL equation of state
A_0	Area over which the impulse is imparted
A_0	Initial cross-sectional area
a_0	Speed of sound in air at ambient pressure
B	Breadth of quadrangular plate
b	Wave decay parameter
C	Material constant governing strain rate sensitivity
c	The convective velocity in ALE formulations
c_d	Dilatational wave speed
C_p	Specific heat
E	Young's modulus or modulus of elasticity
e	Engineering strain
E_A	Activation energy
$e_{int,bal}$	The internal specific energy

E_{TNT}	Nominal energy of the explosive charge
F	Axial force
F	Yield function
f	The von Mises yield function
f_{bal}	Square root factor used for modelling in EUROPLEXUS
H^d_{exp}	Heat of detonation of an explosive
H^d_{TNT}	Heat of detonation of TNT
I	The total impulse
I_0	The impulse per area
I^+_s, I^-_s	Positive and negative impulse for a blast wave
J	Determinant of Jacobian between spatial and material coordinates, $J = det[\partial x_i / \partial X_j]$
k	Thermal conductivity of the material
L	Current length
L	Element length
L	Length of quadrangular plate
L_0	Initial length
L_x, L_y, L_z	Lengths of rectangular box
m_i	Mass of particle
N	Number of particles
N_{els}	Number of elements
P	Pressure
p	Plastic strain
$P(t)$	Pressure-time function for an ideal blast wave
P_0	Ambient (static) pressure
p_0	Atmospheric pressure
p_{bal}	Initial gas pressure
P_{dyn}	Dynamic pressure
P_r	Reflected pressure
P_{stag}	Stagnation pressure

P_s	Side-on (incident) pressure
P_s^+, P_s^-	Positive and negative peak side-on pressure
p_{TNT}	Balloon over-pressure for modelling in EUROPLEXUS
P_x, P_y, P_z	Pressure in the three Cartesian directions
Q	Heat energy
q	Heat flux per unit area
R	Distance from the center of a source of explosion
R	Isotropic hardening variable
s	Engineering stress
s	Specific heat source term
t	Plate thickness
t	Time
T^*	The homologous temperature
t^+, t^-	Duration of positive and negative phase for a blast wave
T_0	Room temperature
t_a	Arrival time of the shock wave
T_m	Material melting temperature
u	Velocity
u_w	Wavefront velocity
V	Current volume of the explosive
v	Fluid velocity (particles)
v	Impact velocity
V_{bal}	Balloon volume for modelling in EUROPLEXUS
v_{det}	The detonation velocity
v_i	Material velocity
v_i	Velocity of particle
V_n	Element volume
V_{sol}	Volume of the explosive in solid state
w	Arbitrary velocity of ALE mesh
w	Hyperelastic potential on reference configuration

W_{EXP}	Weight of an explosive
W_E	TNT equivalent mass of an explosive
W_k	Total particle translational kinetic energy
w_k	The specific translational kinetic energy
W_P	Scalar describing isotropic hardening
x_{air}	Measure of the amount of air modelled in EUROPLEXUS
Z	Scaled distance

Mathematical Symbols

$[\boldsymbol{C}]$	The damping matrix
$[\boldsymbol{K}^{\text{eff}}]$	The effective stiffness matrix
$[\boldsymbol{M}]$	The mass matrix
ΔL	Incremental change in length
Δt	Time increment in numerical integration
Δt_{cr}	Critical time increment in numerical integration
$\frac{\partial f}{\partial t}$	The material time derivative in ALE formulations
$\frac{D\sigma}{Dt}$	The material rate for the Cauchy stress tensor
$\{\boldsymbol{R}^{\text{dmp}}(t)\}$	The damping force vector
$\{\boldsymbol{R}^{\text{ext}}(t)\}$	The external force vector
$\{\boldsymbol{R}^{\text{ine}}(t)\}$	The inertia force vector
$\{\boldsymbol{R}^{\text{int}}(t)\}$	The internal force vector
$\{\boldsymbol{\alpha}\}$	Vector describing kinematic hardening
$\{\dot{\boldsymbol{D}}(t)\}$	The nodal point velocity vector
$\{\boldsymbol{\sigma}\}$	State of stress vector
$\{\boldsymbol{E}\}$	Elastic material property matrix
$\{\boldsymbol{D}(t)\}$	The nodal point displacement vector
$\{\ddot{\boldsymbol{D}}(t)\}$	The nodal point acceleration vector
$\{d\boldsymbol{\sigma}\}$	Stress increment vector
$\{d\boldsymbol{\varepsilon}\}$	Strain increments
$\{d\boldsymbol{\varepsilon}^e\}$	Recoverable (elastic) strain increments
$\{d\boldsymbol{\varepsilon}^p\}$	Nonrecoverable (plastic) strain increments

$d\sigma$	Stress increment
$d\varepsilon$	Strain increment
$d\sigma_i$	Stress increment in the ith direction
$d\tau_{ij}$	Shear stress increment in the i-j plane

Chapter 1

Introduction

Explosions can be caused by numerous reasons. Accidental explosions, military operations or terrorist attacks are examples of causes. In e.g. the petrochemical or nuclear industry, incidents may result in explosions, which may again lead to causalities and severe material damage. Persons who intentionally want to harm others or create fear – terrorists – may also very well make use of the large extent of damage related to explosions to spread their message. Several examples of these type of malicious actions could have been brought up.

Explosion protection is of major importance in many settings, e.g. for oil rigs and civil engineering structures. Protection against both external and internal explosions and deflagrations are important considerations for these type of installations. What type of material have the best properties when it comes to blast resistance? Which one is the most cost effective? And what about portability? These are questions that may be raised when decisions regarding blast load protection are to be taken. In other words there are several aspects that must be taken into consideration when selecting protective solutions.

Research is necessary in order to obtain sufficient protection against blast loading. This includes both full-scale experimental and numerical simulation methods. By obtaining accurate material models and robust simulation programs, effects from blast loads can be predicted and analyzed. The most obvious advantages of simulating blast load problems – instead of performing full-scale experiments, which was widely used in times past – is the reduced cost and that output data can easily be abstracted. Also, since adjustments easily can be done in numerical experiments, studies can be performed on different parameters and their effects on the total solution can be revealed. This type of study is of course more cumbersome for full-scale experiments.

In this thesis, a study of light-weight, aluminum plates subjected to blast loading will be carried out. Through relevant theory, experiments and numerical simulations, the behaviour of the aluminum plates due to the blast loading will be studied. By

comparing experimental results with numerical solutions, an assessment of numerical simulation methods' ability of reproducing the nature of blast load problems will be given. In this way, an increased understanding of the blast load phenomenon and material responses are hopefully obtained.

A short description of the content in each chapter is given below.

Chapter 2 - Theory
In this chapter some relevant theory will be presented. Blast related theory, background for the Johnson-Cook material model, different finite element formulations and an introduction to the computer code EUROPLEXUS are some of the presented topics.

Chapter 3 - Preliminary Studies
An initial exploration of the problem to be studied was performed. This included an analytical evaluation, evaluation of stand-off distance and also a mesh-sensitivity study.

Chapter 4 - Experimental Work
The blast load experiments carried out are described in this chapter. Experimental setup and results are presented for both the calibration and the component tests.

Chapter 5 - Material Tests
Details about the material testing are given. Experimental setup and results from the tensile tests are presented.

Chapter 6 - Material Model
A material model for the tested aluminum alloy is created based on inverse modeling in EUROPLEXUS.

Chapter 7 - Numerical Simulations
Different numerical methods were used to simulate the experiments carried out. Results obtained from a Lagrangian approach and more complex approaches, which take FSI effects into account, are presented. Also, through variation of different parameters, a study of their effect on the numerical solutions were carried out.

Chapter 2

Theory

2.1 State of the Art

Much effort have been put into the study of plates subjected to impulsive loading over the last decades. Numerous papers present several types of problems, with a large variety in geometries, loading and boundary conditions. An important part in scientific research is to get an overview of previous observations in similar studies. This will therefore be emphasized herein. In order to narrow down the area of interest, the focus will mainly be put on square, edge-clamped metal plates exposed to free air blast loading. However, results from other type of studies will be included in some parts if relevance can be found. Hopefully, this will give an overview of available and relevant research results and observations.

Preliminary discussion

What are the objectives of today's research within structures subjected to blast loading? What are the researchers looking for? And what type of approaches do they use? The overall objective in today's research within structures subjected to blast loading, is to obtain realistic descriptions of material responses and of the blast loading itself. Since full-scale testing is both expensive and hard to validate, other alternatives are necessary. This is where the Finite Element Method (FEM) plays an important role. By comparing experimental results with corresponding results obtained by use of finite element codes, researchers are attempting to obtain reliable solution methods, within reasonable costs. These methods can then be used to predict the complex structural behaviour due to blast loading. However, full-scale experiments will never be redundant, as this is the only way of obtaining fully realistic results.

Several approaches exist within the field of numerical simulations of blast load problems, both simple and quite complex ones. Recent advances in commercially

available finite element codes, have introduced numerical methodologies suitable for simulations of coupled blast-structural response. Arbitrary Lagrangian-Eulerian (ALE), embedded formulations, Discrete Particle Method (DPM) and Smoothed Particle Hydrodynamics (SPH), together with classical Lagrangian structural analysis methods, give the opportunity of a so-called fully-coupled approach in the analysis of blast-structure interactions [1]. Accuracy and cost, in terms of computational time, are for all practical purposes factors that are decisive for the choice of numerical approach. Ideally, the most precise method should be chosen, but if this entails an impractical amount in computational time, other alternatives must be considered. These are important considerations – not only within analysis of structures subjected to blast loading – but within many engineering disciplines in which the FEM is employed.

The FEM has unquestionably contributed to progress within research of structures exposed to blast loading. Today, an increasingly reliance on finite element simulations can be observed among engineers who seek to understand the complex structural mechanisms during blast load events. However, in order to obtain precise simulations of blast load problems, a broad and thorough understanding of both the physics in the problem and the limitations in the finite element codes are necessary. Otherwise, simulation results will be worthless. This is something that should be clear to anyone who wants to utilize the opportunities of this comprehensive method.

Previous observations

Menkes and Opat [2] studied the response pattern of fully clamped aluminum beams, subjected to impulsive loading, and divided it into the following three cases:

- Mode I: large inelastic deformation of the entire beam

- Mode II: large deformations and tensile-tearing over the support

- Mode III: transverse shear failure at the support

Subsequently, these modes of failure were identified for other type of structures. Teeling-Smith and Nurick [3] identified these modes for circular plates, while Nurick and Shave [4] observed this for square plates. Nurick and Martin [5, 6] have reported the associated analysis. This way of categorizing the deformation pattern are commonly referred to in the literature, and is therefore considered as fundamental in this context.

Some important results obtained in the recent years will now be highlighted. Several papers can be looked into for a thorough review of results and observations obtained in earlier years. Nurick and Martin [5] presented an overview of theoretical and experimental results up to 1989, primarily for uniformly loaded plates. In the paper by Nurick and Shave [4], a study of the deformation and tearing of thin square plates subjected to impulsive loading is presented. They have also given a review of earlier work within this subject. Nurick et al. [7] highlighted the significant effects of the

boundary conditions for the purpose of predicting tearing, and similar discussion were taken by Wierzbicki and Nurick [8].

Balden and Nurick [9] performed numerical simulations of uniformly loaded circular plates. In fact they described the numerical results from two experimental studies, one of them published by Teeling-Smith and Nurick [3], in which the deformation and post-failure response of a plate subjected to uniform blast loading were investigated. Among others, they emphasized the close correlation to what was observed by Teeling-Smith and Nurick, for both mode I and mode II responses.

Jacob et al. [10] studied fully clamped, circular steel plates subjected to blast loading. They investigated the effect of stand-off distance and charge mass on the response of plates with radius of 53 mm. The blast loads were travelling through tubular structures, giving a focused or localized loading, at least for the nearest stand-off distances. For stand-off distances greater than 100 mm, a uniformly distributed loading over the structure was observed. The response of the plates varied from large inelastic deformation to complete tearing at the boundary.

Neuberger et al. [11] focused on the difference between transient dynamic and residual deflections on blast loaded, fully-clamped, circular steel plates. In this paper they introduced the term *springback*, which represents the difference between the peak transient deflection and the residual plastic deflection. In addition to experimental results, a numerical investigation of the differences is reported. In addition they have presented a quantitative relation between the magnitude of the springback effect and the stand-off distance.

Børvik et al. [12] investigated edge-clamped steel plates subjected to sand-buried blast loading. In a fully coupled approach, they used a discrete particle method to determine the load due to the high explosive detonation products, the air shock and the sand. The method was validated against experimental tests on square, edge-clamped steel plates, where spherical 150 g C4 charges were detonated at various stand-off distances. They observed good quantitative agreement between experimental data and the numerical simulations. Further, they concluded that the discrete particle approach is able to describe the physical interactions in the problem.

Sprangers et al. [13] focused on numerical simulations of blast loaded, thin, square aluminum plates. Numerical results were validated against small-scale blast load experiments. To capture the dynamic response of the plate, 3D high-speed Digital Image Correlation (DIC) was used. In order to study how different parameters affect the accuracy of the solution, different numerical configurations were employed. This included variation in element type and element size, among others. Due to sufficiently small shear strains, employment of shell elements were found to give acceptable results when it comes to modeling the deformation. In addition they concluded that a reduction in computational time, without significant loss of accuracy, can be observed when using an explicit integration scheme instead of an implicit procedure.

Alia and Souli [14] described an air blast simulation by use of Eulerian multi-material formulation. Validation of their numerical approach was done by comparing numerical results with corresponding results obtained from experiments. In addition, simulated pressure-time histories and pressure impulses were in accordance with experimental results. According to Alia and Souli [14], the physical phenomena in a blast load problem can very well be described using a method based on Eulerian multi-material formulations.

Olovsson et al. [15] compared the coupled Eulerian-Lagrangian formulation and the corpuscular approach. They showed that the corpuscular method represents a useful way of simulating close-range blast effect on structures. Numerical robustness, fast and easy to use, were some of the characteristics given by Olovsson et al. [15]. A good agreement was further observed between results obtained from the corpuscular approach, corresponding ALE simulations, and available experimental data. However, they emphasized that several aspects regarding the implementation in the finite element code LS-DYNA should be improved, in order to make the method even more applicable.

Counter-intuitive behaviour of plates have been reported by many authors, e.g. Flores-Johnson and Li [16], Galiev [17] and Li et al. [18]. Flores-Johnson and Li [16] investigated numerically the counter-intuitive response of square plates subjected to blast loading. This effect can in some cases be seen for elastic-plastic materials subjected to blast loading, and for plate materials this means that the deformation end up in the opposite direction of the loading. Flores-Johnson and Li [16] defined a counter-intuitive region for both simply and fully supported plates, in terms of non-dimensional numbers. It was further observed that a reduction in boundary constraints lowered the chance of the rebounding instability to occur. Asymmetrical response of the square plates in the counter-intuitive regions was also reported.

Nowadays, a drastic increase in use of numerical simulation methods can be seen. However, analytical approaches are still employed, and serve as a useful supplement to numerical methods. Nurick and Martin [5, 6] and Jacob et al. [19] focused on predictive, empirical methods, based on experimental observations for different materials and experimental setups. Based on results from previous performed experiments, Nurick and Martin [6] pursued a relation for prediction of mid-point deflection for impulsively loaded plates. By putting both geometrical and material properties, in addition to loading conditions, into a dimensionless number, an expression for the deflection-thickness ratio was obtained. Relations for both circular and quadrangular plates were established.

2.2 Blast Load

In this section relevant theory for the blast phenomenon will be presented.

2.2.1 Groups of Explosions

Explosive materials, or explosives, are reactive materials that contain a great amount of potential energy. Rapid release of this energy is known as an explosion, which is characterized by production of light, heat, sound and pressure [20]. This definition is somewhat incomplete, and more thoroughly definitions exist. However, due to the fact that it is easily understandable and presents the basic concepts quite intuitively, this definition was chosen.

Explosions can be caused by a countless number of different activities, but generally they can be divided into three groups [21]:

- Natural explosions
- Intentional explosions
- Accidental explosions

Volcano eruption and lightning are examples of natural explosions. Intentional explosions are in some way arranged and to some extent controllable. Nuclear weapon explosions and firing of guns are examples of such type of explosions. Accidental explosions are characterized by lack of control regarding the release of the energy. Combustion explosions in enclosures, for instance in gas containers, are most often unintended and are therefore regarded as an accidental explosion.

2.2.2 Explosives Classification

Explosives can either detonate or deflagrate. Explosives that detonate are called High Explosives (HE), while explosives that deflagrate are referred to as Low Explosives (LE). HE are characterized by supersonic combustion propagating through high intensity shock waves, while subsonic combustion through heat transfer is characteristic for LE [20]. LE are included here only for completeness, and will not be discussed extensively in this text.

Comparison of different types of HE can be done in multiple ways. One way, which is widely accepted as a basis for comparison, is to convert the mass of the relevant explosive into TNT equivalent mass. This can be achieved by multiplying the mass of the explosive by a conversion factor, based on its specific energy relative to that of TNT [22]. Thus, a relation between a given explosive's demolition power to that of TNT can be established. In Table 2.1, the relative effectiveness factor for some types of HE are presented [23].

Table 2.1: Relative effectiveness factor for some explosives [23].

Explosive	Relative effectiveness factor
ANFO (94% AN + 6% fuel oil)	0.74
TATP (Acetone peroxid)	0.80
Amatol (50% TNT + 50% AN)	0.91
Trinitrotoluene (TNT)	1.00
Amatol (80% TNT + 20% AN)	1.10
Composition C4 (91% RDX)	1.34
Nitroglycerin	1.54
Hexogen (RDX)	1.60

The values for the relative effectiveness factors in Table 2.1 are not constant. Other values may very well be used, but Table 2.1 gives at least a roughly indication of expected values for different HE. In the case of C4 for instance, use of a relative effectiveness factor ranging from 1.19 to 1.37 have been reported [13]. The variation is related to the scope of the study, i.e. what parameter is to be measured.

2.2.3 Explosion Processes

Different methods can be used to initiate explosives, e.g. percussion or use of electrical energy. The choice of method will depend on both the relevant explosive and area of application. However, the amount of energy needed to initiate the explosives is called the activation energy, E_A. A diagrammatic representation is given in Figure 2.1. The explosive material contains a given amount of energy prior to the ignition. After the reaction process starts, the reaction energy decreases to a level beneath the initial level. For this schematic description of an exothermic reaction, Q is representing the release of heat energy [22].
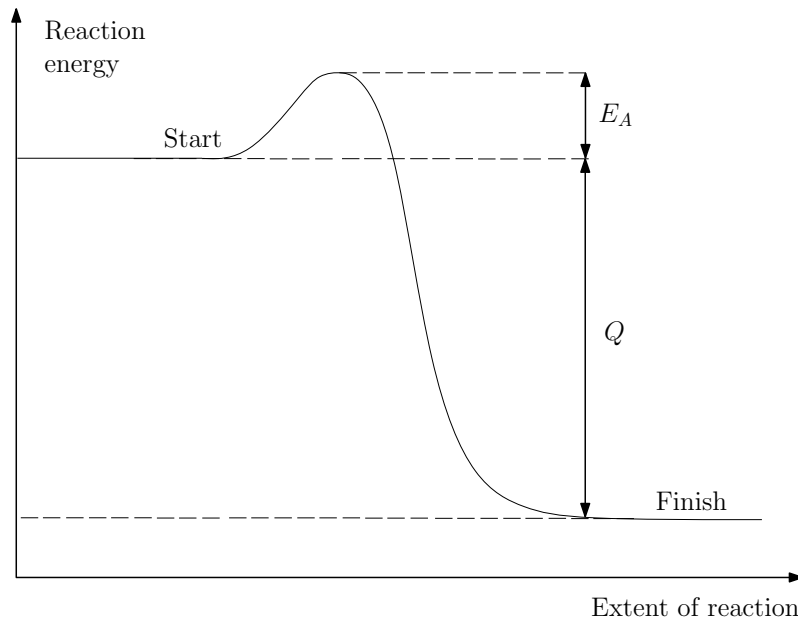
Figure 2.1: Energy changes in explosion reaction.

Explosive can be classified as primary or secondary, based on sensitivity when it comes to ignition. A primary explosive is more sensitive than a secondary explosive, thus less energy is required to obtain ignition. TNT is an example of a secondary explosive. A commonly used method for initiation of secondary explosives is the bridgewire method. For the bridgewire method, a high tension pulse causes a filament to vaporize, resulting in high temperatures and a shock wave. The shock wave is often sufficient to initiate a secondary explosive [22].

In an explosive reaction, hot gases which can be at pressures from 100 kbar up to 300 kbar are generated. The temperatures can be as high as 3000-4000°C. This will in turn force the surrounding air out of the volume it occupies. This lead to the forming of the blast wave - layers of compressed air containing most of the energy released by the explosion. The pressure will decrease as a result of the expansion of the explosive gases. Also, in the front of the blast wave, the pressure will decrease with increasing distance from the source. Before static equilibrium is regained, a state of pressure level below atmospheric is observed, often referred to as the negative phase. This is due to momentum of the gas particles, which will make the gases to "over-expand". Thus, a reversal of flow towards the source of the explosion will occur before static equilibrium is recovered [22].

2.2.4 Ideal Blast Wave

In Chapter 2.2.3, a blast wave was referred to as layers of compressed air. More exact, a blast wave includes both sonic compression waves, shock waves and rarefaction waves. The characteristics of a blast wave can vary, depending on how and

when the energy is released, as well as the distance from the point of detonation [24].

Before going into details regarding the pressure-time history of an ideal blast wave, an introduction of different measures of pressure will be given.

For ideal blast waves, it is assumed that propagation occur freely through the air. However, modification of these waves will occur if interactions with solid or more dense objects are encountered [25]. In order to describe the blast wave induced changes in pressure, different measures must be introduced. Important terms in this discussion are:

- Ambient (static) pressure, P_0

- Dynamic pressure, P_{dyn}

- Side-on (incident) pressure, P_s

- Reflected pressure, P_r

The static pressure is the pressure level prior to the forming of blast waves, and often this corresponds to the atmospheric pressure. The dynamic pressure is directly related to motion of the blast waves, and can be expressed as a function of the flow density, ρ_f, and velocity, u [24]:

$$P_{dyn} = \frac{1}{2}\rho_f u^2 \tag{2.1}$$

The stagnation pressure, P_{stag}, can be given as [24]:

$$P_{stag} = P_{stat} + P_{dyn} \tag{2.2}$$

The stagnation pressure can be defined as the static pressure at a stagnation point in a fluid flow [26].

Two more important definitions are the side-on pressure, P_s, and the reflected pressure, P_r. The side-on pressure, or incident pressure, is measured perpendicular to the propagation direction of the blast wave, while the reflected pressure is measured parallel to propagation of the blast wave. Graphical descriptions of how these pressures are measured are given by Bjerketvedt et al [24], and these are reproduced in Figure 2.2.
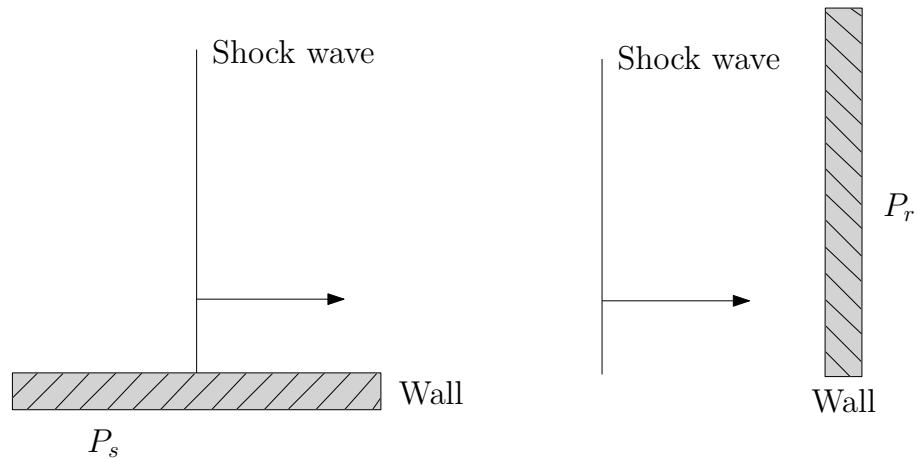
Figure 2.2: Side-on and reflected pressure [24].

Characteristics of the Ideal Blast Wave

By including terms like *ideal* or *idealized*, it is assumed that the explosion occurs in a still, homogeneous atmosphere. In addition, the source is assumed to be spherical symmetric, such that the characteristics of the blast are functions only of the distance from the center of the source, R, and the time, t [25]. The main characteristics of an ideal blast wave are stated below [27]. For a graphical description, see Figure 2.3.

- The arrival time of the shock wave to the point in consideration is represented by t_a. For the idealized case, a discontinuous rise in the pressure level can be observed at this point in time.

- The peak overpressure is reached for $P(t) = P(t_a) = P_0 + P_s^+$. The pressure level starts decaying, and will at time $t = t_a + t^+$ intersect the ambient pressure level, P_0.

- The positive phase have a duration of t^+. The area which the positive phase represents is denoted the positive (incident overpressure) impulse, I_s^+, given in Equation (2.3).

- The positive phase is followed by a negative phase of duration t^-. The expression for the negative impulse, I_s^-, is given in Equation (2.4). Maximum negative pressure is reached for $P(t) = P_0 - P_s^-$.

- Eventually, the pressure level returns to the ambient pressure, P_0, at time $t = t_a + t^+ + t^-$.

11
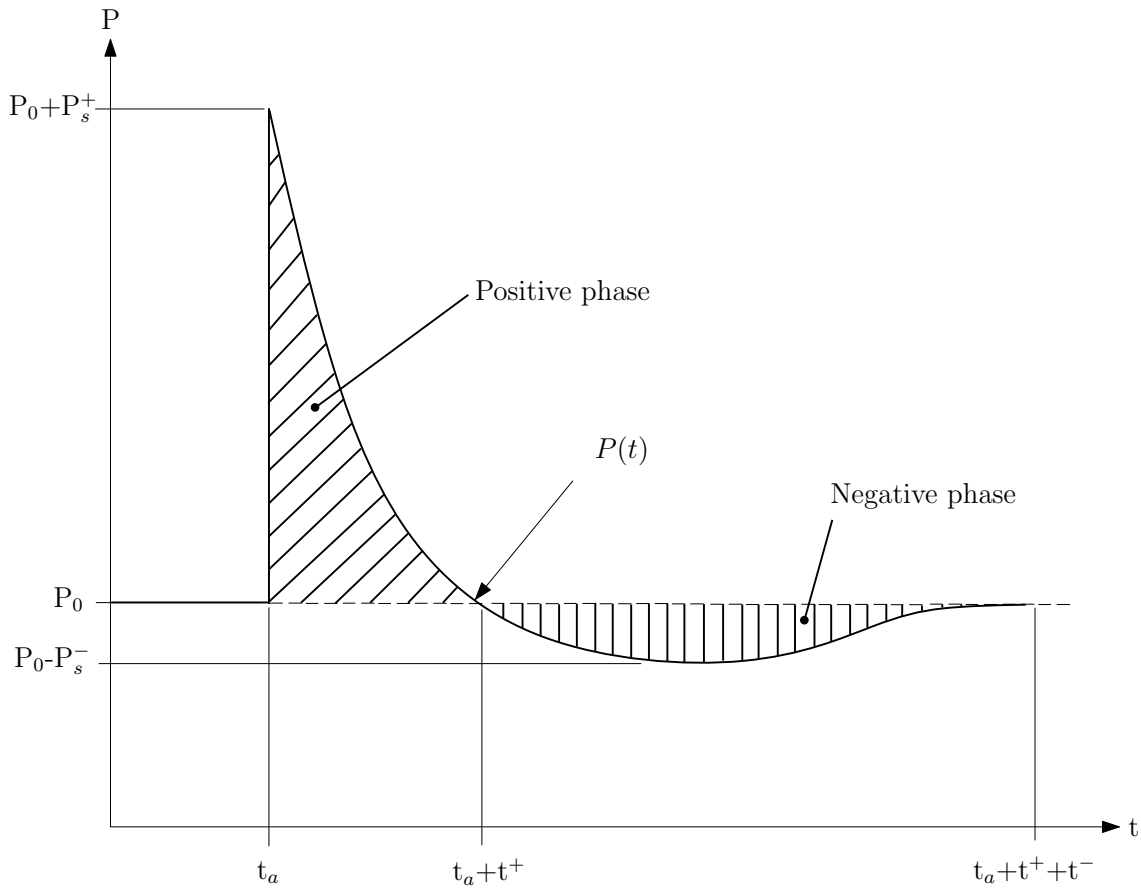
Figure 2.3: Pressure-time profile for ideal blast wave.

$$I_s^+ = \int_{t_a}^{t_a+t^+} [P(t) - P_0]\,\mathrm{d}t \tag{2.3}$$

$$I_s^- = \int_{t_a+t^+}^{t_a+t^++t^-} [P(t) - P_0]\,\mathrm{d}t \tag{2.4}$$

Representation of the Ideal Blast Wave

Several descriptions of the pressure-time history of the ideal blast wave exist, both simple and quite complex formulations. Expressions for this type of formulations are given by Baker [25], where emphasis has been given on fitting the positive phase. The simplest one only includes two parameters, where a linear decay of pressure is assumed. This formulation is given by:

$$P(t) = P_0 + P_s^+(1 - \frac{1}{t^+}), \quad \text{for } 0 < t \le t^+ \tag{2.5}$$

In Equation (2.5), t is the time after arrival of the shock wave. The true value for P_s^+ is usually preserved when fitting this expression to data. Also, the positive phase duration, t^+, is adjusted such that the true positive impulse, I^+, is maintained [25].

A more complex formulation, called the modified Friedlander equation, is also mentioned by Baker [25]. This equation is defined by:

$$P(t) = P_0 + P_s^+(1 - \frac{t}{t^+})e^{-b\frac{t}{t^+}} \tag{2.6}$$

which again stems from the original Friedlander equation. The only difference is the additional parameter, b, which describes the decay of the curve. The modified Friedlander equation is stated to be the best compromise, when both desired accuracy and applicability of the formulation are taken into account. By allowing adjustment to conform to the most important blast wave properties, without getting too complex, the modified Friedlander equation has proven to be an adequate approach [25].

Blast Wavefront Parameters

Expressions for wave front velocity, u_w, air density behind the wave front, ρ_s, and the maximum dynamic pressure, $P_{dyn,max}$, are given as [22]:

$$u_w = \sqrt{\frac{6P_s + 7P_0}{7P_0}}a_0 \tag{2.7}$$

$$\rho_s = \frac{6P_s + 7P_0}{P_s + 7P_0}\rho_0 \tag{2.8}$$

$$P_{dyn,max} = \frac{5P_s^2}{2(P_s + 7P_0)} \tag{2.9}$$

where ρ_0 is the density of air at ambient pressure ahead of the blast wave, and a_0 is the speed of sound in air at ambient pressure. By assuming that air behaves as a perfect gas, it can be shown that the following relation for reflected peak pressure, P_r, may be obtained [22]:

$$P_r = 2P_s\left[\frac{7P_0 + 4P_s}{7P_0 + P_s}\right] \tag{2.10}$$

The lower limit for the reflected pressure, $P_r = 2P_s$, represents very weak shocks, $P_s \ll P_0$, for which acoustic approximations are valid. For stronger shocks, the value

of the reflected pressure increases dramatically. The upper limit is $P_r = 8P_s$. This can be obtained from the Rankine-Hugoniot relations. Note that these limits are constructed under the assumption that air behaves as a perfect gas. Under strong shock conditions however, where high pressures and temperatures are present, this assumption may underestimate the values of the reflected pressure severely [25].

2.2.5 Air Burst

For explosions above ground, the distribution of blast waves will be affected by the reflecting effects from the ground. The first wave that hits the ground is called the incident or initial wave. The reflection of this wave will interact and merge with the initial blast wave, resulting in a so-called Mach front. This front is a result of the reinforcement of the incident wave by the ground surface. A simple, graphical description is given in Figure 2.4.
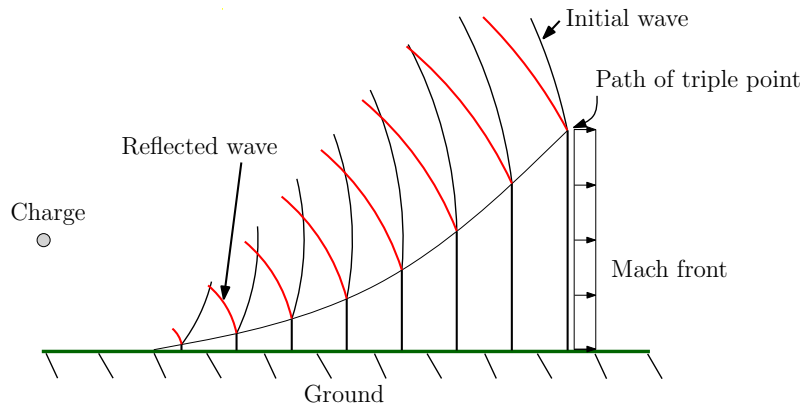
Figure 2.4: Schematic description of the Mach front.

The characteristics of the Mach front are basically the same as for the initial wave. However, the magnitude of the blast parameters are somewhat larger [28].

2.2.6 Internal Explosions

Explosions that occur inside a confined space are defined as internal explosions, see Figure 2.5. Complicated blast wave phenomena can be observed in this type of blast environment. However, initially the characteristics of an ideal blast wave, as described in Chapter 2.2.4, can be recognized. That is a sharp spike in the time-pressure curve, and this phase may be referred to as the *shock pressure* phase. The duration of this phase depends on the shock front velocities and the distance from the charge to the surrounding surfaces. The duration of this phase is in general very short [29].
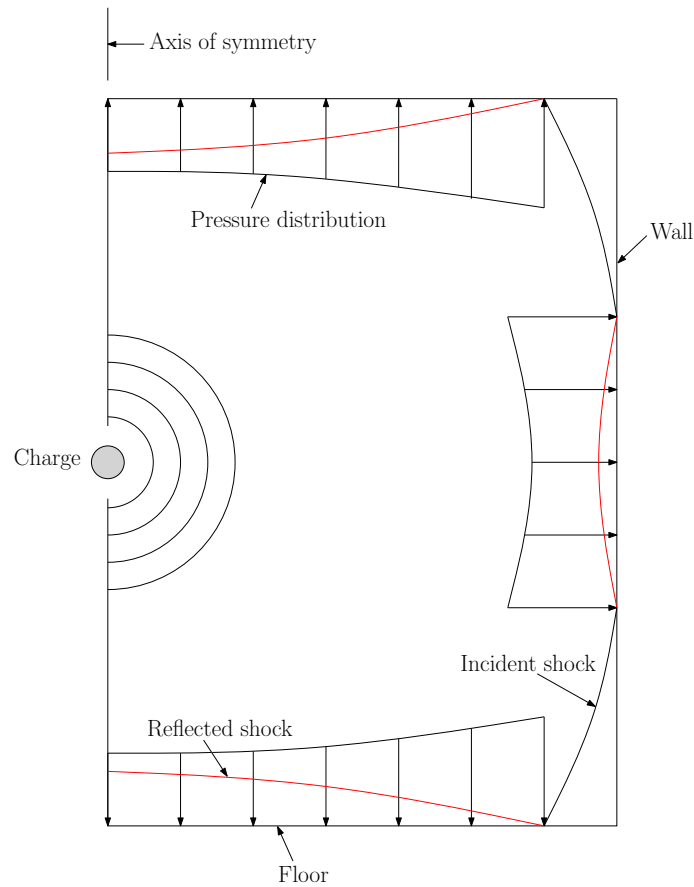
Figure 2.5: Shock reflections from walls during internal detonation [29].

Shortly after the shock pressure phase, the *gas pressure* phase, characterized by a complicated blast environment, comes into existence. Here, reflected shock waves propagate and interact, leading to difficulties with defining the blast environment. This process goes on for quite a long time, compared to the shock pressure phase. The gas pressure phase, sometimes referred to as a quasi-static or a pseudo-static phase, terminate when the pressure reaches the ambient level [29].

2.2.7 Blast Load Design

An important part in design of structures exposed to blast loading is to reveal the characteristics of the relevant blast loading. In the light of research and different type of test programs through out the years, procedures for blast load design have been developed. Examples are the manuals UFC 3-340-02 [28] and TM 5-855-1 [30], in addition to the computer program CONWEP [31].

UFC 3-340-02 is one of the most widely used publications within blast load design. This technical manual contains procedures for designing structures to provide protection against blast effects, both for civilian and military purposes [32]. In UFC

3-340-02, step-by-step analyses and design procedures can be found. This include information about the blast loading, principles of non-linear dynamic analyses, and considerations about design of reinforced concrete and steel structures. The TM 5-855-1, on the other hand, contains design and analysis procedures for structures subjected to blast effects from conventional weapons. Information about blast effects and blast effects on structures can be found in this technical manual. In addition, close-form equations for generating pressure-time histories are given. However, no blast wave-structure phenomena is taken into account, which means that this is a highly simplified approach. Also, for close-range blast loading, these assumptions result in poor approximations.

A commonly used basis within blast load design, is the scaled distance, Z. Given the standoff distance, R, and the TNT equivalent mass, W_E, a cube root scaling method, given in design standards, can be employed to find the scaled blast distance [28]. The scaled distance is given as:

$$Z = \frac{R}{W_E^{\frac{1}{3}}} \tag{2.11}$$

The TNT equivalent mass, W_E, of an explosive of a specific shape can be expressed as a function of the heat of detonations for the given explosive and that of TNT. The following expression is found in TM 5-1300 [28]:

$$W_E = \frac{H_{exp}^d}{H_{TNT}^d} W_{EXP} \tag{2.12}$$

where

H_{exp}^d	heat of detonation of explosive in question
H_{TNT}^d	heat of detonation of TNT
W_{EXP}	weight of the explosive in question

Based on the scaled distance, Z, diagrams given in the manual can be used to estimate different blast wave parameters for three different burst environments, namely free air burst, air burst and surface burst [32]. For free air burst, the ground does not disturb the blast wave propagation. For the air burst group, the reflections from the ground interact with the incident wave, according to Figure 2.4. Surface bursts are valid for detonations close to or on the ground. In this case, the incident wave and the reflected wave due to the ground will merge immediately after detonation. This leads to a hemispherical shaped, reinforced wave propagating away from the point of detonation.

CONWEP is a computer program based on the empirical equations made by Kingery and Bulmash [33]. They developed equations for predicting air blast parameters for both spherical air burst and hemispherical surface bursts. Graphical representations

of the equations implemented in CONWEP can be found in TM 5-855-1. Regarding the representation of the pressure-time curve, CONWEP gives a pressure-time function based on the modified Friendlander equation. This equation was introduced in Chapter 2.2.4. In the TM 5-855-1, on the other hand, the decay of the pressure-time function is assumed to be constant. The estimated impulse is preserved however, even though the triangular representation of the pressure decay is a simplification [32].

The equations made by Kingery and Bulmash are based on experiments. This is important to have in mind when using the fitted curves from these experiments, which is the case when employing the scaled distance, Z. Since very few experiments were performed for scaled distances less than 0.397 m/kg^3, estimates for small scaled distances may therefore be extrapolated. This can represent a considerable source of error [34].

2.3 Equation of State (EoS)

In order to describe the development of an explosion, an equation of state is needed. This is a constitutive equation describing the state of the explosive under a given set of physical conditions. The ideal gas law is an example of a simple equation of state [35].

The Jones-Wilkins-Lee (JWL) empirical equation of state, is commonly used in modeling of expansion of detonation products from HE. The pressure, P, is then given by the following relation [36]:

$$P = A\left(1 - \frac{\omega}{R_1 \bar{\rho}}\right)e^{(-R_1 \bar{\rho})} + B\left(1 - \frac{\omega}{R_2 \bar{\rho}}\right)e^{(-R_2 \bar{\rho})} + \omega \rho e_{int} \qquad (2.13)$$

where $\omega = \gamma - 1$ and γ is the heat capacity ratio. A, B, R_1 and R_2 are material constants that can be found experimentally. The specific internal energy at atmospheric pressure is given by e_{int}. The relative density, $\bar{\rho}$, is defined as:

$$\bar{\rho} = \frac{\rho_{sol}}{\rho} = \frac{V}{V_{sol}} \qquad (2.14)$$

where ρ_{sol} and V_{sol} are the density and volume of the explosive material in solid state, respectively. ρ is the current density and V is the current volume. In Table 2.2, JWL parameters for both TNT and C4 are given. The detonation velocity, v_{det}, which comes from an ignition law related to the release of pressure, is also included in the table.

Table 2.2: JWL-parameters for some explosive materials [36].

	Unit	TNT	C4
A	Pa	$3.738 \cdot 10^{11}$	$5.98155 \cdot 10^{11}$
B	Pa	$3.747 \cdot 10^{9}$	$0.13750 \cdot 10^{11}$
$e_{int,0}$	J/kg	$3.68 \cdot 10^{6}$	$5.4341 \cdot 10^{6}$
R_1	–	4.15	4.5
R_2	–	0.90	1.5
ω	–	0.35	0.32
ρ_{sol}	kg/m^3	1630	1601
v_{det}	m/s	6930	8500

2.4 Failure Modes

In this section, a short introduction to deformation and failure modes of clamped, square plates subjected to impulsive loading will be given. However, the basis for this discussion are failure modes reported by Menkes and Opat [2], in their study of clamped, aluminum *beams* loaded impulsively. Their results have subsequently been used for clamped circular plates, clamped square plates and fully built-in square plates [4]. The failure modes observed by Menkes and Opat [2] will therefore be summarized in this section. The three characteristic failure modes are listed below.

- Mode I: large inelastic deformations of the entire beam

- Mode II: large deformations and tensile-tearing over the support

- Mode III: transverse shear failure at the support

A graphical description of the failure modes are given in Figure 2.6.
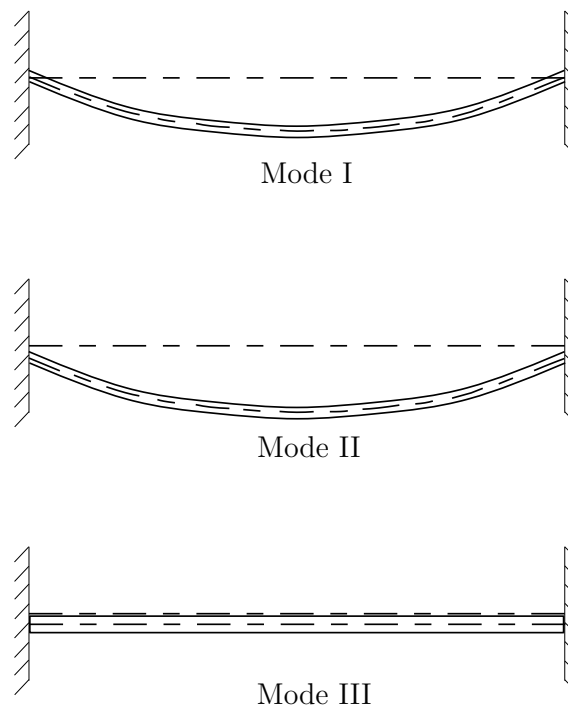
Figure 2.6: Failure modes for beams defined by Menkes and Opat [2].

Nurick and Shave [4] observed several phases in the mode II failure region. According to their work, failure mode II can be divided into three groups of tensile tearing, as listed below.

- Mode II*: Only partial tearing

- Mode II a: Plate is totally torn. Increasing mid-point deflection is observed for increasing impulses.

- Mode II b: Plate is totally torn. Decreasing mid-point deflection is observed for increasing impulses.

It should be noted that mode IIa applies only to square plates, while modes II* and IIb apply to both square and circular plates [4].

2.5 Material Characterization

Characterization of material behaviour is an important part in material mechanics. This means to develop models that are able to predict the behaviour of materials for given load configurations. By performing uni-axial tensile tests on material specimens, the needed material parameters may be obtained.

2.5.1 Strains and Stresses

Different approaches may be used for defining strains and stresses, depending on whether small or large deformations are likely to occur. Small deformations, which implies infinitesimal strains, are often assumed in engineering applications. In this type of problems, where the undeformed and deformed configurations of a body is assumed identical, the engineering stress, s, and engineering strain, e, are defined by the following equations [37]:

$$s = \frac{F}{A_0} \tag{2.15}$$

$$e = \frac{\Delta L}{L_0} \tag{2.16}$$

In Equation (2.15), F represents the axial force, while A_0 represents the initial cross-sectional area. In Equation (2.16), L_0 represents the initial length, while ΔL represents the incremental change in length. Engineering stress and engineering strain are only applicable for deformations within the elastic domain of the material, in which a linear relationship between stress and strain can be observed. This linear relationship is given by Hooke's law:

$$s = Ee \tag{2.17}$$

In Equation (2.17), E represents the elastic modulus, also called the Young's modulus. As mentioned, this relation is only valid for small deformations. For large deformations, the geometrical changes in the material must be taken into account. As the applied force increases, the cross-section of the specimen will decrease. To include this effect, the Cauchy stress, or true stress, σ, and the true strain, ε, are needed. These can be computed by use of the following equations [37]:

$$\sigma = s(1 + e) \tag{2.18}$$

$$\varepsilon = \ln(1 + e) \tag{2.19}$$

It should be noted that within the elastic region, the true stress and strain are approximately the same as the engineering stress and strain.

The true strain in Equation (2.19), consists of an elastic and a plastic part. The elastic part can be developed directly from Hooke's law. Consequently, the expression for the plastic strain ε^p, can be given by:

$$\varepsilon^p = \varepsilon - \frac{\sigma}{E} \tag{2.20}$$

2.5.2 Necking

The plastic strains start to develop after reaching the yield stress limit for the material, which marks the border between the elastic and the plastic domains. From this point on, permanent deformations can be observed. After yielding, further load can increase the stress. This is due to an effect called strain hardening. However, at the ultimate stress, that is at the maximum value for an engineering stress-strain curve, diffuse necking can be observed. Diffuse necking means that the cross-sectional area will start to decrease in a localized region of the specimen, instead of over its entire length [38]. This can be seen as a contraction somewhere along the length of the specimen . For illustration purposes only, the point of diffuse necking is indicated on an engineering stress-strain curve in Figure 2.7.
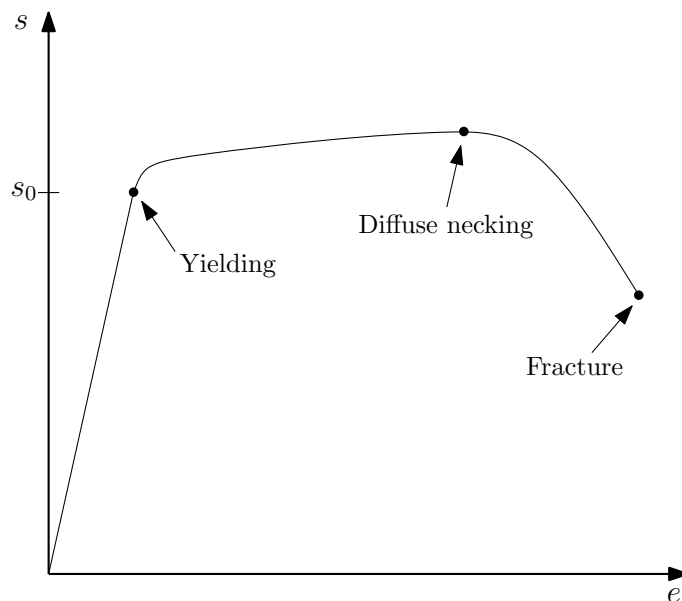
Figure 2.7: Engineering stress-strain curve in tension [37].

Necking is basically an instability that can occur for tensile deformations. This happens when the cross-sectional area starts to decrease at a higher rate than the material strain hardens [39]. Diffuse necking occurs when the following criteria is fulfilled [37]:

$$\frac{d\sigma}{d\varepsilon} = \sigma \tag{2.21}$$

A graphical description of the necking criteria in Equation (2.21) is given in Figure 2.8.
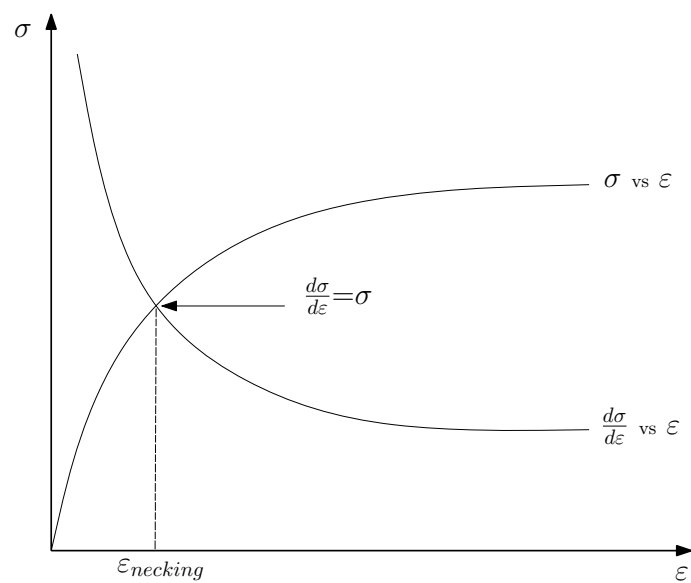
Figure 2.8: Graphical illustration of necking criterion.

It is important to identify the point of necking since it marks the end of the uniform deformations. The relations defined in Chapter 2.5.1 are based on an assumption of uniform deformation, and diffuse necking can therefore be used to appoint the end of the useful part of a material tensile test [37].

After further elongation, localized necking will occur. Normally, this takes place in the region in which diffuse necking initiated.

2.5.3 Fracture

When a material loses its load-carrying capacity, material failure occurs. For ductile materials, the term *failure*, is often related to initiation of yielding, and not the actual fracture, as indicated in Figure 2.7 [38]. For brittle materials, material failure and fracture define the same phenomenon.

Since material fracture is an important part in material science, a lot of research have been carried out on this topic. The object has been to obtain proper material models that are able to give a sufficient description of material fracture.

Material failure can be described on both microscopic and macroscopic level. On a microscopic level, initiation and crack propagation are important. This approach may be useful when studying failure for simple structures and specimens with well-defined load distributions. If the structure is more complex and the load distribution is not that simple, a macroscopic approach may be preferable. Here, load carrying capacity, or energy storage capacity, are used in describing material fracture [40].

In Figure 2.9, a stepwise description of a ductile fracture in tension is given.
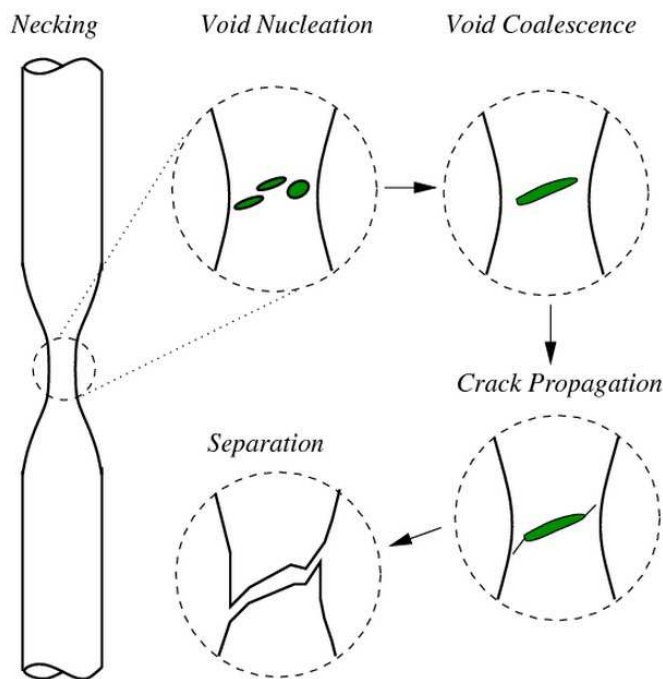
Figure 2.9: Ductile fracture [41].

In Figure 2.9 the necking phenomenon can be seen clearly as a reduction in the cross-sectional area. Due to localized necking in the region where diffuse necking initiated, fracture occurs in the same area.

2.6 Constitutive Equations

To be able to give a mathematical description of the material behaviour, a constitutive equation has to be defined. A constitutive equation gives the stress as a function of the deformation history of the body [42]. For a linear and elastic material, the constitutive equation is given by Hooke's law.

Large deformations are likely to occur for an aluminum plate exposed to blast loading. It is therefore essential to take both the contribution from elastic and plastic strains into account, when establishing the constitutive relation. When a material experiences yielding loads, deformations and stresses become nonlinearly related. In addition they become history-dependent. To handle this, an incremental plasticity relation can be used, where the total strain increment can be divided in to a recoverable (elastic) and nonrecoverable (plastic) part [43]:

$$\{d\varepsilon\} = \{d\varepsilon^e\} + \{d\varepsilon^p\} \tag{2.22}$$

where superscripts e and p refer to elastic and plastic, respectively. When it comes to stress increments, only the elastic part is included [43]:

$$\{d\boldsymbol{\sigma}\} = [\boldsymbol{E}]\{d\varepsilon^e\} \quad \text{or} \quad \{d\boldsymbol{\sigma}\} = [\boldsymbol{E}]\Big(\{d\varepsilon\} - \{d\varepsilon^p\}\Big) \tag{2.23}$$

where

$\{d\boldsymbol{\sigma}\}$ stress increment vector
$[\boldsymbol{E}]$ elastic material property matrix

As stated by Cook et al. [43], $\{d\boldsymbol{\sigma}\}$ contains in general increments of all six stress components. This means that the stress vector can be written as:

$$\{d\boldsymbol{\sigma}\} = \lfloor d\sigma_x \ d\sigma_y \ d\sigma_z \ d\tau_{xy} \ d\tau_{yz} \ d\tau_{zx} \rfloor^T \tag{2.24}$$

where

$d\sigma_i$ stress increment in the ith direction
$d\tau_{ij}$ shear stress increment in the i-j plane

In order to make the description of the elastic-plastic material behaviour possible, the following must be obtained [43]:

- a yield criterion

- a flow rule

- a hardening rule

An yield criterion relates the state of stress to the onset of yielding. When an increment of plastic flow occurs, a flow rule is required to give a relation between the state of stress, given by $\{\boldsymbol{\sigma}\}$, and the corresponding six increments of plastic strain, $\{d\boldsymbol{\varepsilon}^p\}$. In order to take the material hardening into account, a hardening rule is needed. A hardening rule gives a description of how the yield criterion is updated, or modified, by straining beyond the initial yield limit [43].

The yield function, F, can be expressed as [43] :

$$F = F\Big(\{\boldsymbol{\sigma}\}, \{\boldsymbol{\alpha}\}, W_P\Big) \tag{2.25}$$

where

$\{\boldsymbol{\sigma}\}$ state of stress
$\{\boldsymbol{\alpha}\}$ vector describing kinematic hardening
W_P scalar describing the isotropic hardening

$\{\boldsymbol{\alpha}\}$ and W_P, which take material hardening into account, give a description of how a "yield surface" in multidimensional stress space is altered due to plastic straining. The "yield surface" can change both location and size, depending on how the hardening rule is implemented [43].

Depending on which value the yield function, F, takes on, the following can be stated [43]:

$$
\begin{array}{ll}
F < 0 & \text{elastic domain} \\
F = 0 & \text{yielding} \\
F > 0 & \text{physically impossible}
\end{array}
$$

It should be noted that the statements given above are only valid for elastic-plastic materials. In theory of viscoplasticity, the yield function, F, is allowed to take values greater than zero. Theory of viscoplasticity basically describes the rate-dependent inelastic behaviour of solids [37]. The Johnson-Cook material model is an example in which viscoplasic behaviour is allowed.

2.7 Material Model

In order to establish a suitable material model, the physics in the problem should be closely examined. This will enable a proper representation of the physical processes that impact the material behaviour. For blast and penetration problems, three important factors affect the material behaviour [44]:

- strain

- strain-rate

- temperature

The foregoing factors should therefore be taken into account in the process of selecting a suitable material model.

2.7.1 Johnson-Cook Material Model

The Johnson-Cook material model is frequently used in structural impact problems. Calibration of the model can be done by tensile testing of smooth and notched specimens at different strain rates and temperatures. Otherwise, the literature may be used, where details of a large number of materials are available [45].

By adapting a thermoelastic-thermoviscoplastic material model, the listed factors affecting material behaviour are taken into account. In adopting this type of material model, some assumptions regarding the material and strains have been made. The main assumptions are isotropic material behaviour and small elastic strains, while the plastic strains and rotations may be finite [45].

Before outlining the Johnson-Cook material model, a discussion regarding the choice of suitable strain and stress measures will be given. This will give a more thorough understanding of fundamental ideas which the material model is based on.

Strain Measure

There exist a large number of measures for strain and strain rate in nonlinear continuum mechanics. Two of the most widely used measures are [42]:

1. The Green strain, $\boldsymbol{E}$.

2. The rate-of-deformation tensor, $\boldsymbol{D}$.

A strain measure must meet several requirements, e.g. vanish for any rigid body motions, especially for rigid body rotations. If not, it will predict nonzero strains for rigid body motions, which again lead to nonzero stresses. It can be shown that $\boldsymbol{E}$ and $\boldsymbol{D}$ vanish for rigid body motions [42].

When elastic strains are small compared to the plastic strains, a hypoelastic-plastic model is typically used [42]. Therefore, the rate-of-deformation tensor, $\boldsymbol{D}$, will be selected as the measure of strain rate.

The rate-of-deformation, $\boldsymbol{D}$, is defined as the symmetric part of the velocity gradient, $\boldsymbol{L}$, which is defined as [42]:

$$\boldsymbol{L} = \frac{\partial \boldsymbol{v}}{\partial \boldsymbol{x}} = (\nabla \boldsymbol{v})^T = (\text{grad } \boldsymbol{v})^T \tag{2.26}$$

where the symbol ∇ specifies the spatial gradient. Further, the velocity gradient, $\boldsymbol{L}$, can be decomposed into a symmetric and a skew-symmetric part:

$$\boldsymbol{L} = \frac{1}{2}(\boldsymbol{L} + \boldsymbol{L}^T) + \frac{1}{2}(\boldsymbol{L} - \boldsymbol{L}^T) \tag{2.27}$$

The first term on the RHS in Equation (2.27), is defined as the rate-of-deformation, $\boldsymbol{D}$, while the second term is referred to as the spin, $\boldsymbol{W}$. Thus, the following can be stated:

$$\boldsymbol{D} = \frac{1}{2}(\boldsymbol{L} + \boldsymbol{L}^T) \tag{2.28}$$

$$\boldsymbol{W} = \frac{1}{2}(\boldsymbol{L} - \boldsymbol{L}^T) \tag{2.29}$$

Use of an additive decomposition gives the opportunity of separating instantaneous deformation (symmetric part) form rotations (skew-symmetric part) [46].

Stress Measure

Various stress measures can be defined in nonlinear problems. Three well-known measures of stress are [42]:

1. The Cauchy stress, $\boldsymbol{\sigma}$.

2. The nominal stress tensor, $\boldsymbol{P}$.

3. The second Piola-Kirchhoff (PK2) stress tensor, $\boldsymbol{S}$.

The main difference between the stress measures listed above, is that the first one, the Cauchy stress, $\boldsymbol{\sigma}$, is referred to the deformed area, while the two others are referred to the undeformed area. Thus, the Cauchy stress is often called the physical stress, or the true stress [42].

The relation between the three stress measures, are dependent of the deformation gradient, $\boldsymbol{F}$, and the Jacobian determinant, $J=\det(\boldsymbol{F})$. Given the deformation,

the stress can be expressed in any of the aforementioned stress measures [42]. The deformation gradient, $\boldsymbol{F}$, is also discussed in Chapter 2.8.

Having selected a strain rate measure, one should be careful in the choice of a stress measure. An important aspect is that the measure of strain and the measure of stress should be energetically conjugate, or conjugate in power [42]. It can be shown that the Cauchy stress, $\boldsymbol{\sigma}$, and the rate-of-deformation, $\boldsymbol{D}$, is energetically conjugate. As a consequence of this, the Cauchy stress, $\boldsymbol{\sigma}$, is taken as the measure of stress.

Corotational Stress and Rate-of-Deformation

In nonlinear problems, large rotations may be present. This can complicate the handling of structural elements and anisotropic materials. To simplify this, a corotational approach may be introduced. In short, a coordinate system is then attached to the material or the element, which will cause it to rotate with the material. The rate-of-deformation and the Cauchy stress are then expressed in terms of the corotational coordinate system, and are thus referred to as the corotational Cauchy stress, $\hat{\boldsymbol{\sigma}}$, and the corotational rate-of-deformation, $\hat{\boldsymbol{D}}$. The corotated formulations can be expressed as [42]:

$$\hat{\boldsymbol{\sigma}} = \boldsymbol{R}^T \cdot \boldsymbol{\sigma} \cdot \boldsymbol{R} \quad \text{or} \quad \hat{\sigma}_{ij} = R_{ik}^T \sigma_{kl} R_{lj} \tag{2.30}$$

$$\hat{\boldsymbol{D}} = \boldsymbol{R}^T \cdot \boldsymbol{D} \cdot \boldsymbol{R} \quad \text{or} \quad \hat{D}_{ij} = R_{ik}^T D_{kl} R_{lj} \tag{2.31}$$

where $\boldsymbol{R}$ is the rotation matrix. The concept of corotational formulations is to some degree discussed in Chapter 2.8.1.

Hypoelastic Law

In order to obtain a valid hypoelastic law, which is a rate-constitutive equation where the stress rate is related to the rate-of-deformation, rotations of the material have to be accounted for. This can be done by introducing an objective rate of the stress tensor, or a frame-invariant rate. By including the Jaumann rate of the Cauchy stress in the hypoelastic law, aspects regarding rotations of the material are taken care of. The Jaumann rate of the Cauchy stress is given by [42]:

$$\boldsymbol{\sigma}^{\nabla J} = \frac{D\boldsymbol{\sigma}}{Dt} - \boldsymbol{W} \cdot \boldsymbol{\sigma} - \boldsymbol{\sigma} \cdot \boldsymbol{W}^T \tag{2.32}$$

where $\boldsymbol{W}$ is the spin tensor, defined in Equation (2.29). The superscripts ∇ and J refer to objective stress rate and use of Jaumann rate, respectively.

Denoting the Jaumann rate of the Cauchy stress as an *objective* rate, indicates that it is independent of the frame of reference. This is an important property, since the mechanical response should not depend on the frame of reference [47]. One appropriate hypoelastic constitutive equation is given by [42]:

$$\sigma^{\nabla J} = \boldsymbol{C}^{\sigma J} : \boldsymbol{D} \tag{2.33}$$

where $\boldsymbol{C}^{\sigma J}$ is the material tangent moduli.

Now, by rearranging Equation (2.32), the material rate for the Cauchy stress tensor can be written as:

$$\frac{D\sigma}{Dt} = \sigma^{\nabla J} + \boldsymbol{W} \cdot \sigma + \sigma \cdot \boldsymbol{W}^T = \underbrace{\boldsymbol{C}^{\sigma J} : \boldsymbol{D}}_{\text{material}} + \underbrace{\boldsymbol{W} \cdot \sigma + \sigma \cdot \boldsymbol{W}^T}_{\text{rotation}} \tag{2.34}$$

Equation (2.34) gives the material response in terms of the Jaumann objective stress rate. As indicated, the material response consists of two parts: the rate of change due to material response and the change of stress due to rotation [42]. Thus, a valid rate-constitutive relation has been established.

2.7.2 Outline of the Johnson-Cook Material Model

In order to include the effect of temperature, the rate-of-deformation tensor, $\boldsymbol{D}$, can be decomposed into an elastic, a plastic and a thermal part [45]:

$$\boldsymbol{D} = \boldsymbol{D}^e + \boldsymbol{D}^t + \boldsymbol{D}^p \tag{2.35}$$

The elastic part in Equation (2.35) is defined by [45]:

$$\boldsymbol{D}^e = \frac{1+\nu}{E}\boldsymbol{\sigma}^{\nabla J} - \frac{\nu}{E}\text{tr}\left(\boldsymbol{\sigma}^{\nabla J}\right)\boldsymbol{I} \tag{2.36}$$

where

E	Young's modulus
ν	Poisson's ratio
$\boldsymbol{\sigma}^{\nabla J}$	the Jaumann rate of the Cauchy stress, defined in Equation (2.32)
$\boldsymbol{I}$	2nd order unit tensor

When it comes to the thermal part, $\boldsymbol{D}^t$, this is defined as [45]:

$$\boldsymbol{D}^t = \alpha\dot{T}\boldsymbol{I} \tag{2.37}$$

where $\dot{T}$ is the time derivative of the temperature and α is the linear thermal expansion coefficient.

The last part of the decomposed rate-of-deformation tensor, namely the plastic part, $\boldsymbol{D^p}$, is defined by the associated flow rule as [45]:

$$\boldsymbol{D}^p = \dot{p}\frac{\partial f}{\partial \boldsymbol{\sigma}} = \frac{3}{2}\dot{p}\frac{\boldsymbol{\sigma'}}{\sigma_{eq}} \tag{2.38}$$

where

$\dot{p}$ equivalent plastic strain rate
f yield function
$\boldsymbol{\sigma'}$ deviatoric stress tensor, i.e. $\boldsymbol{\sigma'} = \boldsymbol{\sigma} - \frac{1}{3}(\boldsymbol{\sigma})\boldsymbol{I}$
σ_{eq} equivalent von Mises stress, $\sigma_{eq} = \sqrt{\frac{3}{2}\boldsymbol{\sigma'} : \boldsymbol{\sigma'}}$

Isotropic hardening and thermal softening can be implemented in the von Mises yield function in the following manner [45]:

$$f(\boldsymbol{\sigma}, R, T) = \sigma_{eq}(\boldsymbol{\sigma}) - \sigma_0(T) - R(p, T) \tag{2.39}$$

where

$$\sigma_0 = A[1 - (T^*)^m] \quad \text{and} \quad R = Bp^n[1 - (T^*)^m]$$

The material parameters A and B are governing strength, while n and m are governing strain hardening and thermal softening. $T^* = \frac{T - T_0}{T_m - T_0}$ is the homologous temperature, T_0 and T_m are the room temperature and melting temperature of the material, respectively [45]. Having defined the yield function, a multiplicative constitutive relation for the strain-rate dependent material can be defined by:

$$\dot{p} = \begin{cases} 0 & \text{for } f \leq 0 \\ \dot{p}_0 \exp\left(\frac{1}{C}\left[\frac{\sigma_{eq}(\boldsymbol{\sigma})}{\sigma_0(T) + R(p,T)} - 1\right]\right) & \text{for } f > 0 \end{cases} \tag{2.40}$$

where $\dot{p}_0$ is a reference strain rate and C is a material constant governing strain rate sensitivity. By solving for $\sigma_{eq}(\boldsymbol{\sigma})$ in the viscoplastic domain, i.e. for $f > 0$, the following expression can be obtained:

$$\sigma_{eq}(\boldsymbol{\sigma}) = [A + Bp^n]\left[1 + C\ln\left(\frac{\dot{p}}{\dot{p}_0}\right)\right][1 - (T^*)^m] \tag{2.41}$$

Equation (2.41) gives the equivalent stress as a function of plastic strain, plastic strain rate and temperature. These characteristics are typical for a Johnson-Cook type of constitutive equation.

In fast transient, dynamic problems, e.g. in blast load problems, adiabatic conditions may be assumed. This leads to the following expression for the temperature evolution [45]:

$$\dot{T} = \frac{\chi}{\rho C_p} \boldsymbol{\sigma} : \boldsymbol{D}^p = \frac{\chi}{\rho C_p} \sigma_{eq} \dot{p} \tag{2.42}$$

where χ is the Taylor-Quinney coefficient, ρ is the density and C_p is the specific heat.

The temperature effects on the yield stress can be regarded as negligible in some cases. This is due to the fact that the contribution from adiabatic heating often represents only an insignificant increase in temperature [48]. Thus, Equation (2.41) can be reduced to the following:

$$\sigma_{eq}(\boldsymbol{\sigma}) = [A + Bp^n]\left[1 + C \ln\left(\frac{\dot{p}}{\dot{p}_0}\right)\right] \tag{2.43}$$

2.8 Finite Element Formulations

Finite Element Method

The Finite Element Method (FEM), is a numerical method for solving partial differential equations or integral equations. Conceptually, the method consists of dividing a domain into many smaller elements. Based on the fact that the characteristics and behaviour of individual elements are known, the behaviour of the whole domain, or structure, may be obtained [49]. The computerized version is called Finite Element Analysis (FEA), and is employed in a wide variety of application areas. FEA in engineering problems consist of the following three main steps [50]:

1. Pre-processing or modelling of the structure

2. Analysis

3. Post processing

To obtain high-quality results, a thorough understanding of the method is recommended. Thus, the user carries a lot of responsibility.

Two commonly used element formulations are the Lagrangian and the Eulerian formulation. In this section, both the Lagrangian and the Eulerian formulation will be introduced and described in some detail. In addition, the combined version of these two formulation, namely the Arbitrary Lagrangian-Eulerian (ALE) formulation, will be looked into.

The conservation laws, or the balance laws, make up the basis for a group of fundamental equations of continuum mechanics. The aim in FEA, related to continuum mechanics, is to describe a physical system. Therefore, it is of outmost importance that these fundamental equations are satisfied. For a thermomechanical system, the following four conservation laws apply [42]:

- Conservation of mass

- Conservation of linear momentum

- Conservation of energy

- Conservation of angular momentum

In short, the conservation laws state that particular measurable properties of an isolated physical system, do not change as the system evolves [51].

The conservation laws are often expressed by Partial Differential Equations (PDEs), which are referred to as the *strong form*. When applying the conservation laws on to a domain of the body, an integral relation appears, and this results in the so-called *weak form* [42]. Due to the importance of these conservation laws, some of them will be presented in the upcoming sections.

Kinematic Description

To be able to provide models for the behaviour of fluids, solids and structures, kinematic relations have to be established. In other words, this means descriptions of the movements of a body in space and time, which again forms a basis for calculations of strains and stresses.

The domain of a body at an initial state, at time $t = 0$, is denoted by Ω_0. This is said to be the initial configuration. Furthermore, at time $t > 0$, the body is said to occupy the domain Ω, and this is often referred to as the current configuration [42]. A graphical description is given in Figure 2.10.
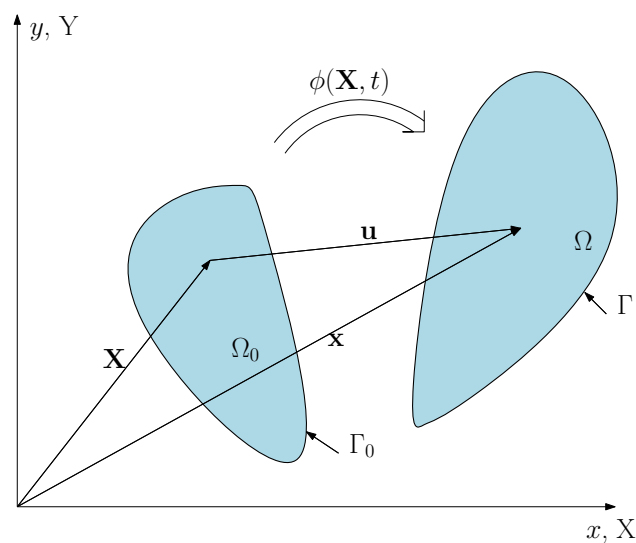
Figure 2.10: Undeformed (initial) and deformed (current) configuration of a body.

In order to describe motions and deformations of a body, a configuration which the various constitutive equations can be referred to is needed. This is called the reference configuration, and often this coincide with the initial configuration. Other reference configurations may also be used. However, the vital property of the reference configuration is that motion of the body is defined with respect to it [42].

Two terms which are often used in the context of configurations of bodies in deformation analyses, are the *undeformed* configuration and the *deformed* configuration. The reference configuration is identified as an undeformed configuration, and occupies the domain Ω_0. The current configuration, on the other hand, is referred to as a deformed configuration, thus is occupies the domain Ω [42]. As depicted in Figure 2.10, the boundary of the two configurations are referred to as Γ_0 and Γ, respectively.

Essential Definitions

The motion of the body can be described by [42]:

$$\boldsymbol{x} = \boldsymbol{\phi}(\boldsymbol{X}, t) \tag{2.44}$$

where $\boldsymbol{x}$ is the position of the material point, $\boldsymbol{X}$, at time t. The function $\boldsymbol{\phi}(\boldsymbol{X}, t)$ is often referred to as a mapping function, since it maps the reference configuration onto the current configuration at time t. Equation (2.44) gives the spatial position of the body as a function of the time, t, and spatial, or Eulerian coordinates, $\boldsymbol{x}$ [42].

The displacement of a material point is defined as the difference between the current and the original position. Thus, it can be expressed as [42]:

$$\boldsymbol{u}(\boldsymbol{X}, t) = \boldsymbol{\phi}(\boldsymbol{X}, t) - \boldsymbol{X} \tag{2.45}$$

The velocity of a material point is defined as the rate of change of the belonging position vector. Thus, it is the time derivative with $\boldsymbol{X}$ held constant. The velocity can be given as [42]:

$$\boldsymbol{v}(\boldsymbol{X}, t) = \frac{\partial \boldsymbol{\phi}(\boldsymbol{X}, t)}{\partial t} = \frac{\partial \boldsymbol{u}(\boldsymbol{X}, t)}{\partial t} \equiv \dot{\boldsymbol{u}} \tag{2.46}$$

Acceleration is defined as the rate of change of the velocity of a material point, and is thus defined by:

$$\boldsymbol{a}(\boldsymbol{X}, t) = \frac{\partial \boldsymbol{v}(\boldsymbol{X}, t)}{\partial t} = \frac{\partial^2 \boldsymbol{u}(\boldsymbol{X}, t)}{\partial t^2} \equiv \dot{\boldsymbol{v}} \tag{2.47}$$

Another important variable in the process of calculating deformations and strains in nonlinear continuum mechanics, is the *deformation gradient*. The deformation gradient is defined by [42]:

$$\boldsymbol{F} = \frac{\partial \boldsymbol{\phi}}{\partial \boldsymbol{X}} \equiv \frac{\partial \boldsymbol{x}}{\partial \boldsymbol{X}} \equiv (\nabla_0 \boldsymbol{\phi})^T \tag{2.48}$$

The expression for the deformation gradient, $\boldsymbol{F}$, is on the form of a Jacobian matrix, which is a matrix of all first order derivatives of a vector valued function. Thus, the deformation gradient can be seen as the Jacobian matrix of the motion $\boldsymbol{\phi}(\boldsymbol{X}, t)$ [42].

An interesting relation related to the deformation gradient comes from its determinant, $J = \det(\boldsymbol{F})$. By finding the determinant of $\boldsymbol{F}$, a relation between integrals in the current and the reference configurations can be established [42]:

$$\int_\Omega f(\boldsymbol{x}, t)\, d\boldsymbol{\Omega} = \int_{\Omega_0} f(\boldsymbol{\phi}(\boldsymbol{X}, t), t) J\, d\boldsymbol{\Omega_0} \qquad (2.49)$$

Having defined some important relations related to motion and deformation of a material, approaches for further characterization of the material behaviour is needed.

2.8.1 Lagrangian Formulation

The characteristic of a mesh in a Lagrangian formulation, is that nodes and elements move according to the material, as illustrated in Figure 2.11. Because of this, constitutive equations are always evaluated at the same material points. In addition, boundaries and interfaces remain coincident with element edges, thus making the treatment of boundaries and interfaces fairly simple. This is of great advantage when it comes to history-dependent materials, and this type of mesh is therefore widely used in solid mechanics. In a Lagrangian description, or a material description, the material coordinates, $\boldsymbol{X}$, and the time, t, make up the independent variables [42].
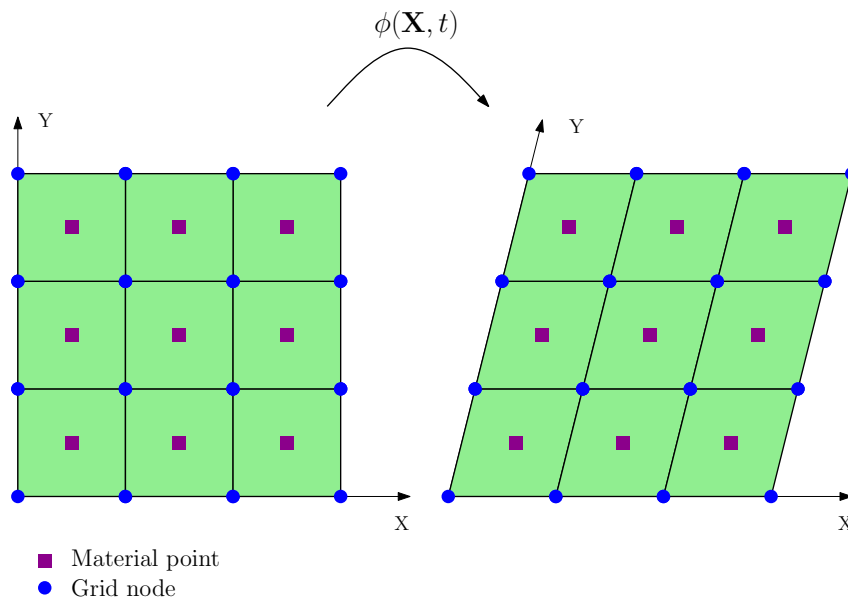
Figure 2.11: Lagrangian mesh.

The limits of a Lagrangian formulation lie in the element's capabilities of dealing with large distortions. Handling of geometric and material nonlinearities are not an issue. The limited distortions most elements can sustain, without degradation in performance or failure, is therefore an important factor in nonlinear analysis where Lagrangian meshes are employed [42].

A Lagrangian type of formulation can be employed in different ways. Three well-known formulations are listed below.

- Updated Lagrangian formulation

- Total Lagrangian formulation

- Corotational formulation

In the updated Lagrangian formulation, the derivatives are taken with respect to the spatial (Eulerian) coordinates. As a result of this, integrals are taken over the

deformed (current) configuration, in contrast to the total Lagrangian formulation, where the derivatives are taken with respect to the undeformed (initial) configuration. However, expressions obtained using an updated formulation can be transformed to a total Lagrangian formulation. This can be done by transformations of tensors and mapping configurations [42].

To get an idea of what conservation equations can look like, the balance laws for the total Lagrangian formulation are presented below [42].

Mass conservation

$$\rho(\boldsymbol{X}, t)J(\boldsymbol{X}, t) = \rho_0(\boldsymbol{X}) \quad \text{or} \quad \rho J = \rho_0 \tag{2.50}$$

Linear momentum conservation

$$\rho_0 \frac{\partial \boldsymbol{v}(\boldsymbol{X}, t)}{\partial t} = \nabla_0 \cdot \boldsymbol{P} + \rho_0 \boldsymbol{b} \quad \text{or} \quad \rho_0 \frac{\partial v_i(\boldsymbol{X}, t)}{\partial t} = \frac{P_{ji}}{\partial X_j} + \rho_0 b_i \tag{2.51}$$

Angular momentum conservation

$$\boldsymbol{F} \cdot \boldsymbol{P} = \boldsymbol{P}^T \cdot \boldsymbol{F}^T, \quad F_{ik}P_{kj} = P_{ik}^T F_{kj}^T = F_{jk}P_{ki}, \quad \boldsymbol{S} = \boldsymbol{S}^T \tag{2.52}$$

Energy conservation

$$\rho_0 \dot{w}^{int} = \rho \frac{\partial w^{int}(\boldsymbol{X}, t)}{\partial t} = \dot{\boldsymbol{F}}^T : \boldsymbol{P} - \nabla_0 \cdot \tilde{\boldsymbol{q}} + \rho_0 s \tag{2.53}$$

where

ρ_0, ρ original and current density
w hyperelastic potential on reference configuration
$\boldsymbol{b}$ force per unit mass
J determinant of Jacobian between spatial and material coordinates, $J = \det[\partial x_i/\partial X_j]$
$\boldsymbol{F}$ deformation gradient, $F_{ij} = \partial x_i/\partial X_j$
$\boldsymbol{S}$ second Piola-Kirchhoff (PK2) stress
$\boldsymbol{P}$ nominal stress (transpose of first Piola-Kirchhoff stress)
$\boldsymbol{q}$ heat flux per unit area
s specific heat source term

The corotational formulation, on the other hand, is regarded as an additional formulation, that can be employed together with other formulations, e.g. a total Lagrangian formulation [52]. This type of formulation is useful in structural elements such as bars, beams and shells [42].

The basic concept of a corotational formulation is to define rotation of a material and create a coordinate system that in some way follows this rotation. There are two approaches to corotational finite element formulations [42]:

1. A coordinate system is embedded at each quadrature point and rotated with the material in some way.

2. A coordinate system is embedded in an element and rotated with the element.

In general, the first approach is valid for arbitrary large strains and rotations. For some elements, like a rod or the constant-strain triangle – where the rigid body rotation is the same throughout the element – the second approach is sufficient [42].

2.8.2 Eulerian Formulation

For problems including very large deformations, a Lagrangian formulation is inadequate. In this type of problems, an Eulerian description may be employed. Fluid related problems are typical examples for which such formulations prove advantageous [42].

In an Eulerian formulation, the nodes are fixed in space, and the independent variables are the spatial coordinates, $\boldsymbol{x}$, and the time, t [42]. Consequently, the material can deform independently of the mesh, as indicated in Figure 2.12.
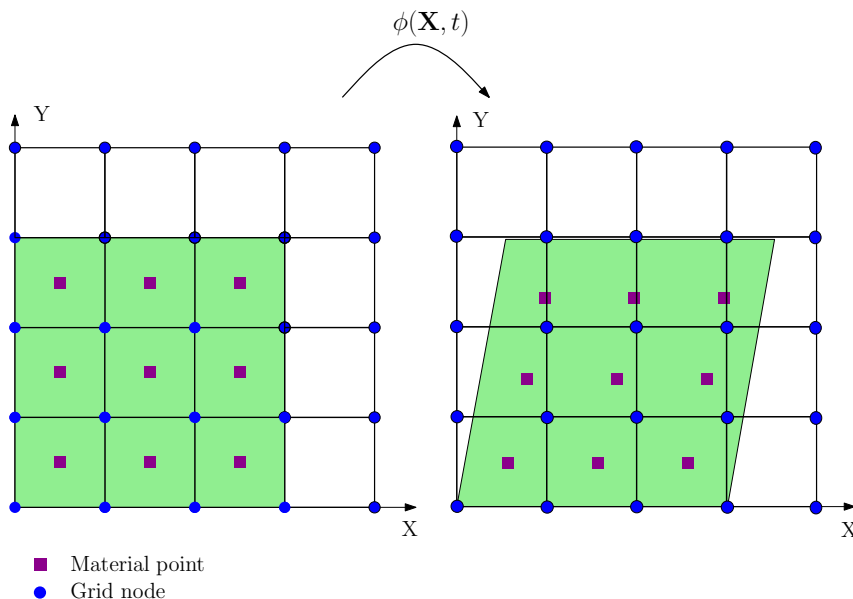
Figure 2.12: Eulerian mesh.

In contrast to a Lagrangian description – where the mesh is fixed on specified material points – material flows through the mesh in an Eulerian description [42]. Thus, treatment of history-dependent material in an Eulerian description turns out to be quite difficult. For Newtonian fluids however, Eulerian descriptions are highly suitable. This is due to the fact that Newtonian fluids are characterized by history-independent behaviour [53].

In the following, the conservation equations for an Eulerian description will be presented.

Mass conservation

$$\frac{D\rho}{Dt} + \rho \mathrm{div}(\boldsymbol{v}) = 0 \quad \text{or} \quad \frac{D\rho}{Dt} + \rho v_{i,j} = 0 \quad \text{or} \quad \dot{\rho} + \rho v_{i,j} = 0 \qquad (2.54)$$

Linear momentum conservation

$$\rho\frac{D\boldsymbol{v}}{Dt} = \nabla \cdot \boldsymbol{\sigma} + \rho\boldsymbol{b} \equiv \text{div}(\boldsymbol{\sigma}) + \rho\boldsymbol{b} \quad \text{or} \quad \rho\frac{Dv_i}{Dt} = \frac{\partial v_i}{\partial x_j} + \rho b_i \qquad (2.55)$$

Angular momentum conservation

$$\sigma = \sigma^T \quad \text{or} \quad \sigma_{ij} = \sigma_{ji} \qquad (2.56)$$

Energy conservation

$$\rho\frac{Dw^{int}}{Dt} = \boldsymbol{D} : \sigma - \nabla \cdot \boldsymbol{q} + \rho s \qquad (2.57)$$

where

$\boldsymbol{v}$ velocity field
$\boldsymbol{D}$ the rate-of-deformation or velocity strain, $\boldsymbol{D} = \text{sym}(\nabla\boldsymbol{v})$
$\boldsymbol{\sigma}$ cauchy stress tensor

The difficulties with an Eulerian formulation are related to the tracking of moving material boundaries and interfaces. This require use of different tracking methods in order to keep track of the material deformations. In contrast to a Lagrangian formulation, where the mesh is defined by the material domain, an Eulerian mesh has to exceed the material boundaries to account for deformed configurations. Otherwise instabilities may occur, leading to inaccurate results [42].

2.8.3 Arbitrary Lagrangian-Eulerian (ALE) Formulation

In ALE formulations, Eulerian and Lagrangian formulations are combined. The aim of these hybrid techniques are to capture the advantages of the two aforementioned formulations, while minimizing the disadvantages [42].

The basic concept of this type of formulation is to optimize the meshing process, and thus reduce the chance of large distortions of elements, which may give numerical instabilities. In order to establish an ALE formulation, another reference coordinate system, known as a referential system, is needed [42]. Also, for this more general framework, velocities and accelerations for both the material and the mesh have to be defined. Since the ALE is based on Eulerian and Lagrangian formulations, several attributes from these two formulations can be recognized, e.g. the motion of the material [42]. Thus, this is still given by Equation (2.44).

The reference domain in the ALE formulation is called the *referential* domain, and is denoted by $\hat{\mathbf{\Omega}}$. Having defined the referential domain, the motion of the mesh can be described independently of the motion of the material. Referential, or ALE coordinates, are denoted by $\boldsymbol{\chi}$. Now, the motion of the mesh can be expressed by [42]:

$$\boldsymbol{x} = \hat{\boldsymbol{\phi}}(\boldsymbol{\chi}, t) \tag{2.58}$$

From Equation (2.58), the mapping function, $\hat{\boldsymbol{\phi}}$, simply maps points, $\boldsymbol{\chi}$, from the ALE domain, $\hat{\mathbf{\Omega}}$, to points, $\boldsymbol{x}$, in the spatial domain, $\mathbf{\Omega}$. Thus, Equation (2.58) clearly plays a crucial role in the ALE finite element formulation [42].

In order to define displacement, velocity and acceleration of the mesh in an ALE formulation, a relation between the ALE coordinates and the material coordinates must be established. This relation can be expressed by a composition of functions [42]:

$$\boldsymbol{\chi} = \hat{\boldsymbol{\phi}}^{-1}(\boldsymbol{x}, t) = \hat{\boldsymbol{\phi}}^{-1}(\boldsymbol{\phi}(\boldsymbol{X}, t), t) = \boldsymbol{\psi}(\boldsymbol{X}, t) \quad \text{or} \quad \boldsymbol{\psi} = \hat{\boldsymbol{\phi}}^{-1} \circ \boldsymbol{\phi} \tag{2.59}$$

A graphical description of the relation between different domains and the mapping expressions are given in Figure 2.13.
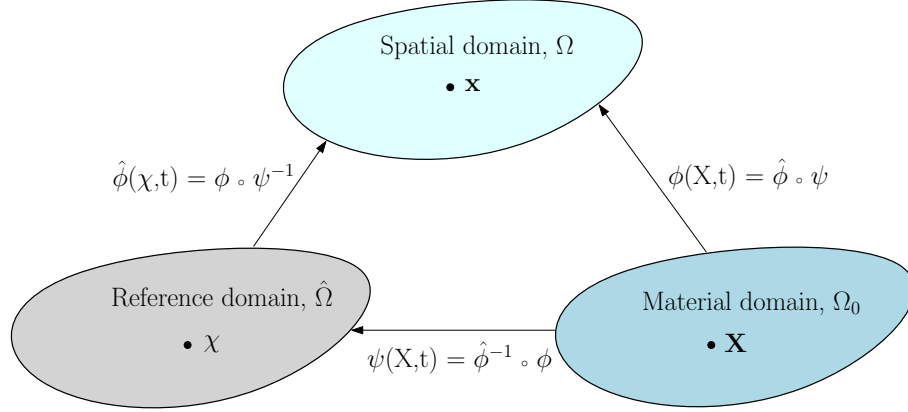
Figure 2.13: Maps between Lagrangian, Eulerian and ALE domains [42].

By combining the motion of the mesh and the $\boldsymbol{\psi}$ map, the material motion can be expressed by the following composition [42]:

$$\boldsymbol{x} = \boldsymbol{\phi}(\boldsymbol{X}, t) = \hat{\boldsymbol{\phi}}(\boldsymbol{\psi}(\boldsymbol{X}, t), t) \quad \text{or} \quad \boldsymbol{\phi} = \hat{\boldsymbol{\phi}} \circ \boldsymbol{\psi} \tag{2.60}$$

From the foregoing equations, expressions for the mesh displacement, mesh velocity and the mesh acceleration can be obtained. The mesh displacement, $\hat{\boldsymbol{u}}$, is defined by [42]:

$$\hat{\boldsymbol{u}}(\boldsymbol{\chi}, t) = \boldsymbol{x} - \boldsymbol{\chi} = \hat{\boldsymbol{\phi}}(\boldsymbol{\chi}, t) - \boldsymbol{\chi} \tag{2.61}$$

Further, the mesh velocity, $\hat{\boldsymbol{v}}$, is defined by:

$$\hat{\boldsymbol{v}}(\boldsymbol{\chi}, t) = \frac{\partial \hat{\boldsymbol{\phi}}(\boldsymbol{\chi}, t)}{\partial t} \equiv \left. \frac{\partial \hat{\boldsymbol{\phi}}}{\partial t} \right|_{\boldsymbol{\chi}} \equiv \hat{\boldsymbol{\phi}}_{,t[\boldsymbol{\chi}]} \tag{2.62}$$

Finally, an expression for the mesh acceleration, $\hat{\boldsymbol{a}}$, can be given as:

$$\hat{\boldsymbol{a}}(\boldsymbol{\chi}, t) = \frac{\partial \hat{\boldsymbol{v}}(\boldsymbol{\chi}, t)}{\partial t} = \frac{\partial^2 \hat{\boldsymbol{u}}(\boldsymbol{\chi}, t)}{\partial t^2} = \hat{\boldsymbol{u}}_{,tt[\boldsymbol{\chi}]} \tag{2.63}$$

Unless the ALE mesh is Lagrangian, neither the mesh acceleration, nor the mesh velocity, have any physical meaning. If the mesh is Lagrangian, mesh acceleration and mesh velocity correspond to material acceleration and material velocity [42].

In order to obtain the conservation laws for the ALE formulation, expressions for the convective velocity, c, and the material time derivative should be stated beforehand.

The convective velocity, c, which is the difference between the material velocity and the mesh velocity, is defines by [42]:

$$c_i = v_i - \hat{v}_i \tag{2.64}$$

The material time derivative can be expressed by:

$$\frac{\partial f}{\partial t} = f_{,t[\chi]} + f_{,j}\, \frac{x_j}{\partial \chi_i} w_i = f_{,t[\chi]} + f_{,j}\, c_j \tag{2.65}$$

Note that the comma, followed by an index, represents the spatial derivative with respect to an Eulerian coordinate.

Having defined the convective velocity, c, and the material derivative, expressions for the conservation laws can be presented.

Conservation of mass

$$\dot{\rho} + \rho v_{j,j} = 0 \quad \text{or} \quad \rho_{,t[\chi]} + \rho_{,j}\, c_j + \rho v_{j,j} = 0 \tag{2.66}$$

Conservation of linear momentum

$$\rho \dot{v}_i = \rho(v_{i,t[\chi]} + v_{i,j} c_j) = \sigma_{ji,j} + \rho b_i \tag{2.67}$$

Conservation of angular momentum

$$\boldsymbol{\sigma} = \boldsymbol{\sigma}^T \tag{2.68}$$

Conservation of energy

$$\rho(E_{,t[\chi]} + E_{,i}\, c_i) = \sigma_{ij} D_{ij} + b_i v_i + (k_{ij}\theta_{,j})_{,i} + \rho s \tag{2.69}$$

where

θ temperature
k thermal conductivity of the material

2.9 Discrete Particle Method

The Discrete Particle Method (DPM), or corpuscular method, is based on Maxwell's kinematic molecular theory. This Lagrangian method origins from an attempt of circumvent difficulties related to continuum-based modeling of airbag deployment simulations. Since the corpuscular method is Lagrangian, treatment of gas-structure contact is simplified. Also, establishment of numerical robust implementation of the governing equations are simplified, due to lack of field equations. For geometrically complex gas-structure interactions, the corpuscular approach is definitely a competitive alternative to continuum-based methods. This is due to the fact that continuum-based methods may lead to numerical difficulties for these type of problems. However, in most situations where macroscopically gas flow is to be studied, other methods are generally applied [54].

For close-range blast loading applications, complex geometries may need to be considered. In simulations of this type of problems, a fully coupled Eulerian approach may be employed. However, this approach is known to be very costly in terms of CPU-time. Olovsson et al. [15] suggested to use a particle-based approach in describing close-range blast loading. They showed that the computational time can be significantly reduced. In addition, the method proved to be numerically robust. Complex geometries in the fluid-structure interaction were also handled easily.

2.9.1 Theory behind DPM

Kinetic molecular theory is the study of gas molecules and their interaction on a microscopic level. This study has brought forth a relation on macroscopic level, namely the ideal gas law. A set of assumptions regarding the behaviour and characteristics of the gas molecules have been made, and these are listed below [54].

- The average distance between the molecules are large compared to their size.

- There is a thermodynamical equilibrium, i.e. the molecules are in random motion.

- The molecules obey Newton's law of motion. Relativistic quantum mechanical effects are negligible.

- The collisions between molecule-molecule and molecule-structure interactions are perfectly elastic.

The idea behind the kinetic molecular theory dates back to 1738, when D. Bernoulli suggested that air pressure against a piston could be represented by discrete molecular collisions. In the light of this, J. C. Maxwell derived an expression for the molecular velocity distribution at thermal equilibrium. From Maxwell's statistical descriptions, quantities, such as mean free path and frequency of collision, can be derived [54].

By employing the kinetic molecular theory and the belonging assumptions, an expression for the pressure can be obtained. To illustrate the concept, a rectangular box with side lengths L_x, L_y and L_z is introduced. Inside this box, a number of N particles with mass m_i and velocity $v_i = [v_{x,i}, v_{y,i}, v_{z,i}]$ are placed, as can be seen in Figure 2.14.
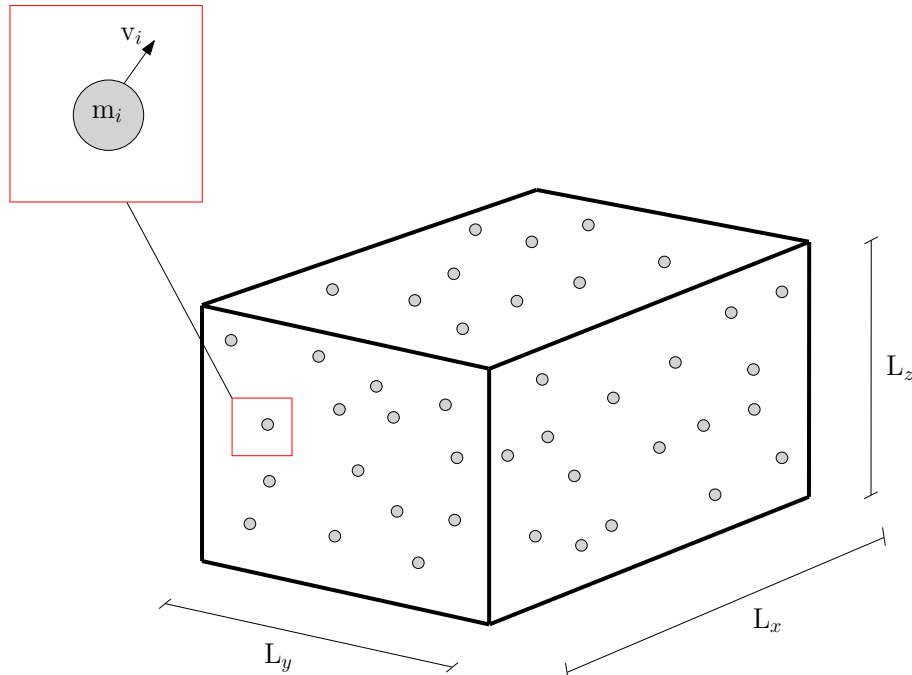
Figure 2.14: Box containing N molecules.

At thermal equilibrium, the kinetic energy will be evenly distributed between the different Cartesian directions. Therefore, the pressure in the different directions can be set equal and expressed as:

$$P_x = P_y = P_z = P = \frac{2W_k}{3V} = \frac{2w_k}{3} \tag{2.70}$$

where

W_k total translational kinetic energy of the particles
V the volume of the box, $V = L_x \cdot L_y \cdot L_z$
w_k the specific translational kinetic energy

From Equation (2.70), it can be seen that at thermodynamic equilibrium, a direct relation between the pressure and the specific translational kinetic energy can be established [54].

When it comes to implementation of the DPM, e.g. in LS-DYNA, some assumptions are necessary in order to sustain computational efficiency. Olovsson et al. [15] have discussed these type of assumptions for modeling in LS-DYNA. First of all, they

stated that all molecules for a detonation product cannot possibly be modeled. Therefore, each particle will represent a large amount of molecules. Particles are also assumed to be rigid with a spherical shape, since this will speed up the contact treatment. For a more thoroughly discussion of the DPM, literature by Olovsson [54] and Olovsson et al. [15] should be revised.

2.10 Numerical Integration

Numerical integration methods are used for calculating the numerical value for a definite integral. However, the term numerical integration can also be used for describing numerical solutions for time-dependent, ordinary and partial differential equations [55]. When trying to describe physical processes, e.g. wave propagation problems created by blast or impact loading and structural dynamic problems, numerical simulation methods are widely used.

The two main groups of approaches, used for solving numerical integration problems, are called explicit and implicit methods. These methods have different strengths and weaknesses, and thus different area of application. In short, implicit methods prove best for problems where either the response period of interest is long, or the nonlinearities are smooth. An implicit method is therefore preferable for structural dynamic problems. Explicit methods, on the other hand, is ideal for high-speed dynamic simulations, e.g. in blast or impact problems. These methods are usually reliable for problems involving discontinuous nonlinearities [56].

2.10.1 Explicit Direct Integration

For an explicit method, each time increment is computationally inexpensive, since equation solving is not necessary. The method is conditionally stable, which requires very small time steps. The time increment, Δt, must be less than the critical time increment, Δt_{cr}. Otherwise, the solution will be unstable and oscillations will occur in the response history [56]. However, for high-speed dynamic simulations, very small time steps are necessary in order to obtain sufficient simulation accuracy. Thus, in order to obtain a bounded solution, the time increment should be less than:

$$\Delta t_{cr} \leq \min\left[\frac{2}{\omega_j}\left(\sqrt{1 - \xi_j^2} - \xi_j\right)\right] \tag{2.71}$$

where

ξ damping ratio in mode j
ω_i eigenfrequency of mode j

In order to evaluate the critical time step for a given finite element mesh, the highest frequency, ω_{max}, for the unsupported elements should be revealed. In can be shown that for an undamped material, the critical time step can be written as:

$$\Delta t_{cr} \leq \frac{2}{\omega_{max}} = \frac{L}{c_d} \tag{2.72}$$

48

where

ω_{max} maximum eigenfrequency of the FE mesh
L element length
c_d dilatational wave speed

Equation (2.72) is often referred to as the CFL condition, after Courant, Friedrichs and Lewy [43]. The equation gives a limit for which information will not propagate more than the distance between adjacent nodes during a single time step [56]. If the time step is within this limit, the solution will be bounded.

When it comes to solving of contact problems, like buckling and material failure, explicit methods are also the most suitable choice [57]. In sum, this makes explicit methods preferable for blast and explosion problems.

Classical Central Differences

The equations of motion for a nonlinear Multi-Degree-of-Freedom (MDOF) system, at time t, may be written as [56]:

$$\{\boldsymbol{R}^{\text{ine}}(t)\} + \{\boldsymbol{R}^{\text{dmp}}(t)\} + \{\boldsymbol{R}^{\text{int}}(t)\} = \{\boldsymbol{R}^{\text{ext}}(t)\} \tag{2.73}$$

where

$\{\boldsymbol{R}^{\text{ine}}(t)\}$ the inertia force vector, which may be written as $[\boldsymbol{M}]\{\ddot{\boldsymbol{D}}(t)\}$
$\{\boldsymbol{R}^{\text{dmp}}(t)\}$ the damping force vector, which may be written as $[\boldsymbol{C}]\{\dot{\boldsymbol{D}}(t)\}$
$\{\boldsymbol{R}^{\text{int}}(t)\}$ the internal force vector
$\{\boldsymbol{R}^{\text{ext}}(t)\}$ the external force vector

$\{\dot{\boldsymbol{D}}(t)\}$ and $\{\ddot{\boldsymbol{D}}(t)\}$ represent the nodal point velocities and the nodal point accelerations, respectively.

Approximations of velocity, $\dot{u}_n(t)$, and acceleration, $\ddot{u}_n(t)$, can be obtained by performing a Taylor series expansion of the displacements u_{n+1} and u_{n-1}, about time t_n. For simplicity, the equations are given for a Single-Degree-of-Freedom (SDOF) system. This enable use of a graphical description, as can be seen in Figure 2.15. This will in turn lead to the following expressions for velocity and acceleration [56]:

$$\dot{u}_n = \frac{u_{n+1} - u_{n-1}}{2\Delta t} \tag{2.74}$$

$$\ddot{u}_n = \frac{u_{n+1} - 2u_n + u_{n-1}}{\Delta t^2} \tag{2.75}$$

It should be noted that terms containing Δt to power higher than second order are neglected in the Taylor series expansion. As a consequence of this, the primary

error term is proportional to Δt^2. Therefore, the displacement, u, has second-order accuracy [56].
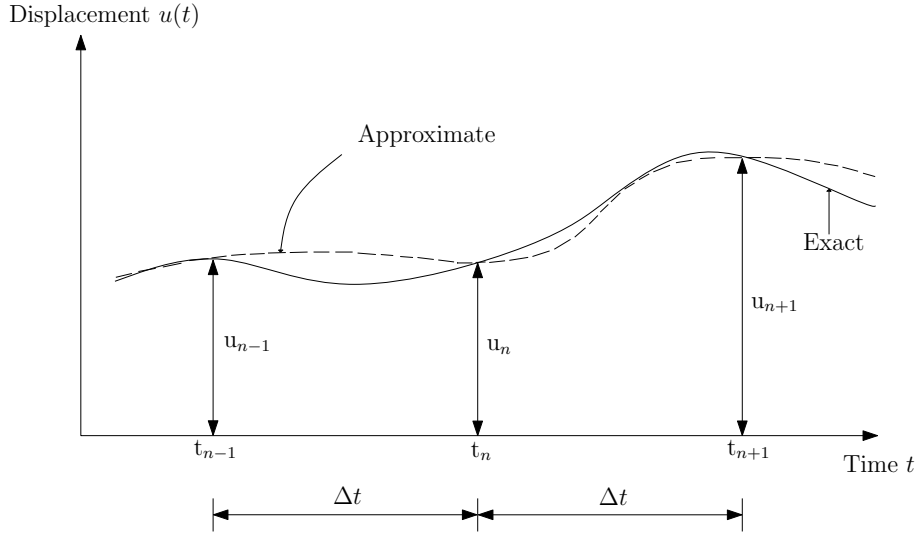
Figure 2.15: The central difference explicit method [56].

The above approximations to velocity, $\dot{u}_n$, and acceleration, $\ddot{u}_n$, are referred to as the conventional central difference equations. Note that these expressions are valid for SDOF systems. However, expressions for MDOF systems may be obtained in a similar manner. By substituting these approximations into Equation (2.73), the following expression may be obtained for a nonlinear MDOF system [56]:

$$\{\boldsymbol{D}\}_{n+1} = [\boldsymbol{K}^{\text{eff}}]^{-1}\{\boldsymbol{R}^{\text{eff}}\}_n \tag{2.76}$$

where

$$[\boldsymbol{K}^{\text{eff}}] = \frac{1}{\Delta t^2}[\boldsymbol{M}] + \frac{1}{2\Delta t}[\boldsymbol{C}] \tag{2.77}$$

$$\{\boldsymbol{R}^{\text{eff}}\}_n = \{\boldsymbol{R}^{\text{ext}}\}_n - \{\boldsymbol{R}^{\text{int}}\} + \frac{2}{\Delta t^2}[\boldsymbol{M}]\{\boldsymbol{D}\}_n - \left(\frac{1}{\Delta t^2}[\boldsymbol{M}] - \frac{1}{2\Delta t}[\boldsymbol{C}]\right)\{\boldsymbol{D}\}_{n-1} \tag{2.78}$$

Unless the mass matrix, $[\boldsymbol{M}]$, and the damping matrix, $[\boldsymbol{C}]$, are diagonal in Equation (2.76), the effective stiffness matrix, $[\boldsymbol{K}^{\text{eff}}]$, has to be established and factorized in order to obtain displacements, $\{\boldsymbol{D}\}_{n+1}$. A computational efficient way of finding displacements, $\{\boldsymbol{D}\}_{n+1}$, arises if only lumped mass matrices are employed. In this case, damping is assumed either set to zero, or to be given as mass-proportional damping, $[\boldsymbol{C}] = \alpha[\boldsymbol{M}]$. However, the dynamic response will contain high-frequency

numerical noise, since mass-proportional Rayleigh damping mainly damps lower modes. Damping of high-frequency numerical noise may be handled by including stiffness-proportional damping, $[\boldsymbol{C}] = \beta[\boldsymbol{K}]$. It should be noted that this will lead to an increase in computational cost per time step, since the effective stiffness, $[\boldsymbol{K}^{\text{eff}}]$, becomes non-diagonal [56].

Half-Step Central Differences

By modifying the equilibrium equations, the increase in computational time, due to the damping of high-frequency noise, can be avoided. If the equilibrium equations are established with velocity lagging by half a time step, it can be shown that the aforementioned problems may be overcome [56]. Now, velocities are approximated in the following manner:

$$\dot{u}_{n-\frac{1}{2}} = \frac{1}{\Delta t}(u_n - u_{n-1}) \quad \text{and} \quad \dot{u}_{n+\frac{1}{2}} = \frac{1}{\Delta t}(u_{n+1} - u_n) \tag{2.79}$$

This leads to the following expression for the acceleration:

$$\ddot{u} = \frac{u_{n+1} - 2u_n + u_{n-1}}{\Delta t^2} \tag{2.80}$$

If damping is approximated in the following manner:

$$\frac{c}{2\Delta t}(u_{n-1} - u_{n+1}) \approx \frac{c}{\Delta t}(u_{n-1} - u_n) \tag{2.81}$$

the preferred form of the central difference method, for a MDOF system, can be written as [56]:

$$\{\boldsymbol{D}\}_{n+1} = \Delta t^2 [\boldsymbol{M}]^{-1} \{\boldsymbol{R}^{\text{eff}}\}_n \tag{2.82}$$

where

$$\{\boldsymbol{R}^{\text{eff}}\}_n = \{\boldsymbol{R}^{\text{ext}}\}_n - \{\boldsymbol{R}^{\text{int}}\} + \frac{1}{\Delta t^2}[\boldsymbol{M}](2\{\boldsymbol{D}\}_n + \{\boldsymbol{D}\}_{n-1})$$
$$- \frac{1}{\Delta t}[\boldsymbol{C}](\{\boldsymbol{D}\}_n - \{\boldsymbol{D}\}_{n-1}) \tag{2.83}$$

The drawback of Equation (2.83), is that only first-order accuracy can be guaranteed, due to the approximations of the viscous forces. However, for practical structures that have light damping, and require very small time steps, the two methods will yield results with insignificant differences when it comes to accuracy [43].

2.11 EUROPLEXUS

In this section, a brief introduction to the computer code EUROPLEXUS will be given.

2.11.1 About EUROPLEXUS

Descriptions below are given according to the EUROPLEXUS user's manual [46].

EUROPLEXUS is a computer code made for numerical simulations. The code has been developed by the French Commissariat à l'Energie Atomique (CEA Saclay) and the Joint Research Centre of the European Commission (JRC Ispra).

EUROPLEXUS is used for analysis of 1D, 2D and 3D domains composed of solids (continua, shells or beams) and fluids. Fluid-structure interactions (FSI) are also taken into account, and it is in fact regarded as the state-of-the-art solver with respect to FSI [58].

EUROPLEXUS fits perfectly well for problems involving rapid dynamic phenomena (fast transient dynamics) such as explosions, impacts, crashes etc. This is due to the fact that the code is based on an explicit, central-difference algorithm. In addition, both geometric and material nonlinearities are fully taken into account.

When it comes to spatial discretization, the Finite Element (FE) and Finite Volume (FV) are the two most commonly employed formulations. Other discretization formulations may also be used, such as Smoothed Particle Hydrodynamics (SPH).

Depending on the type of problem to be modeled, the following element formulations can be used in EUROPLEXUS:

- Lagrangian

- Eulerian

- ALE

Discussions regarding these three element formulations have been given in Chapters 2.8.1, 2.8.2 and 2.8.3. In general, Lagrangian descriptions are used for structural domains, while Eulerian descriptions are used for fluids.ALE formulations, on the other hand, are often used for fluids which are interacting with structural domains.

2.11.2 Modeling in EUROPLEXUS

In subsequent sections, a brief discussion regarding handling of different types of analyses in EUROPLEXUS will be given. Detailed descriptions regarding treatment of structural and fluid domains in EUROPLEXUS will not be given herein. However, it have been made room for a short introduction. The main focus have been to clarify how interactions between structural and fluid domains are treated, in addition to investigate how blast loading may be modeled. The intention is to give an overview of the possibility rendered by EUROPLEXUS, without going into all the details. However, if a more thorough understanding is desired, Kristoffersen [58], Casadei et al. [59] or the EUROPLEXUS User's manual [46] may be useful.

Structural Domain

In EUROPLEXUS, a Lagrangian formulation is employed when a structural domain is to be modeled. In Figure 2.16, a discretized structural domain can be seen. Governing equations for the structural domain are obtained from the principle of virtual work, i.e. equilibrium in a dynamic sense [59]. For applications in the FEM, equilibrium equations are spatial discretized, leading to the following equation [58]:

$$\boldsymbol{M}\boldsymbol{a} = \boldsymbol{F}^{ext} - \boldsymbol{F}^{int} \tag{2.84}$$

where

$\boldsymbol{M}$	lumped mass matrix
$\boldsymbol{a}$	nodal acceleration vector
$\boldsymbol{F}^{ext}$	external forces
$\boldsymbol{F}^{int}$	internal forces
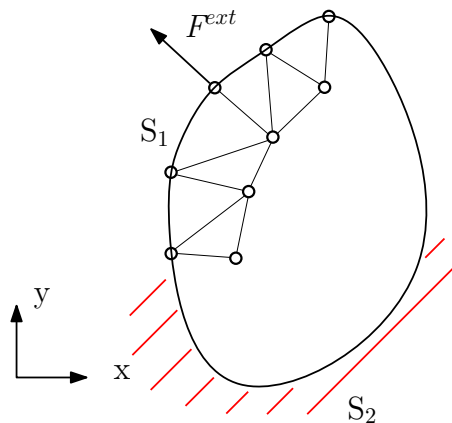
Figure 2.16: Discretization of structural subdomain S_1 [59].

To be more precise, the vector containing internal forces, $\boldsymbol{F}^{int}$, can be given as:

$$\boldsymbol{F}^{int} = \sum_{i=1}^{N_{els}} \int_{V_n} \boldsymbol{B}^T \boldsymbol{\sigma} \, \mathrm{d}V \tag{2.85}$$

where

N_{els}	number of elements
V_n	element volume
$\boldsymbol{B}$	matrix of shape functions derivatives
$\boldsymbol{\sigma}$	the Cauchy stress

Equation (2.84) is solved explicitly, since a lumped mass matrix is employed. Time integration is achieved via the central differences scheme [59].

Fluid Domain

Fluids modeled in EUROPLEXUS are by default set to be compressible and inviscid. In purely fluid problems, an Eulerian description is used. If interactions of fluids and structures are present, an ALE description is preferable [59]. It should be noted that a formulation based on SPH may also be used. In Figure 2.17, a comparison between the Lagrangian, Eulerian and ALE formulations on a node-by-node basis is given.
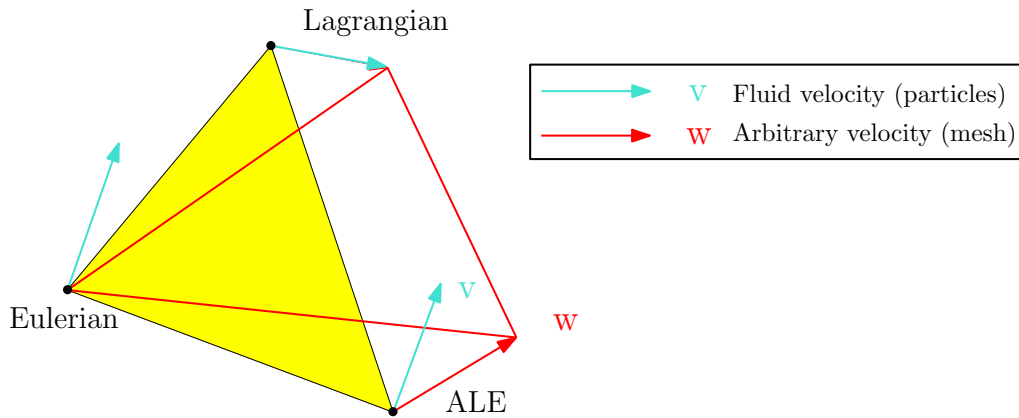
Figure 2.17: Comparison of different element formulations [59].

Since w, in Figure 2.17, is arbitrary, it must be provided either by the user or by automatic rezoning algorithms in EUROPLEXUS [59]. The intention of the rezoning techniques is to avoid large distortions in the element mesh, by rearranging the positions of the nodes included. Automatic rezoning algorithms in EUROPLEXUS are described in both the EUROPLEXUS User's manual [46] and by Kristoffersen [58], and will not be discussed any further herein.

Euler equations, which describe conservation of mass, momentum and energy, make up the governing equations for the fluid domain. These equations are conveniently

expressed in integral form. For more details, see Chapter 2.8.2. In addition, a suitable equation of state is needed, in order to model the fluid domain in EURO-PLEXUS. Often, this implies use of the ideal gas law. Further descriptions of how these equations are treated in EUROPLEXUS are given by Casadei et al. [59].

When it comes to discretization of the fluid domain in EUROPLEXUS, the following three techniques may be employed [58]:

- finite elements (FE)

- finite volumes (FV)

- smoothed particle hydrodynamics (SPH)

Regarding modeling of the structural domain, different kinds of finite elements are generally employed [58].

Figure 2.18 shows three different approaches for discretizing the fluid domain. These are related only to the finite elements and finite volumes formulations.
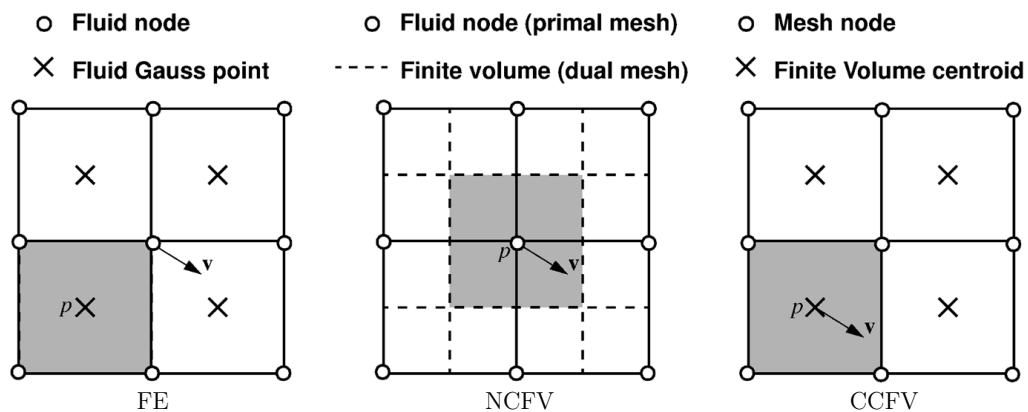
Figure 2.18: Three different ways of discretizing the fluid domain: finite elements (FE), Node-Centered Finite Volumes (NCFV) and Cell-Centered Finite Volumes (CCFV) [59].

If the fluid domain is built up by the use of finite elements, the kinetic variables are discretized at the nodes, while state variables are discretized at Gauss points. The internal pressure is an example of a state variable, and is thus collected in Gauss points. When using a NCFV discretization technique, all variables are discretized at the nodes, while all variables are discretized at the volume center for CCFV discretization [58].
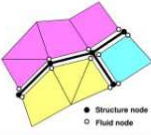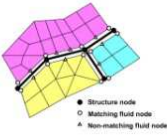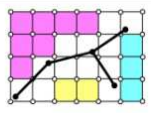
2.11.3 FSI in EUROPLEXUS

A crucial consideration in many engineering disciplines is the FSI, e.g. in designing of aircrafts and bridges. It is important to take the effects from these interactions

into account, in order to avoid unforeseen effects. If this is disregarded, aircraft wings may break and bridges may collapse due to oscillations induced by FSI [60].

For problems including both structural and fluid domains, an effective way of handling interactions between the different type of domains is needed. This can be handled in different ways in EUROPLEXUS. Before going into details, an overview of the available algorithms is presented in Table 2.3. It should be noted that SPH is not included in this presentation.

Table 2.3: Different FSI algorithms available in EUROPLEXUS [58].

	Detection Strategy	Spatial Discretization		Enforcement Strategy	Name / command	Use with
FSI Algorithm	**Basic** (no structural failure)	**Conforming** F-S meshes		**Strong**	**FSA**	FE, NCFV
				Weak	Merge F-S nodes	CCFV
		Non-conforming F-S meshes		**Strong**	**FSA**	FE, NCFV
				Weak	Declare non-matching F-nodes	CCFV
	Embedded (structure can fail)	S-mesh is **Immersed** in the F-mesh		**Strong**	**FLSR**	FE, NCFV
				Weak	**FLSW**	CCFV

In Table 2.3, two different enforcement strategies are listed, namely the "weak" and "strong" formulation. The differences are related to how constraints are imposed. For the weak formulation, the pressure from the fluid is applied as an external force on the structure. In a strong approach, on the other hand, the constraints are imposed on the particle velocity and at the mesh velocity in the interface between the two domains. Constraints on velocity are enforced exactly by use of Lagrange multipliers. In this way, essential conditions set forth by the user, e.g. restraints on movement, contact and symmetries, may be coupled automatically with FSI conditions. Regarding descretizations, finite elements (FE) are traditionally used in strong FSI algorithms, while finite volumes (FV) are most common in weak algorithms [58].

Depending on whether an algorithm is able to handle structural failure or not, it may be classified as either *basic* or *embedded*, as indicated in Table 2.3. A basic formulation is able to handle large deformations, except from structural failure, given a suitable mesh rezoning technique. A basic formulation can further be divided into *conforming* and *non-conforming* discretizations. If a finite element mesh is classified as nodally conforming, this simply means that for each node on the Lagrangian structure, there is a corresponding ALE fluid node, and the other way around. In the case of a non-conforming finite element mesh, the nodes of the structure and

the fluid nodes do not need to occupy the same positions in space. However, some of the nodes will correspond [58].

Embedded FSI algorithms are able to handle structural failure. The concept is to embed the structure in a fixed Eulerian mesh, and the fluid-structure interactions in the vicinity of the structure are handled. In this way, the work related to meshing is reduced compared to a basic algorithm, since it is no longer necessary to make sure that nodes conform, or that nodes merge. For an embedded algorithm, there is no possibility of distortion in the fluid mesh, which implies that use of ALE formulation becomes redundant [58]. Further discussions regarding embedded FSI algorithms will be taken in Chapter 2.11.4.

In Table 2.4 a descriptive summary of the different FSI algorithms in EUROPLEXUS is presented.

Table 2.4: Classification of different FSI algorithms [58].

FSI algorithm	FSI detection	Basic	No structural failure, moderate rotations.
		Embedded	Structure can fail, arbitrary rotation.
	FSI enforcement	Strong	Constraints on fluid and structure velocities are imposed, e.g. by Lagrange multipliers.
		Weak	Pressure forces are transmitted from the fluid to the structure, and structure motion provides weak feedback on the fluid.

2.11.4   Embedded FSI Algorithms

The embedded approach is, as mentioned, able to handle structural failure. This is in contrast to algorithms based on an ALE formulation, where the structure is Lagrangian and the fluid ALE. Approaches based on these formulations, will experience problems with keeping a suitable form of the mesh if the deformations are too severe. In particular, this apply if rotations are involved. Also, difficulties related to merging of the fluid domains after structural failure are regarded as a drawback [58]. Figure 2.19 shows a discretized structure in a completely independent Eulerian fluid mesh.
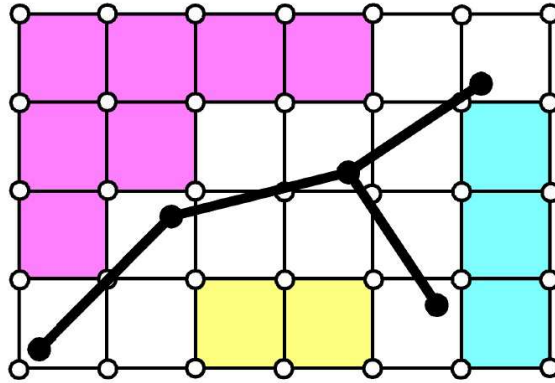
Figure 2.19: Structural mesh embedded in a fixed fluid mesh [59].

In order to include FSI in the embedded approach, information about which nodes that are located close to the structure is needed. The structure's so-called *influence domain*, defines these nodes. Due to deformations of the structure, the influence domain must be obtained for each time step. Thus, a fast search algorithm is required. In short, a user defined circle (or sphere in 3D) with a given radius is defined, and centered at every structural node. By connecting nodes inside these circles, an area (or a volume in 3D) appears. This will then constitute the influence domain, consisting of coupled nodes [58].

2.11.5 Blast Load Simulations

Several methods can be used to simulate the explosion process in EUROPLEXUS. The selection of method depends on the scope of the analysis. Precision, complexity and access to computational power, are some factors that may influence the choice of method. Casadei et al. [59] presented three different ways which can be used to simulate the explosion. In addition, three approaches for simulating the explosive charge in EUROPLEXUS are given. If an explosion is to be simulated in EUROPLEXUS, the following approaches may be employed:

- Structure only (AIRB) - no reflections

- Fluid only (FSR) - only valid for very heavy/stiff structures

- Fluid-structure (FLSR/FLSW) - all effects included
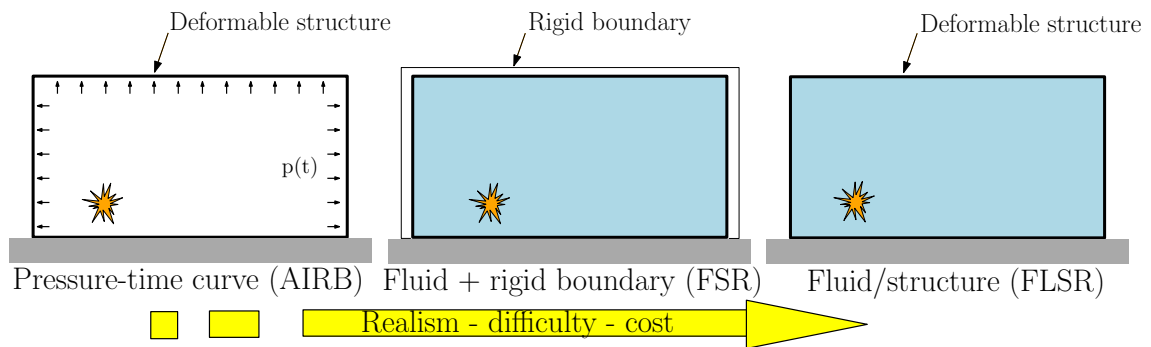
Figure 2.20: Graphical descriptions of different ways of simulating an explosion in EUROPLEXUS [59].

Below, three different approaches for simulating the explosive charge in EURO-PLEXUS are given.

- Pressure-time function (AIRB)

- Compressed balloon (GAZP, BUBB)

- Solid TNT (JWLS)

The AIRB approach is a quick and simple way of simulating air blast problems. Here, a pressure-time function is used for describing the behaviour of the explosive and the intermediate air. The calculation time is relatively low, since only the structure is modeled. Consequently, this is an inexpensive and efficient approach. The pressure-time function is implemented through the modified Friedlander equation, which has been discussed in Chapter 2.2.4. However, the negative phase cannot be described by this equation, and is instead represented by a bilinear curve. This is described in detail by Larcher [27]. The AIRB approach can handle structural failure and fragmentation [59]. However, some drawbacks are related to this approach. Reflections, shadowing, channeling effects and other more complex phenomena are not taken into account. The AIRB approach is therefore limited to simple problems [59].

Another approach, which is given by the GAZP command in EUROPLEXUS, is often referred to as the compressed balloon method. The idea behind this method is to create a "balloon" of compressed gas to represent the explosive. In this way, structures can be loaded without having to model the explosive [46]. Regarding the calculation time, this approach is somewhat more expensive than the AIRB approach.

Initial conditions of the compressed gas are evaluated on the basis of the TNT equivalent mass, W_E, defined in Equation (2.12), and the initial volume of the compressed gas [59]. In the paper by Larcher et al. [36] the following procedure is given for obtaining the initial pressure, p_{bal}, for given values of the TNT equivalent mass, W_E, and balloon volume, V_{bal}.

1. Calculation of the nominal energy of the explosive charge

$$E_{TNT} = W_E \cdot 4.52 \cdot 10^6 \qquad [\text{J}] \tag{2.86}$$

2. Calculation of the over-pressure in the balloon by use of Brode's formula

$$p_{TNT} = p_{Brode} - p_0 = \frac{E_{TNT}}{V_{bal}}(\gamma - 1) \tag{2.87}$$

where γ is the heat capacity ratio of the gas in the balloon, p_0 is the atmospheric pressure and

$$p_{Brode} = \frac{E_{TNT}(\gamma - 1)}{V_{bal}} + p_0 \tag{2.88}$$

3. In order to obtain correct values for impulses, a dimensional scaling factor, α_{bal}, is introduced. This factor is defined by

$$\alpha_{bal} = -0.2205 \log(p_{TNT}) + 2.265 \tag{2.89}$$

4. Then, an expression for the initial pressure, p_{bal}, in the balloon can be given as

$$p_{bal} = \frac{p_{TNT}}{\alpha_{bal}} + p_0 \tag{2.90}$$

5. In order to distribute the scaling factor, α_{bal}, between the internal energy and the density of the gas inside the balloon, a square root scaling factor, f_{bal}, is introduced

$$f_{bal} = \sqrt{\frac{p_{bal}}{p_0}} \tag{2.91}$$

6. In the end, values for the internal specific energy, $e_{int,bal}$, and the density of the gas inside the balloon, ρ_{bal}, are obtained in the following manner

$$\rho_{bal} = \rho_0 \cdot f_{bal} \tag{2.92}$$
$$e_{int,bal} = e_{int,0} \cdot f_{bal} \tag{2.93}$$

where ρ_0 is the density of the uncompressed air and $e_{int,0}$ is the corresponding internal specific energy.

In the paper by Larcher et al. [36], a more detailed description of the balloon approach can be found. In addition, discussions regarding the introduction of the

correction factor, α_{bal}, and the scaling factor, f_{bal}, are given. However, the basic concept of the balloon approach is that a pressure-time function, resulting from a compressed balloon, can be employed to represent the corresponding curve for an air blast wave [36].

EUROPLEXUS also has a command called BUBB. The BUBB command automatically calculates the input values for the balloon method with the help of similar equation as explained for GAZP. Because of this, only the TNT equivalent mass and the assigned elements have to be specified.

In the solid TNT approach, the explosive material is described by use of a material law. This can for instance be the Jones-Wilkins-Lee (JWL) equation of state (EoS) for explosives, which is described in Chapter 2.3. Thus, an initially solid explosive material is the starting point in this way of simulating an air blast problem.

In the paper by Larcher and Casadei [36], it is emphasized that elements close to the explosive should be smaller than the elements which make up the explosive material. If not, sufficient accuracy may not be obtained, leading to awkward results. Since small elements increase the computational time, this method is regarded as expensive with respect to computational cost. In order to reduce the computational time, so-called spatial partitioning may be employed. This method reduces the computational time for models with large variation in element sizes [36]. For more details about this method see the paper by Casadei and Halleux [61].

In Figure 2.21, a graphical comparison between the three approaches is given. Starting from the pressure-time curve in the AIRB approach, an increase in realism, complexity and computational cost can be observed when going from the AIRB approach to the GAZP or BUBB approach. The same tendency can be observed when moving on to the JWLS approach.
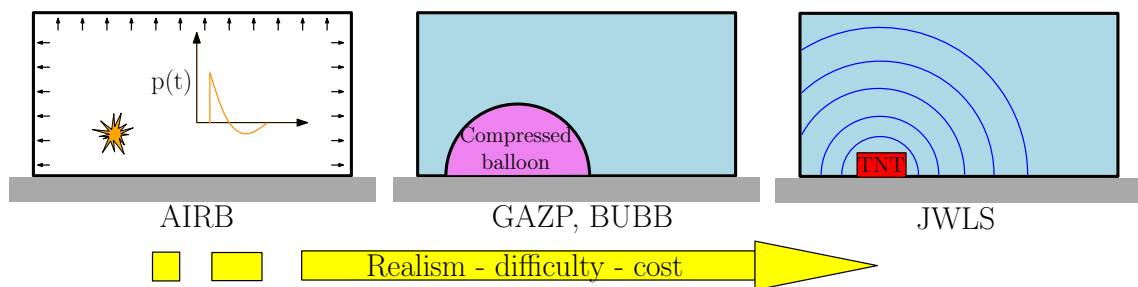
Figure 2.21: Graphical description of different ways of simulating explosives in EU-ROPLEXUS [59].

2.12 Digital Image Correlation (DIC)

In the following, an introduction to Digital Image Correlation (DIC) will be given. Most of the theory and descriptions of the DIC method are taken from a doctoral thesis by Egil Fagerholt [62]. The main part of his thesis is concerning the development of DIC code and the application of this in various mechanical experiments.

DIC is a post-processing technique used for abstraction of field measurements in mechanical experiments. In the context of solid mechanics, DIC methods have been used for measuring of two-dimensional displacement and strain fields for numerous materials. In addition, three-dimensional displacement and strain fields may also be obtained by use of a two-camera (binocular) stereovision system. This principle is called stereo-triangulation. A schematic description of the setup for a 3D DIC analysis is given in Figure 2.22.
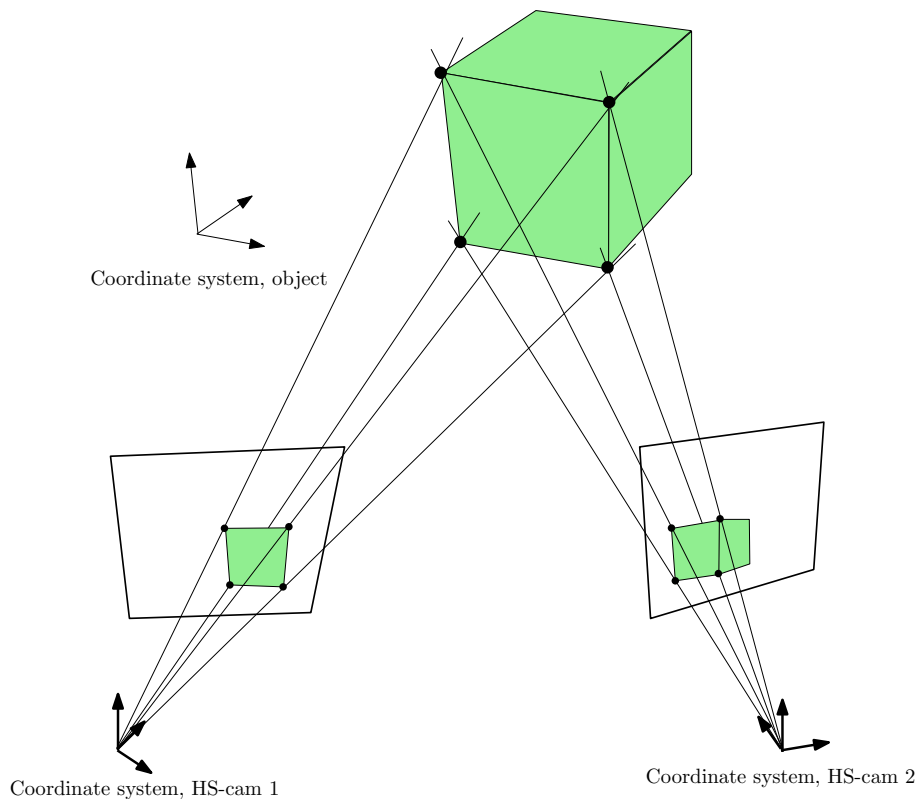
Figure 2.22: Principle of stereo-triangulation [63].

Use of DIC renders the possibility of validating different numerical models, which is of outmost importance in a scientific context. In addition, DIC rarely requires a comprehensive experimental setup, and this is regarded as one of the main reasons for the increasing popularity of DIC within mechanical testing. Further, the considerable development of digital cameras in the later years, e.g. within resolution, recording rate and data storage, have also contributed to the increasing interest for this post-processing technique.

Two main approaches exist when it comes to formulation of DIC. One of them is a subset-based formulation, while the other is based on a finite element (FE) formulation. A graphical description of the FE formulation is given in Figure 2.23. Both have advantages and disadvantages regarding practical applications in mechanical testing. For the FE formulation, which is based on conservation of optical flow, similar formulations in experimental measurements (DIC) and in numerical modeling (FEM) may be employed. This possibility, of combining DIC measurements with numerical modeling, makes the FE formulation of DIC favourable. However, regarding the accuracy of measurements, it is not clear from the literature which of the two approaches that yields the most accurate results.
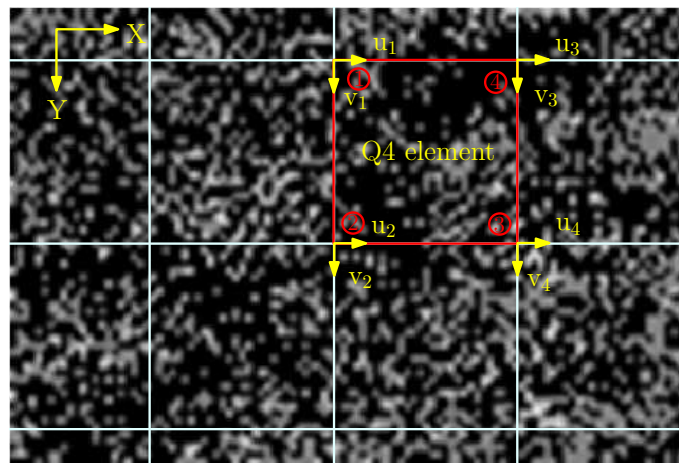
Figure 2.23: Principle of the FE-based DIC approach for a 2D analysis.

The principle of DIC is based on correspondence of distribution of grey values between digital images in an undeformed (reference) and a deformed (current) configuration. Deformations may be described by a set of parameters, that are obtained by minimizing the differences in grey-scale values between the reference and the current image. Mathematically, this lead to minimization of a correlation function, which can be defined in several ways. The sum of squared differences of the grey-scale values within a given subset, is an example of such a correlation function. For the FE-based DIC approach, the optimization of the correlation function is carried out globally on a mesh of elements, rather than individual optimization of subsets.

For the FE-based DIC approach, displacement continuity across boundaries of elements is preserved, in contrast to what is the case for the subset-based approach. This is due to the fact that optimization of displacements are related to different positions. For the FE-based approach, the nodal displacements in the mesh are optimized. For the subset-based approach, on the other hand, optimization is related to the displacements and the displacement gradient of the subset. What is obtained from a DIC analysis however – independent of the choice of method – is a displacement field, from which measures of strains and stresses can be abstracted.

Chapter 3

Preliminary Studies

Before executing the physical experiments, it was decided to do some preliminary calculations to get an impression of expected results. By doing so, stand-off distances which cause significant deformations were revealed. Only stand-off distances that resulted in plastic deformations would be considered for use in the experimental work. Initially, an analytical consideration was carried out.

3.1 Analytical Consideration

Methods for predicting the deformation of thin plates subjected to impulsive loading have been studied for many years. Several theoretical models have been proposed for different type of geometry, loading and boundary conditions. Some of them were supported by experimental studies, while others were based on available experimental data. Nurick and Martin [5] have given a review of earlier work and discussed some of the challenges related to this type of approach. Experimental techniques and approximate methods used for predicting deformation of thin plates subjected to impulsive loading, are summarized in tabular form. Pros and cons related to these methods are also discussed by Nurick and Martin [5].

In order to construct theoretical models for predicting the deformation of thin plates, subjected to impulsive loading, some assumptions, or simplifications have to be made. In the paper by Nurick and Martin [5], different proposals for predicting the deformation are divided into several categories, depending on type of approach. Methods concerning bending effects and membrane stretching effects, either separately or combined, compared favourable with experiments resulting in small deflections, i.e. deflections within one half to one plate thickness. Prediction of larger deflections, 4-9 plate thicknesses, were enabled by approximate methods based on mode concepts. Here, only transverse displacements were considered. Favourable predictions of even larger deflections were obtained by methods with a non-fixed mode shape, in which both transverse and lateral deflections were considered [5].

In the paper by Nurick and Martin [6], a method for comparison of results of deformed plates with similar geometries, boundary and loading conditions is desired. All other variables that impact the deformation are therefore put into dimensionless groups. The basis for their approach is a dimensionless damage number defined by W. Johnson. Johnson's damage number, α, is defined as [6]:

$$\alpha = \frac{\rho v^2}{\sigma_d} \tag{3.1}$$

where ρ is the density of the material, v is the impact velocity and σ_d is the damage stress. For metals in impact situations, this number can be used as a guide for assessing the material behaviour. However, it should be noted that this measure considers neither structural geometry nor loading conditions. Johnson's damage number can be written in terms of the impulse as [6]:

$$\alpha_0 = \frac{I^2}{A_0^2 t^2 \rho \sigma_d} = \frac{I_0^2}{t^2 \rho \sigma_d} \tag{3.2}$$

Here, I is the total impulse, A_0 is the area over which the impulse is imparted, I_0 is the impulse per area and t represents the plate thickness. Nurick and Martin [6] further introduced a geometrical number, β , in the case of quadrangular plates, defined as:

$$\beta = \frac{L}{B} \tag{3.3}$$

where L is the plate length and B is the breadth of the plate. Further, the geometrical damage number, ψ, can be written as:

$$\psi = \left[\beta \alpha_0 \left(\frac{A_0}{A} \right)^2 \right]^{\frac{1}{2}} \tag{3.4}$$

where A is the area of the plate. In addition, an aspect ratio was introduced, giving the relation between the plate thickness and the distance from the center of the plate to the nearest boundary. For quadrangular plates the aspect ratio, λ, is given as:

$$\lambda = \frac{B}{2t} \tag{3.5}$$

By combining the aforementioned equations, Nurick and Martin [6] proposed a modified damage number, which take both dimensions and loading into account. The modified damage number, ϕ, is defined as:

$$\phi = \psi \lambda \zeta \tag{3.6}$$

For quadrangular plates, the expression for the damage number can be given as:

$$\phi_q = \frac{I}{2t^2(BL\rho\sigma_0)^{\frac{1}{2}}} \tag{3.7}$$

Then, by measuring the impulse, I, and the damage stress, σ_d, experimentally, dimensionless plots can be made. For convenience, the damage stress, σ_d, can be given the value of the static yield stress, σ_0. This assumption is made in the work by Nurick and Martin [6], and is therefore regarded as an adequate assumption herein.

By comparing experimental data obtained from testing of uniformly loaded quadrangular plates, and by employing the principle of least squares fit, Nurick and Martin [6] presented the following empirical relation:

$$\left(\frac{\delta}{t}\right) = 0.480\phi_q + 0.277 \tag{3.8}$$

where δ is the mid-point deflection. Similar expressions for circular plates are also given by Nurick and Martin [6]. Jacob et al. [19] performed modifications of Equation (3.7), in order to include a loading parameter for quadrangular plates subjected to circular blast loading. Jones [64] presented a dimensionless numbers for both uniformly loaded circular and quadrangular plates. However, only the expression obtained by Nurick and Martin [6] be will used for a preliminary evaluation of the mid-point deflection.

Input parameters

In order to perform a preliminarily study of the mid-point deflection of the aluminum plates, some assumptions have to be made. Values for the geometrical parameters B, L and t are easily obtained. Reasonable values for the material parameters ρ and σ_0 can be found in the literature [65], while impulses can be taken from CONWEP, which is based on the empirical model made by Kingery and Bulmash [33], as mentioned in Chapter 2.2.7. For simplicity, the peak-impulse for each stand-off distance was used as a basis for obtaining the total impulse, which then was found by multiplying the peak-impulse by the total area of the plate. Parameters employed in these calculations are given in Table 3.1.

Table 3.1: Input values in preliminary study.

Parameters	Value	Unit
Plate		
t	$8 \cdot 10^{-4}$	m
L	0.300	m
B	0.300	m
Material		
ρ	2710	kg/m^3
σ_0	$100 \cdot 10^6$	N/m^2
Loading		
I_{250}	25.335	Ns
I_{375}	14.796	Ns
I_{500}	10.296	Ns
I_{625}	7.845	Ns

Predicted values for the deflection-thickness ratio, $\frac{\delta}{t}$, and deflection, δ, for three stand-off distances are given in Table 3.2.

Table 3.2: Predicted mid-point deflections.

Stand-off distance [mm]	$\frac{\delta}{t}$	δ [mm]
250	61.1	48.9
375	35.8	28.6
500	25.0	20
625	19.1	15.3

From Table 3.2, it can be seen that the predicted mid-point deflections increase for decreasing stand-off distances.

It should be noted that CONWEP is less accurate for close-range blast loading, as discussed in Chapter 2.2.7. This means that there is a greater source of error as the stand-off distance decreases. In addition, the total impulse is introduced by assuming that the peak-impulse value is constant throughout the entire plate. In a design way of thinking this would have been regarded as a conservative approach, since the pressure in fact vary considerably over the plate area. Also, the empirical formulas that Equation (3.8) is based on, do only consider material density and yield stress. In sum this indicates that the analytical approach suggested by Nurick and Martin [6], should be considered only as a quick assessment in estimating values for mid-point deflections. In order to get additional insight in expected values for the mid-point deflection, some preliminary numerical analysis were performed.

3.2 Mesh-Sensitivity Study

When performing preliminary simulations, it was important to obtain high quality results. In addition it was emphasized that the computational time was reasonable, so that the detonation could be tested at multiple stand-off distances. To find a good compromise, a mesh-sensitivity study was performed.

3.2.1 Procedure

A detailed description of the test setup is presented in Chapter 4.3.1.

In this preliminary study, a fixed boundary in the border between the steel clamping frame and the tested aluminum plates were assumed. Therefore, instead of modeling the whole plate as 400 mm x 400 mm, the plate was modeled as 300 mm x 300 mm. All nodes along the edge were restraining in all degrees of freedom. This setup was then used in a Lagrangian approach in EUROPLEXUS.

Since no material model had been established at this stage, the literature was used for inspiration. This led to the use of a Johnson-Cook material model, that is described in Chapter 2.7. The Johnson-Cook parameters obtained by Spranghers et al. [48], were used in order to provide a basis for the simulations. The parameters are given in Table 3.3. Material composition and physical properties are presented in Chapter 4.1.

Table 3.3: Material parameters employed in the mesh-sensitivity study.

Material model	A [MPa]	B [MPa]	n	C
Spranghers et al.	110	150	0.36	0.014

Loading was applied on the modeled plate by use of the AIRB command in EURO-PLEXUS. This command is described in Chapter 2.11.5. In this approach, pressure curves are generated on the form of the modified Friedlander equation. These are generated based on the location of the charge with respect to the structure, as well as the TNT equivalent mass, and updated at each time step. Since only the plate is modeled, and the load is applied onto the structure as pressure, no reflections or additional effects due to the explosion are included [59].

In order to apply the pressure load onto the structure in EUROPLEXUS, two overlapping meshes have to be defined. One mesh consist of elements of the type CL3D. This mesh serves as an absorbing boundary for transferring and distributing the pressure load generated by the AIRB approach onto the structure. Since this mesh only functions as an absorbing boundary, no physical properties are assigned.

The plate was modeled by the use of Q4GS elements. A Q4GS element is a 4-node shell element that can be used in 3D models. The element has 4 integration points

in the plane and 5 integration points through the thickness [46]. Shell elements can represent bending properly, and were therefore chosen due to their computational efficiency compared to solid elements [13].

The quadratic elements in the model were assigned a thickness of 0.8 mm. In Figure 3.1, a mesh with an element size of 10 mm can be seen. The charge was placed in the middle of the plate with a stand-off distance of 500 mm. The mass of the C4 was set to 30 g, which corresponds to a TNT equivalent mass of 40 g.
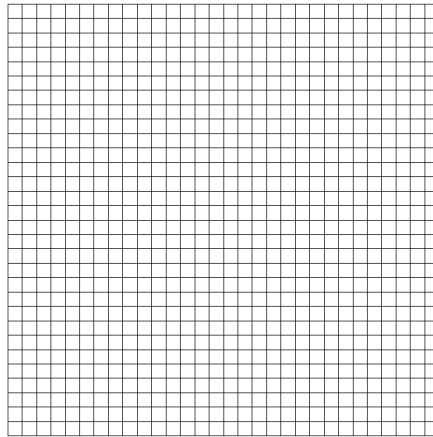
Figure 3.1: Mesh with 10 mm element size.

Apart from the size of the elements, all parameters were kept constant throughout the testing. The element sizes that were tested can be seen in Table 3.4. The total time interval simulated, was set to 5 ms for all analysis. One of the EUROPLEXUS input-files used in these analyses, can be found in Appendix E.2.

Table 3.4: Element sizes tested in the mesh-sensitivity study.

Element size [mm]
25
15
10
5
2.5
1.5

3.2.2 Results

Subsequent to the simulations, the midpoint displacements for all the analyses were plotted against time. This is shown in Figure 3.2. In Table 3.5, the computational

time for the different analyses are given. Keep in mind that although all analyses were performed on the same computer, the computer was also used for other work simultanously. This means that the available memory can vary between the analyses. As a result, the listed times are not directly representative for the different element sizes. However, they can be used for revealing possible tendencies.
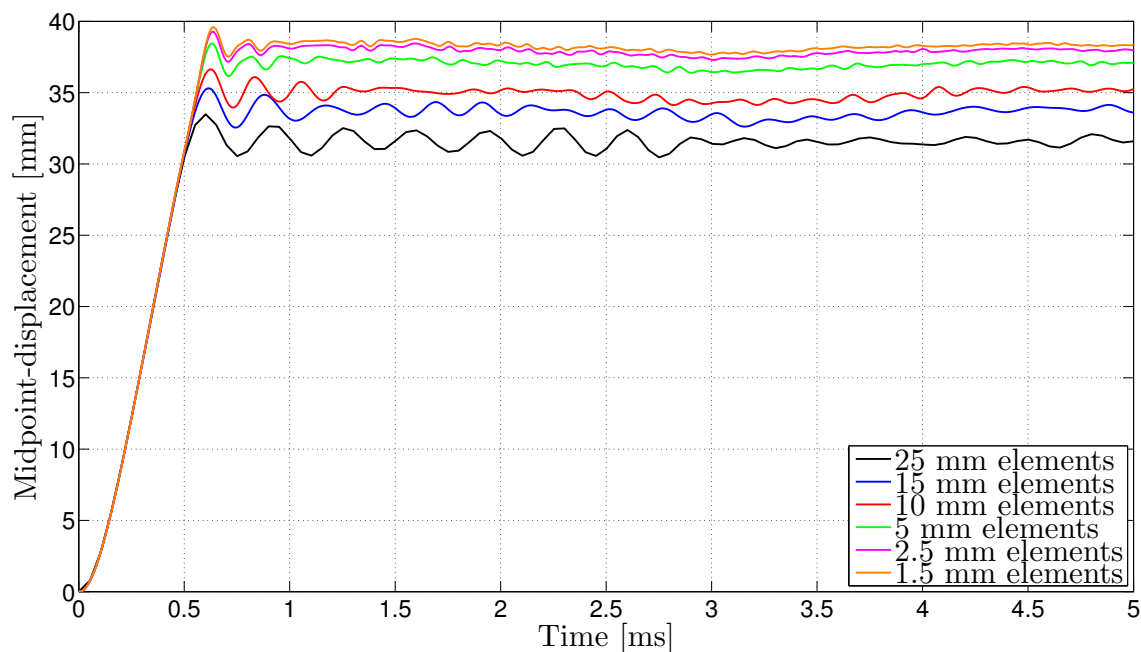
Figure 3.2: Displacement of midpoint with different element sizes.

Table 3.5: Computational time with different element sizes.

Element size [mm]	Computational time [hh:mm:ss]
25	00:00:05
15	00:00:40
10	00:01:44
5	00:08:33
2.5	00:49:49
1.5	03:19:46

From Figure 3.2 it can be seen that the displacement approaches convergence for the smaller element sizes. The computational time however, increases dramatically. By comparing the results from the analyses where 2.5 mm and 5 mm meshes were used, it can be seen that the displacement increases with about 1 mm. At max displacement, this corresponds to an increase of about 2-3%. Based on these results, a mesh with an element size of 5 mm is ideal, as the increase in displacement is fairly low for further reduction in element size. In addition, the computational time is still relatively low.

The computational times listed in Table 3.5 are based on a Lagrangian approach, which is regarded as inexpensive when it comes to computational costs. When performing e.g. an FSI-analysis, modeling of the air is required. The size of the elements for the modeled air have to be less than, or equal, to the size of the elements in the structural domain. As a result of this the computational time will increase exponentially when reducing the element size. This is because the model will contain more elements, and since the elements become smaller, the critical time step will also be reduced. Taking these considerations into account, an element size of 10 mm might be the most reasonable choice as a basis for comparison between the different approaches.

3.3 Evaluation of Stand-off Distances

3.3.1 Procedure

When evaluating the stand-off distance, the total time interval simulated was increased to 10 ms. This was done to ensure that the displacements for all stand-off distances were stabilized when approaching the end of the analyses. Apart from this, the analyses were set up in the same way as described in Chapter 3.2.

The plate was modeled in accordance with the mesh displayed in Figure 3.1. In order to get an initial impression of expected results, the possibility of performing analyses at a lot of different stand-off distances within a short period of time was regarded as important. In addition, it was expected that future analyses taking FSI into account, would require the elements of the plate to be 10 mm or larger due to high computational costs. By selecting 10 mm elements, future analyses would be more suited for comparison.

The AIRB command in EUROPLEXUS does not work as expected for stand-off distances smaller than 250 mm. Because of this, only distances larger than 250 mm were examined. Table 3.6 lists the tested stand-off distances.

Table 3.6: Stand-off distances evaluated.

Stand-off distance [mm]
250
375
500
625
750
875
1000

3.3.2 Results

The mid-point displacements for all the analyses were plotted against time. This can be seen in Figure 3.3. To investigate the relation between stand-off distance and displacement, the maximum positive displacement was identified for each stand-off distance. Positive direction is defined away from the C4 charge. Figure 3.4 shows the maximum displacement plotted against the stand-off distance.
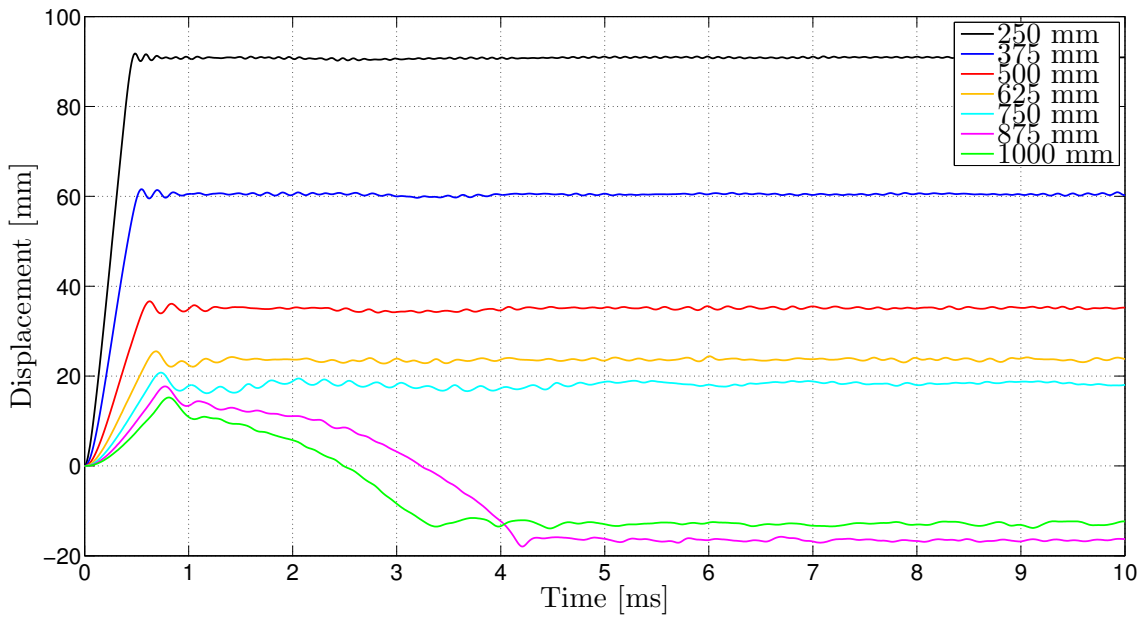
Figure 3.3: Mid-point displacement for different stand-off distances.
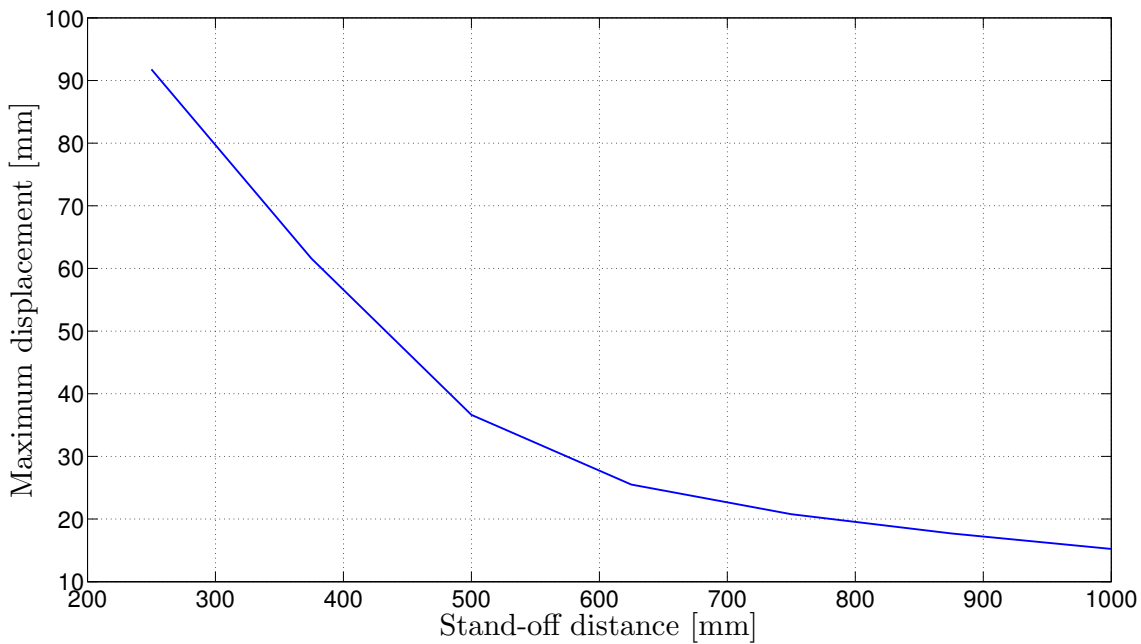
Figure 3.4: Maximum positive displacement plotted against stand-off distance.

From Figure 3.3 it can be seen that all stand-off distances give significant deformations. As expected, shorter stand-off distances result in larger displacements than longer stand-off distances. From Figure 3.4 it can be seen that the maximum displacement increases exponentially when the stand-off distance is reduced.

Most of the deformation is plastic, as all the analysis stabilizes at a deformed state. The oscillations around the residual plastic deformation can be attributed to the so-called springback effect, reported by Neuberger et al. [11]. This effect describes the difference between the peak transient deflection and the residual plastic deflection.

An interesting observation is that negative deformations can be observed for the analyses performed for stand-off distances of 875 mm and 1000 mm. This phenomenon may be referred to as counter-intuitive behaviour, and have been reported by many authors, e.g. by Flores-Johnson and Li [16]. They investigated numerically the counter-intuitive behaviour of square plates subjected to blast loading.

Chapter 4

Experimental Work

Experiments were performed to determine the structural response of 0.8 mm thick plates, subjected to blast loading. The material was the commercial aluminum alloy EN AW-1050A-H14.

Material experiments were performed at SIMLab (NTNU). Uniaxial tensile tests were carried out in order to identify material properties to be used in a constitutive relation.

Component tests were performed at Østøya, Horten, in collaboration with the Norwegian Defence Estates Agency (NDEA). Aluminum plates were subjected to free air explosions generated by detonation of explosive C4 charges. The experimental work was carried out in an exposed and worn-out building, in the property of the NDEA.

4.1 Aluminum alloy EN AW-1050A-H14

Aluminum alloy EN AW-1050A-H14 is commonly used for metal sheet work, especially when only a moderate strength is required. The material is known for excellent corrosion resistance, high ductility and highly reflective finish. Chemical process plant equipment, containers in the food industry or architectural flashings are typical examples of where this aluminum alloy may be used. The specification H14 indicates that the material has been work hardened by rolling until half hard. In addition, no annealing is performed on the material after rolling [65].

Table 4.1 gives the material composition of the aluminum alloy. The composition has to be within the boundaries presented in the first two rows of the table. The bottom row presents the material composition of the tested material. Hydro Aluminum Rolled Products delivered the materials that were used.

Table 4.1: Material composition of aluminum 1050A-H14.

	Si	Fe	Cu	Mn	Mg	Zn	Ti	Al
Min								99.50
Max	0.25	0.40	0.05	0.05	0.05	0.07	0.05	
Used in experiments	0.03	0.36	0.001	0.002	0.000	0.003	0.010	99.61

The following material properties are assumed known and are therefore not investigated further. Young's modulus, E, and the density, ρ, are assumed equal to the values presented by Aalco Metals Limited [65]. Poison's ratio, ν, is assumed equal to the one used by Spranghers et al. [13]. Table 4.2 lists the selected values.

Table 4.2: Physical properties for aluminum 1050A-H14.

Physical properties	Value
Young's modulus, E [GPa]	71
Poisson's ratio, ν	0.33
Density, ρ [kg/m^3]	2710

4.2 Material Tensile Tests

4.2.1 Procedure

In order to get the best possible results when simulating the airblast, it was decided to do some material tests to establish a material model. This was done through material tensile tests. The experiments were performed in a Zwick/Roell Z030 30 kN test machine. A total of 9 specimens were loaded with a deformation rate of 2.1 mm/min. This corresponds to a strain rate of $5 \cdot 10^{-4}$. During loading, the machine were logging the displacements as well as the applied force. In addition, a high-speed camera was installed to take pictures during the deformation. These pictures were taken to be used in a DIC analysis. Figure 4.1a shows a picture of the test setup. Figure 4.1b shows a close-up view of the specimen installed in the test machine.

(a) Complete setup

(b) Close-up view of specimen
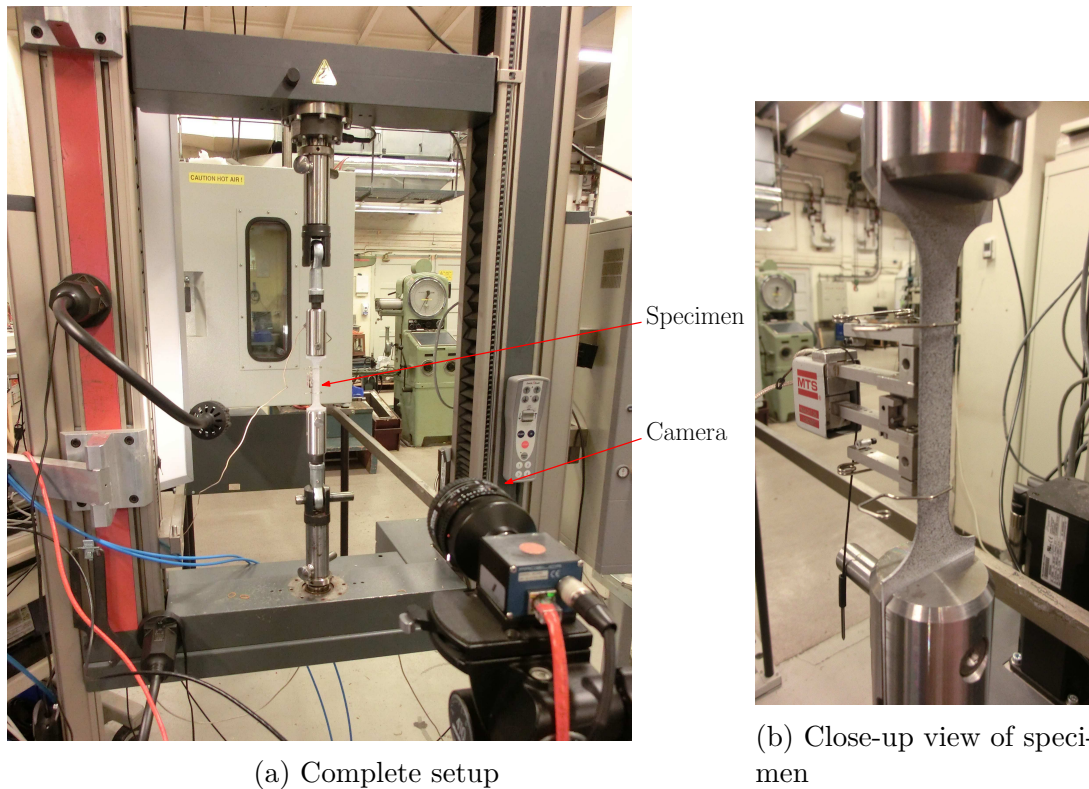
Figure 4.1: Experimental setup for material tests.

The test specimens were made of the aluminum alloy EN AW-1050A-H14. All specimens were cut from 0.8 mm thick, rolled aluminum plates. For rolled plates, the material behaviour can vary depending on the orientation of the material relative to the direction of the rolling. Because of this, three specimens were made from each orientation of 0, 45 and 90 degrees, relative to the rolling direction. The nominal dimensions of the specimens can be seen in Figure 4.2.
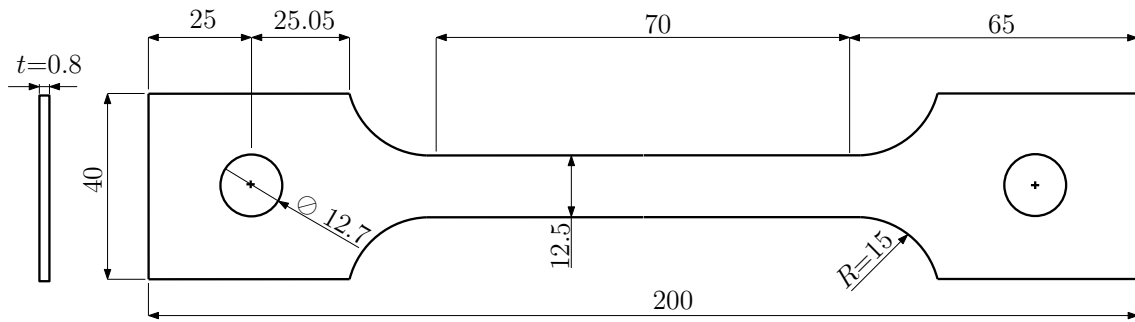
Figure 4.2: Nominal dimensions of specimen in millimeter.

The thickness, as well as the width, of the specimens were measured in three places. At the midpoint, as well as at each end of the gauge length. The measurements were taken by the help of a sliding caliper and a micrometer. Average values, as well as the standard deviations, are listed for all 3 orientations in Table 4.3.

Table 4.3: Average dimensions of material specimens.

Orientation	Width [mm]		Thickness [mm]	
	Average	Standard deviation	Average	Standard deviation
0°	12.483	0.015	0.794	0.003
45°	12.461	0.009	0.792	0.001
90°	12.480	0.012	0.792	0.002
Overall	12.475	0.016	0.793	0.003

Due to the thickness of the specimen, a physical extensometer could potentially damage and reduce the cross-sectional area, and thereby affect the results. Because of this, the specimens were prepared for DIC analysis. All specimens were then spray painted with a speckled pattern of black speckles on a white background. One of the specimens prepared for DIC, can be seen in Figure 4.3. One specimen from each orientation were also installed with an extensometer to investigate whether it would have any negative impact on the results.

Figure 4.3: Specimen prepared for DIC analysis.

4.2.2 Results

After testing it was apparent that the necking initiated close to the shoulder of the specimen. This can be seen in Figure 4.4. This is not ideal as the behavior can be affected by the change in geometry close to the shoulder.
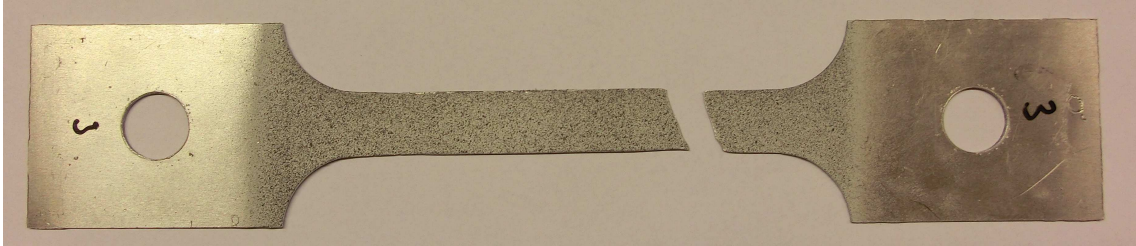
Figure 4.4: Fracture in specimen after testing.

Figure 4.5 shows force-displacement curves for all specimens. The test specimens with the same orientation, relative to the rolling direction, are plotted against each other. This was done to investigate the variation, as well the impact of the physical extensometer. Note that the displacement used, were logged by the machine. These values are inaccurate, but as the source of error is the same for all tests, the curves can give a good basis for comparison.
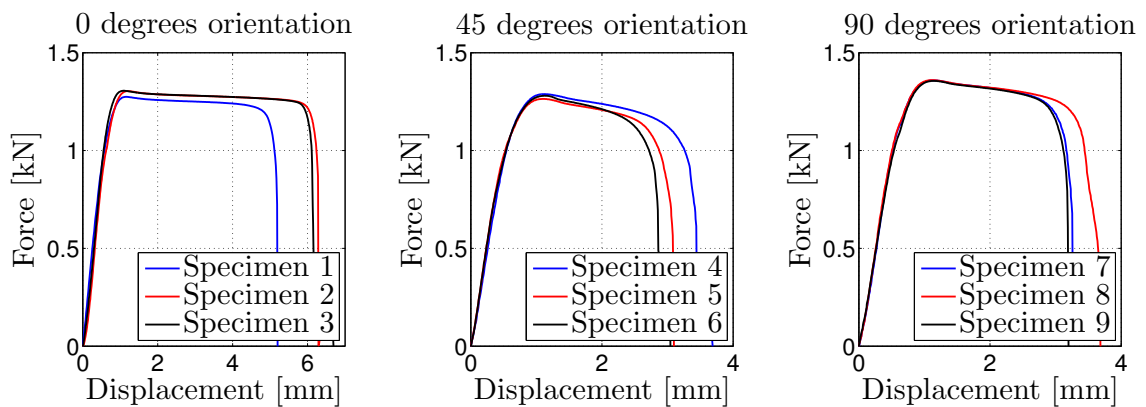
Figure 4.5: Force-displacement curves for all specimens.

From the curves in Figure 4.5, it can be seen that the variations between the tests are small until the specimens approach necking. The difference is larger when approaching failure, but the general behaviour is similar. Specimen 3, 6 and 9 were equipped with physical extensometers. From their respective curves it is apparent that the impact of this is minimal. Figure 4.6 shows force-displacement curves for the three tests that were equipped with extensometers.

81
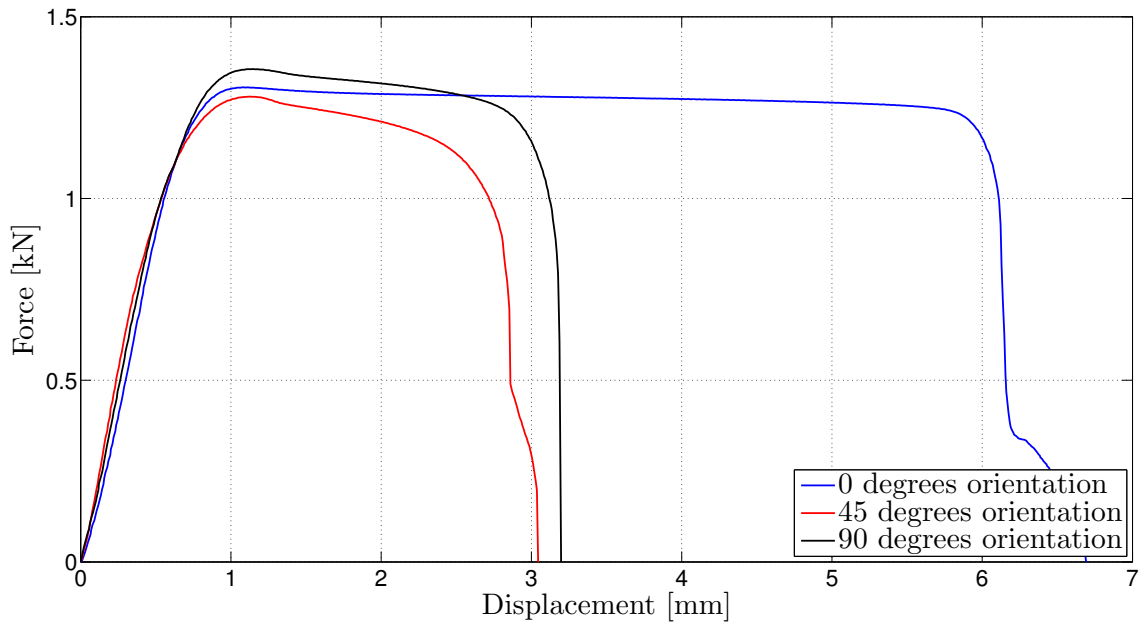
Figure 4.6: Force-displacement curves for one specimen of each orientation.

From Figure 4.6 it can be seen that the material behaviour is fairly similar for the three tests in the elastic region. After necking however, the material shows highly anisotropic behavior.

As the extensometer did not affect the results, extensometer values were used to calculate the strains. The extensometer malfunctioned during the test of the 45 degrees specimen. As a result, only curves for the specimens at 0 and 90 degrees orientation will be shown. Figure 4.7 shows the engineering stress plotted against engineering strain, and Figure 4.8 shows the true stress plotted against true strain. As stated in Chapter 2.5.1, the formula for true stress is only valid until necking. Because of this, all values after necking have been removed from the true stress-true strain curves.

To be able to calculate the plastic strain, a value for Young's modulus, E, is needed. From literature, this value has been assumed to be $E = 71$ GPa [65]. Figure 4.9 shows true stress plotted against the resulting plastic strain.
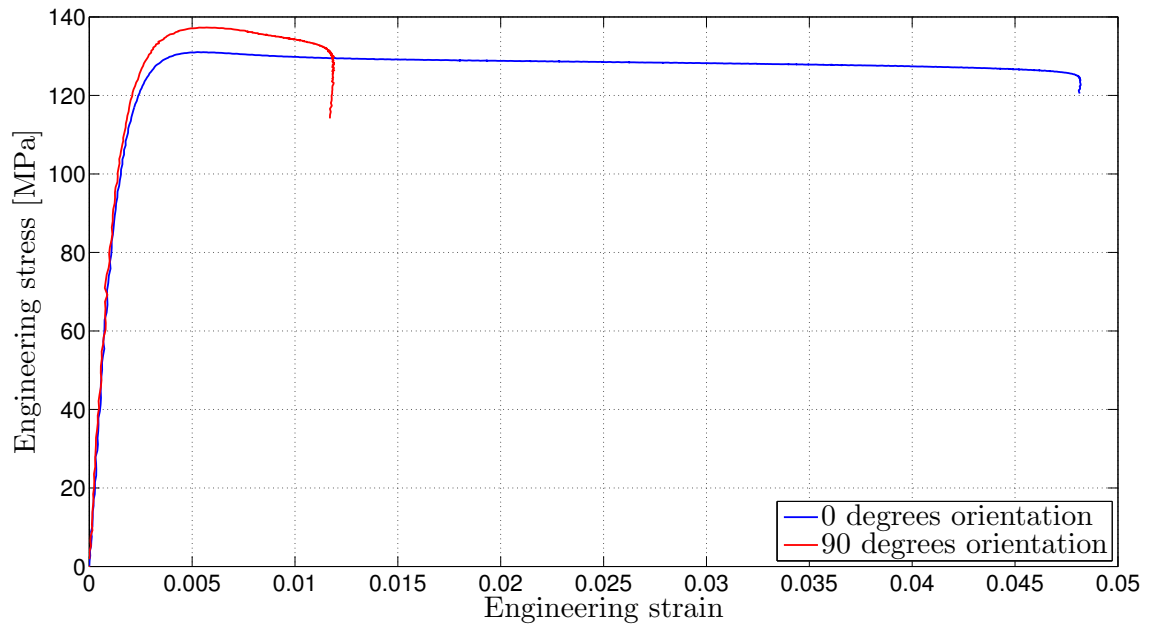
Figure 4.7: Engineering stress-strain curve comparison.
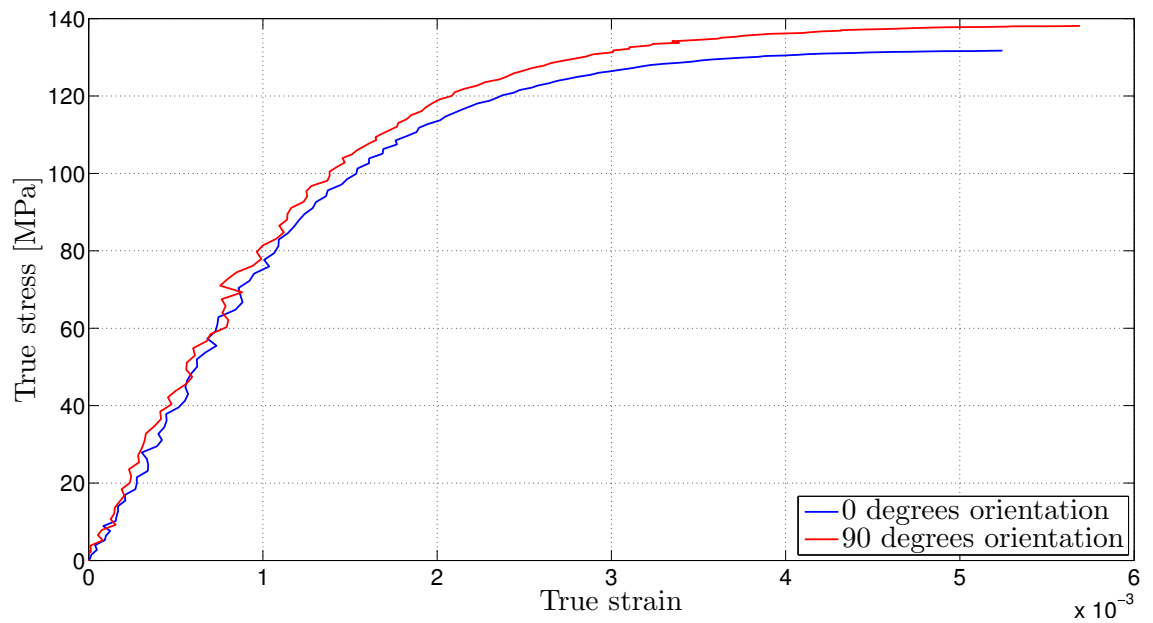
Figure 4.8: True stress-strain curve comparison.
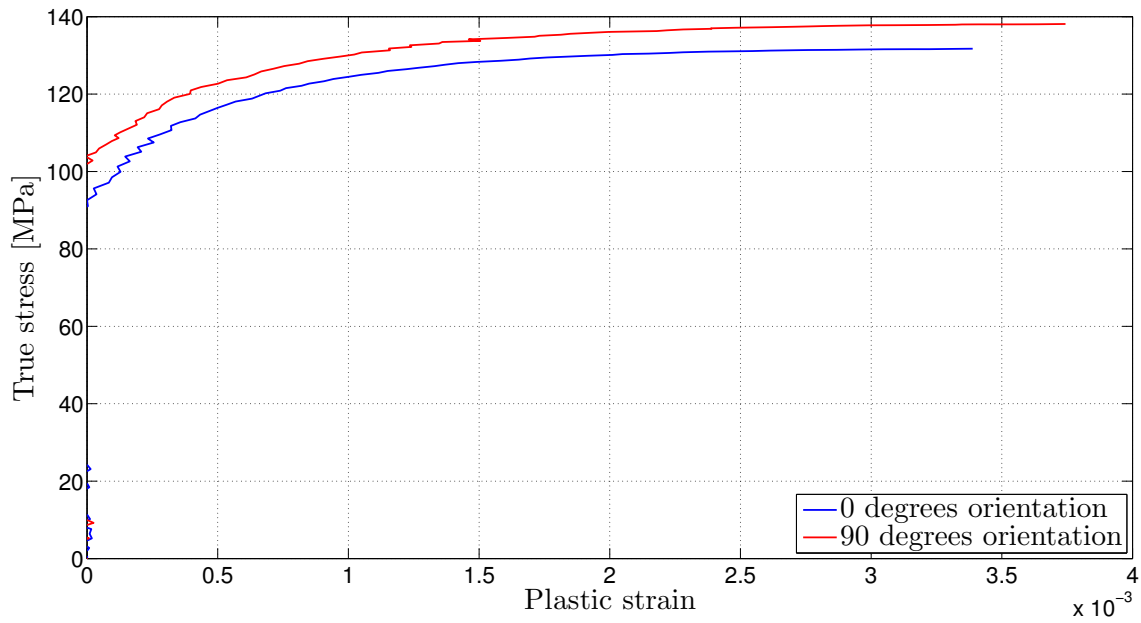
Figure 4.9: True stress - plastic strain curve comparison.

From Figure 4.9, it can be seen that very little remains of the curves when removing all points after necking. This means that necking occurs at a really low plastic strain, which indicate that the material has very little strain hardening.

4.3 Airblast Experiments

4.3.1 Procedure

The experimental setup consisted of a steel frame with dimensions 1000x1000x15 mm^3, with a cavity of 300x300 mm^2 in the center. Steel profiles of HUP50x50 mm were welded to the steel frame in order to make the frame more stable. Plates made of aluminum alloy EN AW-1050A-H14, with a total surface of 400x400 mm^2 and a thickness of 0.8 mm, were installed into the mounting frame by use of bolt connections and a steel clamping frame. The bolts were fastened with a torque of 200 Nm. The experimental setup can be seen in Figure 4.10. In Figure 4.11, a schematic description of the experimental setup seen from above is given.
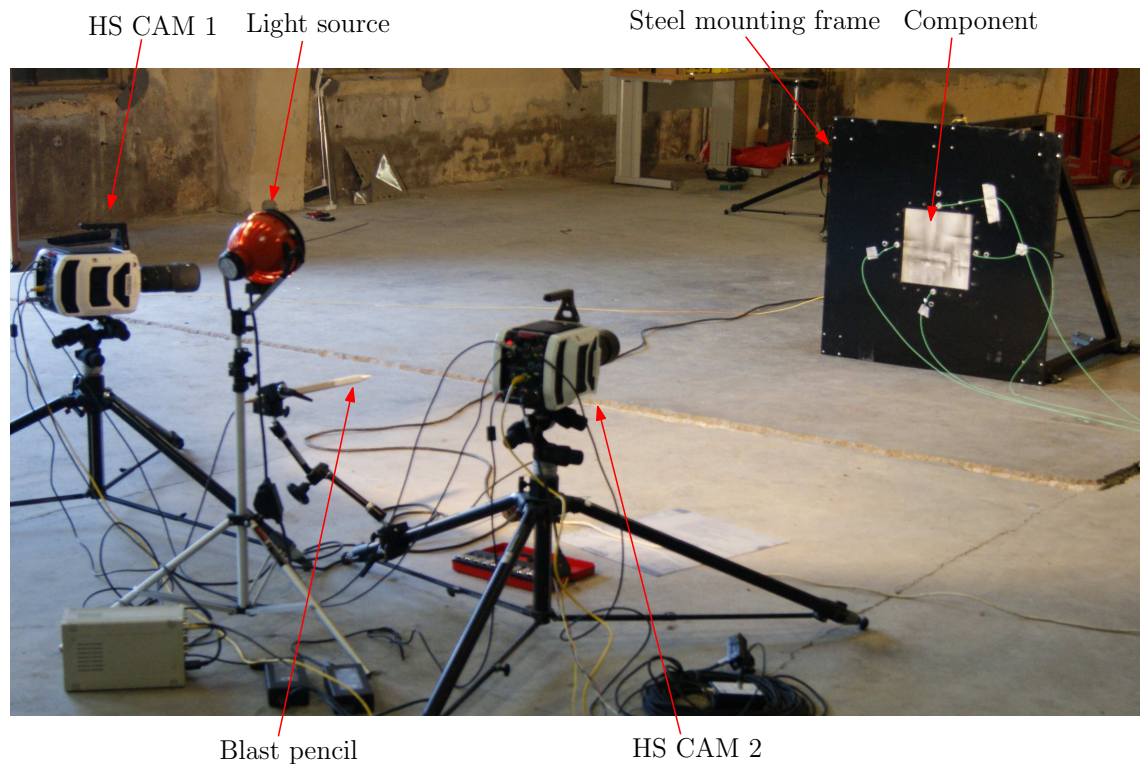
Figure 4.10: Experimental setup.

The light source in Figure 4.10 was later moved to the right side of HS CAM 2. This was done in order to obtain more favourable light conditions when taking the DIC analysis into consideration.
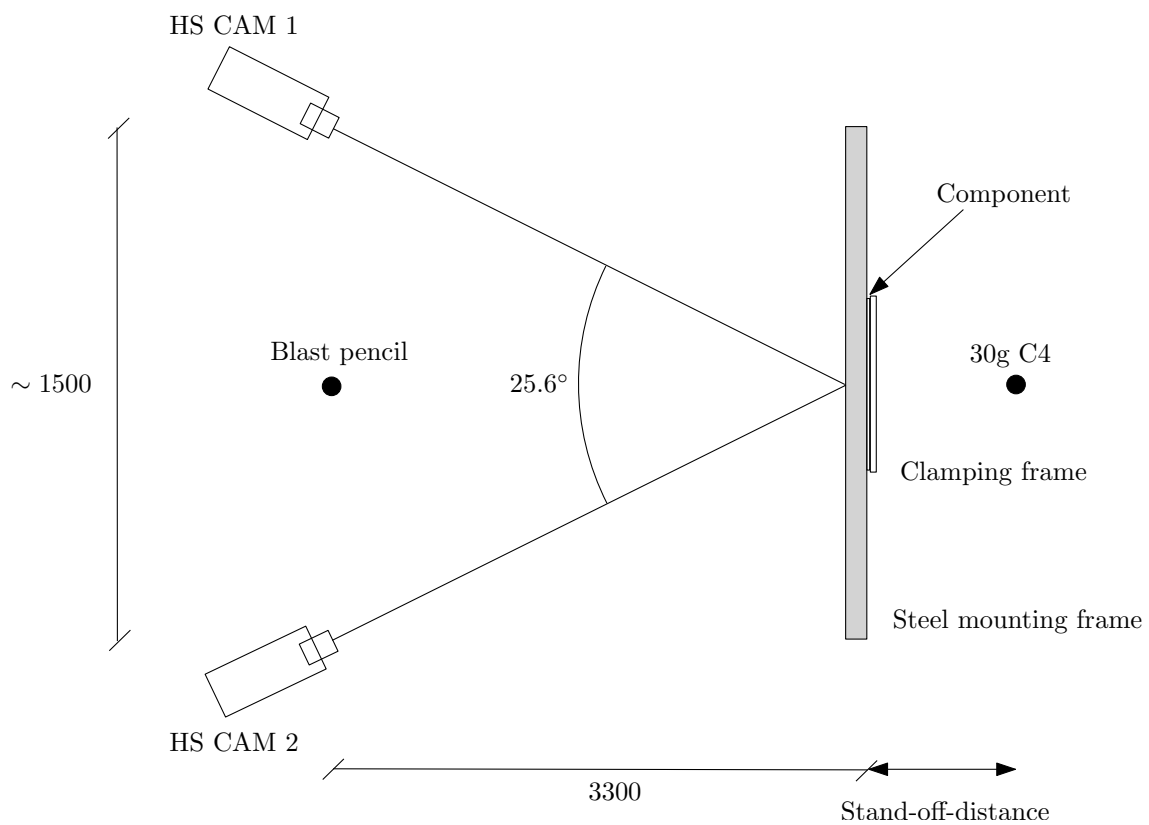
Figure 4.11: Experimental setup seen from above. Dimensions in mm.

Figure 4.12 shows the testing frame with an installed aluminum plate in between the steel mounting frame and the clamping frame.
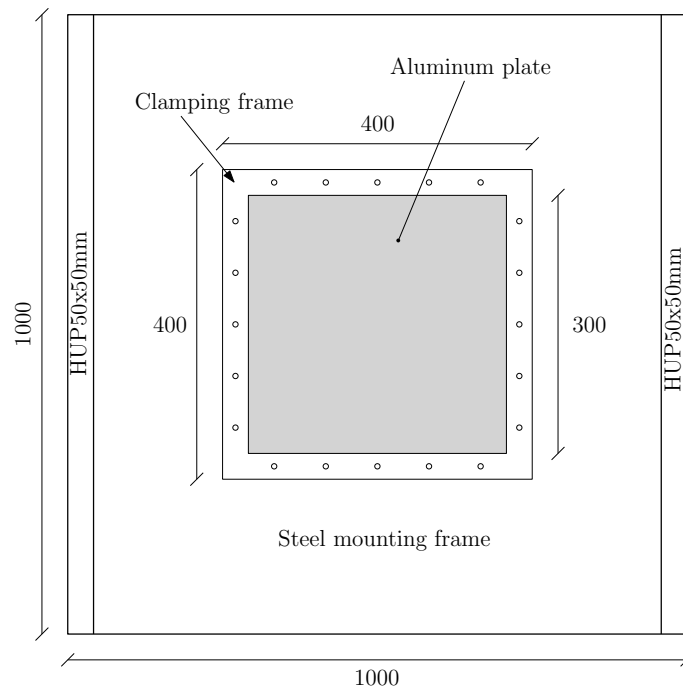
(a) Seen from the side where the charge was placed.
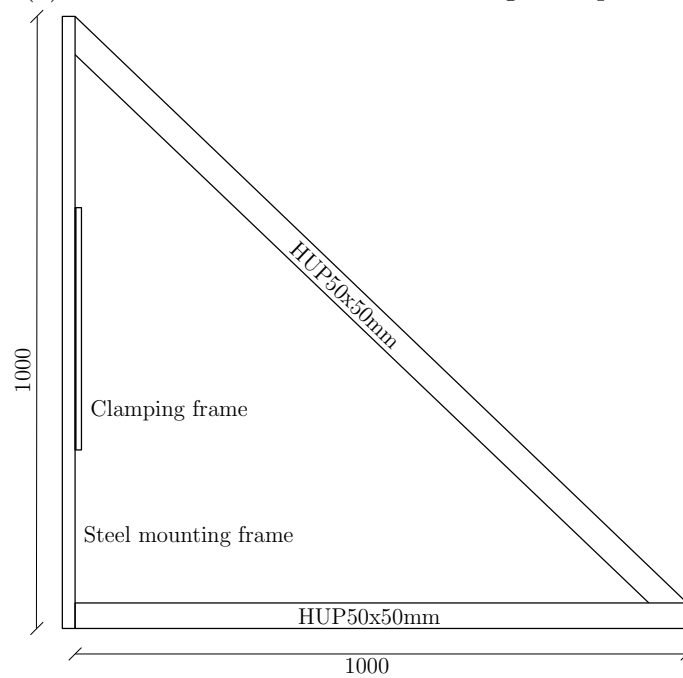
(b) Side view of the testing frame.

Figure 4.12: Experimental setup. Dimensions in mm.

The explosive charges, which consisted of Composition C4, were placed as indicated in Figure 4.11. The mass of the charges were approximately 30 g and the charges had a diameter close to 34.5 mm. The charges were shaped by hand. Because of this, it is possible that geometry and mass varied between the tests. In the experimental

setup, the charges were suspended from the upper girder, as indicated in Figure 4.13.

(a) Suspended C4 charge.

(b) Close-up view of a C4 charge.
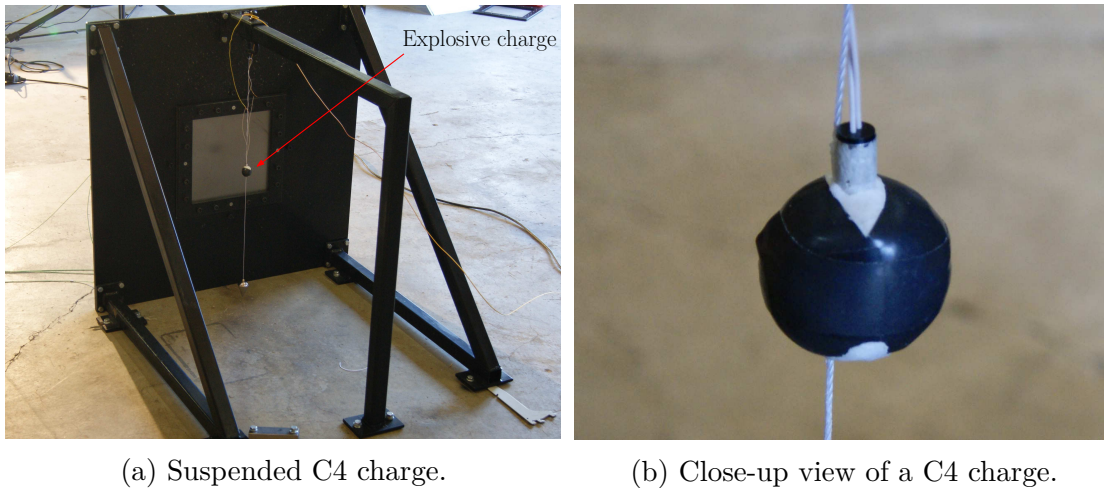
Figure 4.13: Pictures showing the placement and shape of an explosive charge.

The vertical position of the charges was adjusted, such that the center of mass was at the same height as the center point of the tested aluminum plates. The horizontal distance from the plate was adjusted according to the desired stand-off distances.

Prior to the testing of the aluminum plates, experimental validations were carried out on a steel plate with a thickness of 15 mm. Pressure transducers were installed in the steel plate, according to Figure 4.14. A breakwire was installed in order to determine the time of detonation. Three stand-off distances were selected, and these are listed in Table 4.4. The steel plate was mounted on the opposite side of the clamping frame. It should be noted that the stand-off distances given in Table 4.4 are measured with respect to the placement of the steel mounting frame. This means that stand-off distances for the calibration plate are actually 15 mm longer. For simplicity, the stand-off distances in Table 4.4 and Table 4.6 are referred to the same reference point. By conducting these calibration tests, estimates of the pressure distribution over the plates in the actual experiments were obtained.

(a) Pressure transducers installed.   (b) Dimensions in mm.
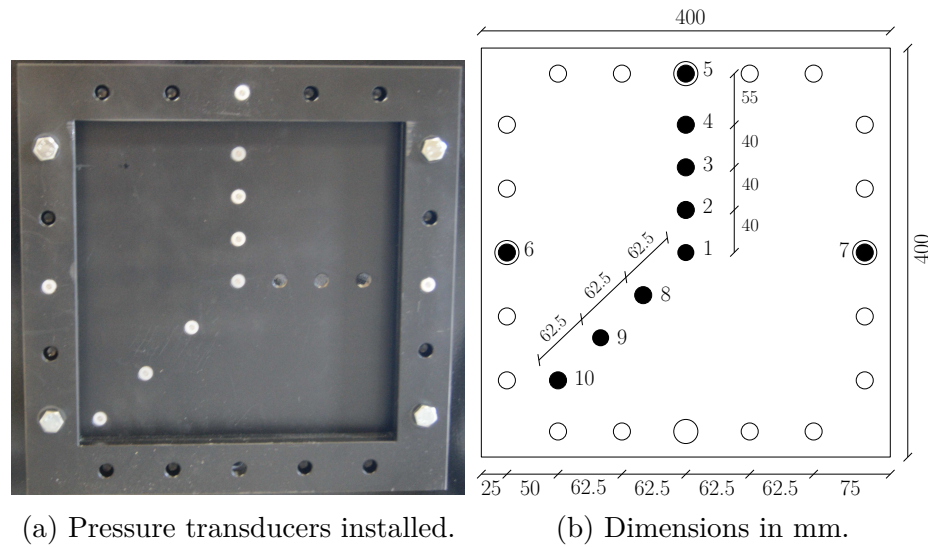
Figure 4.14: Calibration plate seen from the side where the charge was placed.

Table 4.4: Calibration tests performed.

Stand-off distance [mm]	Test name		
250	R11	R12	R13
375	R21	R22	R23
500	R31	R32	R33

Subsequent to the calibration tests, the aluminum plates were tested. In Figure 4.15, the geometry of the tested plates are given. Thicknesses were measured for each plate prior to the tests by use of a micrometer. Points measured were located in the mid-span of each side and were taken close to the boundary. This was done in order to investigate the variation in the plate thickness. The average value and the standard deviation from the measurements are presented in Table 4.5.

Table 4.5: Thickness of plates used in component tests.

Thickness [mm]	
Average	Standard deviation
0.790	0.004

Tested stand-off distances are given in Table 4.6. Stand-off distances used for the calibration plate and the component tests differ, as can be seen by comparing the contents in Table 4.4 and Table 4.6. The reason for this is discussed in Chapter 4.3.3.

89

Table 4.6: Component tests performed.

Stand-off distance [mm]	Test name		
375	A11	A12	A13
500	A21	A22	A23
625	A31	A32	A33

Pressure transducers of the type Kistler 603B [66], were used for both the calibration tests and the component tests. However, the arrangement of the pressure transducers differed. Pressure transducers inside the clamping frame were removed and pressure transducer 1 was moved down to the lower part of the clamping frame, according to Figure 4.14. Thus, pressure transducers were installed in the mid-span of each side of the aluminum plates, corresponding to the holes with diameter of 24 mm in Figure 4.15.
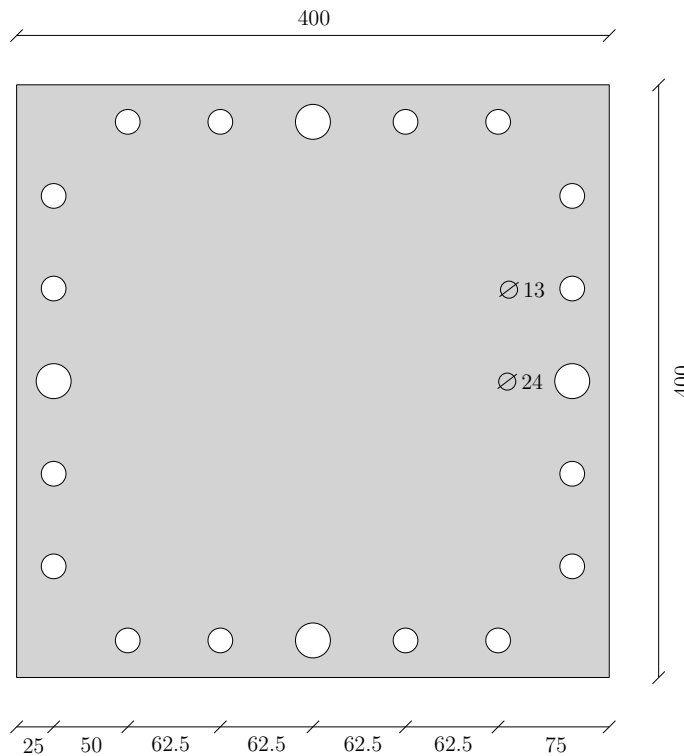
Figure 4.15: Geometry of tested components. Dimensions in mm.

During the experiments, two high-speed cameras of the type Phantom v1610 [67], were taking pictures with a frequency of 21.000 fps. Image size was set to 896x800 pixels. The positioning of the cameras can be seen in Figure 4.11. Synchronized stereo images taken by the two cameras, together with use of DIC, enabled subsequent abstraction of 3D displacement fields from the dynamic response of the plates. An aluminum plate painted in a speckle-pattern is shown in Figure 4.16. This was done in order to obtain contrasts, which is advantageous for use in a DIC analysis.
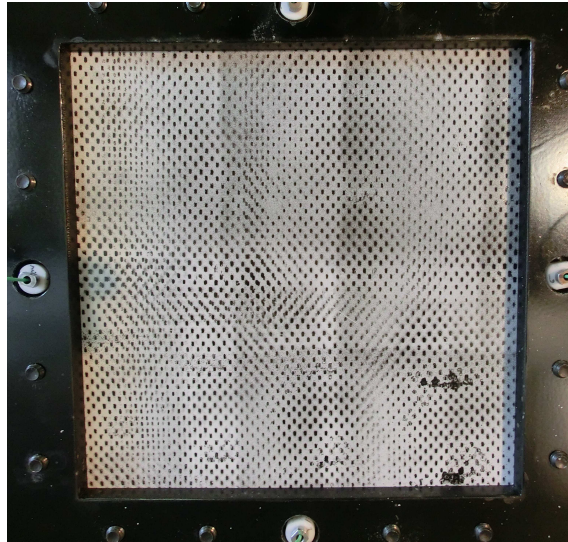
Figure 4.16: Aluminum plate prepared for DIC analysis.

In order to determine the time of arrival for the shock waves, a blast pencil was installed in between the two cameras, as can be seen in Figure 4.11. This was used to define the applicable time window for the DIC analyses, as shock waves potentially could disturb the camera setup and consequently also the DIC analyses.

4.3.2 Results - Calibration Tests

As explained in Chapter 4.3.1, the calibration plate had a total of 10 pressure transducers installed. Each transducer recorded the pressure during the calibration tests. This enabled a graphical description of the variation in pressure as a function of time. Before processing data from the pressure curves, the curves had to be corrected according to the time of detonation. At the time of detonation, a breakwire transmitted a signal that was plotted against time. The pressure curves could then be corrected by identifying the time interval between the start of the time series and the time of detonation.

There were problems with some of the tests. In test R11, pressure transducer 5 gave strange readings. After being exposed to the blast pressure, the pressure failed to return to initial level. In test R21 the breakwire malfunctioned, and in test R22 the response of the breakwire was recorded after the pressure waves arrived at the pressure transducers. For test R31, R32 and R33, transducers 6 through 10, as well as the breakwire, malfunctioned. Because of this, three more test were performed. These were labeled R31-2, R32-2 and R33-2. In test R31-2 and R32-2, transducer 9 malfunctioned.

All tests with functional breakwire were corrected according to the time of detonation. Figure 4.17 shows the breakwire response from test R13. The time of detonation is indicated by a red line.
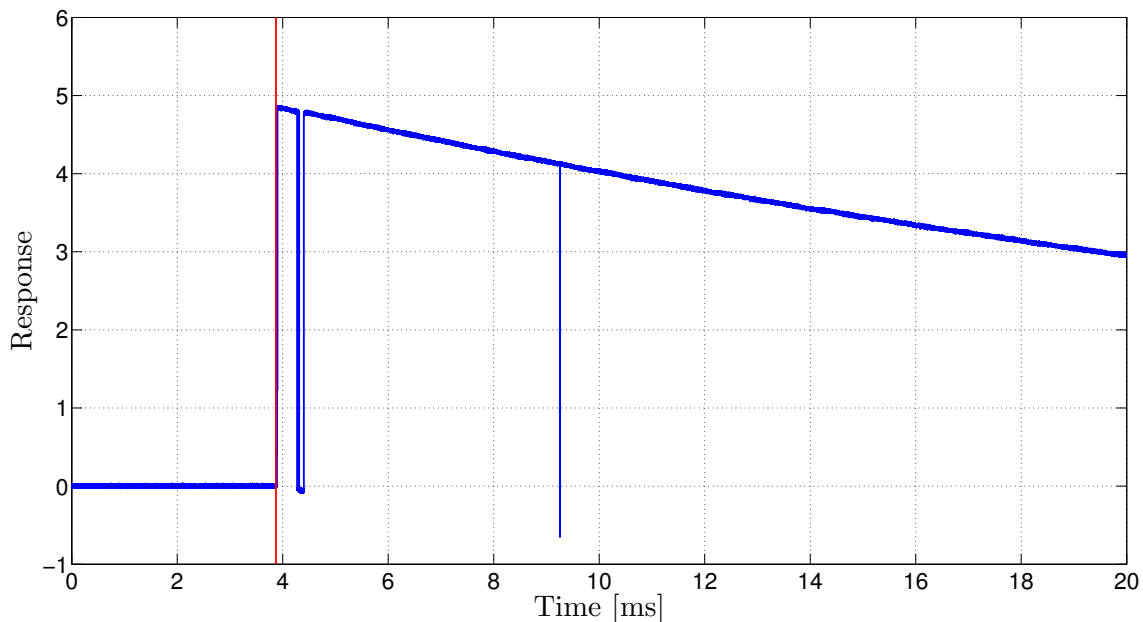
Figure 4.17: Breakwire for test R13.

The pressure transducers were located as shown in Figure 4.14. It was expected that the blast wave would arrive at the middle pressure transducer first, and at

the others shortly after. The pressure curves were plotted against each other to compare differences in pressure. To get a good basis for comparisons, transducer 1 through 4 were plotted together in one plot and 1 plus 8 through 10 in another. This was done because these transducers were aligned in vertical and diagonal directions, respectively. In addition, transducer 1 and 4 through 7, were plotted together. Transducers 4 through 7 were ignored in the other figures due to the fact that the transducers were not located at the same distance as the plate. The time of arrival would therefore not be comparable to the other transducers. A set of figures is presented for one characteristic test at each stand-off distance. Figures for the remaining tests can be found in Appendix A.1. Figure 4.18 shows plots of transducers 1 through 4 for test R13. Figure 4.19 shows plots of transducers 1 plus 8 through 10 for test R13. Figure 4.20 shows plots of transducers 1 plus 5 through 7 for test R13. Figure 4.21, Figure 4.22 and Figure 4.23 show corresponding plots for test R23 while Figure 4.24, Figure 4.25 and Figure 4.26 show corresponding plots for test R33-2.
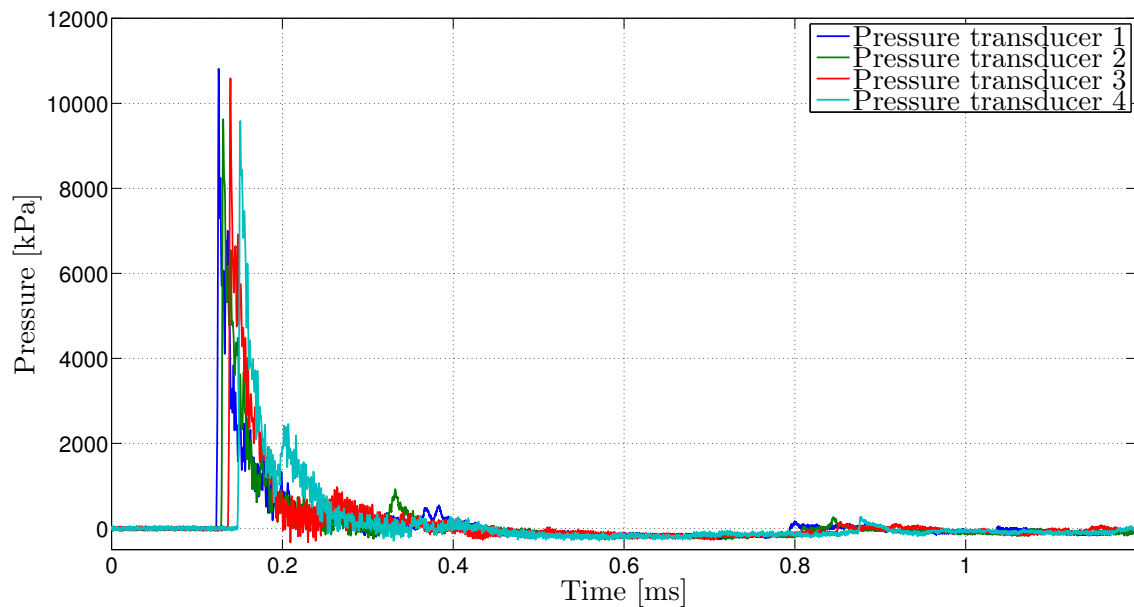
Figure 4.18: Transducers along the vertical for test R13.
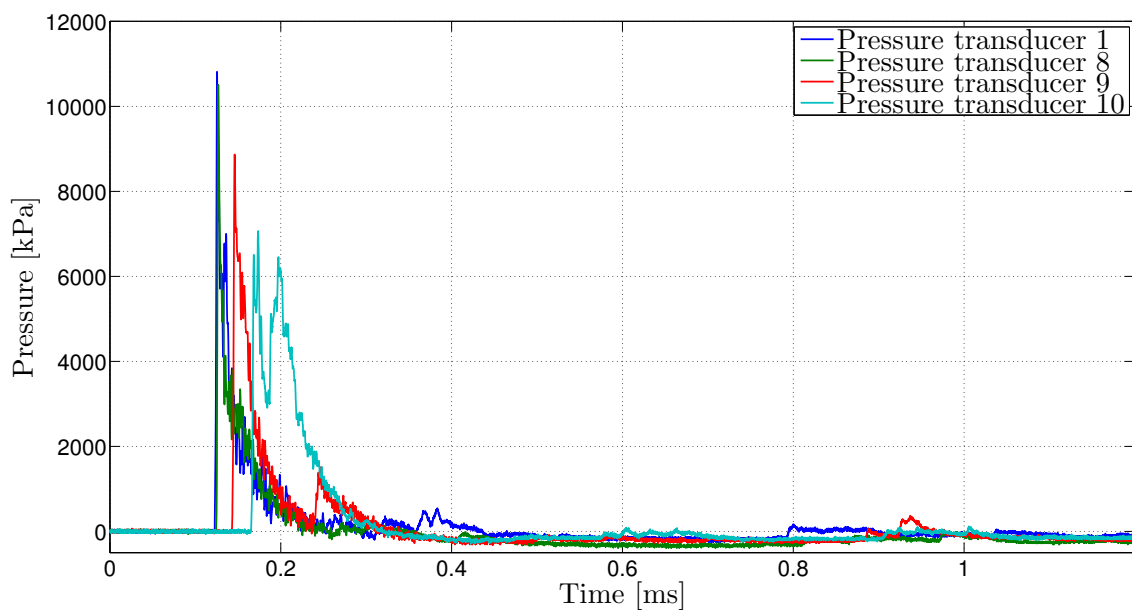
Figure 4.19: Transducers along the diagonal for test R13.
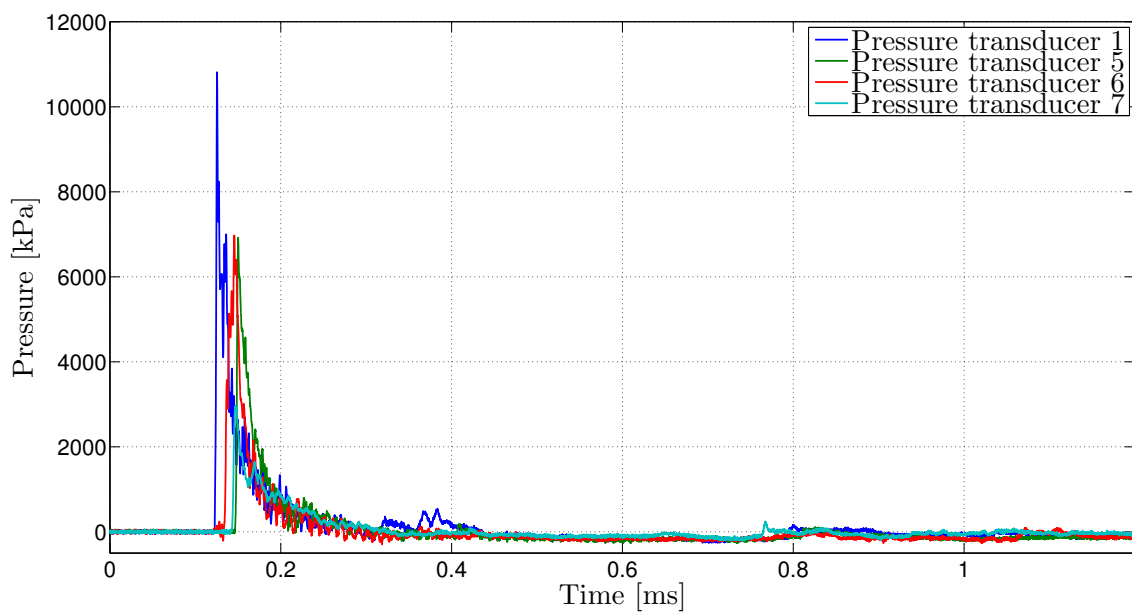
Figure 4.20: Transducers in the middle and in the clamping frame for test R13.
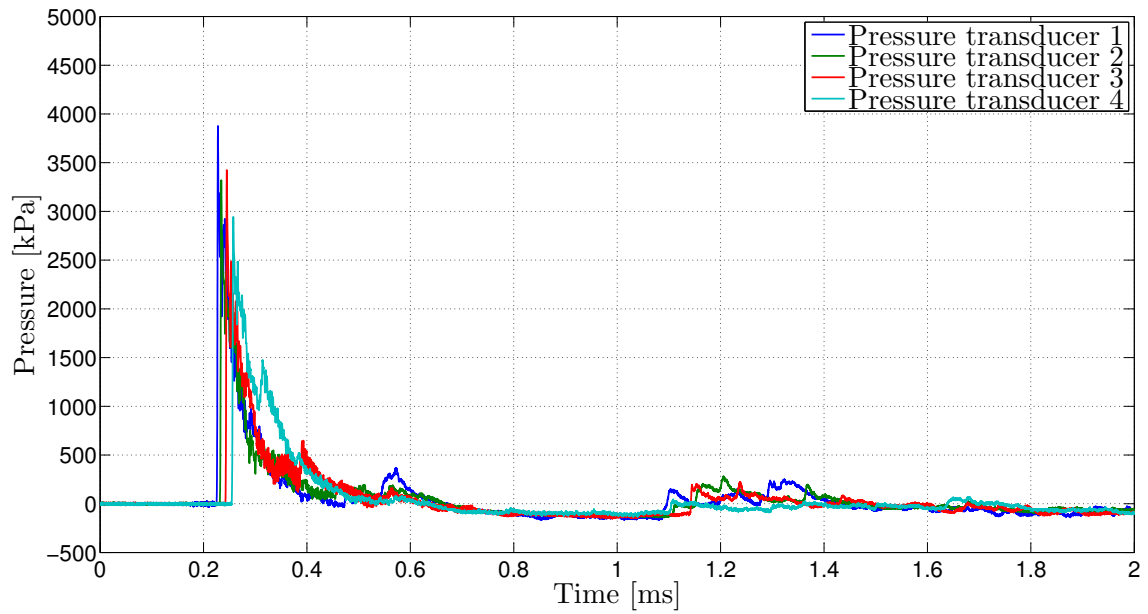
Figure 4.21: Transducers along the vertical for test R23.
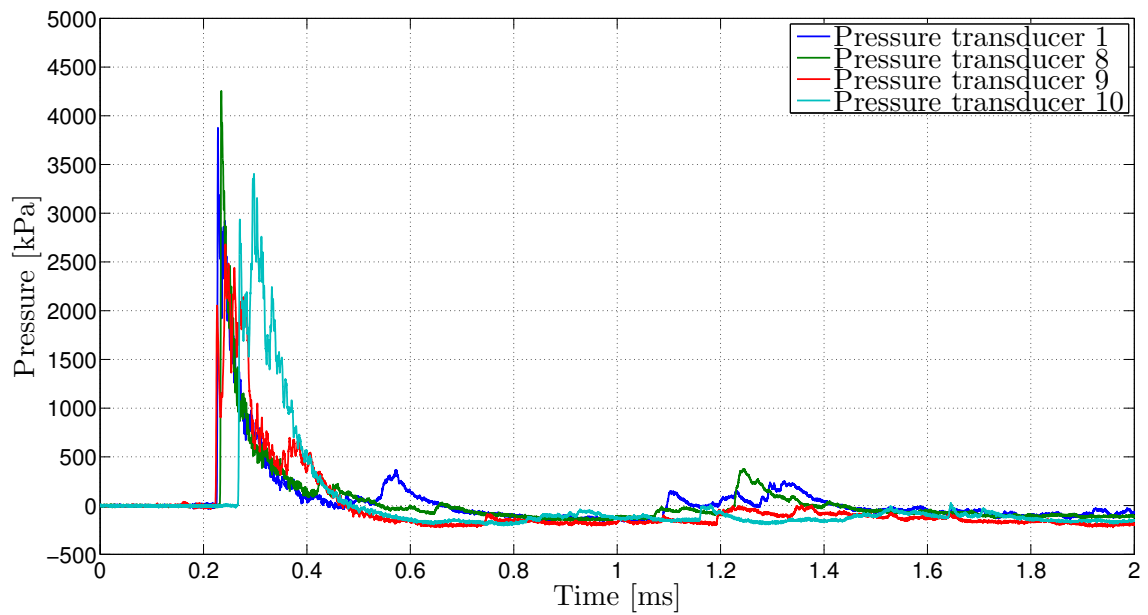
Figure 4.22: Transducers along the diagonal for test R23.
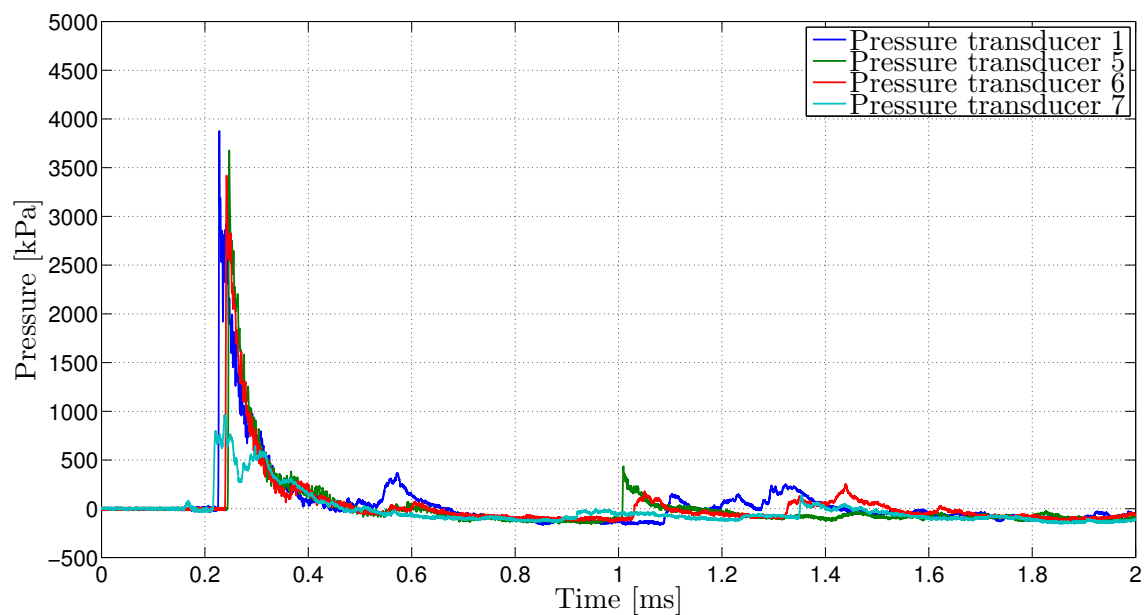
Figure 4.23: Transducers in the middle and in the clamping frame for test R23.
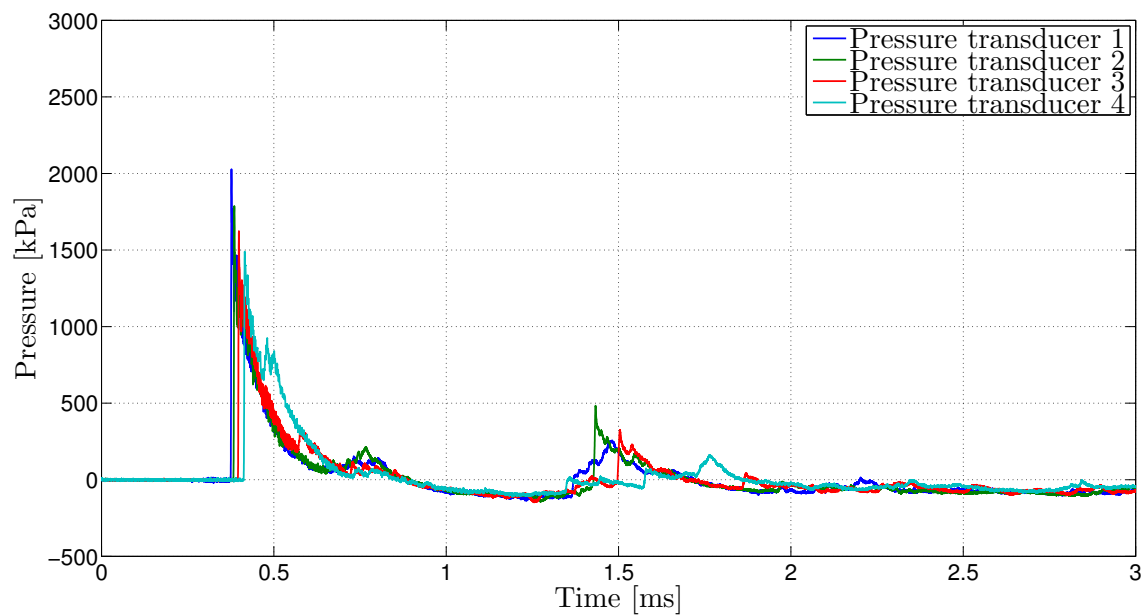
Figure 4.24: Transducers along the vertical for test R33-2.
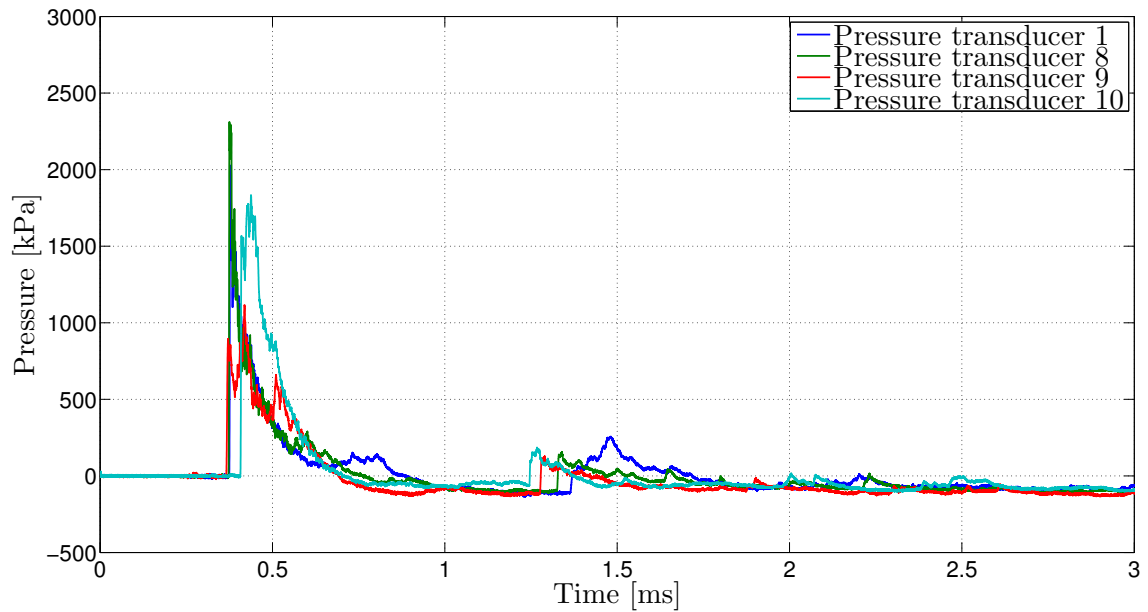
Figure 4.25: Transducers along the diagonal for test R33-2.
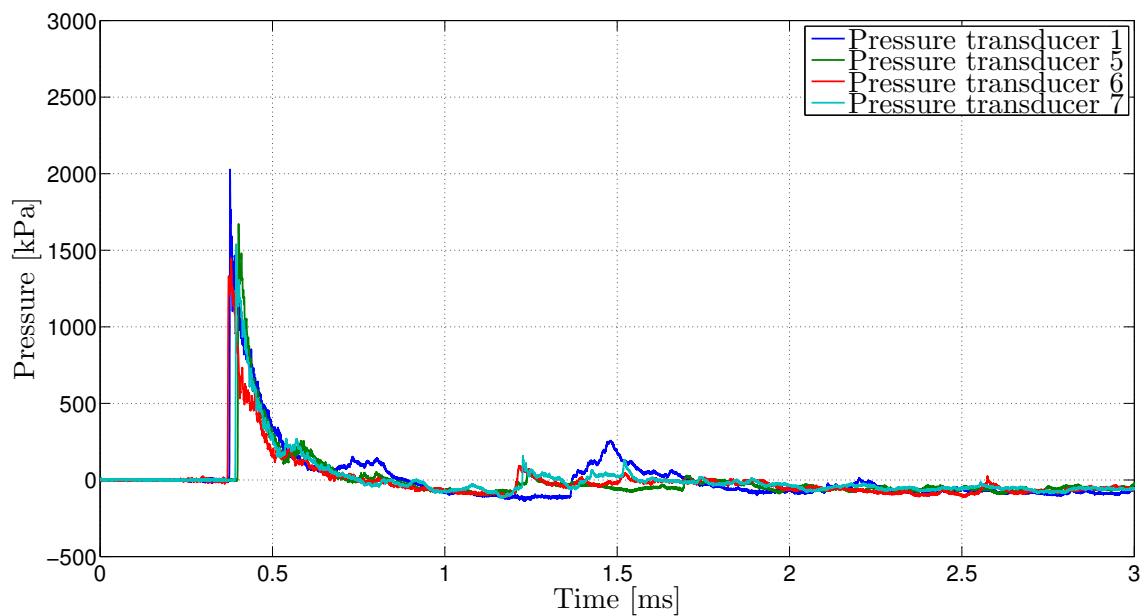
Figure 4.26: Transducers in the middle and in the clamping frame for test R33-2.

From Figure 4.18 it can be seen that the pressure arrives at the pressure transducers in the expected order of 1 to 4. Although transducer 2 indicates a slightly lower peak pressure than transducer 3, the curves still indicate a reduce in peak pressure when moving away from the center of the plate. This can also be observed from Figure 4.19. When looking at the time of arrival, it can be seen that it is approximately the same for transducer 1 and 8. Looking at Figure 4.20 it can be seen that the

97

pressure arrives at transducer 6 before transducers 5 and 7. This can indicate that the load was slightly off-center. As transducer 6 is located at the same half of the plate as transducer 8, this can also explain why the pressure arrives at the same time in pressure transducers 1 and 8.

From Figure 4.19, it can be seen that the positive impulse from transducer 9 and 10 are large compared to the other transducers. It is possible that this is a result of pressure accumulation in the corner of the plate. Similar response can be observed for the other stand-off distances in Figure 4.25 and Figure 4.22.

Figure 4.21 and Figure 4.24 show the same tendency as Figure 4.18. The pressure decreases and the time of arrival increases, when moving away from the centre of the plate. Figure 4.22 and Figure 4.25, both show that the pressure in pressure transducer 1 arrives after some of the others. Looking at Figure 4.23, it is hard to conclude whether this could be due to off-centering of the load. The pressure in transducer 7 arrives before the others. If the load were slightly displaced in this direction, it would explain the big increase in time of arrival for pressure transducer 10. However, it would not explain why the pressure arrives at transducer 9, before transducer 1. This might indicate either other influencing factors, or the possibility that some of the pressure curves may be slightly out of sync. Figure 4.26 indicates the same as Figure 4.20, that the load might be slightly off in the direction of transducer 6.

The pressure curves from the transducers were used to calculate the time of arrival, impulse and the duration of the impulse. Figure 4.27, Figure 4.28 and Figure 4.29 show the pressure in pressure transducer 1 for test R13, R23 and R33-2, respectively. The red lines indicate the time of arrival and the end of the positive impulse. Corresponding plots for all transducers for all the tests are included in Appendix A.2.
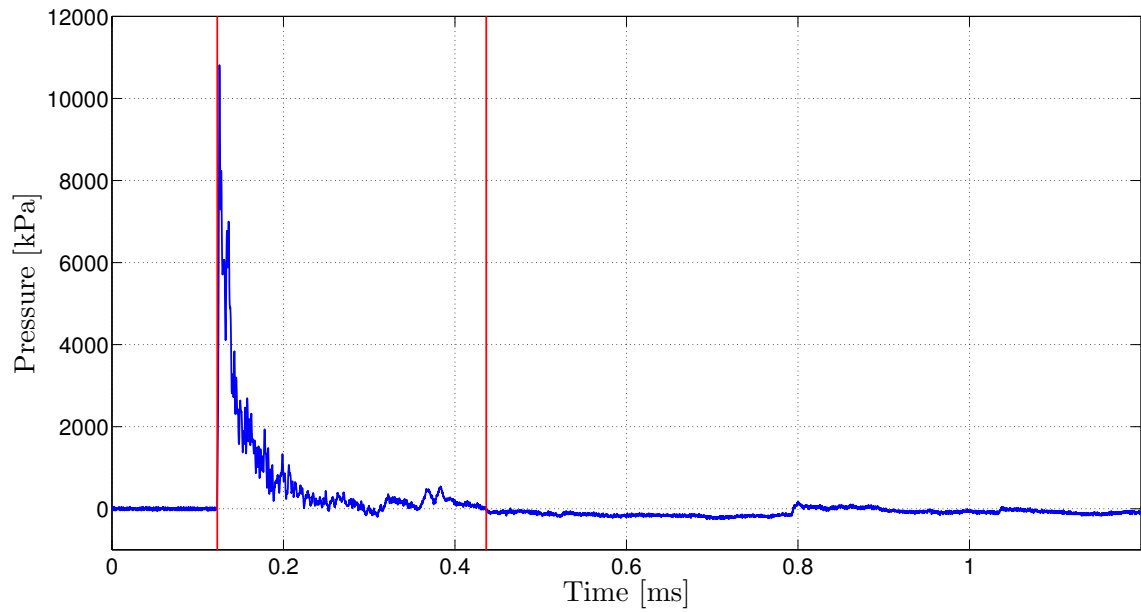
Figure 4.27: Pressure in transducer 1 for test R13.
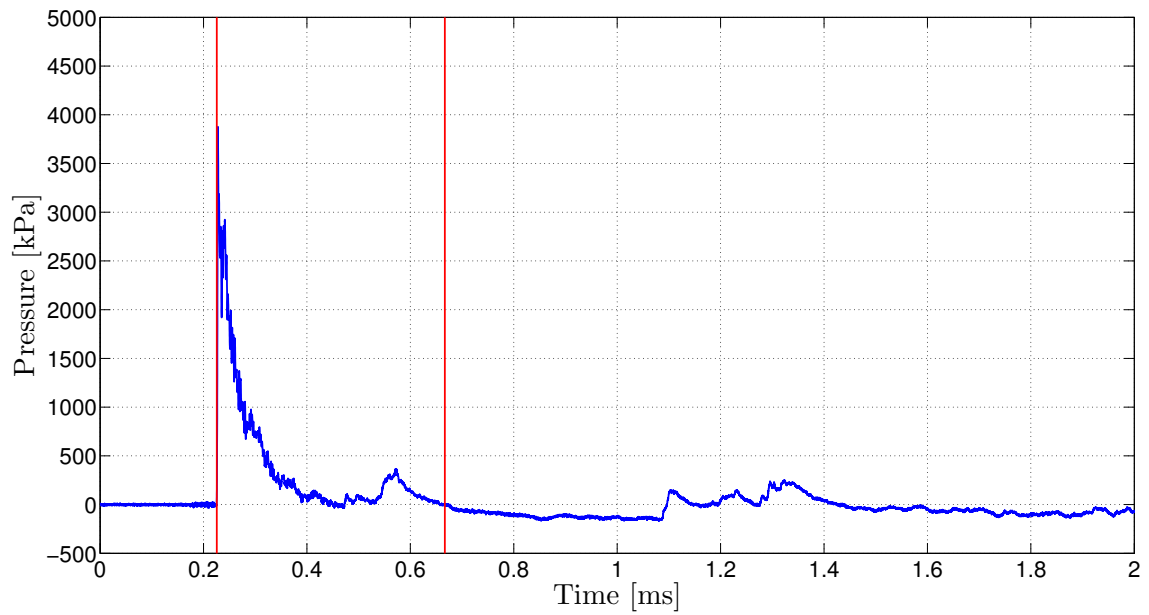
Figure 4.28: Pressure in transducer 1 for test R23.

99
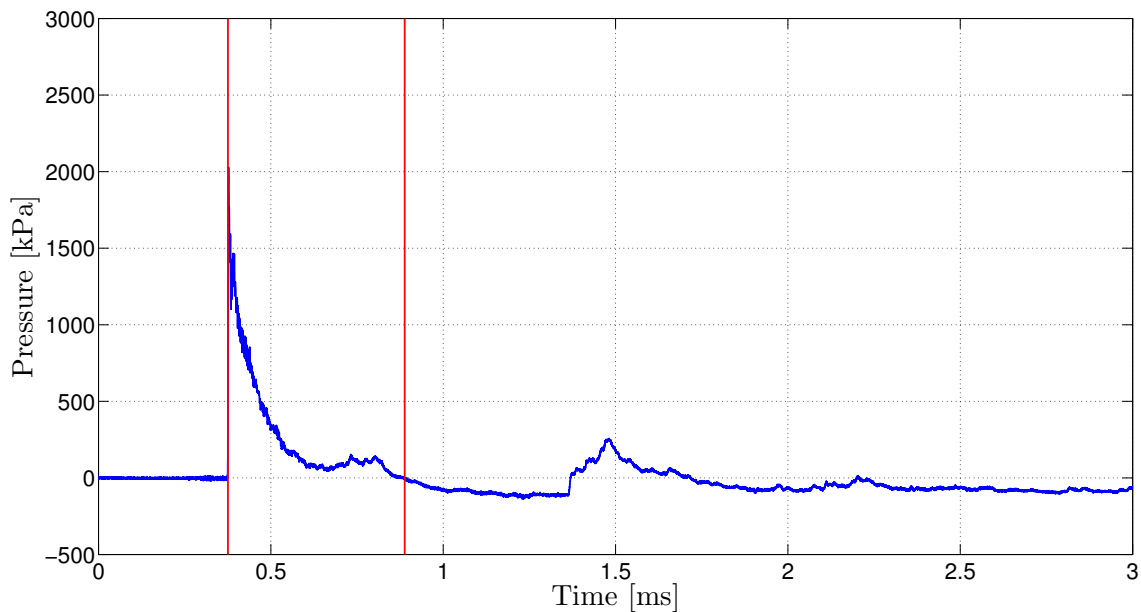
Figure 4.29: Pressure in transducer 1 for test R33-2.

By inspecting the pressure curves, it can be seen that the pressure does not return to ambient pressure. This indicates that the zero level has changed. A weakness with the Kistler 603B pressure transducers, is that they are designed for temperatures up to 200°C [66]. It is therefore possible that the zero level has drifted due to the high temperatures created by the explosion. This means the zero level has changed for all pressure curves. Because of this, it is very hard to identify the negative phase of the explosion. In Figure 4.29, the negative phase can be seen fairly well after the second red line. However, the negative phase is disrupted by a reflection wave at around 1.5 ms. Because the reflection waves give a significant contribution to the pressure, as well as the fact that the negative phase is hard to locate due to the change of the zero level, it was decided not to calculate the negative impulse. When calculating the positive impulse, it was decided to include any positive peaks that hit the pressure transducers before the positive phase ended. This is especially apparent in Figure 4.28.

In addition to the positive impulse, I_s^+, and the positive phase duration, t^+, the time of arrival, t_a, and the maximum pressure, p_{max}, were calculated. These parameters are explained in Chapter 2.2.4. In order to calculate the time of arrival, it was important that all tests were corrected according to the time of detonation. The tests that lacked results from the breakwire, were corrected according to the time of arrival of the tests with functional breakwires. Test R21 and R22 were then corrected according to time of arrival for transducer 1 from test R23. Test R31, R32 and R33 were corrected according to time of arrival for transducer 1 from test R33-2. This adjustment means that the time of arrival for the corrected tests are based on the assumption that the time of arrival for transducer 1 is the same as for the test they were corrected against. Table 4.7 lists the calculated parameters

from pressure transducer 1 and 5 for tests R13, R23 and R33-2. The complete set of results is listed in Appendix A.3. One of the MATLAB-scripts used to calculate the results is included in Appendix C.1.

Table 4.7: Calculated parameters from selected pressure transducers.

Test	Pressure transducer	Time of arrival t_a [ms]	Max pressure p_{max} [kPa]	Positive impulse I_s^+ [kPa·ms]	Positive phase duration t^+ [ms]
R13	1	0.12	10813	233.3	0.31
	5	0.15	6920	149.1	0.28
R23	1	0.23	3876	170.9	0.44
	5	0.24	3676	129.4	0.38
R33-2	1	0.38	2028	142.8	0.51
	5	0.40	1672	101.9	0.44

From the values listed in Table 4.7, it can be seen that the differences in maximum pressure and the time of arrival decrease as the stand-off distance increase. This can be attributed to the fact that the difference in stand-off distance between the pressure transducers will decrease as the stand-off distance increase.

4.3.3   Results - Component Tests

Before performing the tests presented in Table 4.6, it was decided to perform one test at stand-off distance 250 mm. This was done in order to investigate whether it would be possible to perform tests at the same stand-off distances as the calibration tests, rather than the stand-off distances presented in Table 4.6. After testing, it was apparent that this was impossible, as the plate was completely cut off at the supports. Figure 4.30 shows the plate after testing.

(a) Plate.	(b) Support.
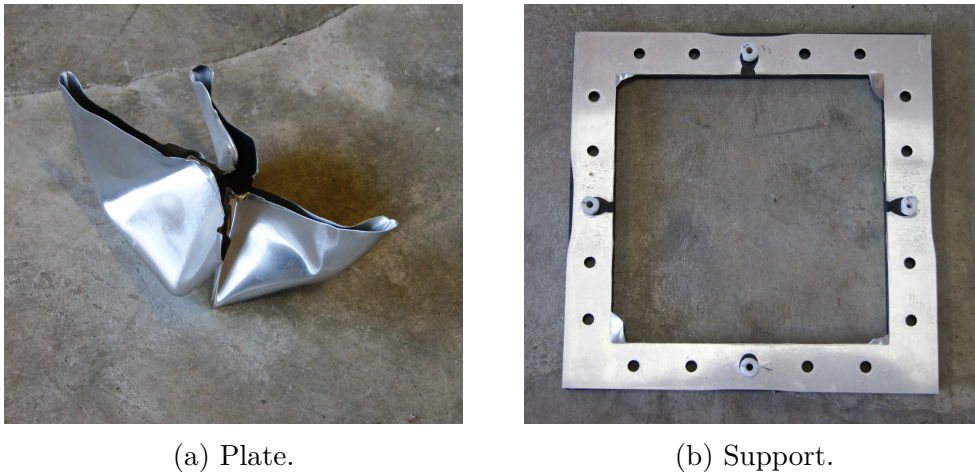
Figure 4.30: Plate after testing with stand-off distance 250 mm.

From Figure 4.30a, it can be seen that the plate is heavily deformed. Comparing it to the failure modes presented in Chapter 2.4, it appears that the failure corresponds to failure mode II. However, looking at Figure 4.30b, it can be seen that the cut is very clean along the support, apart from in the corners. This may indicate that the failure is actually due to shear at the supports. This suggests that the failure might be of mode III, or possibly something in between mode II and III.

In Figure 4.30b, it can be seen that there is very little deformation around the bolts. Around the pressure transducers however, the deformation is larger. As there are no bolts at the midpoint of the edges, it is expected that the friction force is lower. This means that the force required for sliding on the supports is lower than along the rest of the frame.

It was decided to go with stand-off distance 375 mm, 500 mm and 625 mm for the experiments. Stand-off distance 250 mm was omitted due to the complete tearing along the supports. Figure 4.31 shows one plate after testing for each stand-off distance. Two plates are shown at stand-off distance 625 mm, in order to highlight the slight differences in the deformed configuration. The remaining plates can be seen in Appendix B.2.

(a) A11   (b) A21

(c) A31   (d) A33
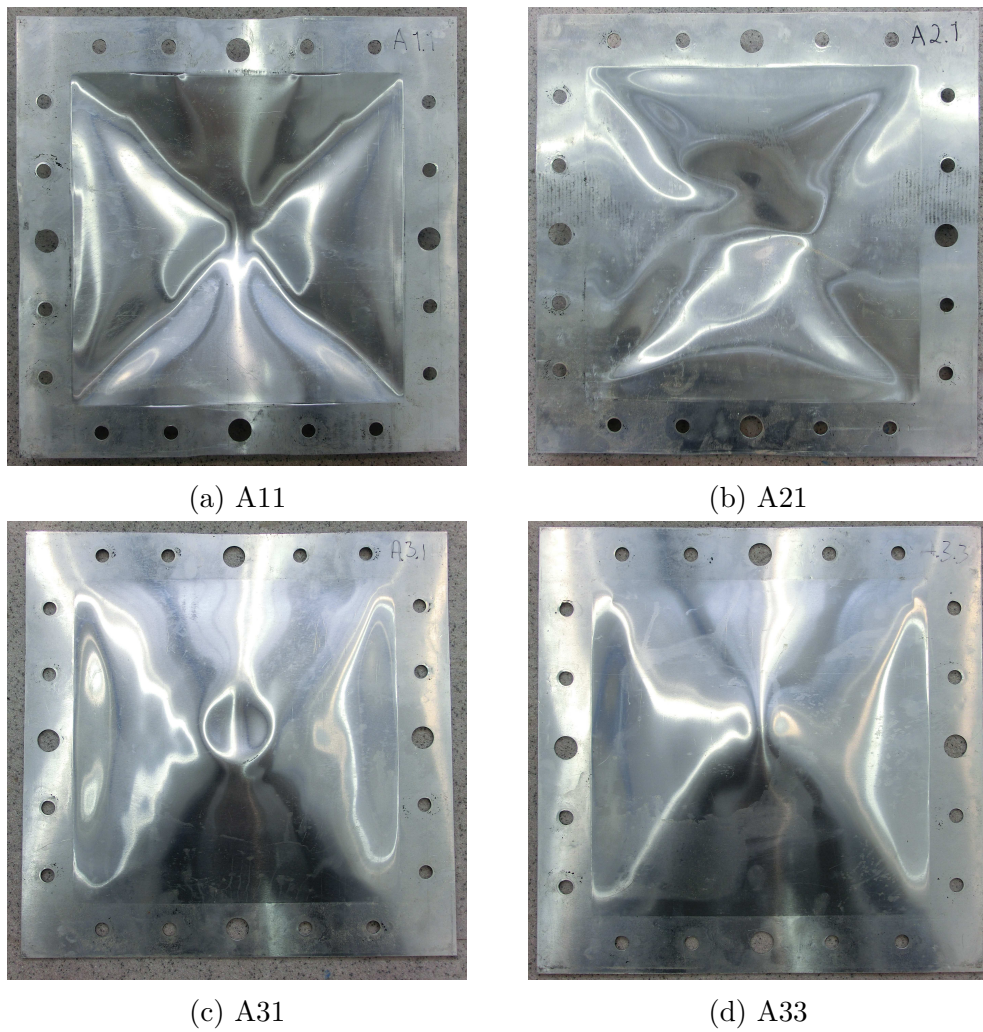
Figure 4.31: Deformed plates after testing.

From Figure 4.31a, it can be seen that stand-off distance 375 mm results in fracture along the support close to the corners. As with stand-off distance 250 mm, the fracture is very clean. A close-up view of a fracture can be seen in Figure 4.32.
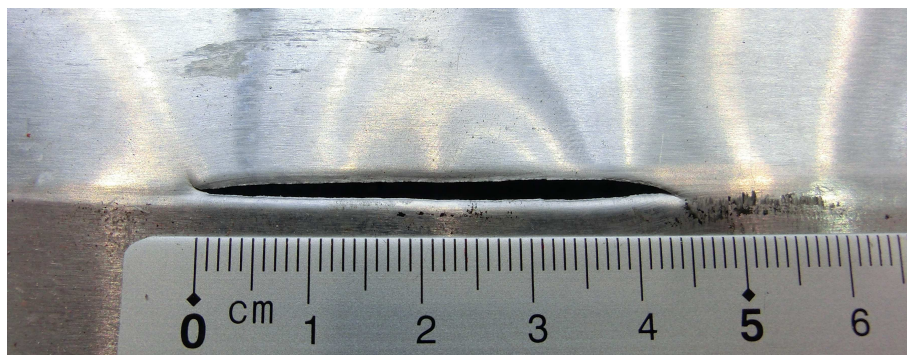
Figure 4.32: Fracture from plate A12.

The fracture in Figure 4.32 is from plate A12. The number of, and length of the fractures, varies from test to test. The length of the fracture shown in Figure 4.32, is approximately 45 mm, but the length can be up to around 60 mm, which is the case for one of the fractures in plate A13.

Figure 4.31b shows that no fracture is observed at stand-off distance 500 mm. This is also the case for the plates at stand-off distance 675 mm.

The most interesting observation come from Figure 4.31c and Figure 4.31d. Here it can be seen that the final deformation is in the opposite direction of the other tests. That means the plate is now closer to the load than before the detonation. This is similar to the counter-intuitive behavior that was investigated by e.g. Flores-Johnson and Li [16]. This counter-intuitive behavior was also observed in the simulations performed in Chapter 3.3. However, this was only observed at stand-off distances of 875 mm or more.

While the plates completely returned to the opposite direction for test A32 and A33, it can be seen from Figure 4.31c, that the midsection of the plate in test A31, still had positive displacement relative to the rest of the plate.

Similar to what was observed in Figure 4.30b, it can be seen that there is more deformation around the pressure transducers than along the rest of the support. Figure 4.33 shows the deformation around pressure transducer 5 for plate A11.
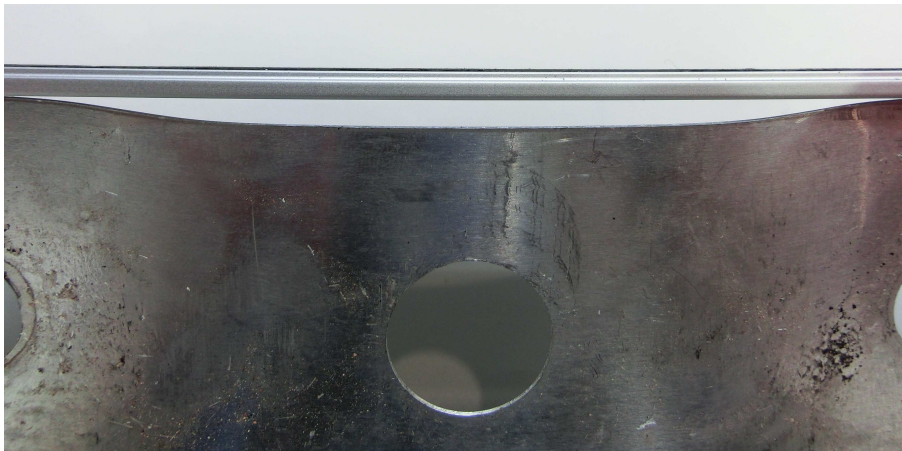
Figure 4.33: Displacement around pressure transducer 5 for plate A11.

From Figure 4.33, it can be seen that there is a significant deformation along the edge. The displacement in the middle is approximately 4 mm relative to the initial configuration. It can be seen from the figure that the displacement decreases as it gets closer to the bolt holes. After passing the first bolt, there is no visible deformation further along the edge. Figure 4.34 shows the hole to the right in Figure 4.33, as well as the hole further along to the right.

(a) Close to pressure transducer.

(b) Close to corner.
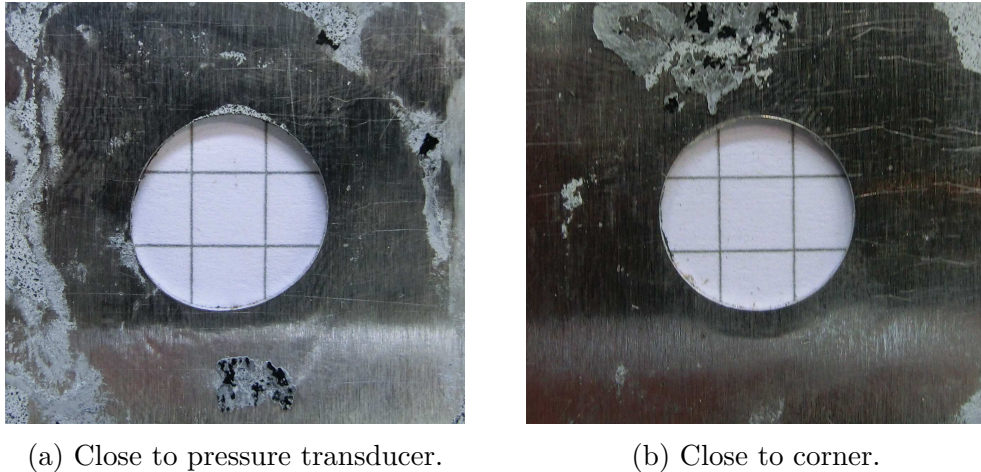
Figure 4.34: Bolt holes between pressure transducer 5 and upper right corner of plate A11.

From Figure 4.34a, it can be seen that the hole has been slightly deformed in the direction of the pressure transducer to the left. From Figure 4.34b, it can be seen that this is not the case when getting close to the corner. Controlling with a sliding caliper indicated that there were very little difference in the diameter. It was apparent from the tests at higher stand-off distances, that the deformation around the pressure transducers were decreasing as the stand-off distance increased. This also meant that the deformation of the holes decreased, and already at stand-off 500 mm, very little deformation was noticeable. This indicates that the friction, produced by the bolts, is enough to prevent sliding of the plate along the support. Because of this, it is possible that the boundary conditions will function almost as fixed boundaries when the load is small. The friction force will be the highest right under the bolts, and then gradually decrease as the distance to the bolts increases. Due to less friction forces around the transducers, sliding along the supports will happen at weaker loading.

The displacement of the plates were measured by the help of a sliding caliper, before the plates were removed from the clamping frame. In addition, the plates were measured again after being brought back to Gløshaugen, NTNU. This was done to account for possible restrained, elastic deformations. The measurements were taken at the points marked in Figure 4.35. The displacements were not measured in points 2, 4, 7 and 9 at Østøya. These points were included when measuring at Gløshaugen, in order to give a more complete representation of the deformation. Table 4.8 lists the measurements from the plates shown in Figure 4.31. The complete set of measurements is included in Appendix B.1. The displacements are considered positive when moving away from the detonation.
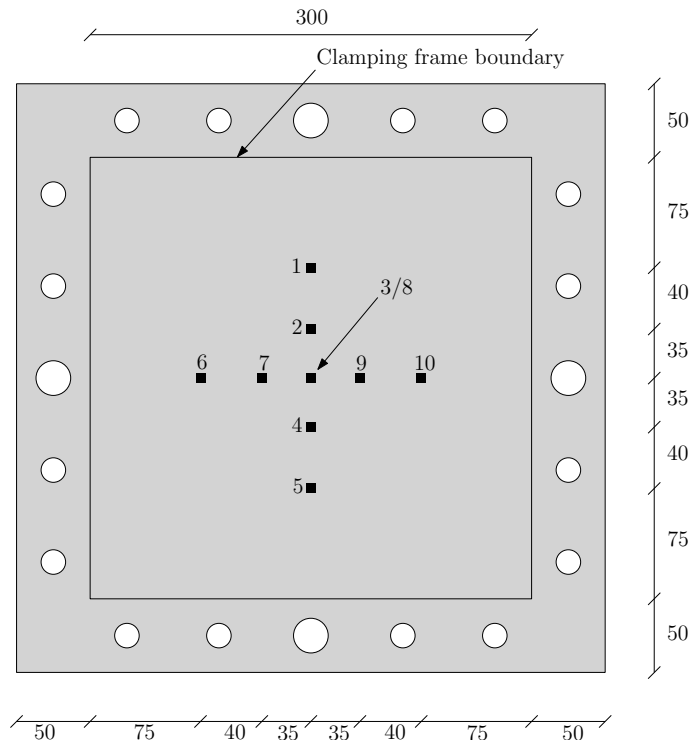
Figure 4.35: Points where displacements were measured. Measurements in mm.

Table 4.8: Displacements of deformed plates.

Plate	Location	Displacement at measure point [mm]									
		1	2	3	4	5	6	7	8	9	10
A11	Østøya	22.2	N/A	39.1	N/A	16.2	15.9	N/A	39.1	N/A	17.7
	Gløshaugen	21.9	33.5	37.9	26.3	14.4	17.8	30.8	38.4	29.1	15.9
A21	Østøya	8.6	N/A	24.5	N/A	6.3	8.1	N/A	24.5	N/A	13.7
	Gløshaugen	9.4	18.5	24.6	15.5	6.4	9.2	18.9	24.5	21.1	13.8
A31	Østøya	-14.1	N/A	-15.9	N/A	-12.9	-12.5	N/A	-15.9	N/A	-14.6
	Gløshaugen	-14.6	-16.5	-18.4	-18.3	-12.7	-13.4	-19.5	-16.8	-19.8	-14.2
A33	Østøya	-12.0	N/A	-23.7	N/A	-12.0	-10.1	N/A	-23.7	N/A	-10.1
	Gløshaugen	-11.8	-20.2	-21.4	-15.5	-11.0	-11.3	-18.3	-23.6	-18.1	-12.3

From Table 4.8, it can be seen that the difference in displacements measured at Østøya and at Gløshaugen, are fairly small. In most points, the difference is lower than 2 mm, and in some points the displacements are almost identical. The measurements taken at Østøya were taken rather quickly, and it is likely that the measurements were not taken at the exact same points on Østøya and at Gløshaugen. Because of this, any variation, or lack thereof, may potentially be due to error in the measurements. Regardless, the results from Table 4.8 still indicate that the deformation is pretty similar between the two sets of measurements. This indicates that any remaining elastic deformations were small, or the clamping frame did not prevent the plates from releasing the elastic deformations. Comparing the displacements at the midpoint, with the results from the preliminary studies, it can be seen

that the displacements are way lower than the ones resulting from the numerical simulations. The analytical calculations, on the other hand, resulted in values lower than the actual displacements, but still closer than what the numerical simulations suggested.

In order to investigate the behavior of the plates, they were all prepared for DIC analysis. On most plates, the experiments were performed before the paint were completely dry. For plate A23 and A32 however, this were not the case. When the plates reached maximum displacement, the paint at the center of the plates detached. This prevented the DIC analyses from giving reliable results after maximum displacement, as the DIC-mesh was heavily destorted around the affected area. Figure 4.36a shows where the paint disappeared on plate A23. The affected area is marked in red. A close-up view of the affected area is shown in Figure 4.36b.
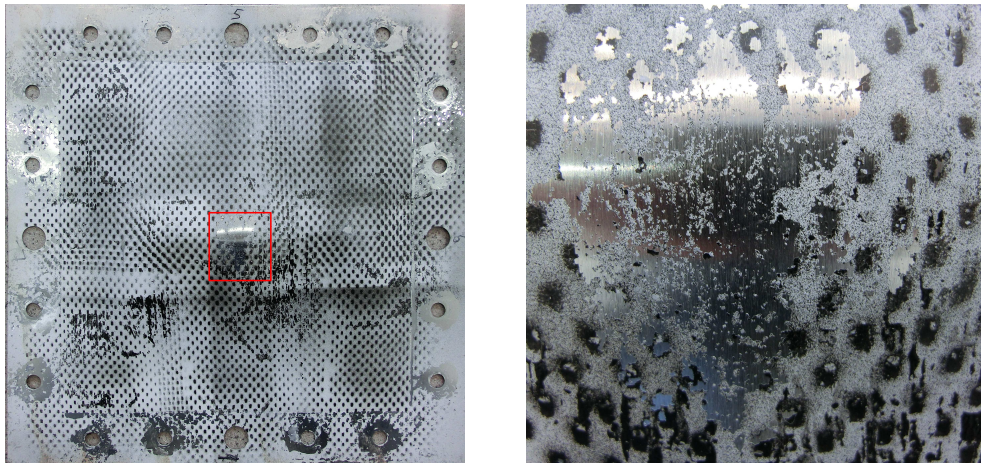
(a) Plate A23   (b) Close-up view of affected area.

Figure 4.36: Damaged DIC pattern of plate A23.

Before performing DIC analyses on the plates, a mesh had to be applied. Figure 4.37 shows the mesh used in the analyses. The same mesh was used for all the plates. eCorr was used to carry out the DIC analyses.

(a) HS CAM 1   (b) HS CAM 2
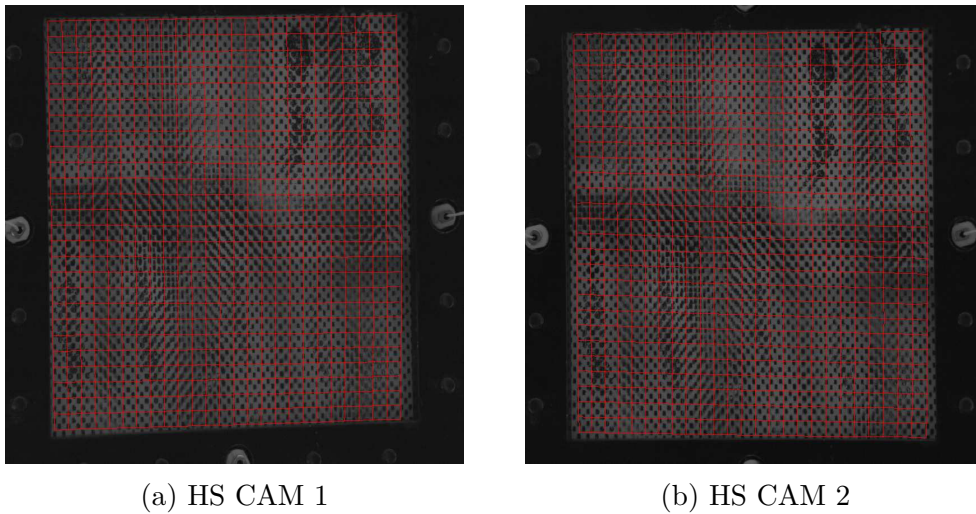
Figure 4.37: Mesh used in DIC analyses.

When performing the analyses, it was apparent that there were some additional, minor problems. For plate A11, A12 and A13, the fracture made it possible for light from the explosion to get through. This affected the DIC-mesh close to the fracture, but didn not have any negative impact on the remaining mesh. When investigating the pictures used in the DIC analyses, it was apparent that the fracture at stand-off distance 375 mm appeared at around 17 mm midpoint displacement. This is lower than the maximum displacement of the plates at 500 mm stand-off. Because the plates at 500 mm stand-off, did not get any fracture, this further indicates that the fractures are a result of shear at the supports.

Some of the pictures used for the DIC analysis of plate A33, were disturbed by light during the experiment. This may have been due to an unexpected light source, or due to reflection created by deforming the plate. This light source impacted the mesh around the affected area. Most of the mesh however, was still unaffected.

During the experiments, the pressure were logged by pressure transducers 1, 5, 6 and 7. The pressure were logged by the pressure transducers at the same frequency as in the calibration tests. In order to know the pressure associated to each picture, a separate set of measurements were logged at the frequency of the camera. Because the cameras took pictures and logged pressure at a lower frequency than the pressure transducers, the DIC-pictures had to be synchronized with the complete pressure curves logged by the pressure transducers. This was done by adjusting the sets of pressure curves so that the pressure in transducer 5, had the same time of arrival when logged by the transducers, as when logged by the camera. Because no breakwire was installed, the time of arrival had to be adjusted according to the calibration tests. The tests at stand-off distance 375 mm were corrected according to the time of arrival of transducer 5 in test R23, while the tests at stand-off distance 500 mm were corrected according to transducer 5 in test R33-2. As no calibration tests were performed at stand-off distance 625 mm, these tests had to be corrected

in another way. At the time of detonation, an impulse were sent out from the detonation mechanism. This impulse was captured by the pressure transducers. Because the response only appeared in a few of the transducers, it was decided to correct all the tests according the same time of arrival. The tests were therefore adjusted according to transducer 5 from test A32. It should be noted that the potential source of error is great, as the time of arrival of the pressure created by the detonation mechanism, is unknown. Still, comparing the time of arrival to the values used for the other tests, the value seems reasonable. Table 4.9 lists the time of arrival used to correct the different tests.

Table 4.9: Time of arrival used to correct component tests.

Stand-off distance [mm]	Time of arrival [ms]
375	0.2443
500	0.3995
625	0.5935

After correcting the pressure curves according to the time of arrival, the pressure transducers were compared. Figure 4.38 shows the pressure in transducers 1, 5, 6 and 7 for test A11. Figure 4.39 and Figure 4.40 show the same plots for test A21 and A31, respectively. Corresponding plots for the remaining tests can be found in Appendix B.3.
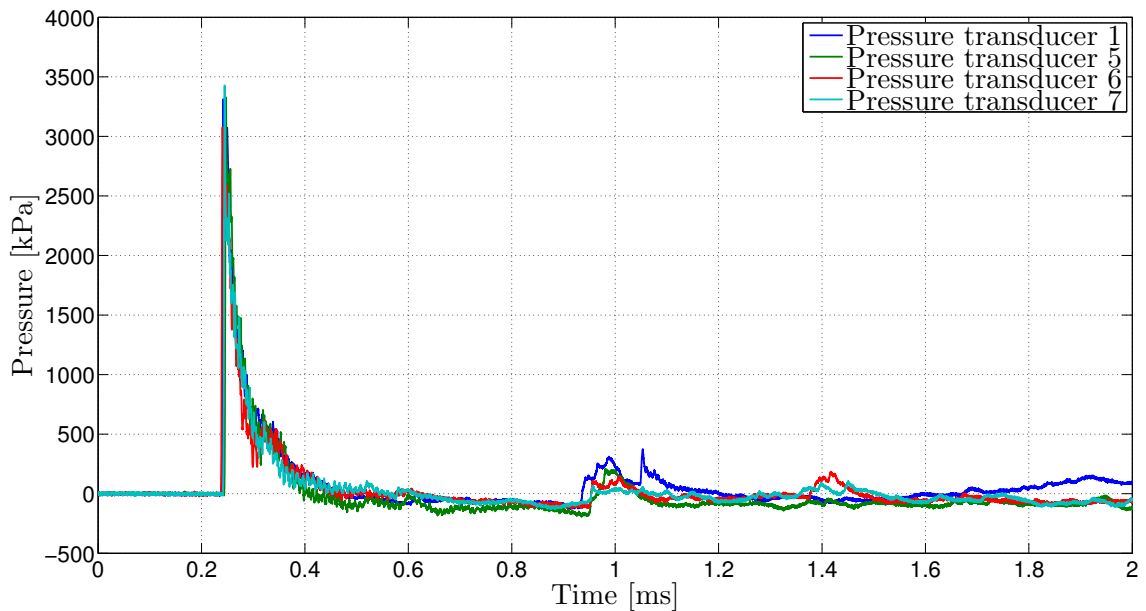
Figure 4.38: Pressure transducers in the clamping frame for test A11.
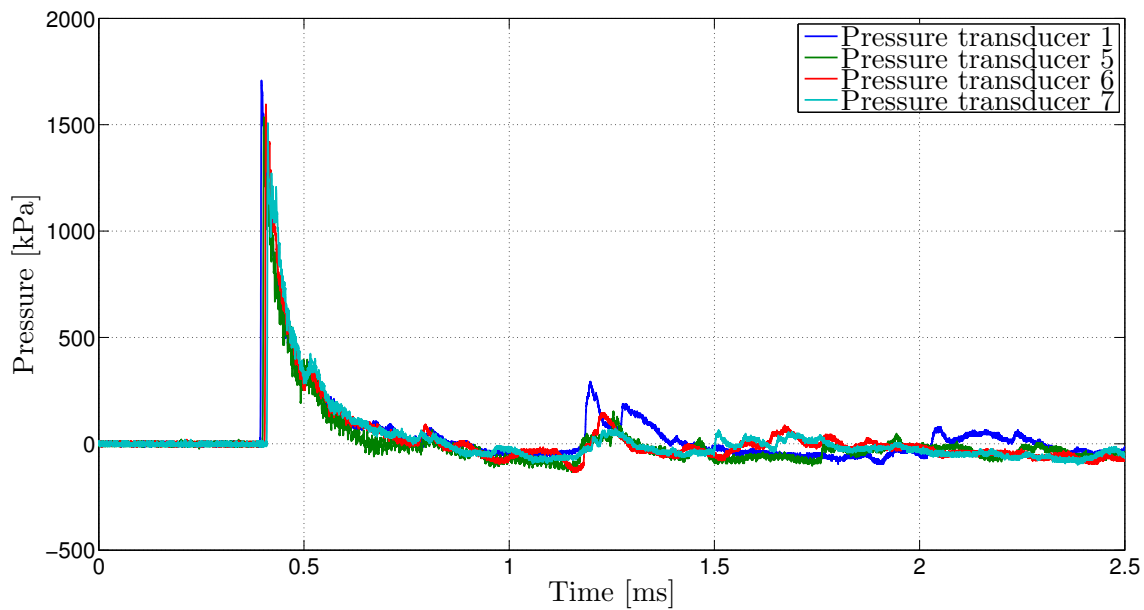
Figure 4.39: Pressure transducers in the clamping frame for test A21.
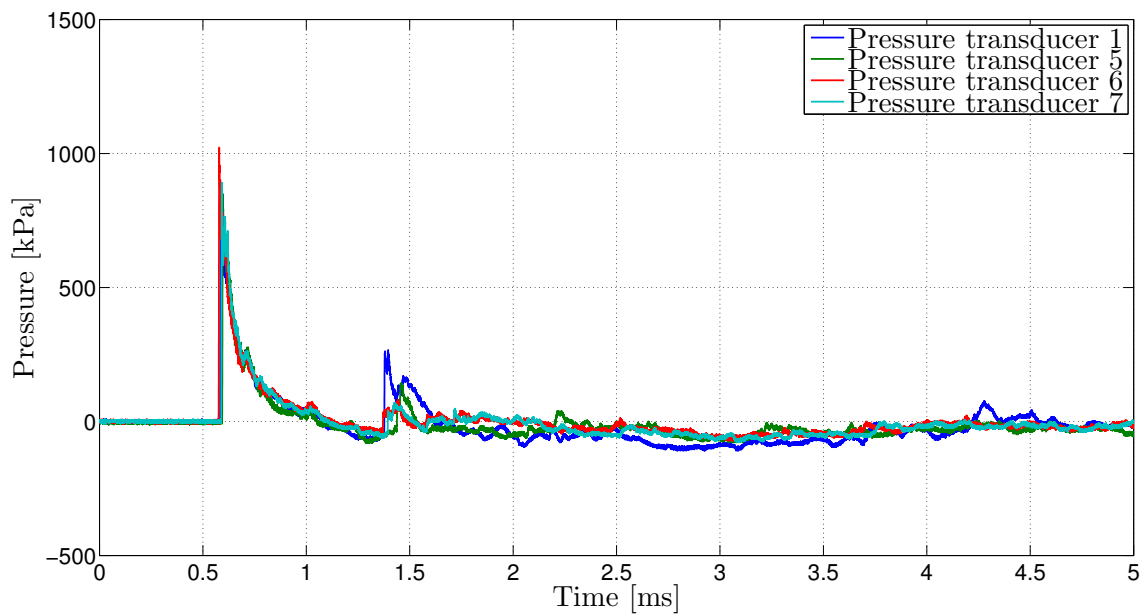
Figure 4.40: Pressure transducers in the clamping frame for test A31.

In all the above figures, it can be observed that the time of arrival of the pressure transducers are very similar. In addition, the peak pressure is almost the same between the pressure transducers. This indicates that the load have been centered pretty well during the experiments. There are slightly more variations for a couple of the other tests, but the results are still fairly consistent.

From the DIC analyses, it is possible to extract the displacement of the midpoint. This can then be plotted against time in order to investigate the behavior of the plate. Figure 4.41 shows the midpoint displacement plotted against time for the tests. Test A23 and A32 have not been included in the figure. This was because the removed paint made it impossible to get accurate values after maximum positive displacement. Based on the maximum displacements meassured, it can be assumed that the behaviour of plate A23 was similar to plate A21, and the behavior of plate A32 similar to A33.
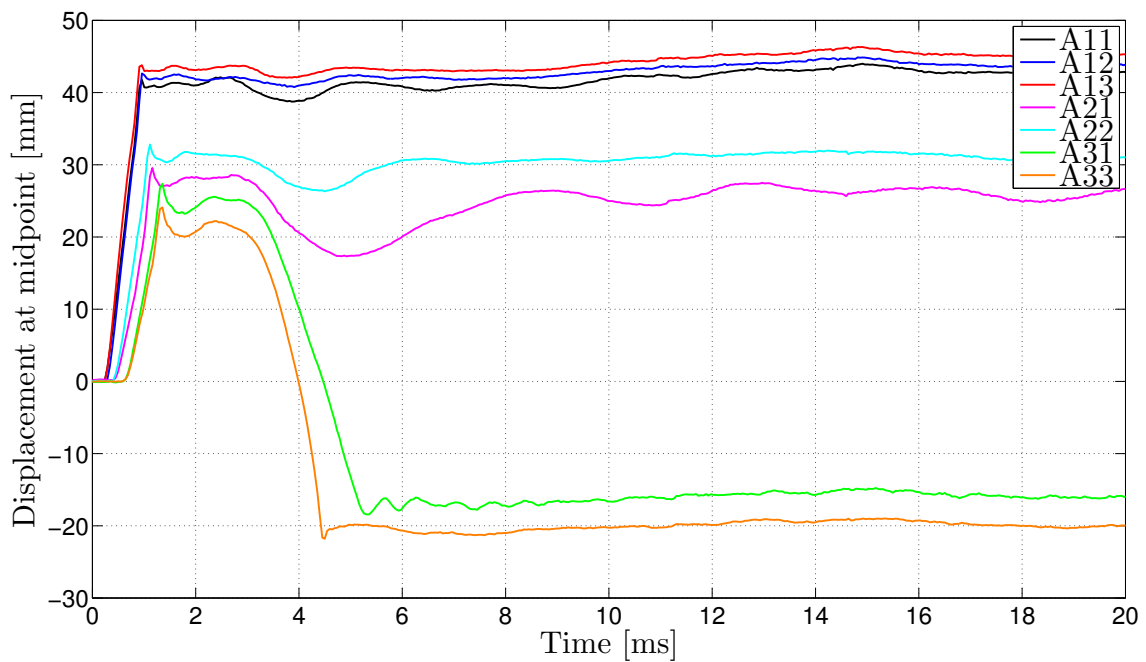
Figure 4.41: Displacement at midpoint plotted against time.

From Figure 4.41 it can be seen that the displacement stabilizes fairly quickly at around 41 mm displacement for test A11. Similar behavior can be observed from all the plates at 375 mm stand-off, although the maximum displacement vary at values between 40 to 45 mm. It can be seen that the displacement seems to stabilize at around 27 mm displacement for test A21. After reaching maximum displacement, the plate returns back to almost 17 mm displacement before it starts to increase again. Test A22, on the other hand, stabilizes at around 31 mm. Similar behaviour as for plate A21 can be observed, although with less change in the displacements. For test A31 and A33, it can be seen that the displacements start as positive. After reaching maximum displacement, the plates snap back to a negative displacement. Comparing the curves at stand-off 500 mm and at stand-off 625 mm, it seems like the counter-intuitive behaviour seen from test A31 and A33, may result from the same behaviour observed from plate A21, when the displacements decrease after initally reaching the peak. It is possible that the plates at 625 mm stand-off reach an instable configuration, where the plates continue their displacement in the negative

direction. Because the change in displacement is smaller at 500 mm stand-off, the plate does not reach the instable configuration, and therefore returns back to the positive deformations. This is supported by the observations made by e.g. Flores-Johnson and Li [16]. It is possible that the negative displacement is assisted by the negative impulse resulting from the blast load.

In order to investigate the correlation between the displacement and the pressure, they were plotted in the same figure. In addition, deformation profiles at different time steps were plotted in both 2D and 3D. Figure 4.42 shows 3D and 2D deformation profiles, as well as the midpoint displacement and pressure, from pressure transducer 5, at different time steps. The time at the different time steps, has been highlighted with a red line in the displacement and pressure plot. The 2D deformation profile is taken from the middle of the plate, from left to right along the x-axis in the 3D plot. Figure 4.43 and Figure 4.44 show corresponding plots for test A21 and A31, respectively. Corresponding figures for the rest of the tests are included in Appendix B.4. One of the MATLAB-scripts used to generate the 2D and pressure plots, is included in Appendix C.2. One of the MATLAB-scripts used to generate the 3D plots, is included in Appendix C.3.

(a) $t = 0.39$ ms

(b) $t = 0.39$ ms

(c) $t = 0.39$ ms

(d) $t = 0.58$ ms

(e) $t = 0.58$ ms

(f) $t = 0.58$ ms

(g) $t = 0.77$ ms

(h) $t = 0.77$ ms

(i) $t = 0.77$ ms

(j) $t = 0.96$ ms

(k) $t = 0.96$ ms

(l) $t = 0.96$ ms
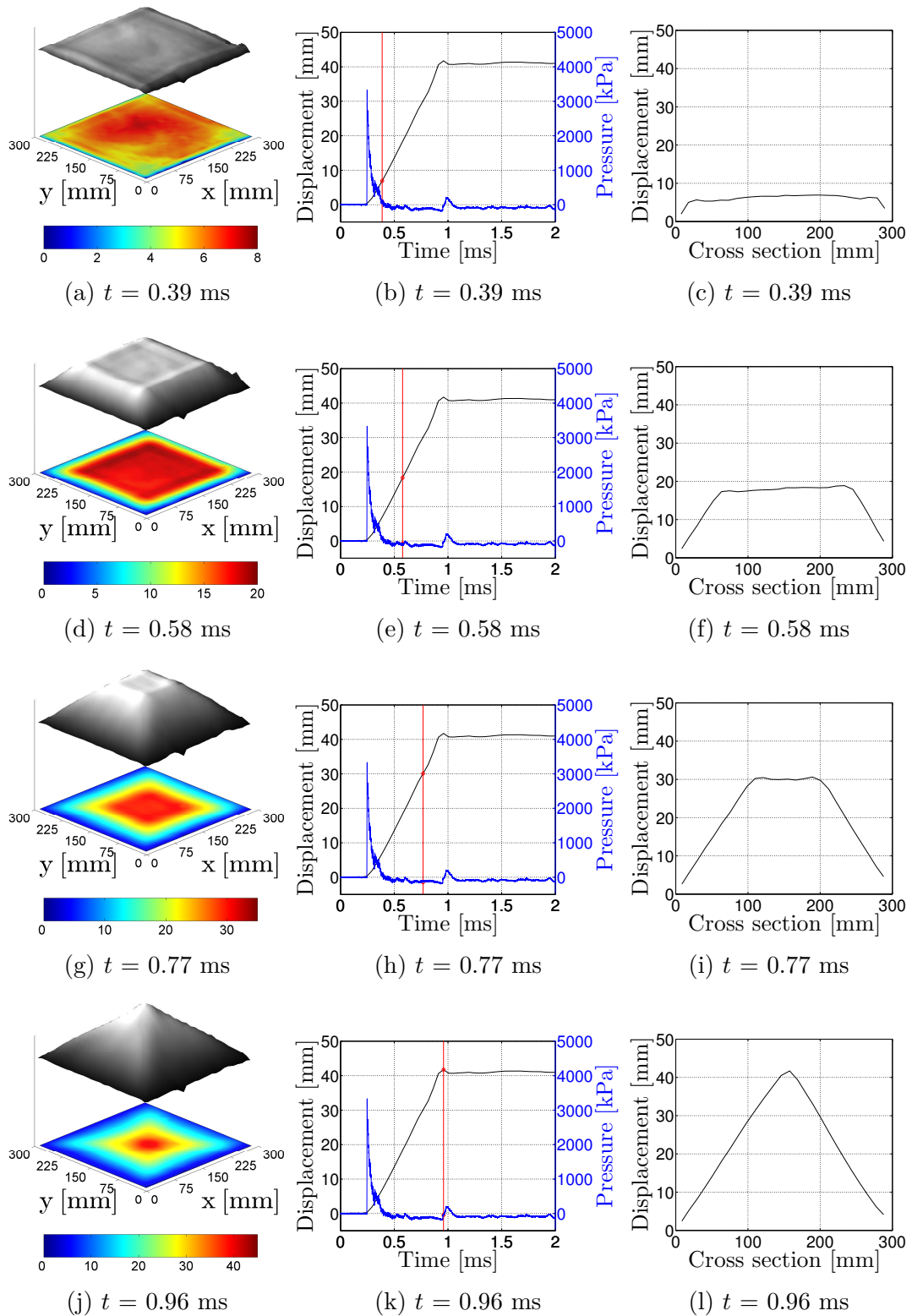
Figure 4.42: Displacement of plate A11.
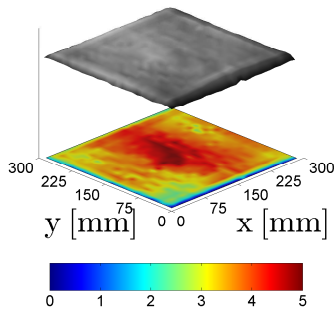
(a) $t = 0.59$ ms

(b) $t = 0.59$ ms

(c) $t = 0.59$ ms

(d) $t = 0.78$ ms

(e) $t = 0.78$ ms

(f) $t = 0.78$ ms

(g) $t = 0.97$ ms

(h) $t = 0.97$ ms

(i) $t = 0.97$ ms

(j) $t = 1.16$ ms

(k) $t = 1.16$ ms

(l) $t = 1.16$ ms

(m) $t = 4.92$ ms

(n) $t = 4.92$ ms
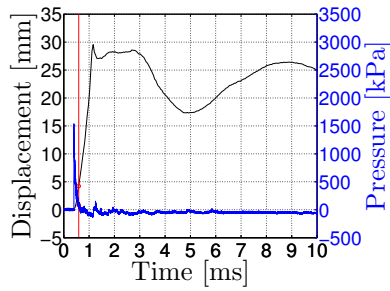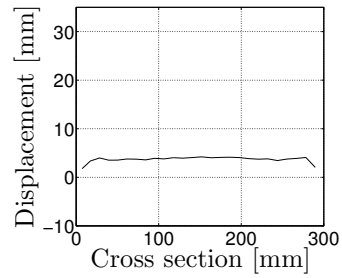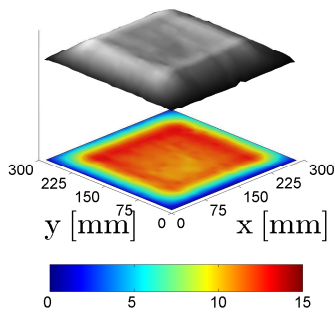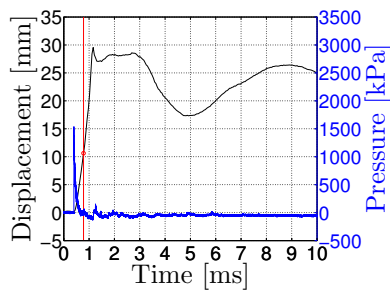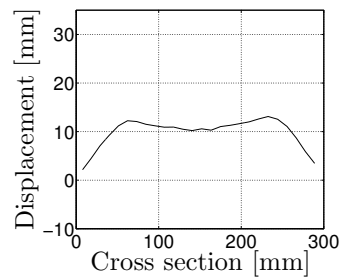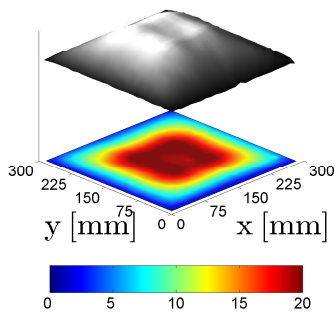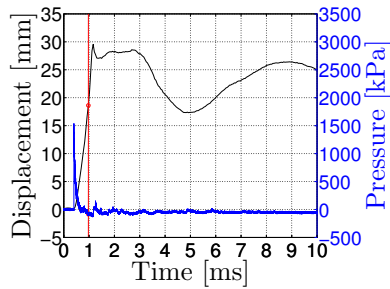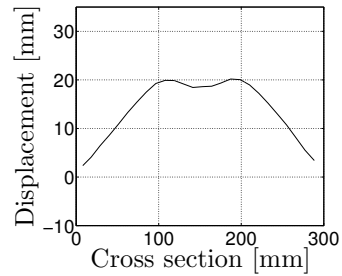
(o) $t = 4.92$ ms
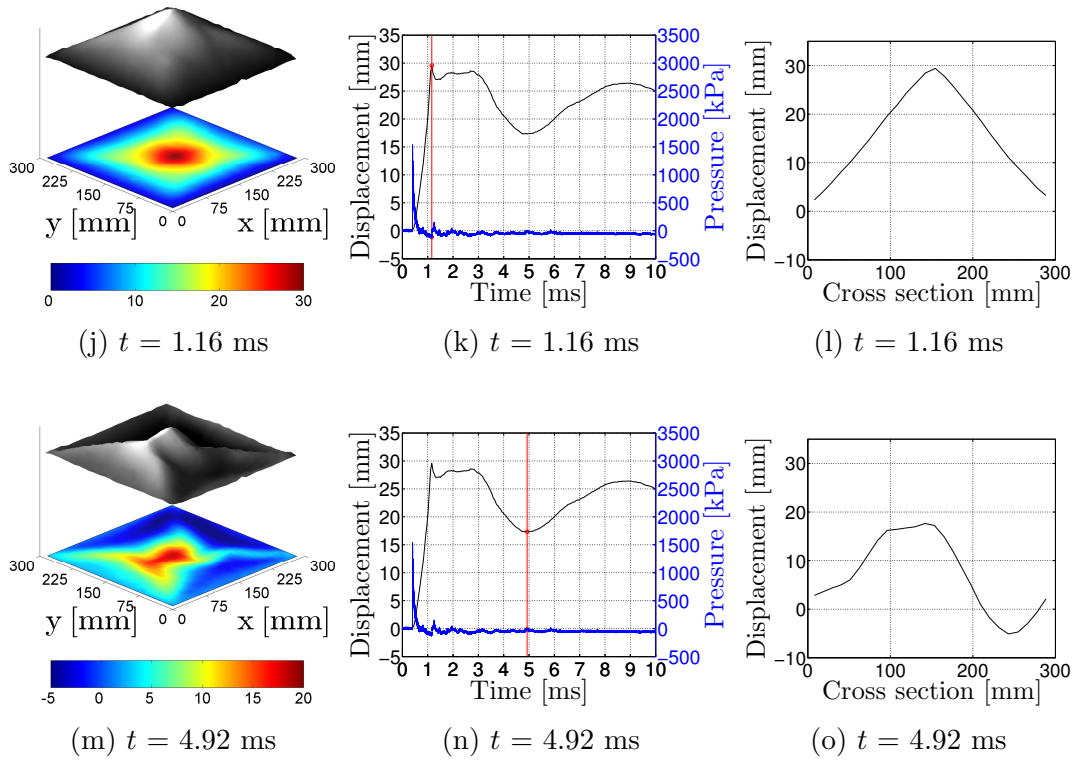
Figure 4.43: Displacement of plate A21.
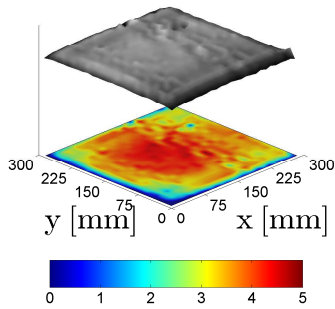
(a) $t = 0.78$ ms
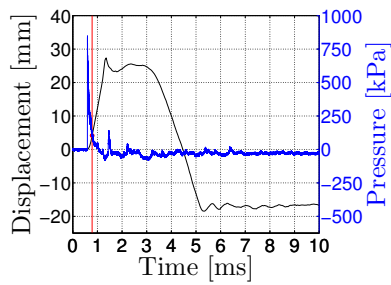
(b) $t = 0.78$ ms
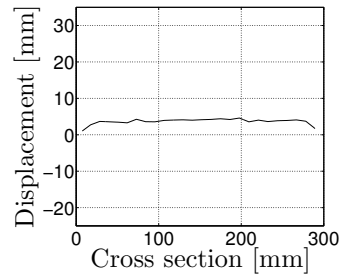
(c) $t = 0.78$ ms

(d) $t = 0.97$ ms

(e) $t = 0.97$ ms

(f) $t = 0.97$ ms

(g) $t = 1.16$ ms

(h) $t = 1.16$ ms

(i) $t = 1.16$ ms

(j) $t = 1.36$ ms

(k) $t = 1.36$ ms

(l) $t = 1.36$ ms

116

(m) $t = 3.88$ ms

(n) $t = 3.88$ ms

(o) $t = 3.88$ ms

(p) $t = 4.45$ ms

(q) $t = 4.45$ ms

(r) $t = 4.45$ ms

(s) $t = 4.83$ ms

(t) $t = 4.83$ ms

(u) $t = 4.83$ ms

(v) $t = 5.36$ ms

(w) $t = 5.36$ ms
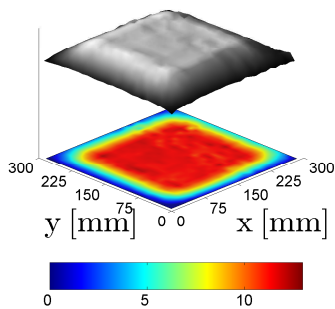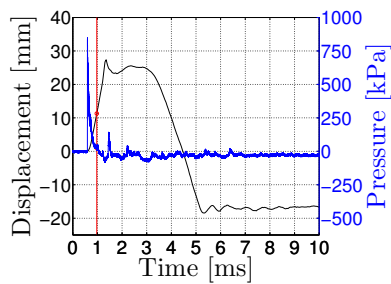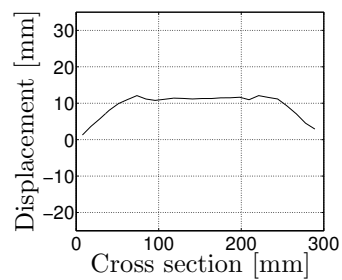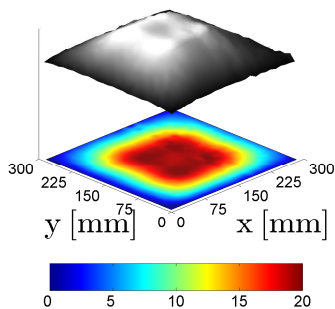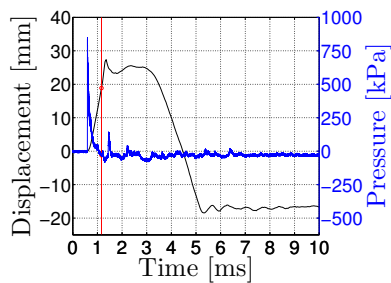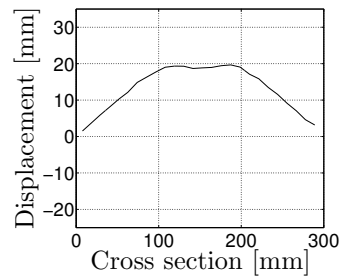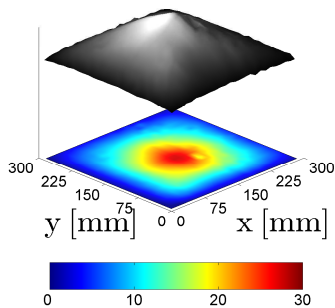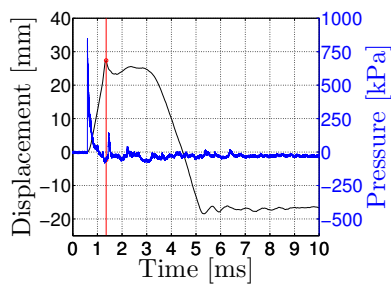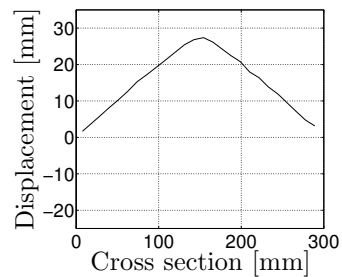
(x) $t = 5.36$ ms
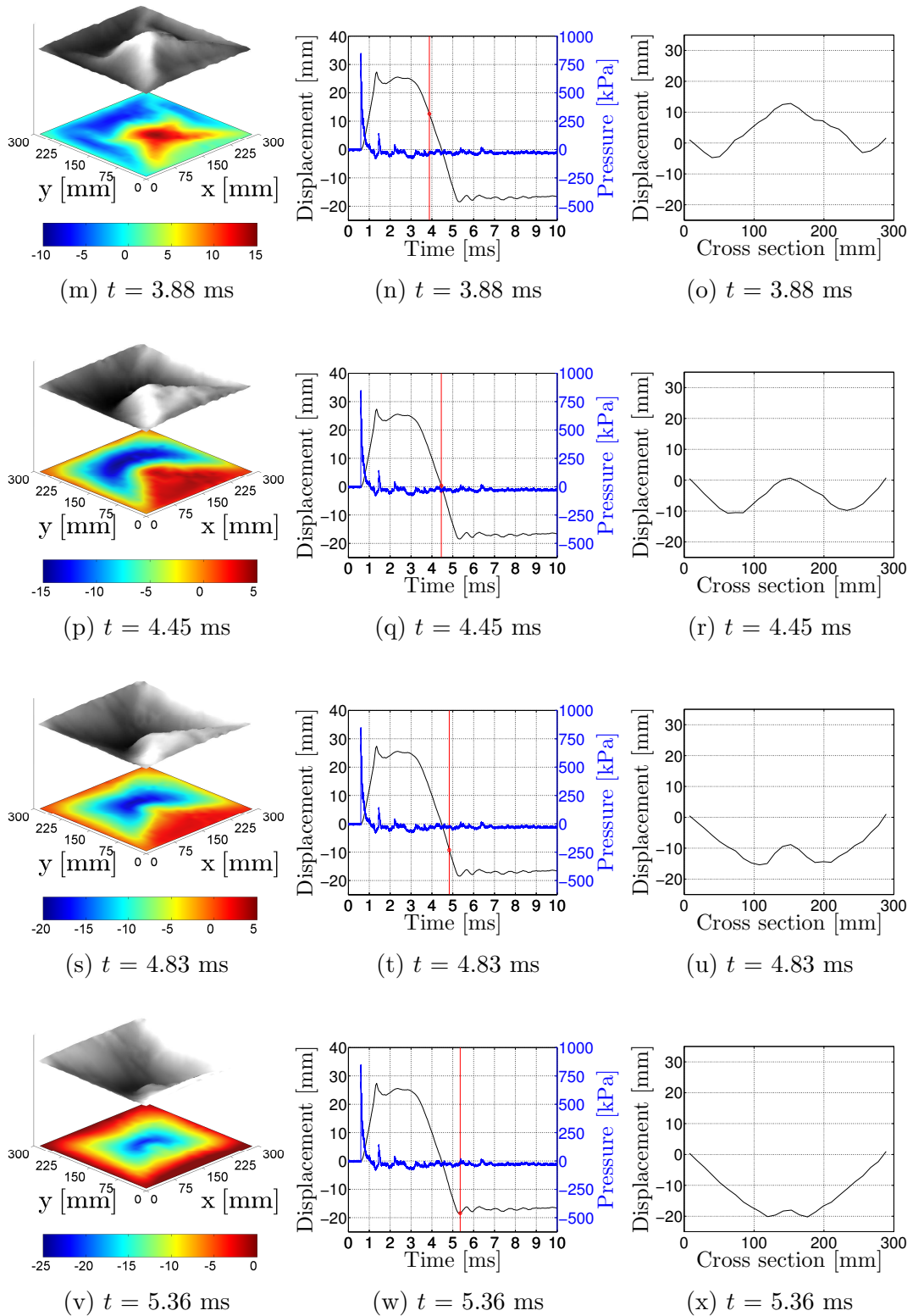
Figure 4.44: Displacement of plate A31.

From Figure 4.42, Figure 4.43 and Figure 4.44, it can be seen that the positive impulse ends very early compared with the displacement curves. That means most of the deformations are caused by the impulse load. It should also be noted that pressure transducer 5 is located in the clamping frame, above the plate. That means the pressure actually hits the plate slightly earlier than what is shown in the figures. Because the impulse is finished early in the displacement progress, it can be assumed that there is very little fluid-structure interaction during the deformation.

From Figure 4.44, it can be seen that the negative impulse is likely to be finished as the displacement start to decrease. It is possible that the negative impulse gives a similar effect as the positive impulse, resulting in deformations after the impulse has ended. However, looking at the pressure curves, this is unlikely. Due to pressure from reflection waves, the negative impulse is almost nullified, making it unlikely that this could be the reason for the negative displacements. In addition, very little change in the displacements during the negative phase, can be observed. Due to the duration of the negative phase, it should be expected that any effect would be noticeable earlier than what can be observed from the figures.

Comparing Figure 4.43m and Figure 4.43o with Figure 4.44m and Figure 4.44o, it can be seen that there are similarities between the deformation profiles. This indicate that the behaviour would have been similar if the displacement had reached an unstable configuration. After the configuration in Figure 4.43o, the plate returned to a deformed configuration similar to Figure 4.43l.

When investigating the results from the blast pencil, it was apparent that the blast pressure hits the cameras at around 10 ms. The exact time varies depending on the stand-off distance. Because the pressure hits the cameras, it is possible that the cameras are distorted, and that the results therefore will be affected. Looking at the results from the DIC analyses, it was apparent that the later deformation profiles were displaced slightly more along the whole cross-section. Consequently, the results from the DIC has been assumed incorrect after around 10 ms. Because the plates were still in motion at this point, it was not possible to get accurate deformation profiles of the final deformation configuration from the DIC.

When comparing all the DIC-results, it can be seen that the behaviour is fairly similar between the tests at corresponding stand-off distances. There are still slight variations, and there are multiple possible causes for this. As the C4 loads were made by hand, it is possible that there were slight variations in mass and geometry. It is also possible that there are slight differences in the positioning of the loads, or differences in the plates that were tested. Considering all the potential sources of error, the experiments still indicate decent repeatability, given approximately the same setup and conditions.

Chapter 5

Material model

5.1 Initial Evaluation

Choosing a material model can be done i multiple ways. Either the model can be chosen by using an established model from the literature, or a new model can be established based on material tests. Establishing a material model based on tests, can be done by direct calibration or through inverse modeling. Inverse modeling is based on trial and error, but can also be done automatically by the use of iteration, e.g. in programs like LS-OPT [68].

The material model is going to be used in numerical simulations in EUROPLEXUS. Because of this, the Johnson-Cook model, as explained in Chapter 2.7, will be employed. This model uses a power law as basis for strain hardening. This is not optimal as aluminum is expected to have an asymptotic behaviour during strain hardening. Considering this, Voce's law would give a better description of the behavior. As a result, the modified Johnson-Cook model would be the optimal choice. However, as this model is not supported by EUROPLEXUS, the Johnson-Cook model was chosen instead.

To determine a material model by direct calibration, the true stress-plastic strain curve is used as a basis. The material model is then fitted to the values and extrapolated to larger strains. The slope of the true stress-plastic strain curve is often very steep just after yielding. Because of this, the stress at 0.2% plastic strain is often used as the yield stress when fitting the material model. Because the model is extrapolated to larger strains, the accuracy of the model will improve when the material tests give usable values for larger plastic strains.

From Figure 4.9, it can be seen that the plastic strain is very low at the point of necking. For both specimens, the last value recorded is lower than 0.4%. Using the stress at 0.2% plastic strain as yield stress, would leave less than 0.2% of the total plastic strain. As a result, determining a material model by the use of direct calibration would be hard. Even if all the values for plastic strain were used, it

would still be too hard to get an accurate result. Due to this, it is better to use inverse modeling to determine the material model.

5.2 Inverse Modeling

The inverse modeling was performed by trial and error in EUROPLEXUS. To get an impression of reasonable values, the values from literature used in Chapter 3 were employed as a basis. When modeling, it was decided to compare the force-displacement curve from the material test, with the equivalent curve from EURO-PLEXUS. Even though the material tests indicated anisotropy, it was decided to define an isotropic material model, based on the specimen with 0 degree orientation, relative to the rolling direction. From Figure 4.5, it can be seen that specimen 3 gave values in between values from specimen 1 and specimen 2. Hence, specimen 3 was chosen as the test to be used for comparison with the numerical simulations.

5.2.1 Mesh

Due to symmetry, it was decided to only model a quarter of the specimen. The mesh was modeled in a program called SALOME [69]. The mesh created in SALOME, is not directly compatible with EUROPLEXUS. Because of this, the mesh was converted by the help of another program called Cast3M [70]. The resulting mesh can be seen in Figure 5.1. The Cast3M-file used to convert the mesh, is included in Appendix D.1. The mesh is composed of shell elements with a thickness of 0.8 mm. The element size is varying between approximately 1.5 mm and 2.0 mm. At the midpoint of the specimen, the element width is varying. This was done to ensure that the elements were as square as possible at larger displacements. Q42L elements were used. This is a 4-node quadrilateral element, that can be used in Lagrangian calculations with full integration [46].
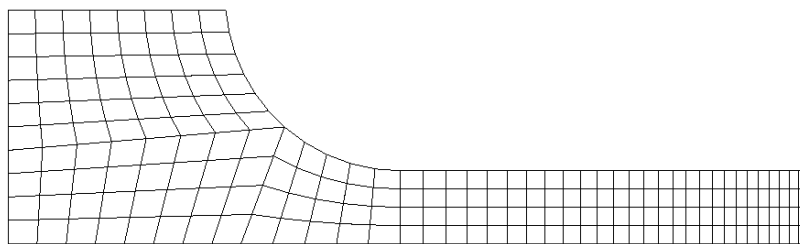
Figure 5.1: Mesh of specimen used in material tests.

5.2.2 DIC vs. EUROPLEXUS

The displacement values logged by the machine were inaccurate. In addition, the physical extensometer was placed over the middle 50 mm of the specimen. From Figure 4.4, it can be seen that the fracture appears close to the shoulder of the specimens. This means that the physical extensometer is unable to fully record the

increase in displacement due to necking. Because of this, values recorded by the help of DIC were used.

The DIC analyses were performed in a program called eCorr. This is an in-house DIC software, developed by Ph.D. Egil Fagerholt at SIMLab, NTNU. To find comparable results between DIC and EUROPLEXUS, it was important to use displacement values recorded from approximately the same place on the specimen. To ensure that the entire necking phenomenon was included in the displacement values, a vector was drawn from one shoulder to the other in the DIC analysis. This vector had a length of approximately 88 mm. Figure 5.2 shows the vector in one of the pictures used for the DIC analysis. To get comparable results from EUROPLEXUS, displacement values were extracted from a node approximately 44 mm from the midpoint. Figure 5.3 shows the selected node highlighted in the mesh. One of the EUROPLEXUS input-files, used for the simulation of the tensile test, is included in Appendix E.1.
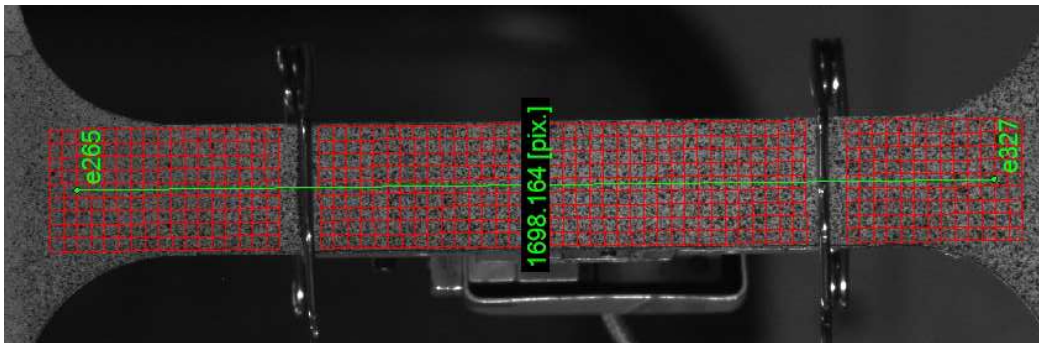
Figure 5.2: Vector used to extract displacement from DIC.
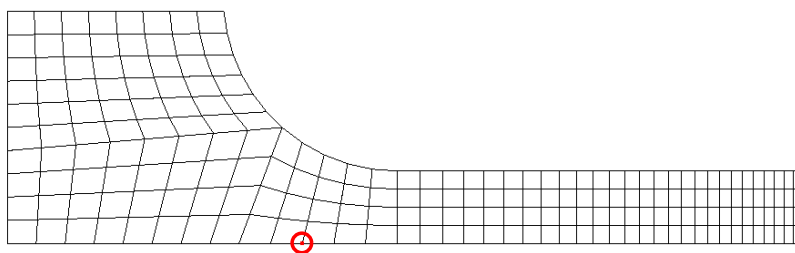
Figure 5.3: Node used to extract displacement from numerical simulations.

5.3 Results

When testing different material models, the reference strain rate, $\dot{p}_0$, was set equal to 1.0. C is usually determined by dynamic tensile tests. As no such tests were performed, it was decided set this parameter equal to a value found in the literature. C was then assumed equal to 0.014, as used in Chapter 3.

To reduce the computational time, all analyses were run with mass scaling. Initial tests indicated that EUROPLEXUS were unable to run the analyses when the strain hardening parameter, n, was set lower than 0.21. After removing the mass scaling, it turned out that the analyses were unable to run when n were lower than 0.26. Because of this, all alternatives that were tested, had n equal to 0.26 or larger.

After a lot of trial and error, several alternatives were found. Table 5.1 shows the parameters used in the different alternatives. Figure 5.4 shows the force-displacement curves found in EUROPLEXUS, compared with the results from the DIC-analysis.

Table 5.1: Material models established.

Material model	A [MPa]	B [MPa]	n	C
Spranghers et al.	110	150	0.36	0.014
Alternative 1	115	57	0.26	0.014
Alternative 2	130	55	0.50	0.014
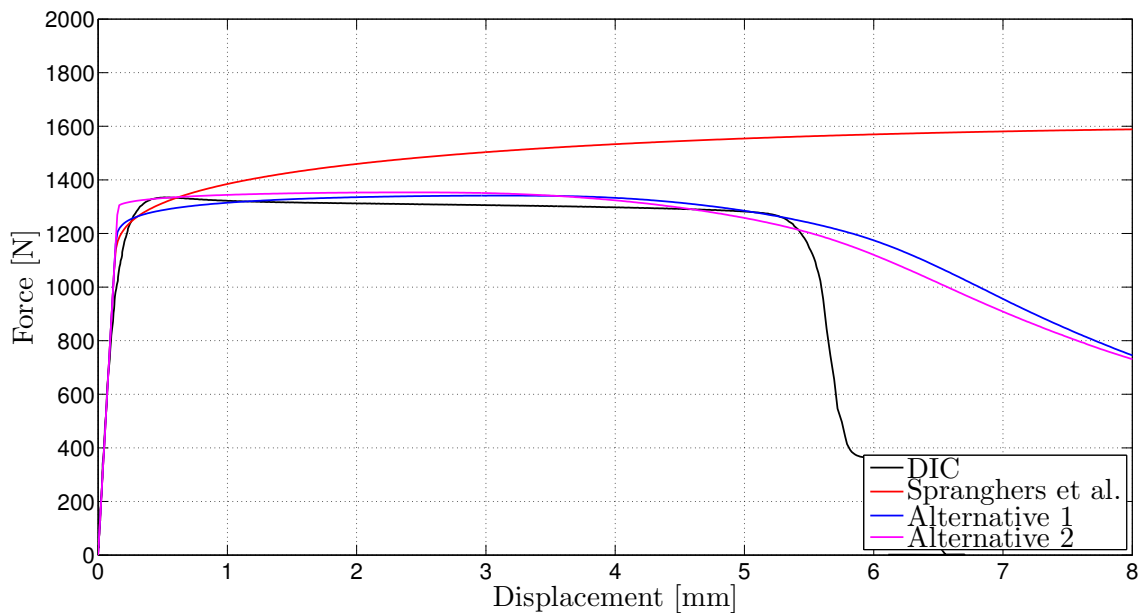
Figure 5.4: Force-displacement curves of the different material models.

From Figure 5.4, it can be seen that both alternatives give pretty good results, compared with the DIC. The material model used by Spranghers et al. [48], on

the other hand, appears to be too stiff. Looking at the employed parameter values, it can be assumed that alternative 1 is the better alternative. A reason for this is that the strain hardening parameter, n, is unusually large for alternative 2, while alternative 1 has values in a more reasonable area.

Setting the strain-rate component of the Johnson-Cook model equal to 1, only the strain dependent part is remaining. By inserting the parameters from Table 5.1 into Equation (2.43), the true stress - plastic strain curve of the material model can be plotted. Figure 5.5 shows the true stress generated by the material models. The results from the material tests have not been included in the figure, as the results from the material tests only cover very small strains. Plotting them in the same figure would render them almost invisible, due to the large strains included in the figure.
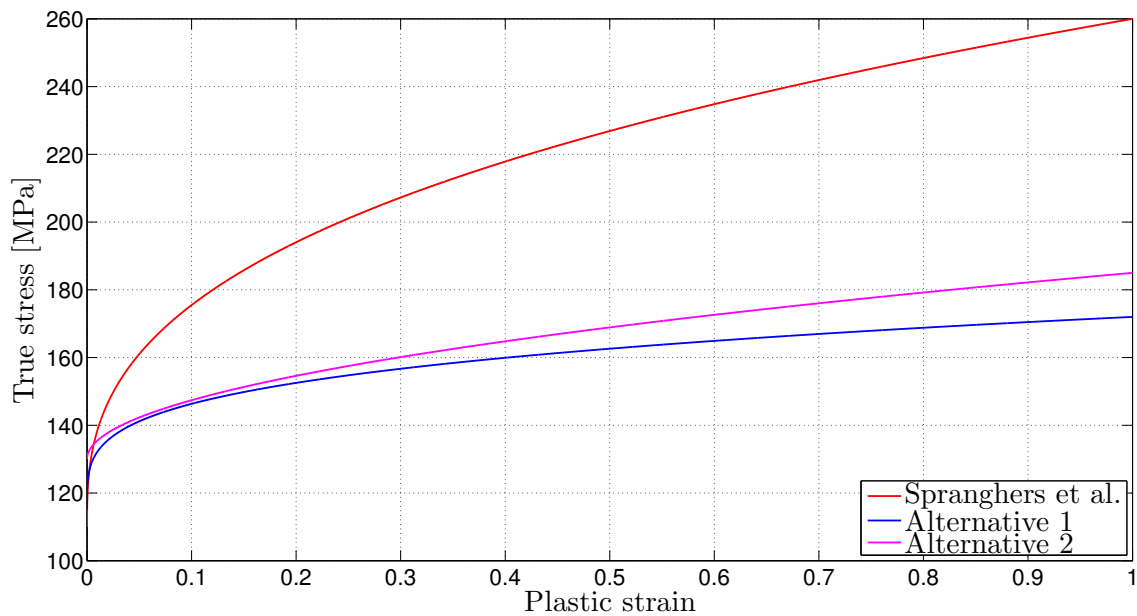
Figure 5.5: Trues stress - plastic strain curves for the material models.

From Figure 5.5, it can be seen that the behaviour of the models are a lot closer to an asymptotic behaviour than the material model used by Spranghers et al. [48]. At the same time, the material models still have a very steep slope. Because of this, it is possible that the material models are still too stiff.

Chapter 6

Numerical Simulations

6.1 Lagrange

When comparing experimental results, with results from numerical simulations, there are a lot of factors that can affect them. This can include sources of error from the experimental work, e.g. the placement of the load or deviation of the mass. In addition, there can be differences due to the material model or other parameters, like the value used for the relative effectiveness factor. To investigate the effect of some of these parameters, sensitivity studies were performed.

The test setup were the same as previously used in Chapter 3.3. It was decided to stick with an element size of 10 mm, due to the low computational time, and to keep the results comparable with the results from the FSI-analyses. In most of the simulations, the stand-off distance was kept at 500 mm. This was decided, as stand-off distance 500 mm produced neither fracture, nor counter-intuitive behaviour. The load is still generated by the help of the AIRB command in EUROPLEXUS.

6.1.1 Material Models

Procedure

In Chapter 5.2, two potential material models were established. It was concluded that alternative 1 probably was the most suitable. However, it would still be interesting to see how the other material models affect the results of the numerical simulations. Because of this, simulations were performed with the established material model from Chapter 5, as well as the material model presented by Spranghers et al. [48]. All the material models, as well as the Johnson-Cook parameters, are listed in Table 6.1.

Table 6.1: Material models evaluated.

Material model	A [MPa]	B [MPa]	n	C
Spranghers	110	150	0.36	0.014
Alternative 1	115	57	0.26	0.014
Alternative 2	130	55	0.50	0.014

Results

Figure 6.1 shows the midpoint displacement, plotted against time for all the analyses. In addition, the midpoint displacement from plate A22 is included for comparison.
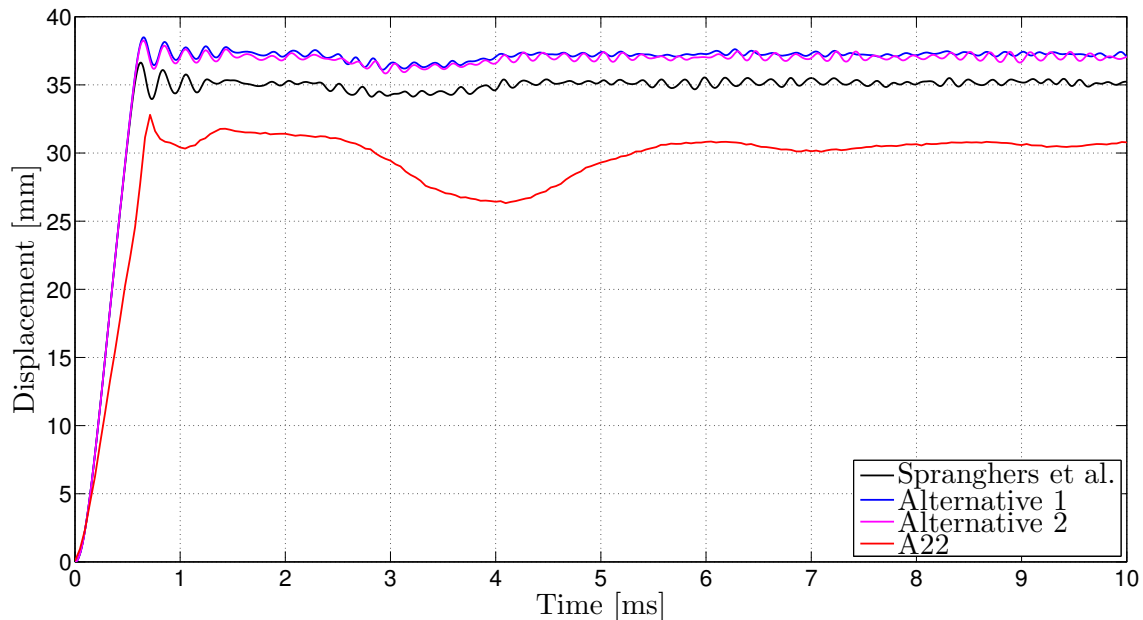
Figure 6.1: Displacement at midpoint with different material models.

From Figure 6.1, it can be seen that all material models give larger deformations than observed in the physical experiments. Alternative 1 and Alternative 2 give almost identical results, while the material model used by Spranghers et al. [48], gives slightly smaller deformations. Despite the fact that the material model used by Spranghers et al. [48] produces displacements closer to the experimental values, it was decided to stick with the material models established in Chapter 5.3. This was decided because the inverse modeling indicated that Alternative 1 and 2 had a behaviour closer to the actual material behaviour. Because both Alternative 1 and 2 gave almost the same results, it was decided to stick with Alternative 1, due to the reasons mentioned in Chapter 5.3.

6.1.2 Boundary Conditions

Procedure

In Chapter 4.3.3, it was observed that the plates slided along the supports close to the pressure transducers. In the area around the bolts however, very little deformations were visible. Based on this, it can be assumed that the boundary conditions of the plates were somewhere between fixed and simply supported. In order to investigate the effect of the boundary conditions, it was decided to model the plate, both as fixed and as simply supported.

When modeling the plate as fixed, the setup was kept the same as in previous simulations. In the case of modeling a simply supported plate, it was decided to neglect all effect from the clamping frame, besides preventing displacements out of the plane. It was decided to only include effects from the bolts, when restricting in-plane displacements. As the pressure transducers were made of plastic, it is unlikely that they would be able to prevent much deformation anyway. Because of this, it was decided to ignore them.

Figure 6.2 shows the mesh that were used when modeling the simply supported boundary conditions. The middle 300x300mm^2 section of the plate, was modeled as when fixed. That means the mesh is made up of Q4GS shell elements. The surrounding frame was meshed with triangular shell elements. This was done in order to model the holes in the plate as circular as possible, without having to use extremely small elements. The element type employed in EUROPLEXUS, is called T3GS. This is a 3-node, thick shell element, with one integration point in the plane. T3GS is considered to be the best suited element, in combination with the Q4GS element [46].
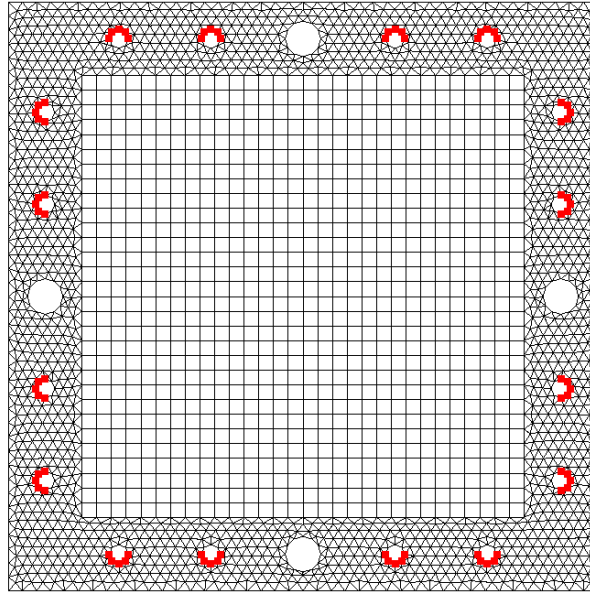
Figure 6.2: Mesh when using simply supported boundary conditions.

In Figure 6.2, some of the nodes around the holes have been marked in red. These nodes have been fixed in all directions. Because the bolts would prevent displacement of the outer edge of the holes, it has been assumed that the selected nodes do not change their position. This simplification makes it redundant to model the actual bolts. The other side of the bolt holes are still free to move in the plane.

All the nodes in the outer frame has been restricted against movement out of the plane. This was done to represent the restriction made by the clamping frame. This simplification has one significant weakness. Because the nodes are restricted against movement out of the plane, it means that the nodes will still be restricted, even though they move out of the area restricted by the clamping frame. As a result, the model will not be able to describe the behaviour seen at the shorter stand-off distances in Chapter 4.3.3. Despite this, the model should still give a decent basis for comparing fully fixed and simply supported boundary conditions.

A boundary condition where friction restricts the movement, would have been an interesting study. However, no tests were performed in order to determine the friction coefficient. Because of the uncertainty, it was decided not to test this possibility.

Results

Figure 6.3 shows the midpoint displacement, plotted against time, for the two different boundary conditions. The results from test A22 are included for comparison.
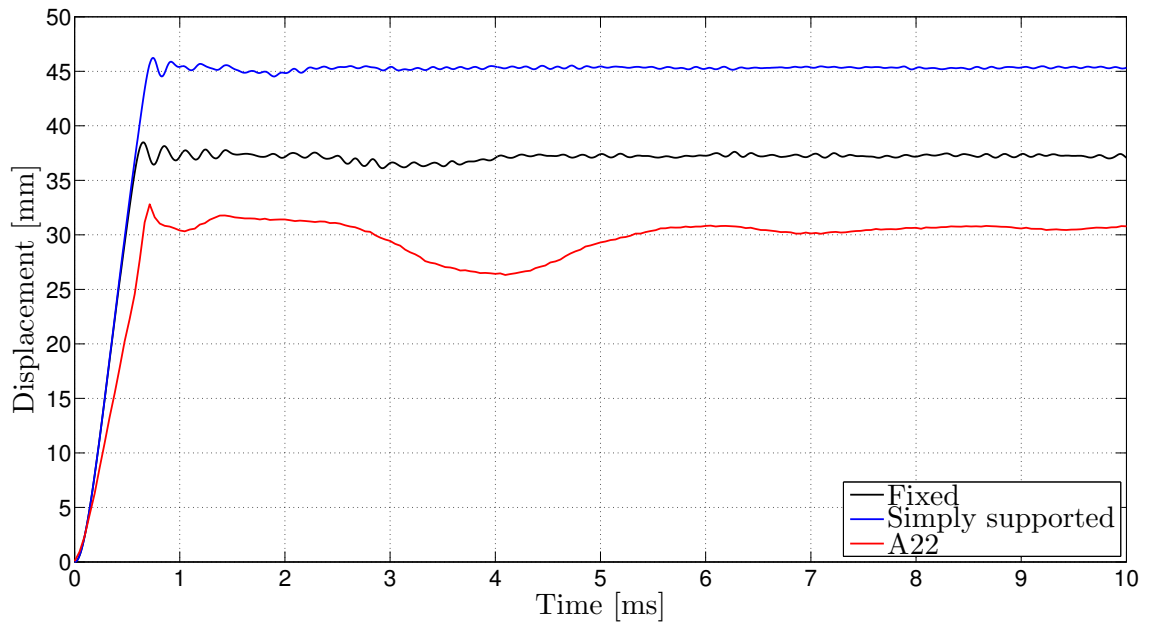
Figure 6.3: Displacement at midpoint with different boundary conditions.

From Figure 6.3, it can be seen that the midpoint displacement increases by about 8 mm when using simply supported boundary conditions. Figure 6.4 shows a projection of the deformed mesh.
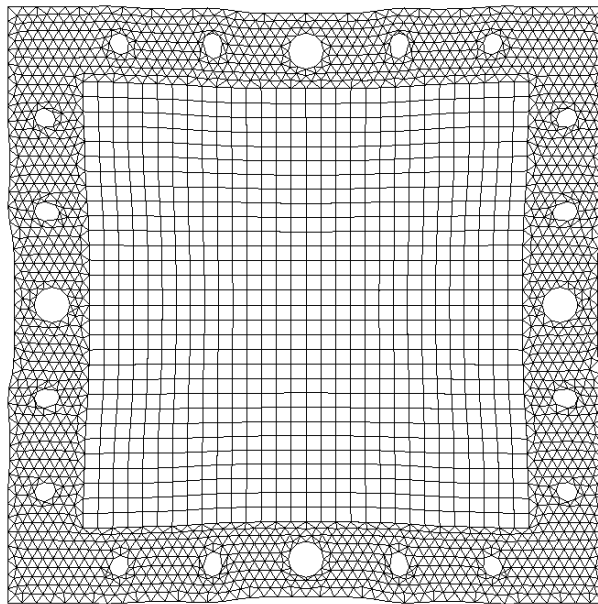
Figure 6.4: Projection of deformed mesh.

From Figure 6.4, it can be seen that the deformation around the pressure transducers are similar to what was observed in Chapter 4.3.3. The mesh is also deformed around

the bolt holes, in contrast to what was observed in the physical experiments. Because the nodes were restricted against movement out of the plane, it is possible that the deformation shown in Figure 6.3, would have been even larger if this have not been the case. Because both boundary configurations resulted in larger deformations than in the physical experiments, it was decided to stick with fixed boundaries, as this behaviour was closest to what was experienced at stand-off distance 500 mm.

6.1.3 Load Placement

Procedure

The charge was suspended by the use of a wire in the experiments. Even though the placement of the wire was closely measured, it is likely that the placement of the load had small variations between the tests. This could either be due to variation in length of the wires, the wires not being completely centered, or the shape of the charge causing the center of mass to vary. Because of this, it would be interesting to see how small variations in the load placement would affect the simulations.

It was decided to investigate the effect of placing the charge slightly closer or further away, from the plate than intended. In addition, it was decided to investigate the effect if the charge had been offset slightly to the side. Because the AIRB approach does not account for reflections from the surroundings, it is expected that the same results would be found if the charge was slightly elevated or lowered. Table 6.2 lists the investigated configurations. x is defined as the direction of the load, y is along the horizontal, and z is along the vertical. The origin is defined as the midpoint of the plate.

Table 6.2: Variations in load placement.

Alternatives	Location of charge		
	x [mm]	y [mm]	z [mm]
Reference	500	0	0
$x + 10$ mm	510	0	0
$x - 10$ mm	490	0	0
$y + 10$ mm	500	10	0

Results

Figure 6.5 shows the midpoint displacement when varying the location of the charge. The results from test A22 have been included for comparison.
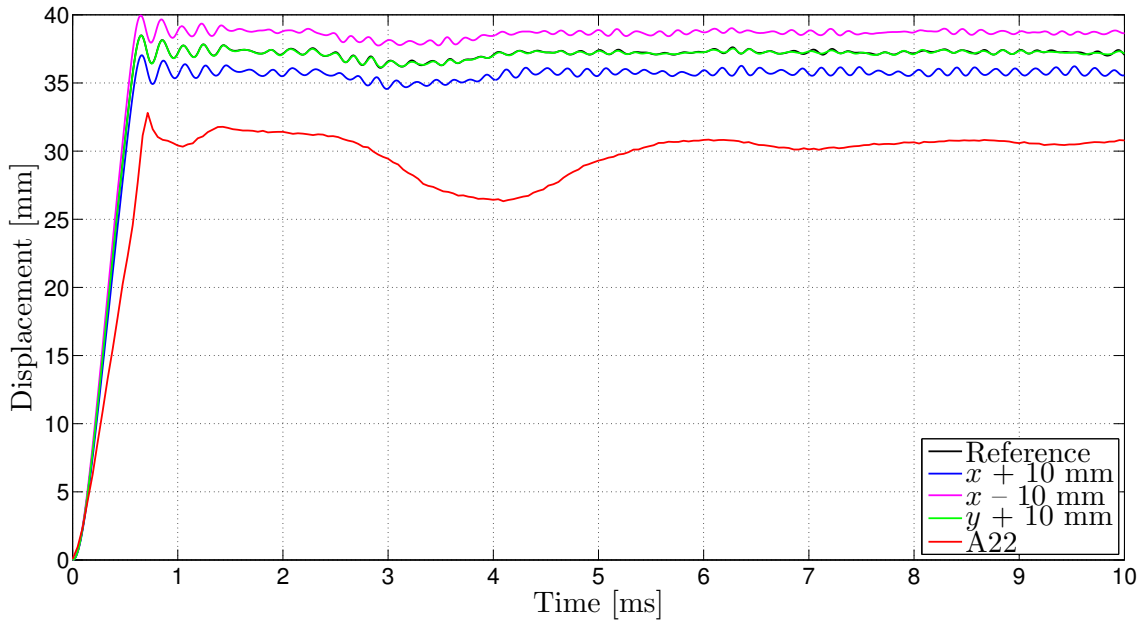
Figure 6.5: Displacement at midpoint with varying load placement.

From Figure 6.5, it can be seen that the deformations change slightly when varying the placing of the explosive charge along the x-axis. It is unlikely that the variations during the experiments were as high as 10 mm, but it is still possible that minor variations have contributed to the differences between the experiments. At the same time, the contribution is fairly low when the variations are small. Because of this, it is possible that any effect from varying the load placement may be neglected compared to other factors.

By varying y and keeping x constant, it can be seen that the displacement curve almost completely overlaps the reference curve. In order to investigate this further, the 2D cross-section were plotted at different time steps up to maximum displacement. Figure 6.6 shows the 2D cross-section along the y-axis at different time steps. The cross-sections from alternative "$y + 10$ mm" have been mirrored in order to visualize the corresponding curves for a theoretical case of "$y - 10$ mm".
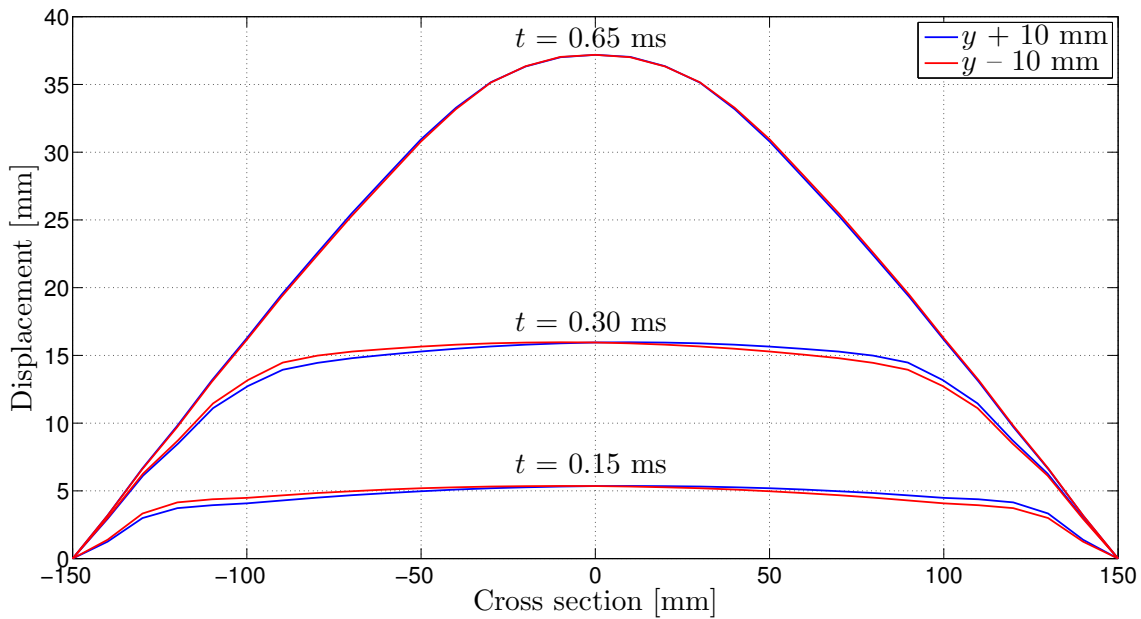
Figure 6.6: Cross section with off-center load at different time steps.

From Figure 6.6, it can be seen that there are variations in the cross-sectional displacement during the deformation. As the displacement gets closer to maximum, the differences disappear. The reason for this seems to be that the deformations follow the yield lines. That means that as long as the load is large enough to produce yield lines all the way to the midpoint, the final deformations should be fairly symmetric, even though the load is slightly off-centered.

6.1.4 Relative Effectiveness Factor

Procedure

Literature reports different values for the relative effectiveness factor for C4. The values used can vary a lot. CONWEP uses 1.190 or 1.370 depending on whether it is the impulse or the peak pressure that is of interest [13]. The most common value however, is 4/3. The relative effectiveness factor has been discussed in Chapter 2.2.2. In order to investigate the effect of the relative effectiveness factor, it was decided to perform simulations with the most common value, as well as the values used by CONWEP. Table 6.3 lists the alternatives that were investigated.

Table 6.3: Alternative relative effectiveness factors.

Alternatives	Relative effectiveness factor	Mass [g]
Standard	4/3	40
Min	1.190	35.7
Max	1.370	41.1

In order to compare the differences in pressure, additional sets of simulations were carried out. In addition to the normal simulations, with stand-off distance 500 mm, a second set with stand-off distance 515 mm were performed. This was done in order to get the same stand-off distance used in the calibration tests in Chapter 4.3.2. In that way, the results from the calibration tests could be used as comparison.

Results

Figure 6.7 shows the midpoint displacement, for the different relative effectiveness factors. The results from test A22 have been included for comparison.
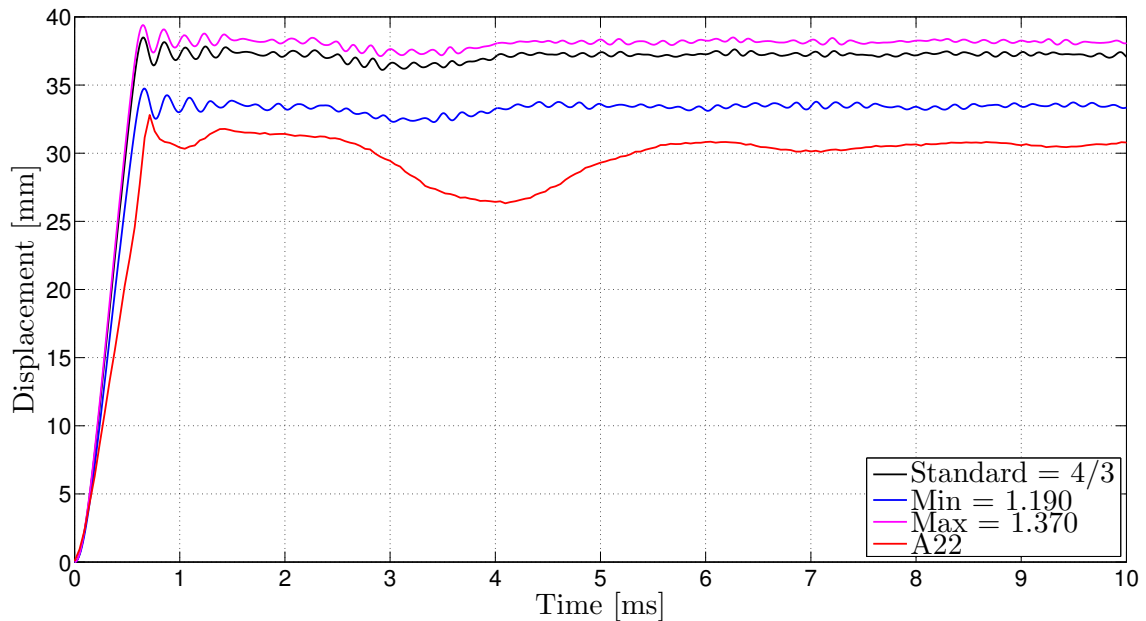
Figure 6.7: Displacement of midpoint with different relative effectiveness factors.

In Figure 6.7, it can be seen that the displacement increases, as the mass increases. The increase when using a relative effectiveness factor of 1.370 is only about 1 mm. Using 1.190 however, decreases the displacement quite a lot.

The curves in Figure 6.7 can also give an indication of what would happen if there were slight variations is mass. As the loads in the experiments were created by hand,

it is likely that this was the case. Looking at the standard curve, compared to the max curve, it can be seen that an increase of about 1 g in mass, would increase the displacement with about 1 mm. Based on this, it is possible that variations in mass have been a contributing factor to the variations in the displacements from the experiments in Chapter 4.3.3.

To investigate the pressure generated by the different relative effectiveness factors, the pressure at the midpoint was plotted against time. This can be seen in Figure 6.8. The pressure from pressure transducer 1 in test R33-2, has been included for comparison.
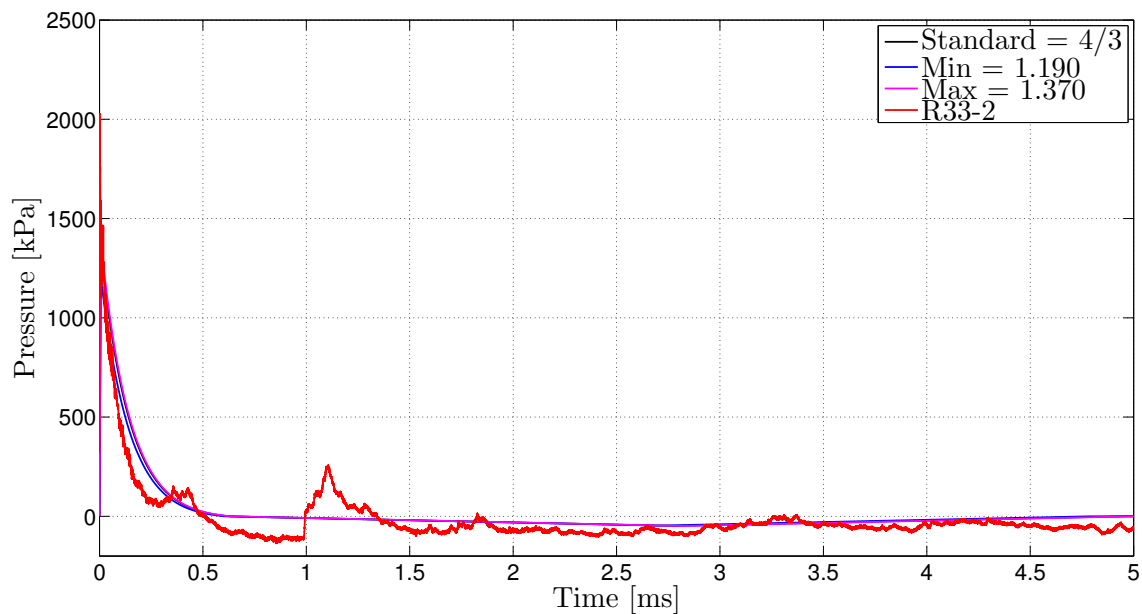
Figure 6.8: Pressure in the middle with different relative effectiveness factors.

From Figure 6.8, it can be seen that the pressure curves generated from the three different relative effectiveness factors, are fairly similar. The curve from test R33-2 declines faster than the curves from the simulations, but the second peak, hitting the plate at around 0.3 ms, makes up for some of the difference. In order to get a closer look at the difference in peak pressure, it is necessary to zoom in on a smaller area. Figure 6.9 shows a close-up view of the peaks of the pressure curves.
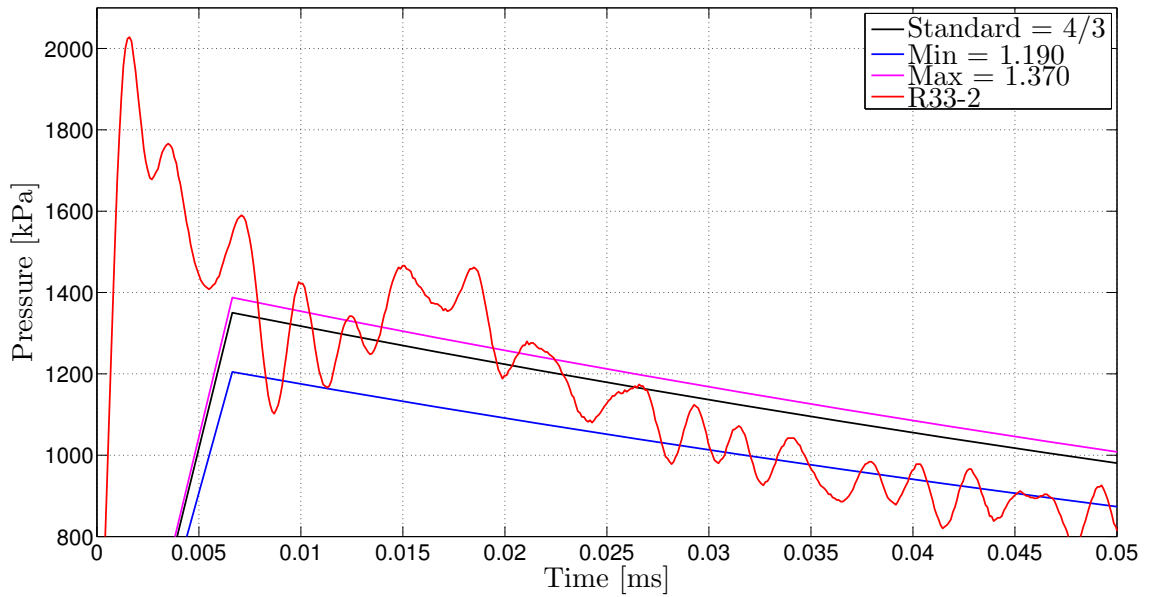
Figure 6.9: Close-up view of the peaks of the pressure curves.

From Figure 6.9 it can be seen that the peak pressure is lower than in the experiment for all the simulations. Note that the peak pressure is a little higher in the simulations than shown in the figure. Due to the size of the time steps, the peak value is not registered in the plots. The peak pressures shown in the figure, does not explain why the displacement from the simulations are larger than from the experiments. To investigate further, the positive impulse were calculated from the curves. The resulting values are listed in Table 6.4.

Table 6.4: Positive impulse with different relative effectiveness factors.

Alternatives	Positive impulse [kPa·ms]
Standard	180.8
Min	159.4
Max	186.5
R33-2	142.8

In Table 6.4, it can be seen that the positive impulse is higher in the numerical simulations than in the physical experiments. This is the case, even when using the lowest value for the relative effectiveness factor, and including additional peaks as part of the positive impulse for the physical experiments. Based on this, it is possible that EUROPLEXUS overestimates the deformations because the AIRB approach generates an impulse that is too high compared to the physical experiments. In order to say more about this, it is necessary to investigate the pressure distribution over the whole plate.

6.2 Pressure Distribution from the AIRB Approach

In Chapter 6.1.4 it was observed that the impulse generated from AIRB was too large compared to the experimental results. In order to investigate the distribution of the pressure over the plate, it was decided to simulate the calibration tests when using AIRB, and then compare the pressure at the different stand-off distances.

6.2.1 Procedure

In order to simulate the calibration tests, Lagrangian analysis were performed at all stand-off distances. The model used was the same as in Chapter 6.1.4, with a relative effectiveness factor of 4/3. Because of the way the calibration plate were installed, the stand-off distance increased by 15 mm. Because of this, the simulations had to be run at the stand-off distances listed in Table 6.5.

Table 6.5: Stand-off distances when simulating the calibration tests.

Stand-off distance [mm]
265
390
515

When comparing results between the simulations and the experiments, it was decided to compare the pressure transducers in the plate, and ignore the ones in the frame. The elements shown in Figure 6.10 were selected in order to extract the pressure.
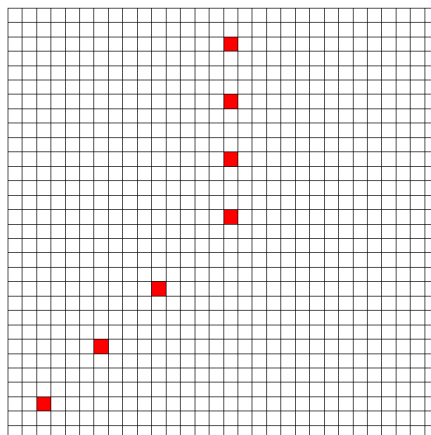
Figure 6.10: Elements selected in order to extract pressure corresponding to pressure transducers.

6.2.2 Results

Figure 6.11, Figure 6.12 and Figure 6.13, show the pressure plotted against time for stand-off 265 mm, 390 mm and 515 mm respectively.
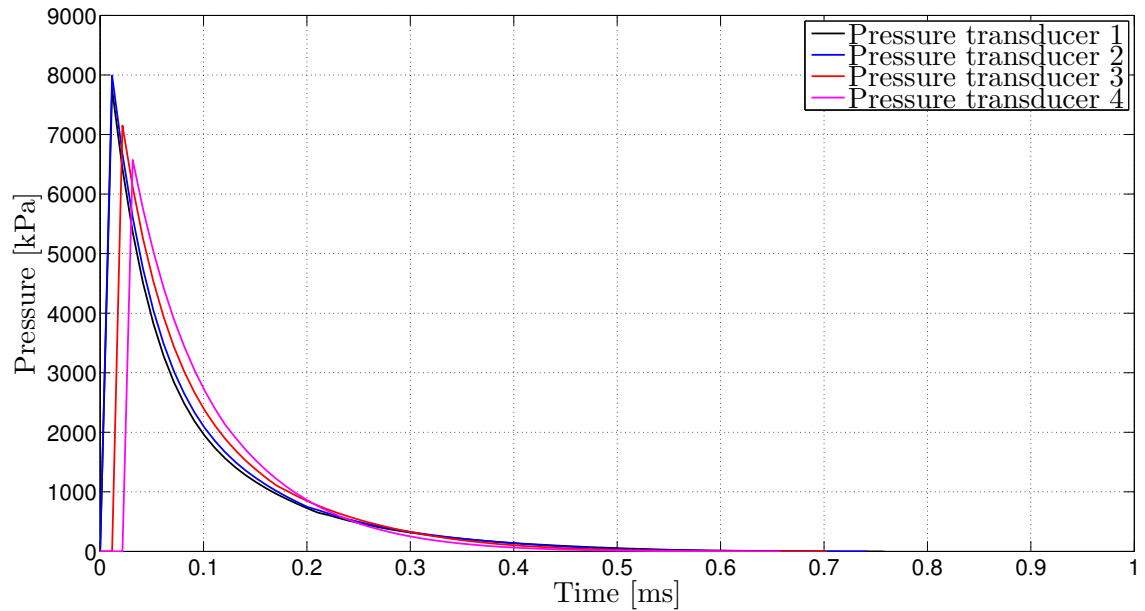
(a) Pressure transducers along the vertical.
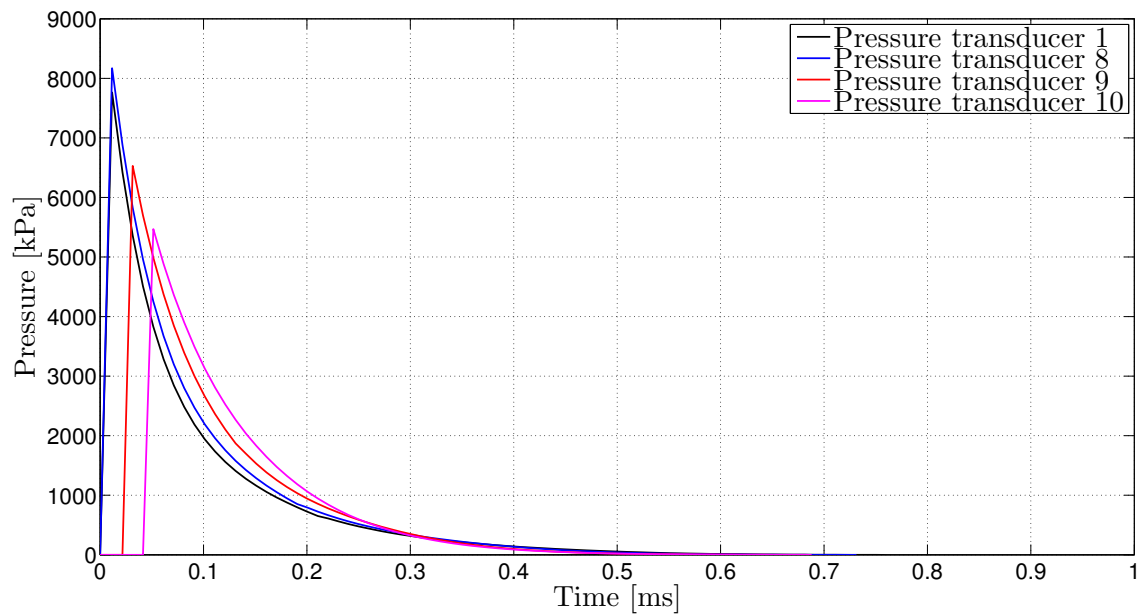
(b) Pressure transducers along the diagonal.

Figure 6.11: Pressure curves from simulation at stand-off distance 265 mm.
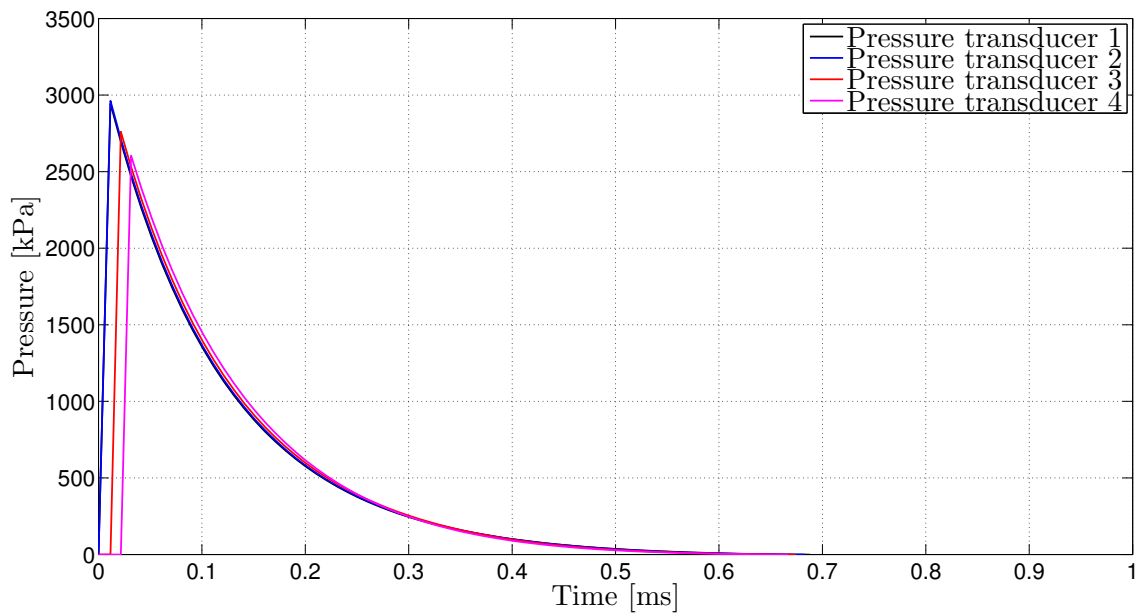
(a) Pressure transducers along the vertical.
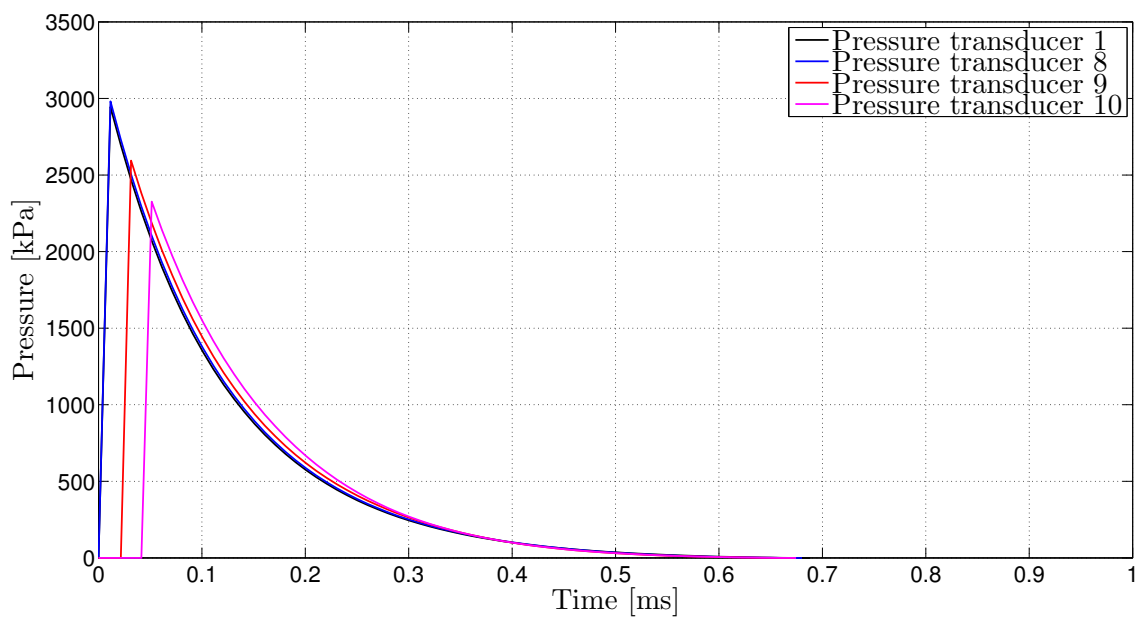
(b) Pressure transducers along the diagonal.

Figure 6.12: Pressure curves from simulation at stand-off distance 390 mm.
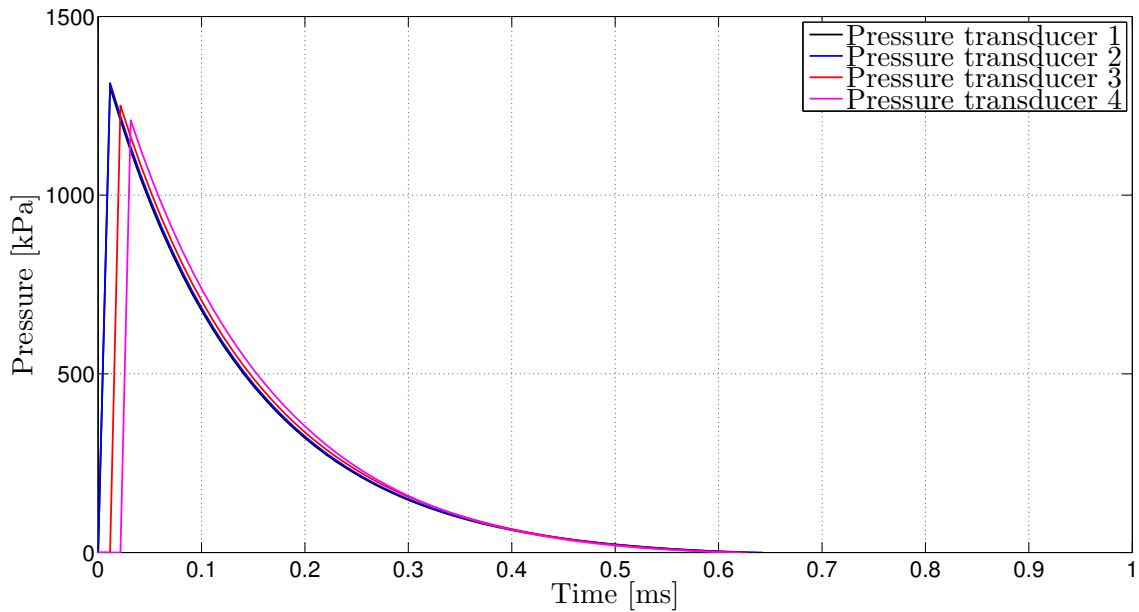
(a) Pressure transducers along the vertical.
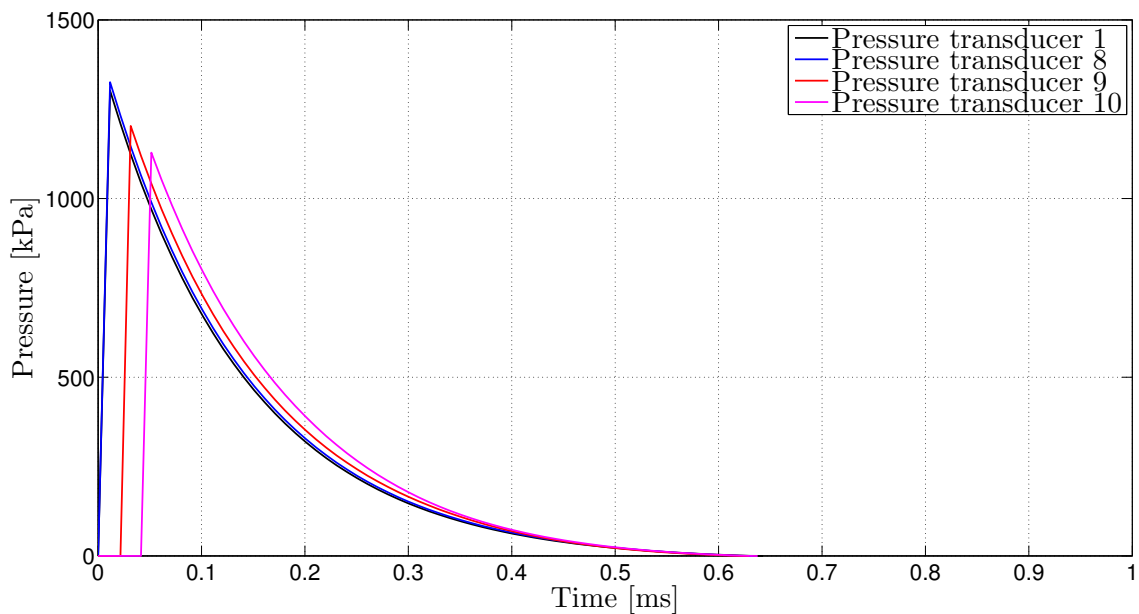
(b) Pressure transducers along the diagonal.

Figure 6.13: Pressure curves from simulation at stand-off distance 515 mm.

From the figures, it can be seen that the time of arrival increases and the peak pressure decreases when moving away from the center of the plate. Note that the peak pressures of pressure transducer 1 did not register due to the time step when logging the results. As a result, it may seem from the figures that the peak pressure is lower in pressure transducer 1 than in pressure transducers 2 and 8. This is not the case though, but only a miss caused by the logging frequency.

In order to get an impression of the load, compared to the calibration tests, the positive impulse was calculated. Table 6.6 lists the positive impulse for pressure transducer 1, 2, 3, 4, 8, 9 and 10 for the three simulations, as well as for test R13, R23 and R33-2.

Table 6.6: Positive impulse from simulations and experiments.

Experiment/Simulation	Positive impulse in pressure transducers [kPa·ms]						
	1	2	3	4	8	9	10
R13	233.3	220.4	236.8	246.3	190.6	234.2	334.4
AIRB - 265 mm	605.3	632.8	596.7	560.5	658.0	577.3	512.6
R23	170.9	156.4	159.6	178.7	157.1	200.0	230.8
AIRB - 390 mm	352.8	355.7	329.9	309.2	358.6	311.8	279.2
R33-2	142.8	139.0	133.9	142.4	142.6	128.8	176.1
AIRB - 515 mm	177.4	179.5	170.1	163.6	181.6	164.5	154.5

From Table 6.6, it can be seen that the differences, between experiments and simulations, get smaller as the stand-off distance increases. The results from the experiments show an increase in positive impulse from pressure transducer 8 to pressure transducers 9 and 10. This is possibly due to accumulation of pressure in the corner, and is therefore not representative of the load under ideal conditions. Based on this, the AIRB approach seems to generate pressure that corresponds well with actual experiments when the stand-off distance increases past 500 mm. At distances shorter than 500 mm however, the load is overestimated a lot.

6.3   FSI

In Chapter 4.3.3 it was observed that most of the deformations of the plate happened after the positive load was finished. This means that the impulse from the blast only initiates the deformations, while the inertia keeps the deformation going. Based on this, it can be assumed that there is little fluid-structure interaction in the physical experiments. In Chapter 6.1 it could be seen that the simulations with the AIRB approach in EUROPLEXUS overestimated the displacements of the plate. It is possible that the other methods explained in Chapter 2.11.5 can give a better representation of the loading. FSI-simulations are therefore performed as both the GAZP approach and JWL approach require FSI in order to represent the loading.

6.3.1   Mesh-Sensitivity

FSI-simulations are mesh-sensitive, and smaller element size will usually give more accurate results [59]. As cubic elements are used, the number of elements will increase cubically when decreasing the element size. In addition, the critical time steps will decrease with the element size. Combined, this can result in a considerable increase in the computational time. In order to find the element size best suited for FSI-simulations, a mesh-sensitivity study were performed.

Procedure

Before running the simulations, a proper model has to be created. In the following section, the x-axis will be assumed out of the plate, the y-axis will represent the horizontal axis and the z-axis the vertical axis. The origin is assumed at the midpoint of the plate.

By ignoring all the surrounding area, the setup presented in Chapter 4.3.1 can be assumed symmetric over the xz-plane. Because of this it could have been possible to model the setup with symmetry conditions over this plane. It would not have been possible to model with symmetry conditions over the xy-plane. The reason for this is that the floor will work as a reflecting boundary while the pressure can pass freely over the top of the frame. Despite the possibility of symmetry, it was decided to model the whole plate. This was done in order to make it possible to investigate the effect of non-symmetric loading or other non-symmetric influences.

The model was created by the help of Cast3M. The Cast3M-file used to generate the mesh is included in Appendix D.2.

The plate was modeled the same way as in Chapter 6.1, with Q4GS elements. The frame was modeled as seen in Figure 6.14. Around the frame, 200 mm of air was included. 300 mm of air was modeled at the back of the plate in order to include possible suction effects from the back. The amount of air included in the front of the

plate was dependent on the stand-off distance used, and how the explosive charge was modeled. When modeling the fluid with 25 mm elements, and the charge as shown in Figure 6.15d, 625 mm of air was included in the front of the frame. The fluid mesh was modeled as finite volumes. All elements used for both the fluid and the explosives, were assigned the element type CUVF in EUROPLEXUS. This is a 3D cubic finite volume element, that is defined as cell centered [46]. The frame and the floor were modeled as reflecting boundaries, while the remaining sides of the fluid mesh were modeled as absorbing boundaries. The absorbing boundaries were assigned the CL3D element type.

(a) Seen from the front.

(b) Seen from the side.
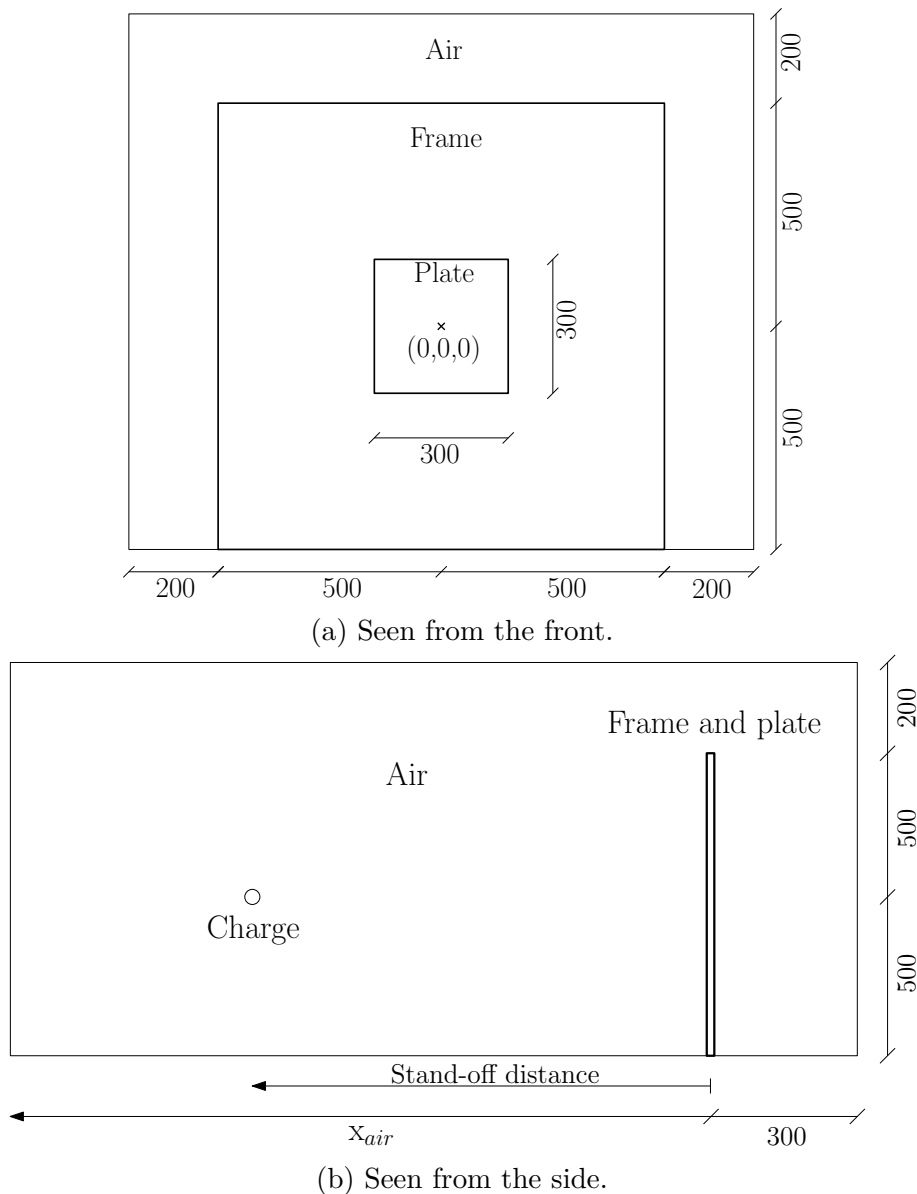
Figure 6.14: Geometry used in numerical model. Measures in mm.

Figure 6.15 shows the finished mesh when using element size 25 mm. In Figure 6.15a, the plate is marked in red. In Figure 6.15c, the plate is marked by a thick black line, while the explosive charge is marked in red. Figure 6.15d shows a close-up view of the explosive charge. The charge was modeled with the same dimensions as used in Chapter 4.3.3. This means that the explosive charge was modeled as a sphere with diameter 34.5 mm. In order to model the charge properly, smaller elements were used for the charge than for the rest of the model. A transition zone was made around the sphere, eventually leading out to the regular fluid mesh. As the elements in the center of the charge were really small, the critical time step would be very low. In order to prevent this, a EUROPLEXUS command called PART, was activated. This command makes the analysis pay more attention to the smaller elements without carrying out useless computation on the big ones [46].

(a) Plate and frame

(b) Fluid mesh

(c) Cut through middle showing plate and explosive charge.

(d) Closeup of explosive charge.
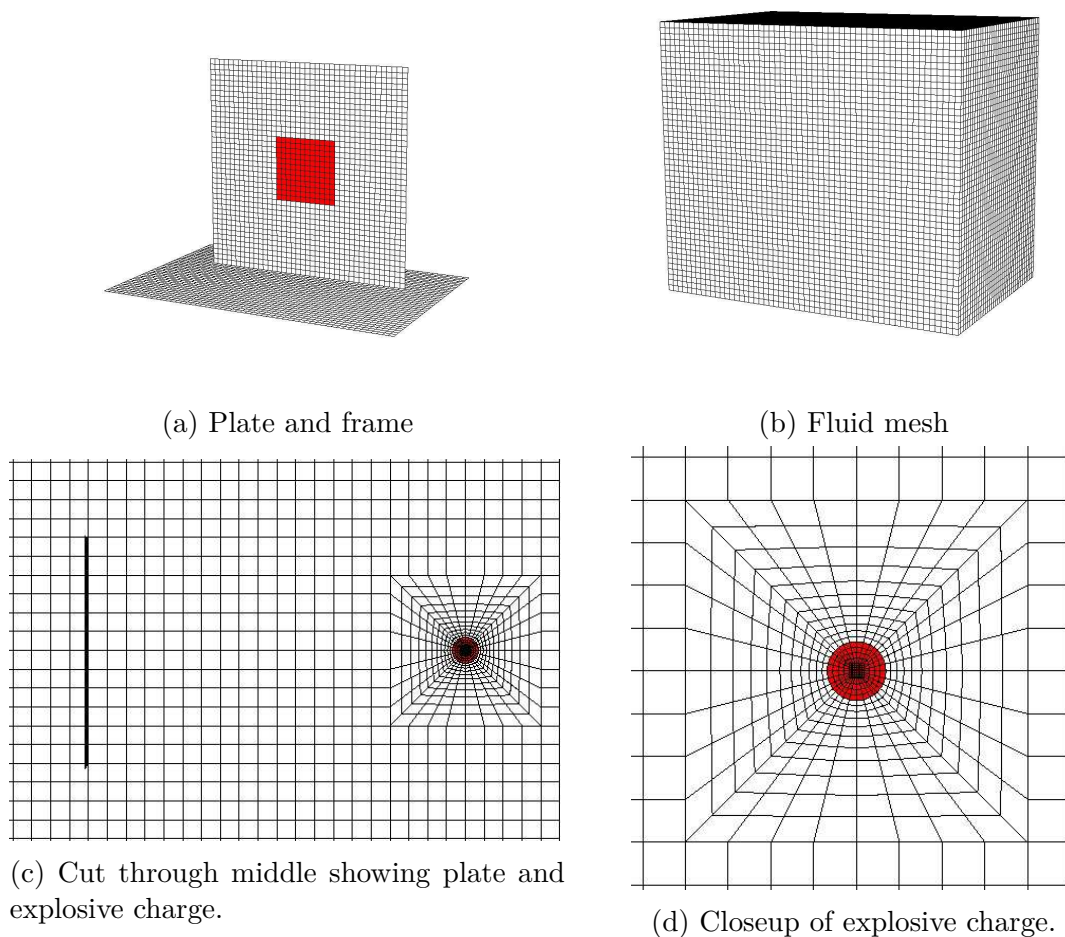
Figure 6.15: Mesh in FSI-model.

The loading was simulated by the use of the GAZP command in EUROPLEXUS. This method is explained in Chapter 2.11.5. The input parameters had to be calculated by the help of the equations explained there. The value used for γ was set to

143

1.4 [59]. The values used for p_0 and ρ_0 are the same as used by Larcher et al. [36]. Due to the way the explosive charge is modeled, the volume of the balloon, V_{bal}, is the volume used in the experimental work. Table 6.7 lists the parameters used in the model, as well as parameters necessary to compute them.

Table 6.7: Parameters used in the GAZP model.

Parameter	Value
E_{TNT} [J]	180800
p_0 [Pa]	10^5
ρ_0 [kg/m^3]	1.3
V_{bal} [m^3]	$2.15 \cdot 10^{-5}$
γ	1.4
p_{bal} [Pa]	$2.05 \cdot 10^{10}$
ρ_{bal} [kg/m^3]	588.1

From Chapter 4.3.3, it could be seen that the transition from positive to negative displacement during the counter-intuitive behaviour, ended at around 5 ms. In order to make sure that the displacement has stabilized, the simulations should be run a little longer. Because of this, it was decided to use 10.5 ms as the total time interval simulated.

The simulations performed in Chapter 6.1, used a mesh with element size 10 mm. This was done as this was the element size expected to be used in the FSI-simulations. Initial tests discovered that the computational time with 10 mm elements was very high, which made it necessary to investigate the use of larger elements. Because the loads had stand-off distances of 375 mm, 500 mm and 625 mm, it was desired that the stand-off distance was dividable by the element size. This meant that 25 mm elements and 5 mm elements were the best possibilities. 10 mm would also work well, but would make it harder to model identical loads at the three stand-off distances. Table 6.8 lists the element sizes that were tested in the end. It was planned to test element size 5 mm as well, with the plate using both 5 mm elements and 10 mm elements. However, this was not done due to lack of time.

Table 6.8: Element sizes evaluated.

Element size [mm]
25
10

The simulations were run with the embedded FSI approach. This means that the plate can deform freely within the fluid mesh. Embedded FSI approach is explained in detail in Chapter 2.11.4. The EUROPLEXUS input-file used for this analysis is included in Appendix E.3.

Results

When testing, it was apparent that the computational time increased more than expected for the mesh with element size of 10 mm. Due to lack of time, it was decided to stop the calculation when the displacement passed the maximum point. Because of this, the total time interval simulated was only 1 ms.

Figure 6.16 shows the midpoint displacement from the two simulations. The results from test A22 have been included for comparison. Note that the curve from the experiment has been adjusted so that the displacement starts in the origin. This was done as the displacements from the simulations start a lot earlier than for the experiment when not corrected.
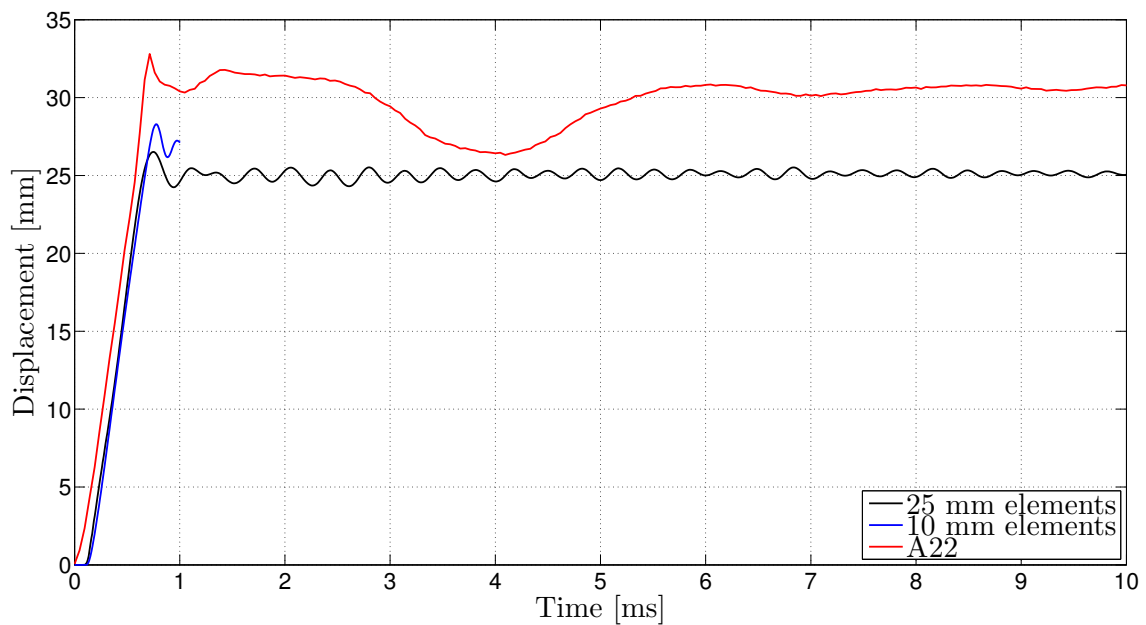
Figure 6.16: Displacement at midpoint with different element size.

From Figure 6.16, it can be seen that maximum displacement increases by about 1.8 mm when using 10 mm elements compared with 25 mm elements. Both element sizes still show lower displacements than the experiments. This is different from the Lagrangian simulations performed in Chapter 6.1, as the simulations there produced larger displacements than the experiments. If the displacement continue to increase when reducing the element size further, it is possible that the displacement would be fairly similar to the experiments.

The simulation with element size 10 mm was run for a shorter time interval. Table 6.9 lists the computational times for the two analyses.

Table 6.9: Computational time with different element sizes.

Element size [mm]	Total time interval simulated [ms]	Computational time [hh:mm:ss]
25	10.5	05:12:31
10	1	35:39:22

It should be noted that the computational times listed in Table 6.9, are not directly comparable. The simulation with element size 25 mm, was run at a computer which was used for other work at the same time. As the computer was not powerful enough to run the analysis with element size 10 mm, this analysis had to be run at a more powerful computer.

The computational time with element size 10 mm would be almost 70 times as large, if the time continued to increase at the same rate. The reason for this is most likely a combination of an increased number of elements, as well as a lower critical time step due to smaller element size. The elements at the center of the explosive charge gets particularly small. Another way of modeling the explosive charge could therefore give much improvement to the computational time.

The version of EUROPLEXUS used for the simulations, did not support Massively Parallel Processing (MPP). If this option had been available, it would have been possible to decrease the computational time substantially. With the current version, even using a model employing symmetry, the computational time would be unreasonably high at element size 10 mm or lower. Because of this, it was decided to stick to an element size of 25 mm for the FSI-simulations.

6.3.2   Load Shape

Modeling the explosive charge with exact dimensions, results in very small elements in the center of the explosive charge. This increases the computational time, and it is therefore interesting to see whether it is possible to model the explosive in a more efficient way.

Procedure

When testing different load shapes, it was decided to keep the stand-off distance constant at 500 mm. In addition, it was decided to stick with 25 mm elements in order to reduce the computational time needed for each simulation. The volume of the load, was kept as close to the actual volume as possible. Figure 6.17 shows the different load shapes that were investigated. The figures presented are vertical cross sections.

(a) Big box

(b) Small box with transition zone

(c) Small sphere with transition zone

(d) Detail
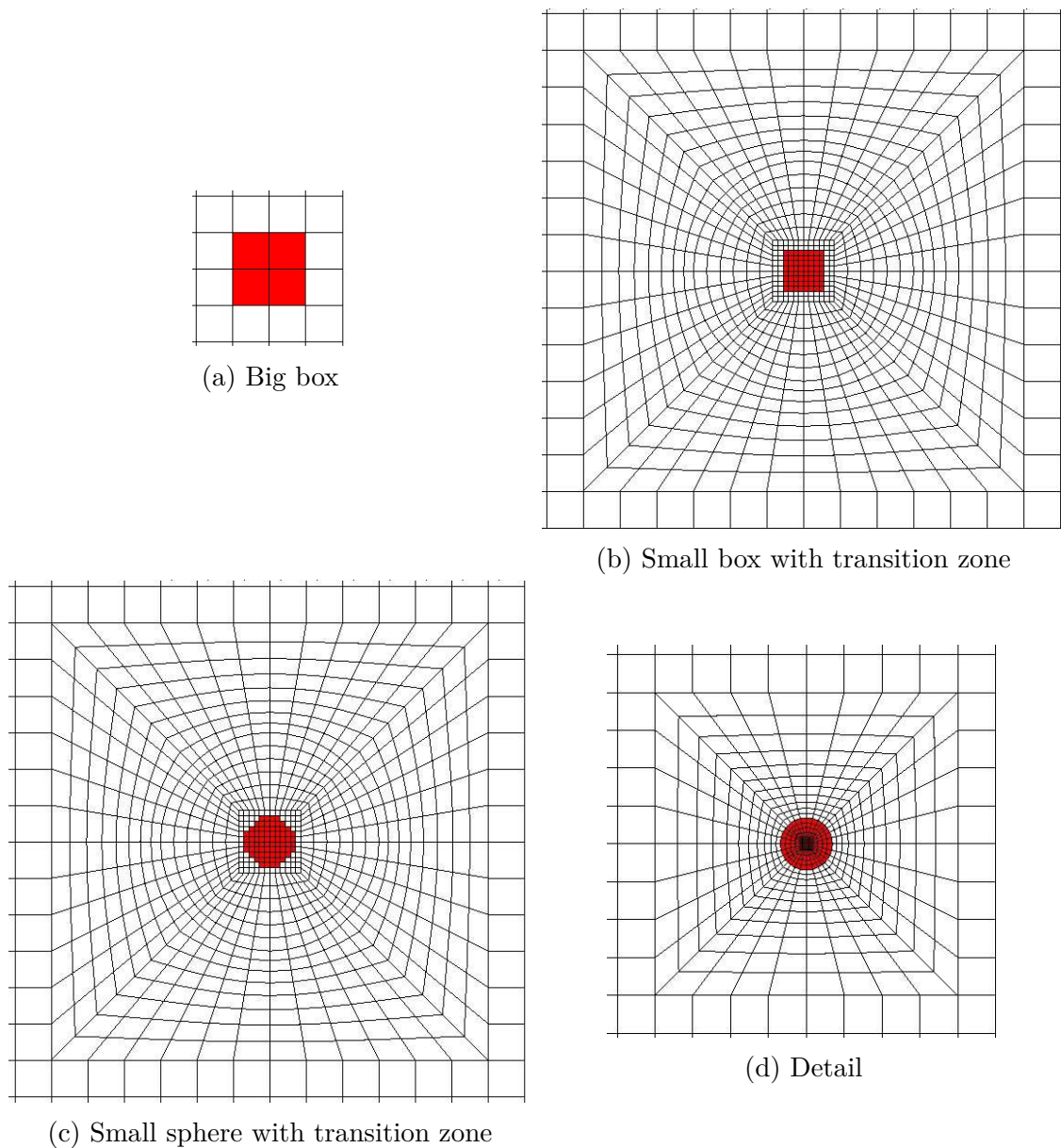
Figure 6.17: Different load shapes investigated.

The alternative presented in Figure 6.17a, was made up of 8 elements with element size of 25 mm. This was the lowest possible number of elements to use, if the load was going to be symmetrical.

Figure 6.17b is based on the mesh in Figure 6.17d. In order to model a box with correct volume, the transition zone, as well as the cubic mesh in the center of the charge, were expanded. The cubic mesh was expanded such that it was possible to model the explosive charge as different shapes, with correct volume. In order to get the correct volume, the small box presented in Figure 6.17b, was composed of 512 elements with element size 3.4758 mm.

The mesh presented in Figure 6.17c, is similar to the one in Figure 6.17b. Instead of modeling the charge as a box, the elements were selected by the help of the COND SPHERE command in EUROPLEXUS. This command selects all elements within a sphere defined by a radius and a center point. By using the correct radius in the same mesh, as for Figure 6.17b, 480 elements were selected. In order to get the correct volume, the element size was increased to 3.5514 mm.

The fluid mesh were modeled such that there was one row of 25 mm elements along the absorbing boundary, in the back of the model. That means the length, x_{air}, shown in Figure 6.14b, is equal to 550 mm for the the alternative in Figure 6.17a, 675 mm for the alternative in Figure 6.17b and Figure 6.17c, and 625 mm for the alternative shown in Figure 6.17d.

Table 6.10 shows the volumes of the charges, as well as the GAZP parameters used in the simulations. The GAZP parameters were calculated by the equations presented in Chapter 2.11.5.

Table 6.10: GAZP parameters for different load shapes.

Alternative	V_{bal} [mm^3]	γ	p_{bal} [Pa]	ρ_{bal} [kg/m^3]
Big box	$1.25 \cdot 10^{-4}$	1.4	$1.738 \cdot 10^9$	171.4
Small box with transition zone	$2.15 \cdot 10^{-5}$	1.4	$20.467 \cdot 10^9$	588.1
Small sphere with transition zone	$2.15 \cdot 10^{-5}$	1.4	$20.467 \cdot 10^9$	588.1
Detail	$2.15 \cdot 10^{-5}$	1.4	$20.467 \cdot 10^9$	588.1

Results

Figure 6.18 shows the displacement of the midpoint, plotted against time, for all the simulations. The results from test A22 have been included for comparison.
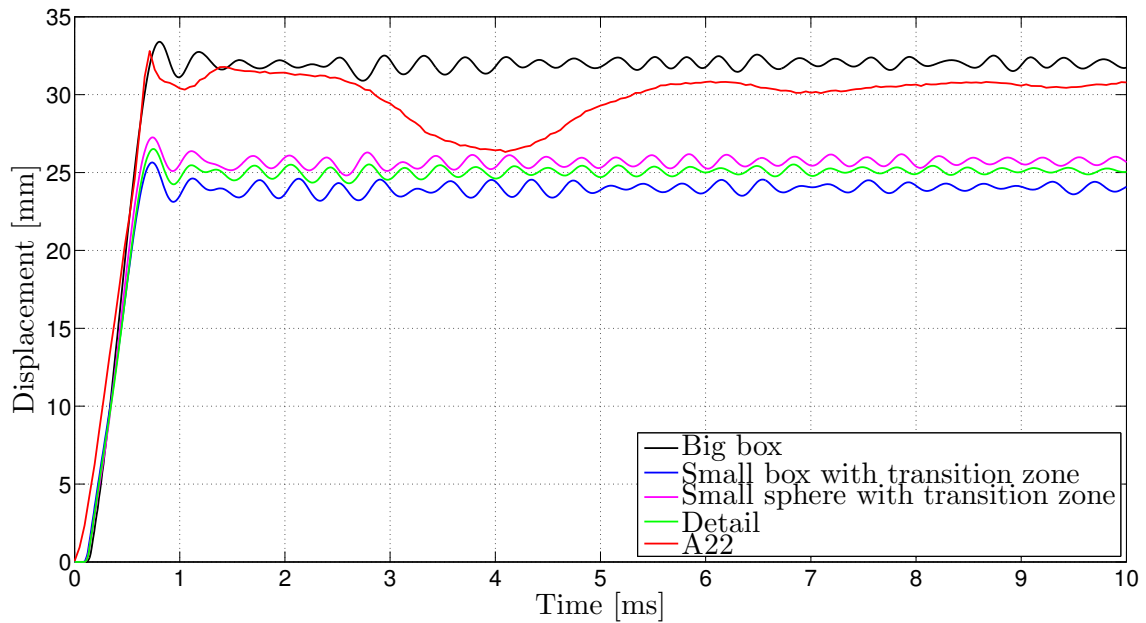
Figure 6.18: Displacement at midpoint with different load shapes.

In Figure 6.18, it can be seen that the big box model gives displacements slightly larger than the physical experiments, while the other simulations give lower displacements. While the detail results in larger displacements than the small box, the small sphere results in even larger ones. This indicates that both the volume and the shape of the charge are important for the pressure generated by the blast. In order to get a closer look at the reason for the differences in displacement, the pressure at the midpoint was plotted against time. This is presented in Figure 6.19. It should be noted that the pressure curves were extracted from one of the fluid elements at the middle, right next to the plate. As the embedded FSI approach was used, the selected fluid element did not move during the displacement of the plate. This means that the pressure is not necessarily representative for the pressure hitting the plate.
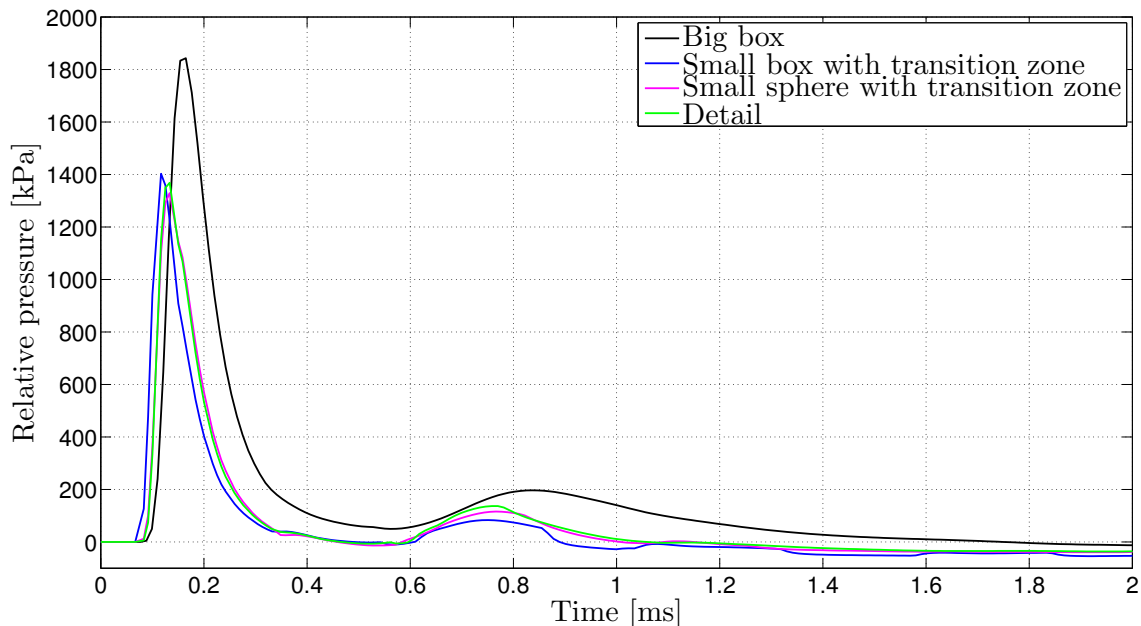
Figure 6.19: Relative pressure at midpoint with different load shapes.

From Figure 6.19, it can be seen that the variations between the tests, correspond to the variations seen in Figure 6.18. Because the pressure is extracted from a fluid element that does not follow the plate, it is hard to define the end of the positive impulse affecting the plate. Based on the results from the calibration tests, as well as the displacement curves in Figure 6.18, it can be assumed that the positive impulse ends at around 0.5 ms for the three simulations. It is possible that the second peak is a result of pressure reflected from the plate. By assuming the first peak as the positive impulse, the values listed in Table 6.11 were calculated. The result from test R33-2 is included for comparison.

Table 6.11: Positive impulse with different load shapes.

Alternatives	Positive impulse [kPa·ms]
Big box	221.5
Small box with transition zone	125.5
Small sphere with transition zone	131.5
Detail	129.3
R33-2	142.8

From Table 6.11, it can be seen that the positive impulse is larger for the big box than for test R33-2, and lower for the rest. This corresponds well with the displacements. The impulse from the big box is a lot higher than from test R33-2. Comparing the

displacements, the difference is not too large. The difference is a lot bigger for the other simulations, when comparing the difference in impulse and in displacements. Based on the observations from Chapter 3.2 and Chapter 6.3.1, it is possible that the differences had been more reasonable with a smaller element size. Considering the assumptions made when calculating the positive impulse, it is difficult to draw any clear conclusions.

Table 6.12 lists the computational time of the different analyses. It should be noted that the workload on the computer were varying when running the simulations. Because of this, the time can only be used as an estimate.

Table 6.12: Computational time with different load shapes.

Alternatives	Computational time [hh:mm:ss]
Big box	02:15:22
Small box with transition zone	02:07:08
Small sphere with transition zone	02:26:56
Detail	05:12:31

From Table 6.12, it can be seen that the time increases a lot for the simulation with detailed model of the charge load. This is most likely due to the very small element size in the center of the charge. The time when simulating the charge as a big box, is longer than the time for the small box and sphere. This is unexpected, due to an increased amount of elements, as well as smaller elements in the small box and small sphere models. Because of the small differences, it is likely that the big box model was run at a time when there were less memory available, than for the other simulations.

6.3.3   Load Type

In EUROPLEXUS, there are several different ways to simulate the explosive load. In addition to the AIRB and GAZP commands, it is also possible to use BUBB or JWL. BUBB works in the same way as GAZP, but calculates the input parameters automatically based on the mass of the load and the volume of the elements. JWL models the explosive charge with the Jones-Wilkins-Lee equations of state. The available methods are explained further in Chapter 2.11.5.

Procedure

When investigating the different approaches, it was decided to use detail model from Chapter 6.3.2. When using the JWL approach, the input parameters listed in Chapter 2.3 were used. In order to get the correct representation of the load, the volume had to be exact. The reason for this, is that the equation of state does not take a theoretical volume and TNT-equivalent mass into consideration, but rather assigns an equation of state specific to C4 and its abilities. The input parameters for the JWL equation is listed in Table 2.2.

The GAZP model uses the same input parameters as in Chapter 6.3.2. The BUBB model calculates the input parameters automatically based on a TNT-equivalent mass. Because of this, the TNT-equivalent mass was the only input. Table 6.13 lists the alternatives investigated.

Table 6.13: Blast load methods.

Method
GAZP
BUBB
JWL

Results

Figure 6.20 shows the midpoint displacement plotted against time for the different simulation methods. The results from test A22 have been included for comparison.
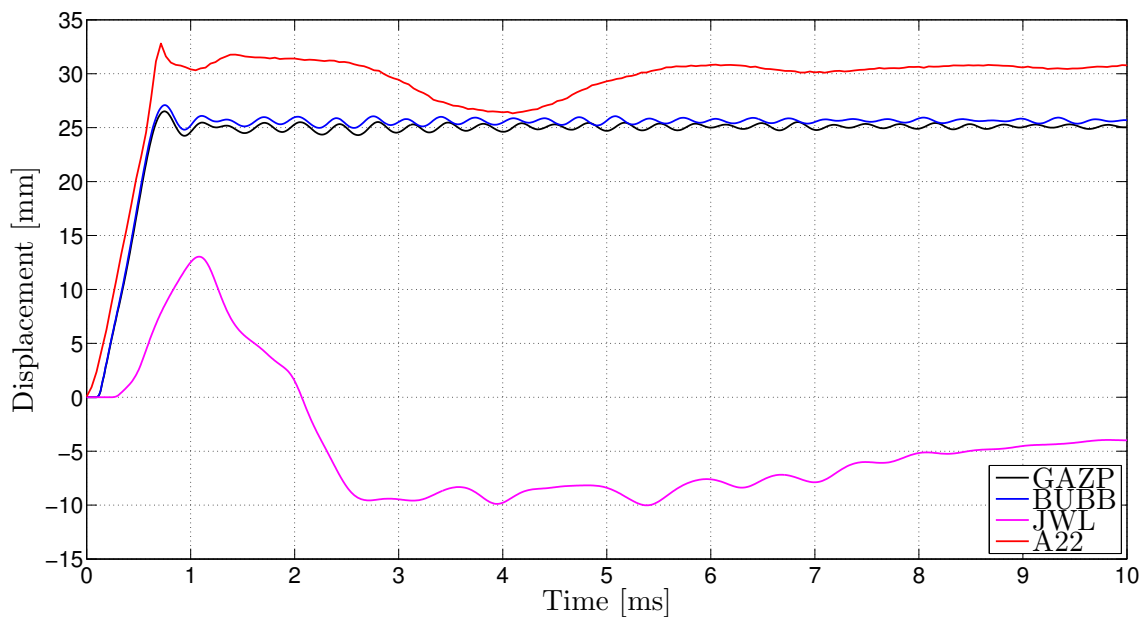
Figure 6.20: Displacement at midpoint with different load types.

In Figure 6.20, it can be seen that the displacements from the GAZP model and the BUBB model are very similar. The BUBB model produces a little more displacement than the GAZP model. It is possible that the BUBB model uses a different value for the heat capacity ratio, γ, as well as a different function in order to calculate the initial balloon pressure, p_{bal}.

The JWL model results in a lot smaller displacements than the GAZP and BUBB models. Larcher et al. [36] states that a fine mesh is essential when using the JWL model. Ideally, the element size around the charge should be a lot smaller than the ones used to model the explosive charge. This means that this particular approach is especially mesh sensitive, which could explain the lower deformations. An interesting observation from the JWL curve, is that the JWL model is able to simulate the counter-intuitive behavior, observed for the aluminum plates at stand-off distance 625 mm.

Figure 6.21 shows the pressure at the midpoint, plotted against time, for the different approaches. As in Chapter 6.3.2, the pressure is extracted from an element in the fluid mesh, next to the center of the plate. As the model uses the embedded approach, this element does not move together with the plate.
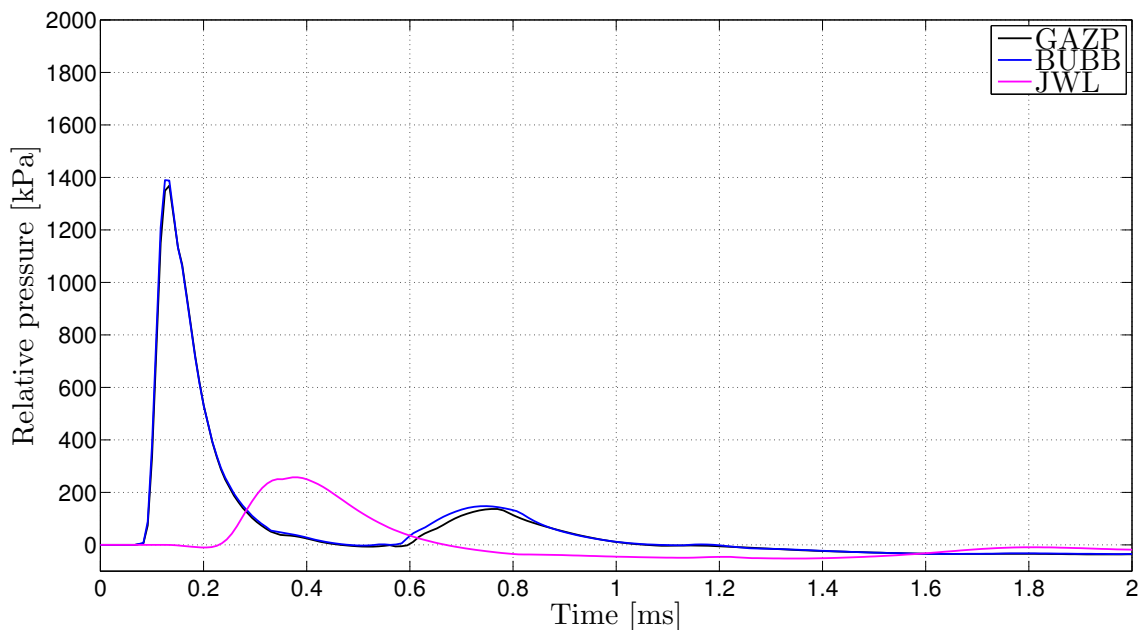
Figure 6.21: Relative pressure at midpoint with different load types.

From Figure 6.21, it can be seen that the pressure from the GAZP model and the BUBB model are almost the same. Due to the time steps of the simulations, the peak pressure has not been registered on the curves. The pressure of the JWL curve, is much lower than the other models. It can also be seen that the JWL curve has a fairly long negative phase. It is therefore possible that the displacements in Figure 6.20, may have been influenced by this negative phase.

By making the same assumptions as in Chapter 6.3.2, the positive impulse can be calculated. Table 6.14, lists the positive impulse calculated for the three methods. The value from test R33-2 has been included for comparison.

Table 6.14: Positive impulse with different load types.

Alternatives	Positive impulse [kPa·ms]
GAZP	129.3
BUBB	132.6
JWL	57.5
R33-2	142.8

From Table 6.14, it can be seen that the impulse is slightly higher for the BUBB model than for the GAZP model. This explains the slightly larger displacements produced by the BUBB model compared to the GAZP model.

Table 6.15 lists the computational times for the different models. The times are not directly comparable as the workload on the computer varied between the simulations.

Table 6.15: Computational time with different load types.

Alternatives	Computational time [hh:mm:ss]
GAZP	05:12:31
BUBB	06:04:44
JWL	03:06:27

From the times listed in Table 6.15, it can be seen that the GAZP model and BUBB model are pretty close. This is expected, considering the fact that both models are based on the same equation of state. The time from the JWL model, on the other hand, is much lower. It should be noted that an ideal model of JWL probably would have a lot smaller elements. This means that the computational time for a fully functional JWL model, probably would be a lot longer than for a fully functional balloon model.

6.3.4 Embedded vs ALE

In Chapter 2.11.3 and Chapter 2.11.4, the difference between an embedded FSI approach, and ALE is explained. It was decided to run simulations with both approaches in order to investigate the difference.

Procedure

The difference between an embedded FSI approach and ALE, will be most important when reaching fracture in the model. In addition, embedded will usually be better when dealing with large deformations. In order to get the largest deformations possible, it was decided to model the experiments performed at stand-off distance 375 mm. In addition, it was decided to model the explosive charge as the "big box" used in Chapter 6.3.2.

In order to perform an ALE simulation, the fluid elements around the plate have to be allowed to deform. The elements selected are shown in Figure 6.22. All the selected elements are within a box with dimension 200x300x300 mm^3. The center of the box is in the origin of the plate. Selected elements are colored blue in the figure. The nodes in the plate are marked in red. The EUROPLEXUS input-file for the ALE-simulation, is included in Appendix E.4.
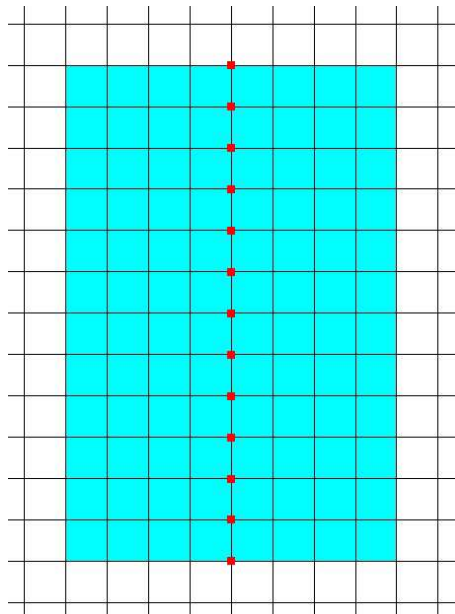
Figure 6.22: ALE-mesh before loading.

Results

Figure 6.23 shows the midpoint displacement, plotted against time, for the two FSI-approaches. The results from test A22 have been included for comparison.
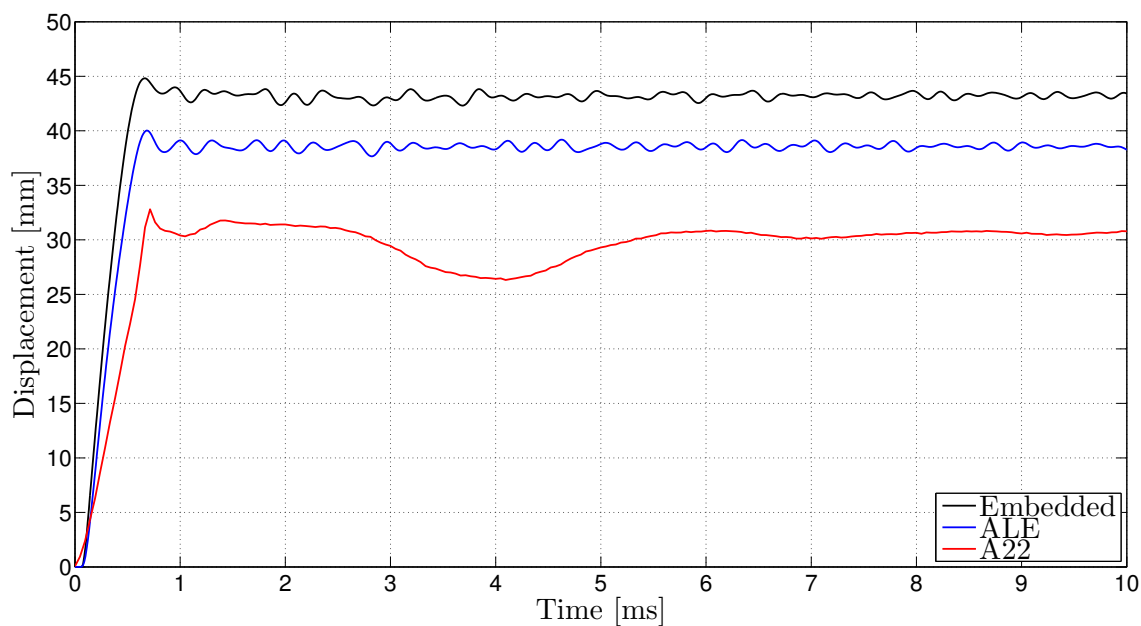
Figure 6.23: Displacement of midpoint with different FSI-approaches.

From Figure 6.23, it can be seen that both simulations result in larger displacements than the experiments. This is expected due to the choices that were made when running the simulations. It is interesting however, that the ALE-simulations result in smaller displacements than the embedded FSI-approach.

Figure 6.24 shows the fluid mesh around the plate for both the ALE-simulation and the embedded FSI-approach. The nodes in the plate are marked in red. Both of the figures present the displacements at the end of the time series.

(a) Embedded   (b) ALE
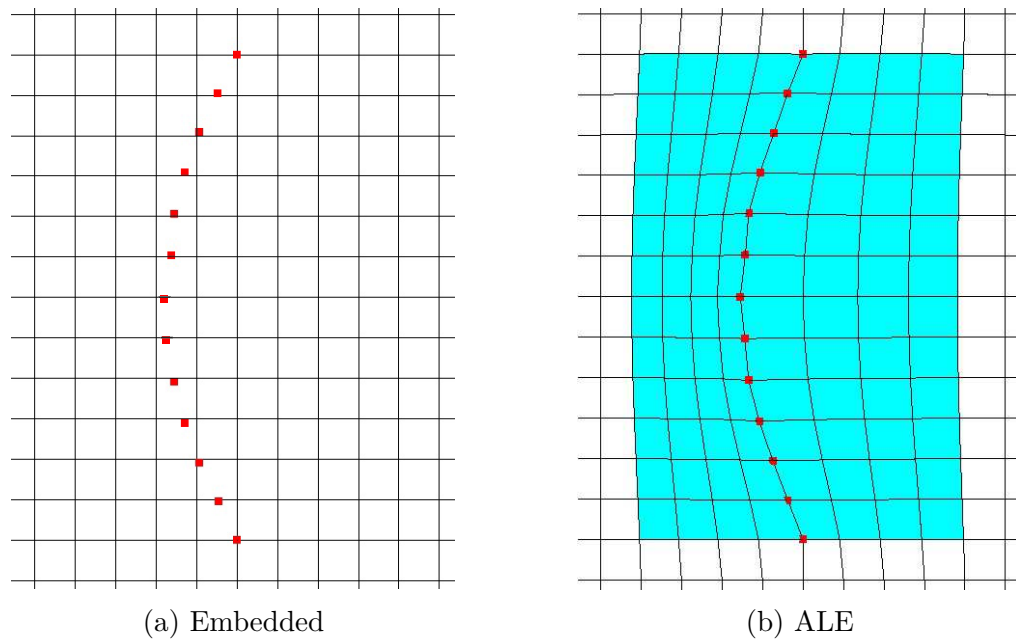
Figure 6.24: Mesh around plate after loading.

From Figure 6.24b, it can be seen that the mesh is deformed around the plate. The elements on one side of the plate, have been stretched out, while the ones on the other side have been compressed. The displacements present, are not large enough to cause any major problems. However, if the displacements are even larger, it may eventually become a problem. Looking at the mesh in Figure 6.24a, it can be seen that the plate has deformed without affecting the surrounding mesh. As the fluid mesh in ALE follows the structure when deforming, it causes problems when fracture occurs. This is because the nodes are splitting and the fluid mesh then has trouble following the nodes. In problems where large deformations occur, or fracture might be a problem, an embedded FSI-approach is the preferred method.

6.4   Simulation of the Component Tests

6.4.1   Procedure

In Chapter 6.1 it was seen that the Lagrange simulations, generally overestimated the displacements. On the other hand, it was observed in Chapter 6.3, that the FSI-simulations resulted in too small deformations. Because of this, it was decided to run simulations of the three stand-off distances used in Chapter 4.3.3, with both the Lagrangian approach as well as with en embedded FSI-approach.

The model for the Lagrangian approach was the same as used in Chapter 6.1.3. This means that the plate was modeled with 10 mm elements and fixed boundary conditions. Alternative 1, from the inverse modeling, was used as material model, and 4/3 was used as the relative effectiveness factor of the charge load. Table 6.16 lists the important choices made for the analyses.

Table 6.16: Values used for the Lagrangian-approach.

Plate	
Element size	10 mm
Boundary conditions	Fixed
Material constants	
Young's modulus, E	71 GPa
Density, ρ	2710 kg/m^3
Poisson's ratio, ν	0.33
Johnson-Cook parameters	
A	115 MPa
B	57 MPa
n	0.26
C	0.014
Loading	
EUROPLEXUS approach	AIRB
TNT equivalent mass	40 g
Stand-off distances	375 mm
	500 mm
	625 mm

The model used for the embedded FSI-approach, was the same as used in Chapter 6.3.1. Element size of 25 mm were used, for both the plate and the fluid. As in the Lagrangian simulation, the plate was modeled with fixed boundaries. The charge

load was modeled with exact dimensions and with the use of the GAZP approach. Table 6.17 lists the important choices made for the analyses.

Table 6.17: Values used in the embedded FSI-approach

Plate	
Element size	25 mm
Boundary conditions	Fixed
Fluid	
Element size	25 mm
Material constants	
Young's modulus, E	71 GPa
Density, ρ	2710 kg/m ^{3}
Poisson's ratio, ν	0.33
Johnson-Cook parameters	
A	115 MPa
B	57 MPa
n	0.26
C	0.014
Loading	
EUROPLEXUS approach	GAZP
TNT equivalent mass	40 g
Stand-off distances	375 mm
	500 mm
	625 mm
Input parameters GAZP	
V_{bal}	$2.15 \cdot 10^{-5}$
γ	1.4
p_{bal}	$2.05 \cdot 10^{10}$
ρ_{bal}	588.1

6.4.2 Results

Figure 6.25 shows the results from the simulations at 375 mm stand-off, compared with the results from test A11. Figure 6.26 shows the results from the simulations at 500 mm stand-off, compared with the results from test A22. Figure 6.27 shows the results from the simulations at 625 mm stand-off, compared with the results from test A31. Note that the deformation curves from the component tests have been adjusted so that the deformation starts at $t = 0$ ms. This was done in order to give

the best basis for comparison, as the displacements from the physical experiments, start fairly late, compared with the results from the simulations.
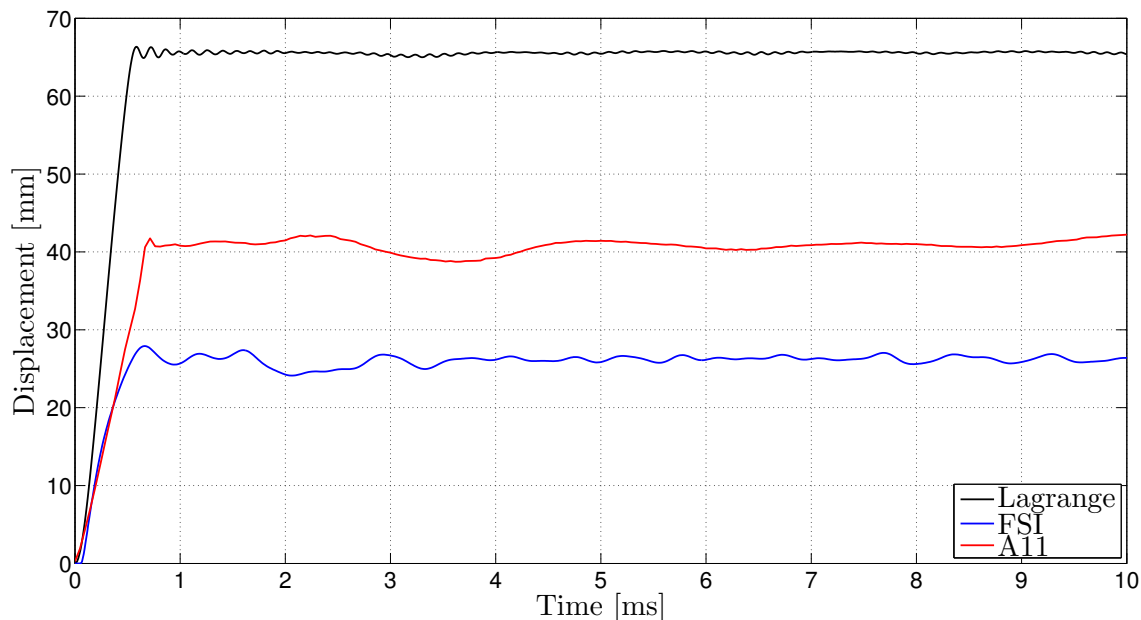
Figure 6.25: Displacement of midpoint at stand-off distance 375 mm.
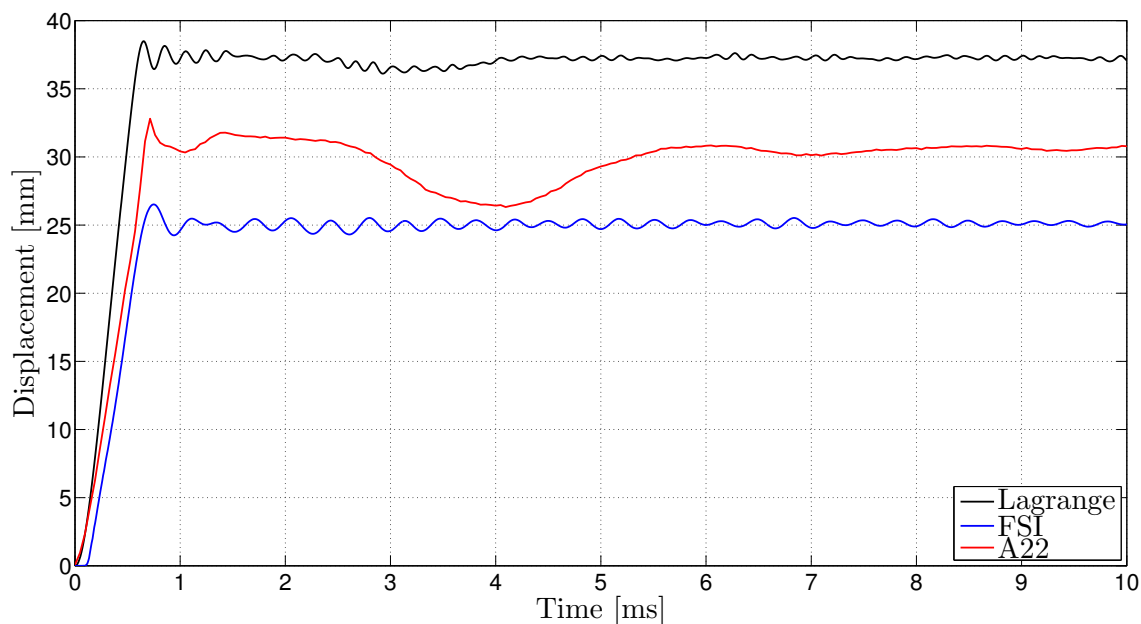
Figure 6.26: Displacement of midpoint at stand-off distance 500 mm.
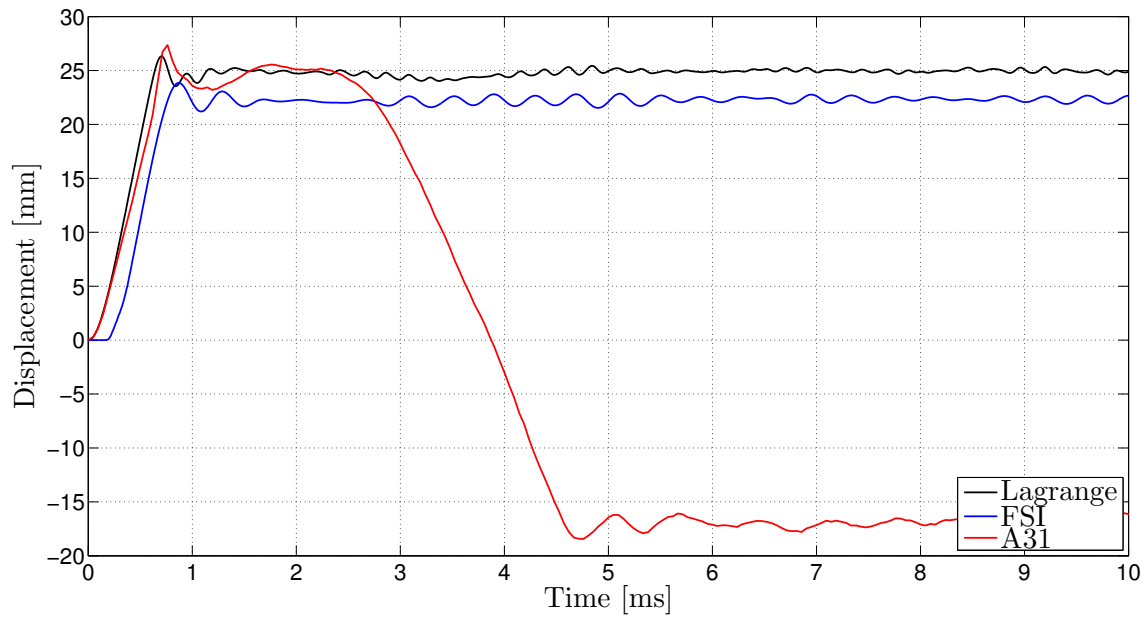
Figure 6.27: Displacement of midpoint at stand-off distance 625 mm.

In Figure 6.25, it can be seen that the displacements from the Lagrangian analysis is way too large compared with the experiments. Looking at Figure 6.26, it can be seen that the displacements are getting closer to the experiments, and in Figure 6.27, the maximum positive displacement is very similar for the Lagrangian analysis and the experiment. However, the Lagrangian analysis does not manage to represent the counter-intuitive behaviour present at this stand-off distance.

Looking at the displacements resulting from the FSI-simulations, it can be seen that the displacements in general are lower than from the experiments. It is possible that this is due to the element size, and would therefore improve with a finer mesh. An interesting observation from the figures, is that the maximum displacements from the FSI-simulations actually vary fairly little between the stand-off distances.

161

Chapter 7

Discussion

Calibration tests

The calibration tests in general provided fairly good results, as seen in Chapter 4.3.2. By comparing pressure measured in transducers, decreasing peak pressures and increasing values for the time of arrivals could be observed when moving away from the center of the plate. This was the case for most of the tests.

In some of the tests, one or two pressure transducers provided results that deviated from the rest, e.g. unusually low peak pressure or that the pressure arrived at the pressure transducers in unexpected order. It can be seen that the time of arrival is different in the pressure transducers in the clamping frame, for some of the tests. As all three pressure transducers have the same stand-off distance, it is expected that the pressure should arrive at the same time.

Comparing the different tests at the same stand-off, it can be seen that there are slight variation in peak pressure and positive impulse. For most pressure transducers, the values are within range of each other, and it can clearly be seen which results are from which stand-off distance. The time of arrival is pretty similar between the tests, but the peak pressure and positive impulse have a lot more variation.

By inspecting the pressure curves, it can be seen that most of the curves have additional pressure peaks right after the initial peak. It is possible that these peaks are results of reflection pressure from the floor or other parts of the surroundings. The second peak however, occurs very shortly after the first one. It is hard to say what surface would be able to reflect the pressure this early. It is therefore possible that this has another explanation. Spranghers et al. [63] used a very similar test setup, but did not experience this behavior.

It can be seen that the pressure and positive impulse in the pressure transducers close to the edge of the plate, tend to have higher values than the ones a little closer to the center. It is likely that this happens due to an accumulation of pressure, created when the pressure moves out to the side and is stopped by the thickness of

the frame.

There are multiple possible sources of error that can have caused the deviations in the results. The primary source is probably related to the shape and location of the blast load. As the charge was created by hand, it is possible that both the mass and geometry vary between the tests. To ensure that the mass and shape were the same, it would have been better if the charges had been casted. Another likely source of error, is the location of the explosive charge. The charge was elevated by a wire that was not constant between the tests. Because of this it is possible that there have been variations, both in terms of the centering of the load, as well as the stand-off distance. A variation in the centering, would explain the variations in time of arrival of the pressure transducers in the frame. Slight variations in the stand-off could also explain the variations in peak pressure between the tests.

As explained in Chapter 4.3.2, the pressure transducers had drifting of the zero level due to temperature. Based on the pressure curves, it can be seen that the amount of drifting varies between the stand-off distance. The change is biggest at the lowest stand-off distance. This is most likely because the temperature is higher when the stand-off distance is low. As the heat created by the explosion moves slower than the pressure, it is assumed that the drifting did not have much effect on the positive phase, but it is likely that this is a problem for the negative phase. As the zero level has changed, it is very hard to determine the end of the negative phase, and therefore the negative impulse.

Component tests

In Chapter 4.3.3, it can be seen that the component tests provided good results, but there were still minor differences in the displacement curves when comparing the tests at the same stand-off distances. For the tests at stand-off distance 375 mm, the difference was only a couple of millimeters between the tests. Fractures occurred several places along the supports, for the plates at stand-off distance 375 mm. The DIC-pictures indicate that this happens due to shear at the support. As the fractures occur before the plate reaches maximum displacement, it is possible that the fractures have contributed to an increase in the midpoint displacement.

The DIC paint was destroyed at one of the plates at stand-off distance 500 mm, and one plate at stand-off distance 625 mm. This made it hard to get a good impression of the displacement development of the two plates. The permanent deformations measured still indicate that the two plates behaved similar to the other plates at the same stand-off distance.

For the plates at stand-off distance 500 mm, it can be seen that plate A21 and A22 had around 4 mm difference in the final displacement of the midpoint. In addition, it can be seen that the displacement development is different.

The plates at stand-off distance 625 mm ended with negative displacement. Similar

behavior was investigated by e.g. Flores-Johnson et al. [16]. The reason for this may be a combination of many factors. The negative impulse may have some effect. In addition, it is possible that some change in displacement is caused by the release of elastic deformations in the plate. Similar behavior can be seen in test A21, but in this case the displacements return back to a positive. It is possible that the counter-intuitive behaviour happens if the deformation reaches an unstable state, where the inertia of the plate causes the plate to displace in the opposite direction. A lot is unknown about the phenomenon, and it is therefore difficult to determine the exact cause.

There are multiple possible causes for the slight differences in the displacement of the plates. One possibility is that there might be minor differences between the plates in terms of material quality, or the geometry of the plates. When measuring the thickness of the plates, the differences were pretty small. If it is assumed that the quality of the plates were similar, differences in load is the most likely cause of the variations. This can be due to slight changes in mass, or the placement of the load. From the simulations in Chapter 6.1.3, it can be seen that there are little difference in deformation if the load is off-center. If the explosive charge is slightly closer or further away, the displacement will change. Similar could be seen from the simulations in Chapter 6.1.4. The results indicate that slight changes in mass can cause changes in the displacement.

Analytical methods

In Chapter 4.3.3 it can be seen that the midpoint displacement of the plates are a lot larger than the displacements calculated in Chapter 3.1. This is despite the fact that maximum impulse was assumed distributed over the whole plate. Looking at the impulses calculated from the experiments in Chapter 4.3.2, it can be seen that the positive impulse at the middle of the plate are larger than the impulses used in Chapter 3.1. This indicate that CONWEP underestimates the positive impulse from the blast.

Figure 7.1 shows the results from the experiments compared with the empirical relation established by Nurick and Martin [6]. The impulse has been taken from the calibration tests, and the displacement has been taken from the component test. The impulse used is not directly representative for the displacement. This is due to the fact that the stand-off in the calibration tests were slightly larger due to the thickness of the frame. In addition, the value used is not representative for the variations between the tests. In order to keep the sources of error as small as possible, it was decided to use the positive impulse from the experiments with the median value. Because of this, the impulse from test R21 and R31-2 were used. The impulse at the middle of the plate has been assumed constant and distributed across the whole plate. Only stand-off distances 375 mm and 500 mm are included, as these were the only stand-off distances tested in both the calibration tests and the component tests.
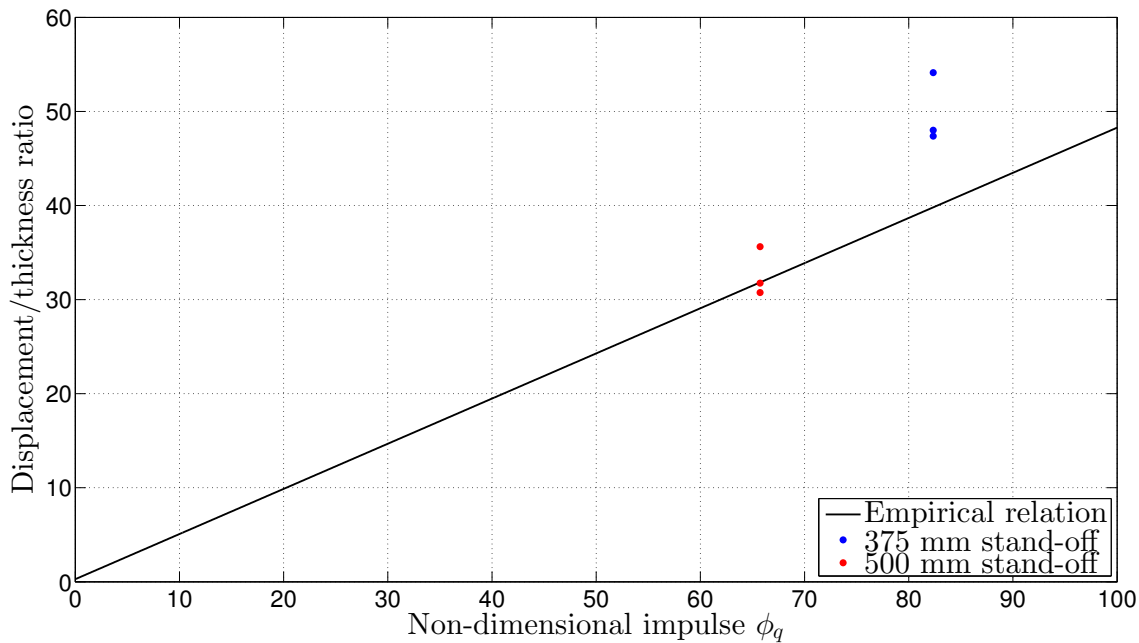
Figure 7.1: Empirical relation compared to experimental results

From Figure 7.1 it can be seen that the results from the tests at stand-off distance 375 mm are missing the empirical relation by a lot. It is possible that this is due to increased deformation beacuse of the fractures along the support. The tests at stand-off distance 500 mm however, fit fairly well. When calculating the non-dimensional impulse, total impulse over the plate should be used. In Figure 7.1, the total impulse is assumed to be the same as the impulse at the middle multiplied by the area. This is most likely higher than the total impulse actually present. This means that the non-dimensional impulse in reality should have a lower value. Based on the difference in the values between the stand-off distances, it is still possible that the empirical relation would give a better estimate at smaller displacements. In order to investigate this, a more accurate value has to be measured for the total impulse over the plate.

Numerical simulations

From the results in Chapter 3.3 and Chapter 6.1, it can be seen that the Lagrangian simulations overestimated the displacements. Based on the result from Chapter 6.2, it can be assumed that the main reason for this, is that the AIRB command that generates the load, overestimates the load applied to the structure. In Chapter 6.2 and Chapter 6.4, it can be seen that the pressure and displacement gets closer to the experiments when the stand-off distance increases.

The AIRB command in EUROPLEXUS is based on the empirical equations established by Kingery and Bulmash [33]. This is explained further in Chapter 2.2.7.

The equations were established based on a lot of experiments at different scaled distances. That means that the equations are the most accurate for scaled distances within the same range tested. For scaled distances outside of this, the applied load have to be calculated by extrapolation. Extrapolating can potentially produce large sources of error. Because of this, it is possible that AIRB overestimates the load for shorter distances, as the scaled distance might be outside, or at the boundary of the range tested when establishing the relation. When increasing the stand-off distance, the scaled distance gets closer to basis for the equations, and the load gets closer to experimental values. In order to investigate whether larger stand-off distances give more accurate results, it is necessary to perform more experiments.

The FSI-simulations performed in Chapter 6.3, resulted in pressure and positive impulse much closer to that of the experiments. This was the case when using the GAZP command in EUROPLEXUS. However, the displacements were smaller than the experimental results. Based on the results in Chapter 6.3.1, it can be seen that the results are mesh sensitive. Based on the results in Chapter 3.2, it is possible that a reduced element size can give significant increase in the displacement. A reduced element size increases the computational time exponentially. In order to do this, it would be best to use a model with symmetry conditions or use a version of the EUROPLEXUS program that supports MPP.

In Chapter 6.3.2 it can be seen that the shape and size of the explosive charge is important when generating the load in EUROPLEXUS. Modeling the load exactly gave the best result, but using another shape with exact volume, worked good as well. To model the sphere is approximately the same work as when modeling the explosive charge exactly. Because of this, it is better to just model the explosive charge exactly, as long as the increased computational time due to the reduced element size is acceptable. The sphere model could be preferred if the element size is small enough, such that the sphere can be modeled with correct volume without reducing the element size.

In Chapter 6.3.3, different ways of simulating the blast load in an FSI-simulation in EUROPLEXUS, were investigated. It can be seen that the results when using the BUBB command are fairly similar as when using the GAZP command. This is expected considering both approaches are based on the same theory. When modeling the solid explosive with the JWL equation of state, it resulted in displacements that were a lot lower than the experiments. This is due to the low pressure generated by the approach. Larcher et al. [36] states that JWL requires a very fine mesh around the explosive charge. Because the elements used in the model are pretty large, it is possible that this is why the resulting pressure is so low.

Chapter 8

Concluding Remarks

In this thesis, experiments and numerical simulations have been performed in order to investigate the response of thin aluminium plates exposed to blast loading. The goal was to investigate what numerical or analytical methods could provide the best results when simulating the response.

Material tensile tests were performed in order to determine a material model. Necking occurred at low plastic strains. As a result, the material model had to be determined through inverse modeling. Inverse modeling was performed with the computer code EUROPLEXUS. Due to limitations in the code, the material properties were identified and fitted to the Johnson-Cook material model.

Experiments were performed with free air explosions generated by using 30 g of composition C4. The load was applied in calibration tests with a stiff steel plate, as well as in component tests of thin plates made of the commercial aluminum alloy EN AW-1050A-H14.

The calibration plate was outfitted with pressure transducers. These were used to measure the pressure at different points on the surface of the plate. Examining the results revealed that the time of arrival was consistent between the experiments, while the peak pressure and positive impulse varied a lot more between the tests. It is probable that some of the variation is a result of variation in mass and shape of the explosive charges, and some is likely due to variations in the location of the load.

The component tests showed that a stand-off distance of 375 mm produced fracture along the support. It is possible that the fractures are a result of shear failure. The plates at 625 mm stand-off showed counter-intuitive behavior, as the final deformed configuration had deformation towards the explosive charge, instead of away from the charge as observed at the other stand-off distances. All the stand-off distances indicated a good degree of repeatability, as there were only minor differences in the displacements. Numerical simulations performed, indicates that the differences can be a result of variation in mass, or deviations in the stand-off distance. The

deformation appears to be following the yield lines, which causes the deformation to be similar, even if the explosive charge should be somewhat off-center. By comparing the pressure curves with the displacement curves, it is apparent that most of the deformation happens after the positive impulse is finished. Based on this, it can be assumed that the deformations happens as a result of impulsive load, and that very little fluid-structure interaction is present during the deformation.

The analytical approach investigated, appears to underestimate the displacements from the experiments. Results indicate that this may be due to the large displacements present in the experiments. From the tests at stand-off distance 500 mm, it appears that the analytical approach might give better indication of the response when the expected displacements are smaller.

Numerical simulations were performed in EUROPLEXUS. The results show that neither the Lagrangian, nor the embedded FSI approach give convincing results when simulating the component tests. The AIRB approach, used to simulate the load in the Lagrangian simulations, seem to overestimate the load on the plate. As a result, the deformations resulting from the simulations are too large. When the stand-off distance increases, the load gets closer to what was measured during the experiments. It is therefore possible that the approach will be able to represent the loading better, if the stand-off distance is increased even further.

The embedded FSI approach resulted in deformations that were too low, compared to the experiments. Comparing the pressure and impulse, indicated that the GAZP approach was able to give a pretty good representation of the load. Mesh-sensitivity studies indicated that the element size was important when determining the displacements from the simulations. It is therefore possible that the embedded FSI approach would be able to give a good representation of the experiments using a smaller element size.

Chapter 9

Further Work

During the work with this thesis, there have been revealed several aspects that could be interesting to investigate further. This includes aspects related to the experimental work, as well as to the analytical and numerical computational methods. Following is a list of suggestions for further work:

- More experimental work should be performed in order to get a larger set of results to use for comparison with computational methods. This includes both calibration tests and component tests, in order to get results for both pressure and displacement. It should be prioritized to do experiments at larger stand-off distances, but experiments with variation in mass could be interesting as well. The explosive charges should be casted in order reduce the chance of large geometric deviations.

- Additional tests should be performed in order to investigate the causes of the additional positive peaks in the pressure curves. This particularly applies for the second pressure peak, as the time between this peak and the initial positive peak is very low. It is therefore possible that the peak is a result of something else than reflection waves from the surroundings.

- The drifting of the zero level of the pressure transducers, should be investigated in order to see if it is possible to predict when the zero level changes, and by how much. By doing this, it would be possible to get a more accurate understanding of the load conditions.

- The counter-intuitive behaviour observed at stand-off distance 625 mm, should be investigated further, in order to identify possible causes.

- The boundary conditions of the experimental setup should be investigated in order to make it possible to do numerical simulations with more accurate boundary conditions.

- Numerical simulations that take fracture into consideration, should be performed in order to investigate the effect of the fractures in the plates at stand-

off distance 375 mm.

- The analytical approach should be compared with experimental results at distances larger than 500 mm. Alternatively, it could be compared to experiments with other load conditions, as long as the displacement is lower. The total impulse from the explosion should be measured more precisely in order to get correct input values.

- Lagrangian analyses with the AIRB approach in EUROPLEXUS, should be compared with experiments at larger stand-off distances. This should be done in order to investigate whether the AIRB-approach gives a better representation of the loading at larger stand-off distances.

- Embedded FSI analyses with the GAZP approach should be performed with smaller elements. This should be done in order to investigate if the approach is able to give an accurate representation of the experiment when the mesh-sensitivity is taken into consideration. In order to reduce the computational time, a version of EUROPLEXUS that supports MPP should be used.

- More analyses should the performed with the JWL approach in EUROPLEXUS. This should be done in order to investigate whether the approach gives better results when using a finer mesh.

Chapter 10

Bibliography

[1] Applied Research Associates Inc, "Showcase Project: Finite Element Simulation for Blast Response of Structures." URL `http://www.ara.com/Projects/SVO/blast_response.html`. Accessed: May 12, 2014.

[2] S. B. Menkes and H. J. Opat, "Broken beams - tearing and shear failures in explosively loaded clamped beams," *Experimental Mechanics*, vol. 13(11), pp. 480–486, 1973.

[3] R. G. Teeling-Smith and G. N. Nurick, "The deformation and tearing of thin circular plates subjected to impulsive loads," *International Journal of Impact Engineering*, vol. 11(1), pp. 77–91, 1991.

[4] G. N. Nurick and G. C. Shave, "The deformation and tearing of thin square plates subjected to impulsive loads - an experimental study," *International Journal of Impact Engineering*, vol. 18(1), pp. 99–116, 1996.

[5] G. N. Nurick and J. B. Martin, "Deformation of thin plates subjected to impulsive loading - a review. Part I: Theoretical considerations," *International Journal of Impact Engineering*, vol. 8(2), pp. 159–170, 1989.

[6] G. N. Nurick and J. B. Martin, "Deformation of thin plates subjected to impulsive loading - a review. Part II: Experimental Studies," *International Journal of Impact Engineering*, vol. 8(2), pp. 171–186, 1989.

[7] G. N. Nurick, M. E. Gelman, and N. S. Marshall, "Tearing of blast loaded plates with clamped boundary conditions," *International Journal of Impact Engineering*, vol. 18(7-8), pp. 803–827, 1996.

[8] T. Wierzbicki and G. N. Nurick, "Large deformation of thin plates under localised impulsive loading," *International Journal of Impact Engineering*, vol. 18(7-8), pp. 899–918, 1996.

[9] V. H. Balden and G. N. Nurick, "Numerical simulation of the post-failure motion of steel plates subjected to blast loading," *International Journal of Impact Engineering*, vol. 32(1-4), pp. 14–34, 2005.

[10] N. Jacob, G. N. Nurick, and G. S. Langdon, "The effect of stand-off distance on the failure of fully clamped circular mild steel plates subjected to blast loads," *Engineering Structures*, vol. 29(10), pp. 2723–2736, 2007.

[11] A. Neuberger, S. Peles, and D. Rittel, "Springback of circular clamped armor steel plates subjected to spherical air-blast loading," *International Journal of Impact Engineering*, vol. 36(1), pp. 53–60, 2009.

[12] T. Børvik, L. Olovsson, A. G. Hanssen, K. P. Dharmasena, H. Hansson, and H. N. G. Wadley, "A discrete particle approach to simulate the combined effect of blast and sand impact loading of steel plates," *Journal of the Mechanics and Physical of Solids*, vol. 59(5), pp. 940–958, 2011.

[13] K. Spranghers, I. Vasilakos, D. Lecompte, H. Sol, and J. Vantomme, "Numerical simulation and experimental validation of the dynamic response of aluminum plates under free air explosions," *International Journal of Impact Engineering*, vol. 54, pp. 83–95, 2013.

[14] A. Alia and M. Souli, "High explosive simulations using multi-material formulations," *Applied Thermal Engineering*, vol. 26, pp. 1032–1042, 2006.

[15] L. Olovsson, A. G. Hanssen, T. Børvik, and M. Langseth, "A particle-based approach to close-range blast loading," *European Journal of Mechanics A/Solids*, vol. 29(1), pp. 1–6, 2010.

[16] E. A. Flores-Johnson and Q. M. Li, "A brief note on the counter-intuitive region of a square plate," *International Journal of Impact Engineering*, vol. 38(2-3), pp. 136–138, 2011.

[17] S. U. Galiev, "Distinctive features of counter-intuitive behaviour of plates and shells after removal of impulse load," *International Journal of Impact Engineering*, vol. 19(2), pp. 175–187, 1997.

[18] Q. M. Li, L. M. Zhao, and G. T. Yang, "Experimental results on the counter-intuitive behaviour of thin clamped beams subjected to projectile impact," *International Journal of Impact Engineering*, vol. 11(3), pp. 341–348, 1991.

[19] N. Jacob, S. Chung Kim Yuen, G. N. Nurick, D. Bonorchis, S. A. Desai, and D. Tait, "Scaling aspects of quadrangular plates subjected to localised blast loads – experiments and predictions," *International Journal of Impact Engineering*, vol. 30(8-9), pp. 1179–1208, 2004.

[20] Wikipedia, "Explosive material." URL `http://en.wikipedia.org/wiki/Conservation_law`. Accessed: March 21, 2014.

174

[21] W. E. Baker, P. A. Cox, J. J. Kulesz, R. A. Strehlow, and P. S. Westine, *Explosion Hazards and Evaluation.* Elsevier, 1983.

[22] P. D. Smith and J. G. Hetherington, *Blast and Ballistic Loading of Structures.* Linacre House, Jordan Hill, Oxford OX2 8DP: Butterworth-Heinemann Ltd, 1994.

[23] Wikipedia, "Relative effectivness factor." URL `http://en.wikipedia.org/wiki/Relative_effectiveness_factor`. Accessed: March 22, 2014.

[24] D. Bjerketvedt, J. R. Bakke, and K. van Wingerden, "Gas explosion handbook," *Journal of Hazardous Materials*, vol. 52, pp. 1–150, 1997.

[25] W. E. Baker, *Explosions in Air.* Austin: University of Texas Press, 1973.

[26] Wikipedia, "Stagnation pressure." URL `http://en.wikipedia.org/wiki/Stagnation_pressure`. Accessed: April 8, 2014.

[27] M. Larcher, "Pressure-Time Functions for the Description of Air Blast Waves," tech. rep., European Commision, Joint Research Centre, Institute for the Protection and Security of the Citizen, 2008.

[28] Department of Defence, "Unified Facilities Criteria, Structures to Resist the Effects of Accidental Explosions, UFC 3-340-02," 2008.

[29] T. Krauthammer, *Modern protective structures.* 6000 Broken Sound Parkway NW, Suite 300, Boca Raton, FL 33487: CRC Press, Taylor & Francis Group, 2007.

[30] Department of the Army, "Fundamentals of Protective Design for Conventional Weapons, TM 5-855-1 ," 1986.

[31] United States Army Corps of Engineers, "ConWep - Protecting Design Center." URL `https://pdc.usace.army.mil/software/conwep/`. Accessed: June 7, 2014.

[32] A. Remennikov, "A review of methods for predicting bomb blast effects on buildings," *Journal of Battlefield Technology*, vol. 6(3), pp. 5–10, 2003.

[33] C. N. Kingery and B. G., *Airblast Parameters from TNT Spherical Air Burst and Hemispherical Surface Burst.* Aberdeen Proving Ground, Maryland: U.S. Army Ballistic Research Laboratory, 1984.

[34] E. J. Conrath, T. Krauthammer, K. A. Marchand, and P. Mlakar, *Structural Design for Physical Security: State of the Practice.* Amer Society of Civil Engineers, 1999.

[35] Wikipedia, "Equation of state." URL `http://en.wikipedia.org/wiki/Equation_of_state`. Accessed: April 10, 2014.

[36] M. Larcher and F. Casadei, "Explosions in Complex Geometries - A Comparison of Several Approaches," tech. rep., European Commission, Joint Research Centre, IPSC European Laboratory for Structural Assessment, Ispra, 2010.

[37] O. S. Hopperstad and T. Børvik, "Lecture Notes - Material Mechanics Part 1." Structural IMpact Laboratory (SIMLab), Trondheim, 2013.

[38] R. C. Hibbeler, *Mechanics of Materials.* Jurong, Singapore: Prentic Hall, Pearson Education South Asia Pte Ltd, 7th ed., 2008.

[39] Wikipedia, "Necking (engineering)." URL `http://en.wikipedia.org/wiki/Necking_(engineering)`. Accessed: April 26, 2014.

[40] Wikipedia, "Material failure theory." URL `http://en.wikipedia.org/wiki/Material_failure_theory`. Accessed: May 4, 2014.

[41] Wikipedia, "Fracture." URL `http://en.wikipedia.org/wiki/Fracture`. Accessed: May 4, 2014.

[42] T. Belytschko, W. K. Liu, B. Moran, and K. I. Elkhodary, *Nonlinear Finite Elements for Continua and Structures.* Chichester, West Sussex: Wiley, 2nd ed., 2014.

[43] R. D. Cook, *Concepts and Applications of Finite Element Analysis.* New York: Wiley, 4th ed., 2002.

[44] K. G. Rakvåg, "Combined blast and fragment loading on plates," Master's thesis, NTNU - Norwegian University of Science and Technology, 2009.

[45] A. Kane, T. Børvik, T. Berstad, A. Benallal, and O. S. Hopperstad, "Failure criteria with unilateral conditions for simulations of plate perforation," *European Journal of Mechanics A/Solids*, vol. 30(4), pp. 468–476, 2011.

[46] E. C. J. R. Centre, "EUROPLEXUS - A Computer Program for the Finite Element Simulation of Fluid-Structure Systems under Transient Dynamic Loading." User's manual, URL `http://europlexus.jrc.ec.europa.eu/public/manual_pdf/manual.pdf`, 2014.

[47] Wikipedia, "Objective stress rates." URL `http://en.wikipedia.org/wiki/Objective_stress_rates`. Accessed: March 24, 2014.

[48] K. Spranghers, I. Vasilakos, D. Lecompte, H. Sol, and J. Vantomme, "Identification of the plastic behavior of aluminum plates under free air explosions using inverse methods and full-field measurements," *International Journal of Solids and Structures*, vol. 51(1), pp. 210–226, 2014.

[49] Store norske leksikon (SNL), "Elementmetoden." URL `http://snl.no/elementmetoden`. Accessed: April 27, 2014.

[50] R. B. Agarwal, "ME 273 Lecture Notes: An Overview of the Finite Element Analysis." URL `http://www.engr.sjsu.edu/ragarwal/ME165/ME165_`

`Lecture_Notes_files/FEA_Lectures/Chapter_1_%20Introduction.pdf`.
Accessed: April 27, 2014.

[51] Wikipedia, "Conservation law." URL `http://en.wikipedia.org/wiki/Conservation_law`. Accessed: March 10, 2014.

[52] K. M. Hsiao, "Corotational total lagrangian formulation for three-dimensional beam element," *AIAA Journal*, vol. 30(3), pp. 797–804, 1992.

[53] Wikipedia, "Newtonian fluid." URL `http://en.wikipedia.org/wiki/Newtonian_fluid`. Accessed: March 26, 2014.

[54] L. Olovsson, *Corpuscular method for airbag deployment simulations.* 6th European LS-DYNA User's Conference.

[55] Wikipedia, "Numerical integration." URL `http://en.wikipedia.org/wiki/Numerical_integration`. Accessed: May 31, 2014.

[56] K. M. Mathisen, "Lecture 7: Solution of the dynamic equilibrium equations by explicit direct integration." Lecture Notes in TKT4197 Nonlinear Finite Element Analysis, NTNU (Norwegian University of Science and Technology), 2013.

[57] K. M. Mathisen, "Lecture 9: Solution of the nonlinear dynamic equilibrium equations." Lecture Notes in TKT4197 Nonlinear Finite Element Analysis, NTNU (Norwegian University of Science and Technology), 2013.

[58] M. Kristoffersen, "Fluid-structure interaction simulations of pipeline impact using europlexus." NTNU (Norwegian University of Science and Technology), 2013.

[59] F. Casadei, G. Solomos, and G. Valsamos, "Numerical Simulation of Fast Transient Dynamic Phenomena in Fluid-Structure Systems," tech. rep., European Commission, Joint Research Centre, Institute for the Protection and Security of the Citizen, 2013.

[60] Wikipedia, "Fluid-structure interaction." URL `http://en.wikipedia.org/wiki/Fluid%E2%80%93structure_interaction`. Accessed: April 24, 2014.

[61] F. Casadei and J.-P. Halleux, "Binary spatial partitioning of the central-difference time integration scheme for explicit fast transient dynamics," *International Journal for Numerical Methods in Engineering*, vol. 78(12), pp. 1436–1473, 2009.

[62] E. Fagerholt, "Field Measurements in Mechanical Testing Using Close-Range Photogrammetry and Digital Image Analysis," Doctoral thesis, NTNU (Norwegian University of Science and Technology), 2012.

[63] K. Spranghers, I. Vasilakos, D. Lecompte, H. Sol, and J. Vantomme, "Full-Field Deformation Measurements of Aluminum Plates Under Free Air Blast Loading," *Experimental Mechanics*, vol. 52, pp. 1371–1384, 2012.

177

[64] N. Jones, *Structural Impact.* 32 Avenue of the Americas, New York, NY 10013-2473, USA: Cambridge University Press, 2nd ed., 2012.

[65] Aalco Metals Limited, "Aluminium Alloy - Commercial Alloy - 1050A H14 Sheet." URL `http://www.aalco.co.uk/datasheets/Aluminium-Alloy_1050-H14_57.ashx`. Accessed: April 26, 2014.

[66] Kistler, "Type 603B - Piezoelectric Pressure Sensor (Miniature)." URL `http://www.kistler.com/ca/en/product/pressure/603B`. Accessed: June 9, 2014.

[67] Phantom Camera Products, "Phantom v1610." URL `http://www.visionresearch.com/Products/High-Speed-Cameras/v1610/`. Accessed: June 9, 2014.

[68] Livermore Software Technology Corporation, "LS-OPT - Graphical Optimazation Tool." URL `http://www.lstc.com/products/ls-opt`. Accessed: June 9, 2014.

[69] Open Cascade EDF CEA, "SALOME - The Open Source Integration Platform for Numerical Simulations." URL `http://www.salome-platform.org/`. Accessed: June 8, 2014.

[70] Commissariat à l'énergie atomique et aux énergies alternatives (France), "Cast3M." URL `http://www-cast3m.cea.fr/index.php`. Accessed: June 8, 2014.

Appendix A

Calibration Tests

A.1 Comparison of pressure in transducers
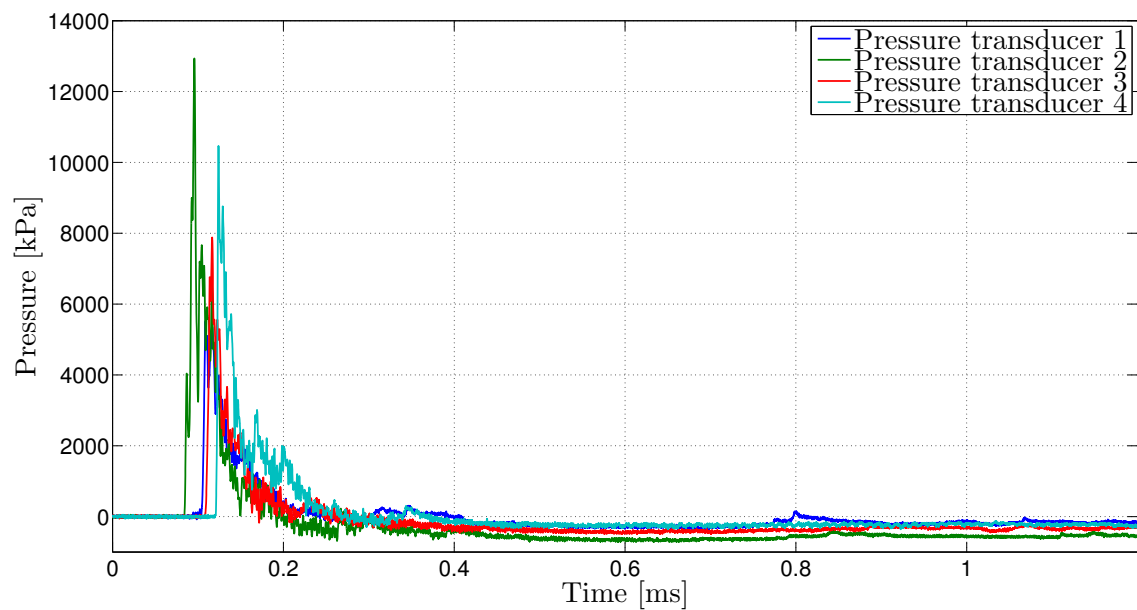
(a) Pressure transducers along the vertical.
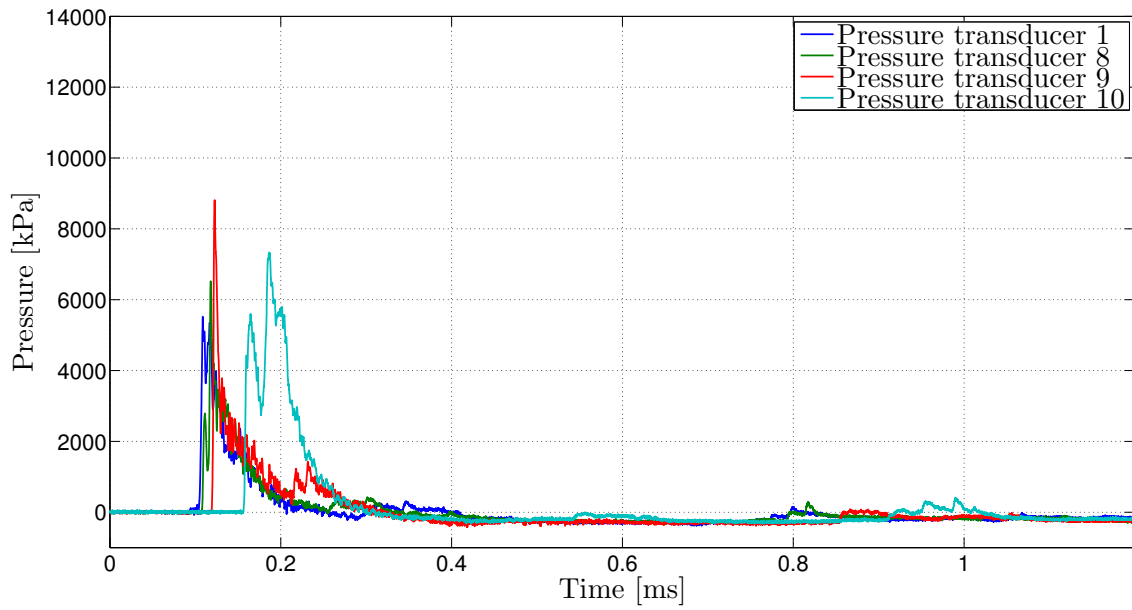
(b) Pressure transducers along the diagonal.
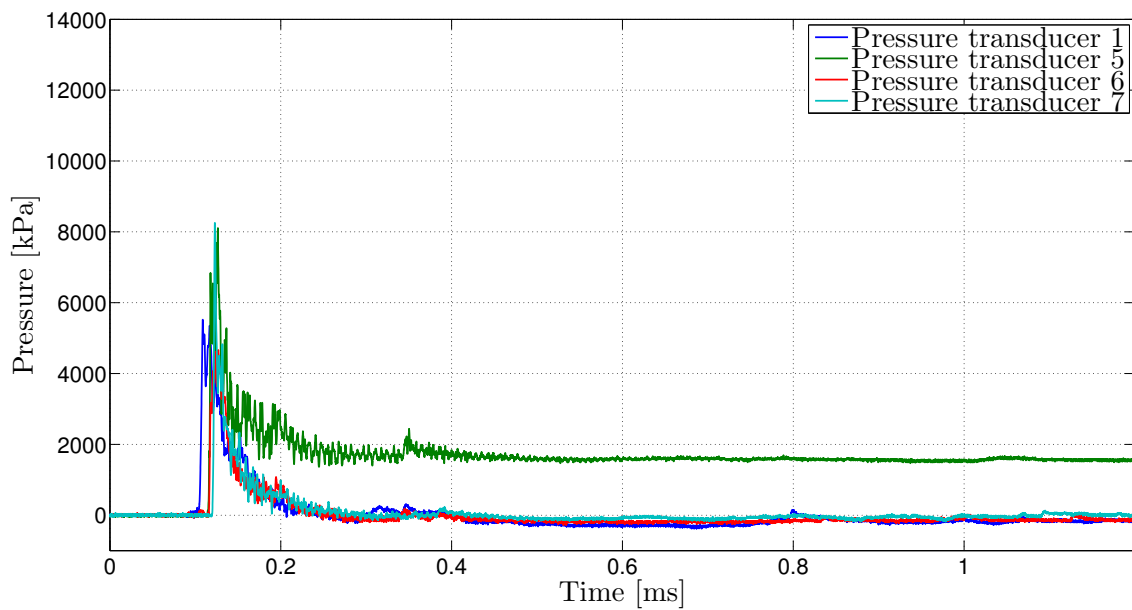
(c) Pressure transducers in the middle and in the clamping frame.

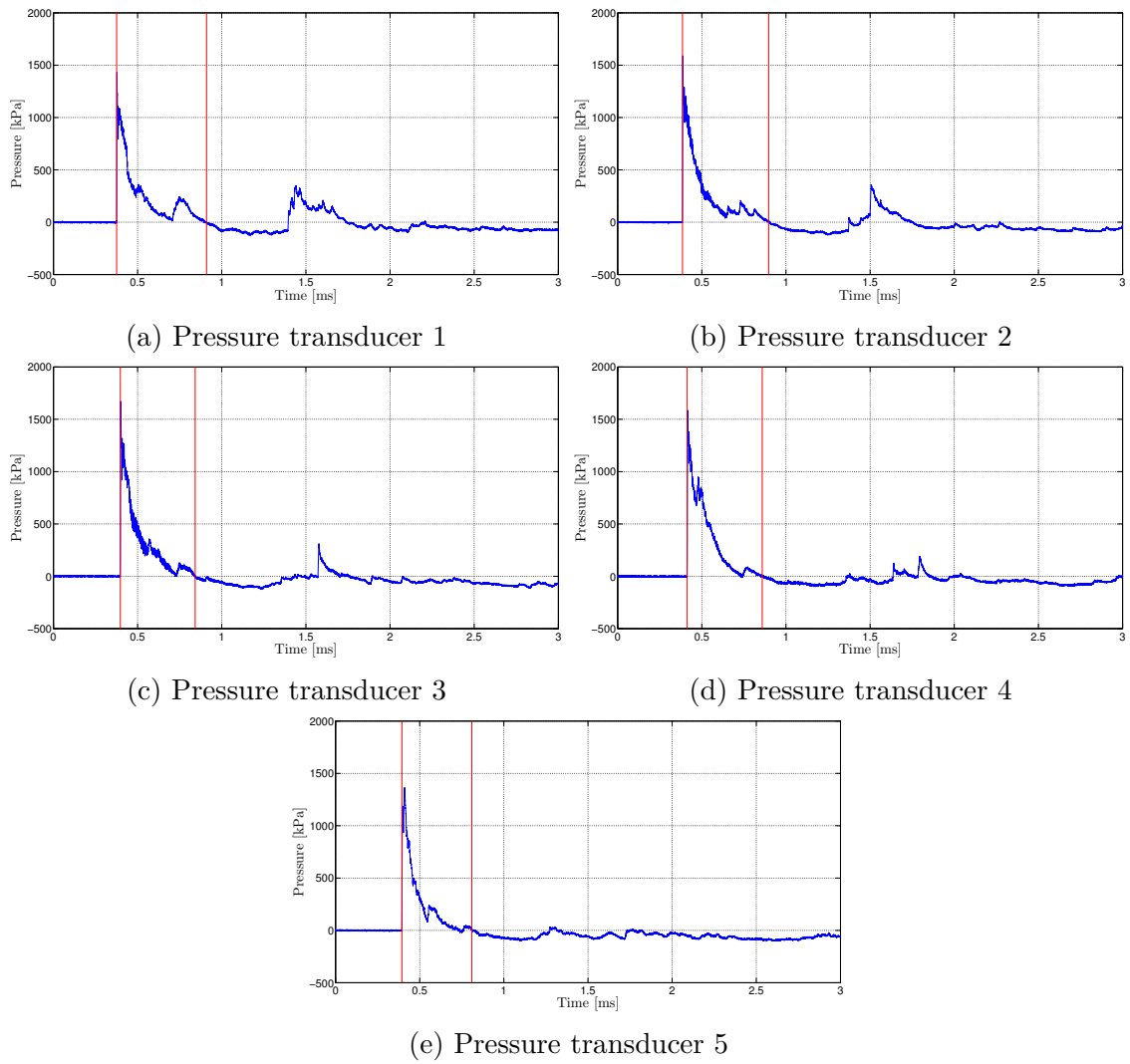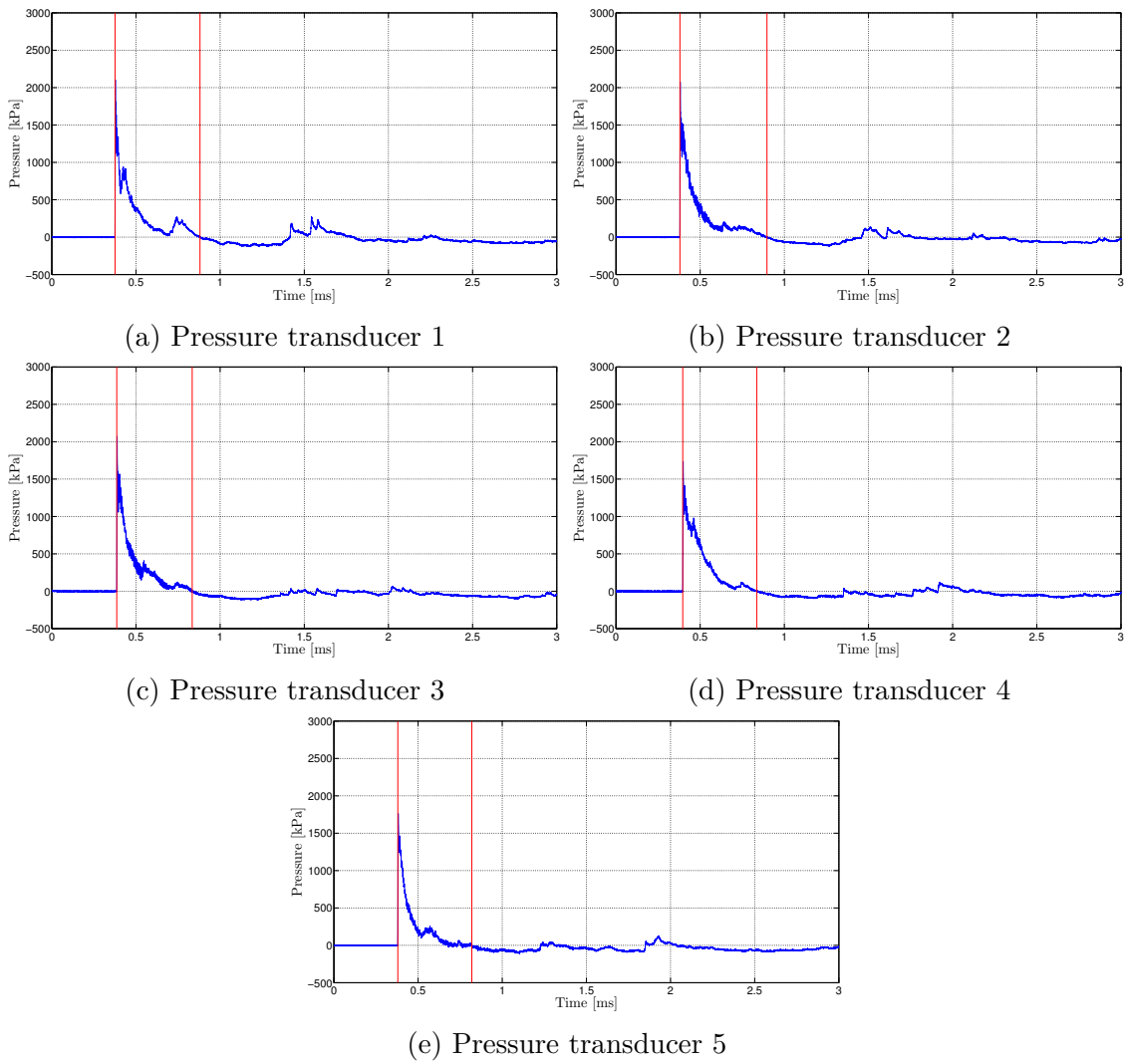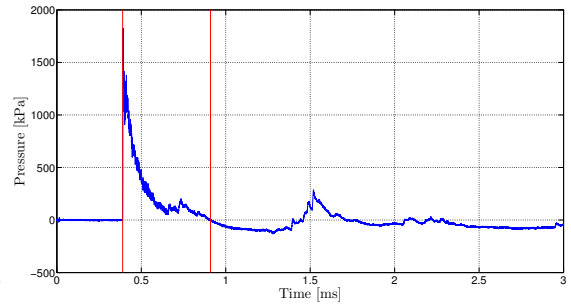Figure A.1: Pressure in calibration test R11.
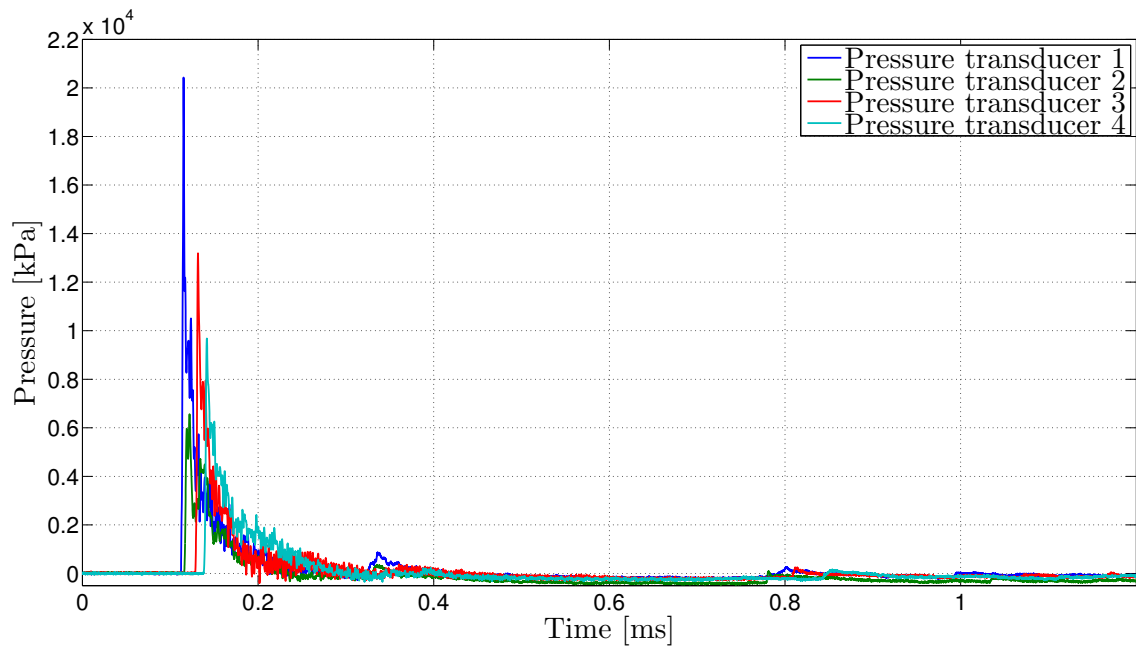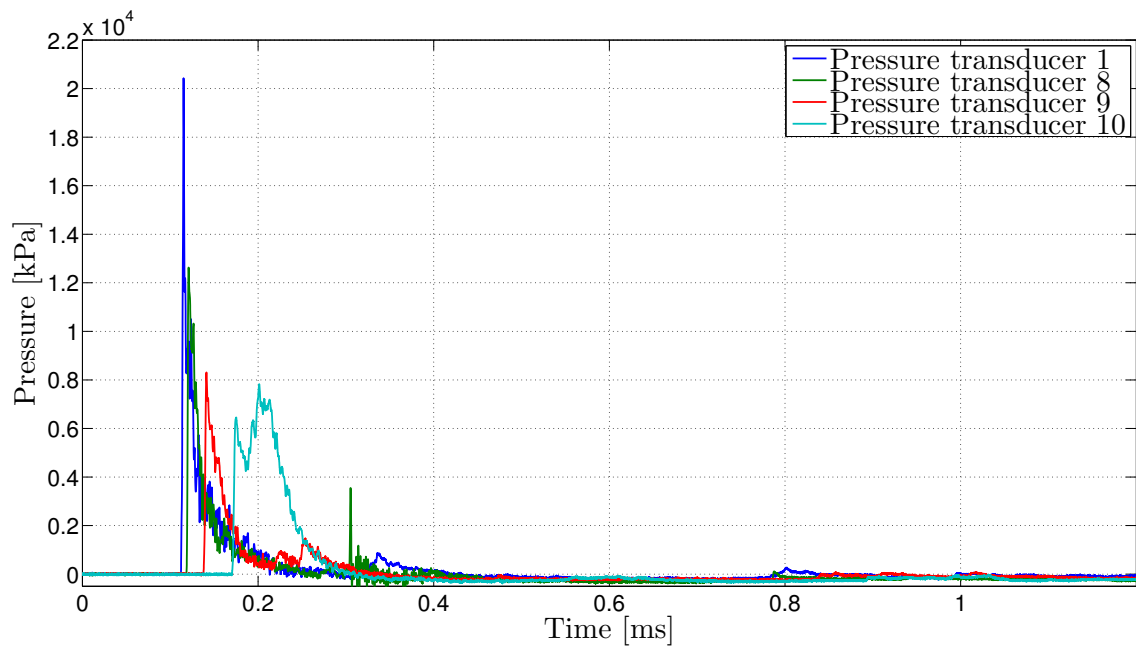
(a) Pressure transducers along the vertical.

(b) Pressure transducers along the diagonal.

A3
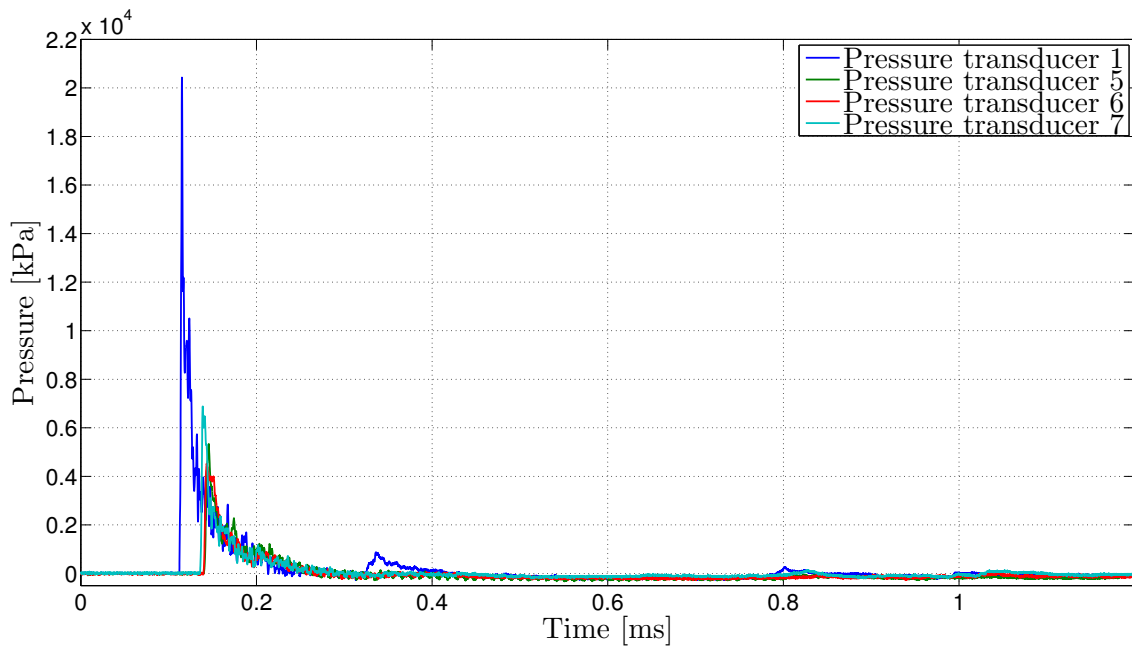
(c) Pressure transducers in the middle and in the clamping frame.

Figure A.2: Pressure in calibration test R12.
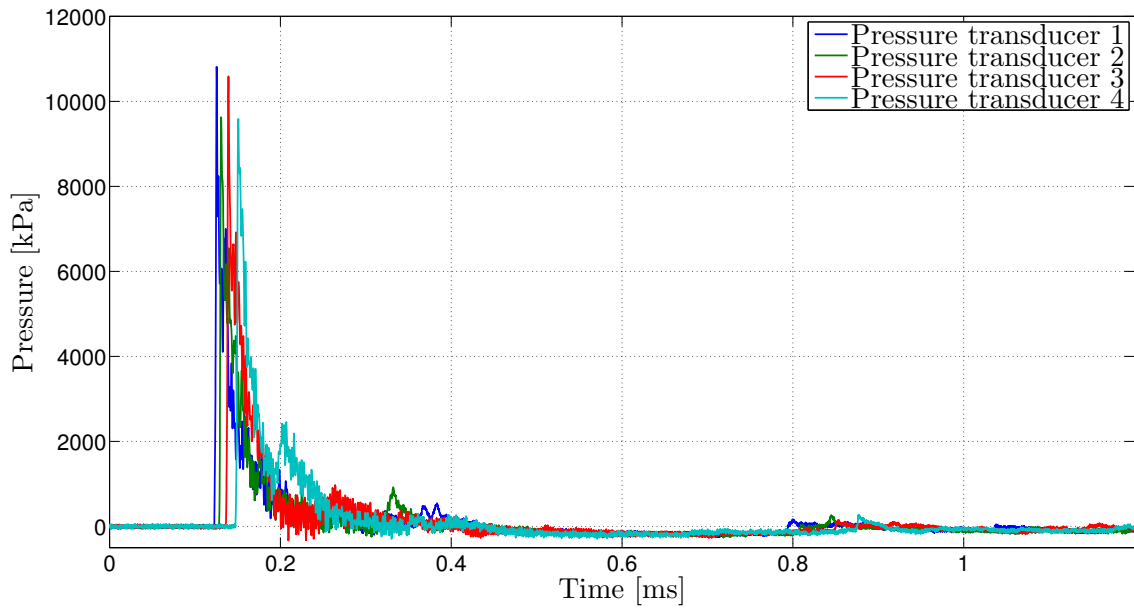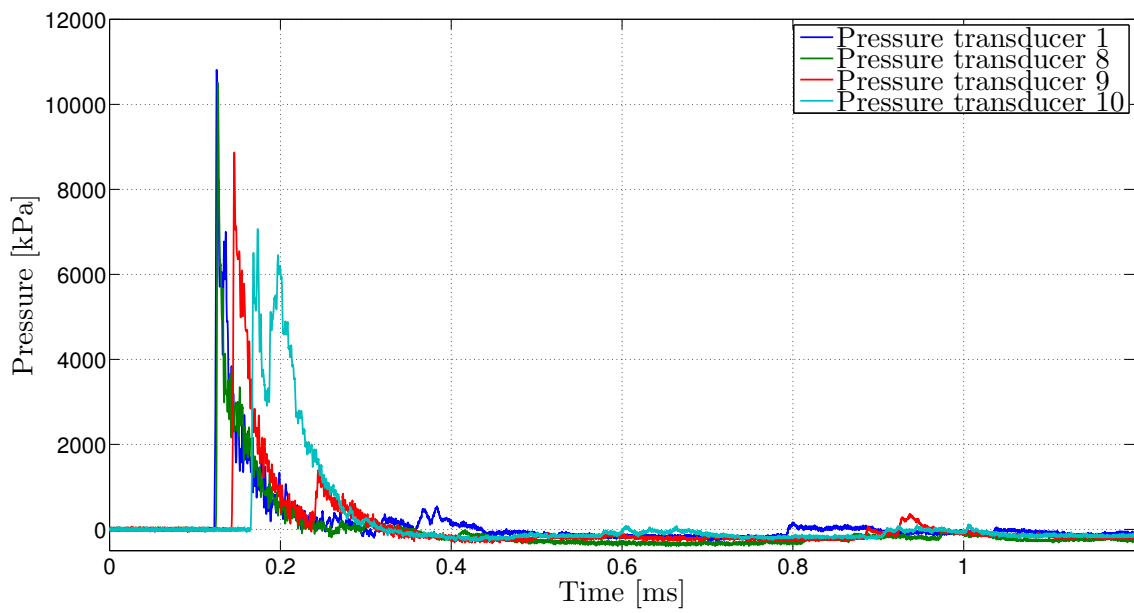
(a) Pressure transducers along the vertical.

(b) Pressure transducers along the diagonal.

A5
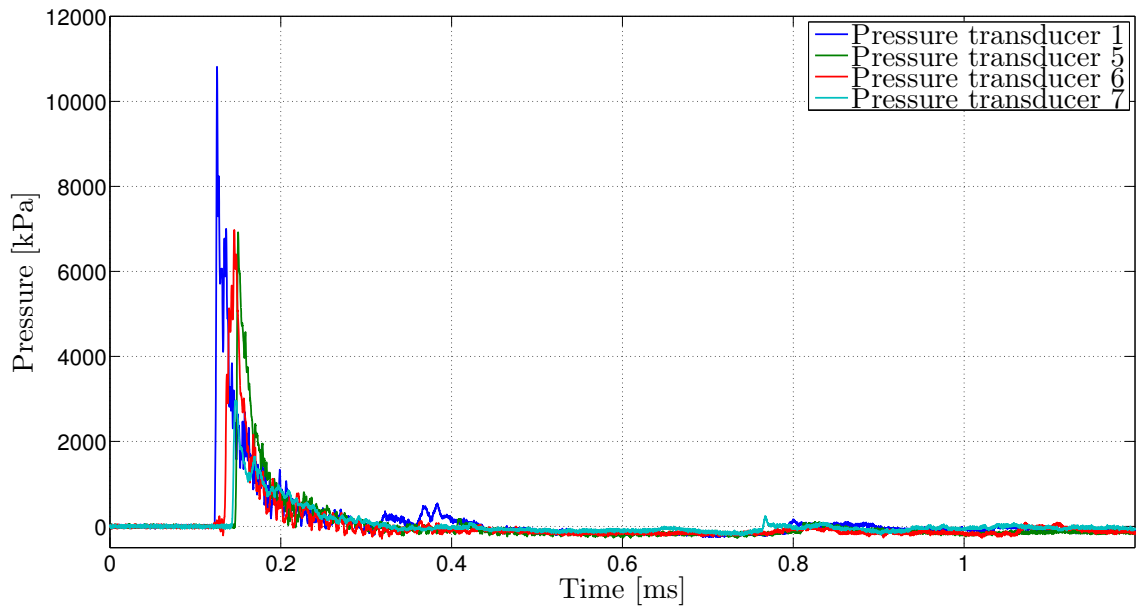
(c) Pressure transducers in the middle and in the clamping frame.

Figure A.3: Pressure in calibration test R13.
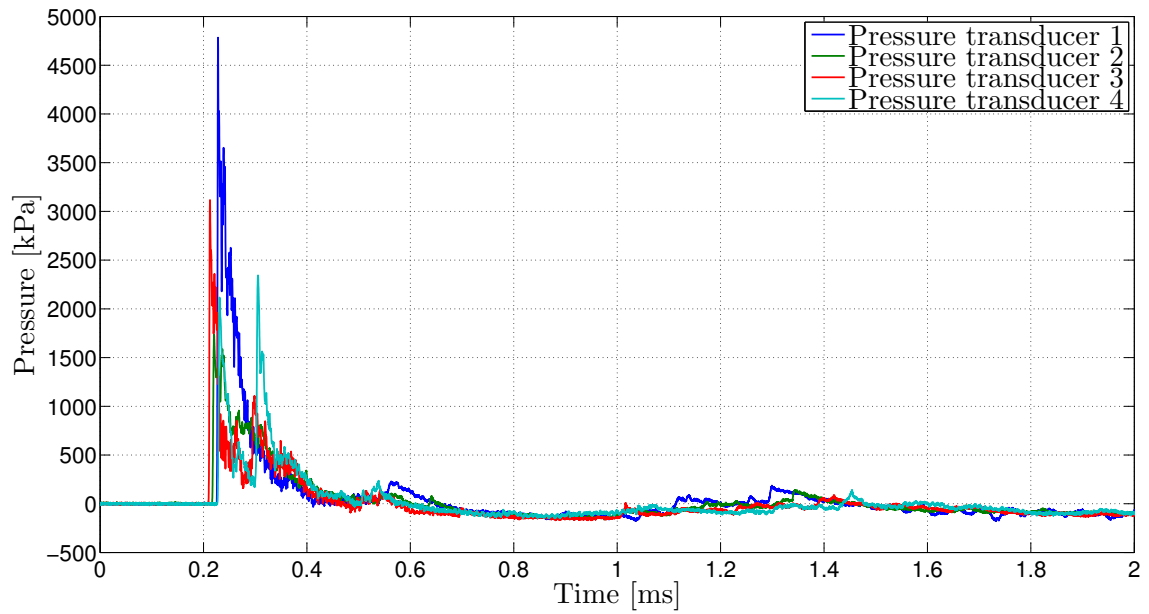
(a) Pressure transducers along the vertical.
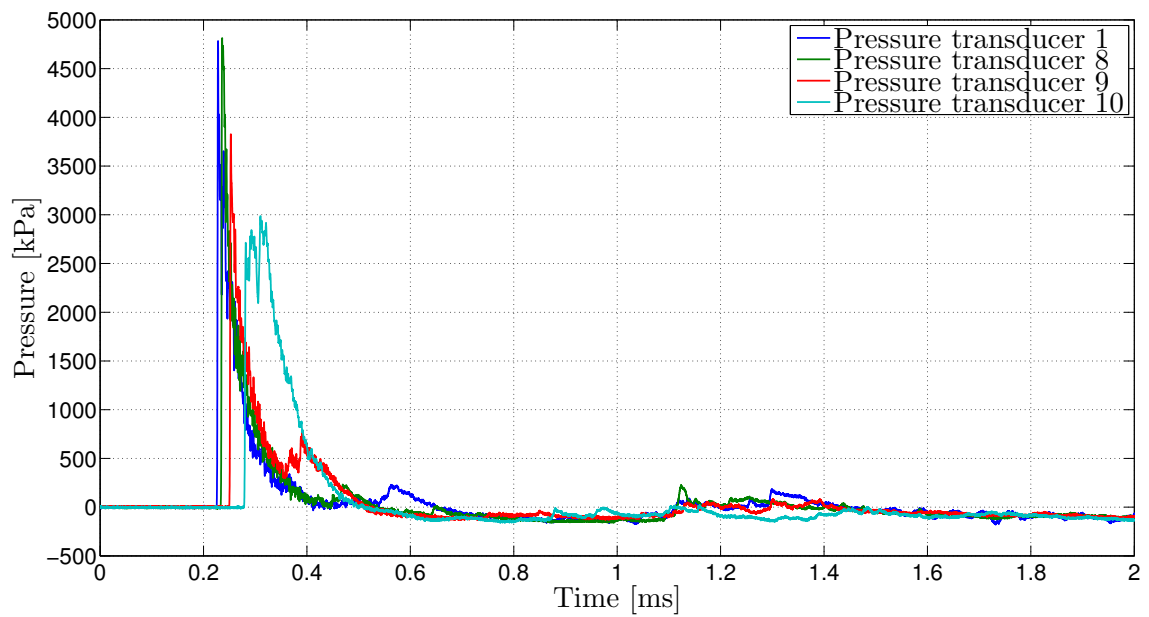
(b) Pressure transducers along the diagonal.
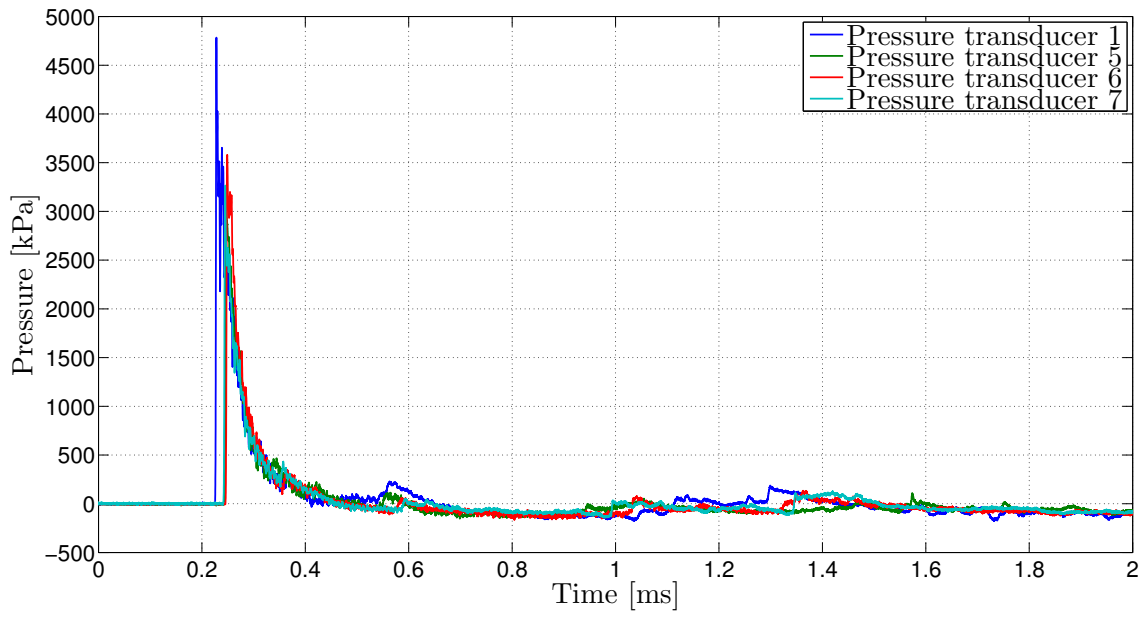
(c) Pressure transducers in the middle and in the clamping frame.

Figure A.4: Pressure in calibration test R21.
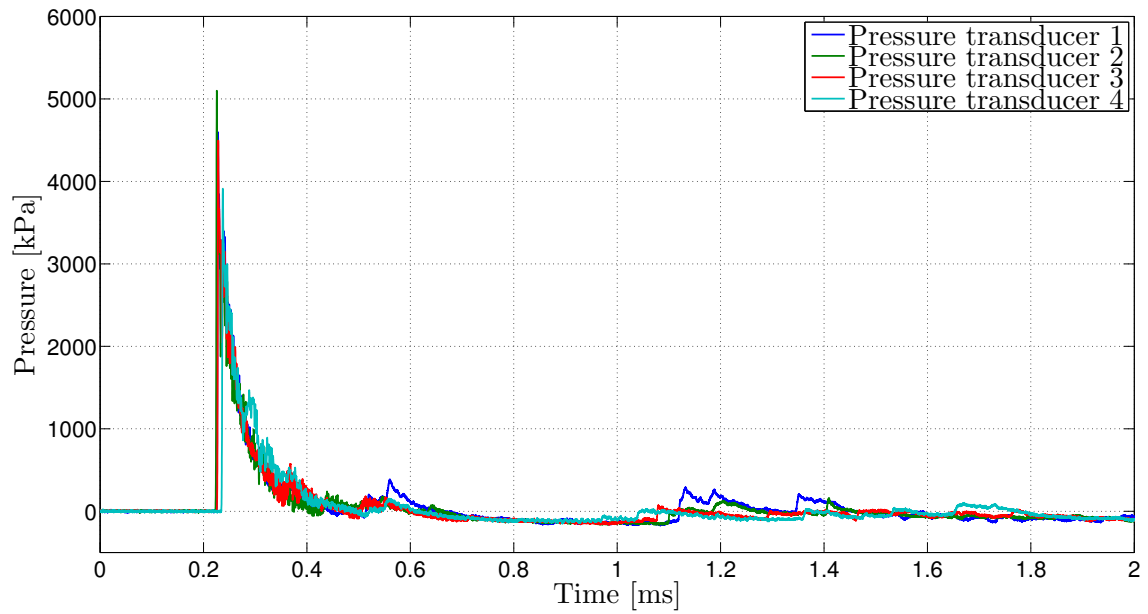
(a) Pressure transducers along the vertical.
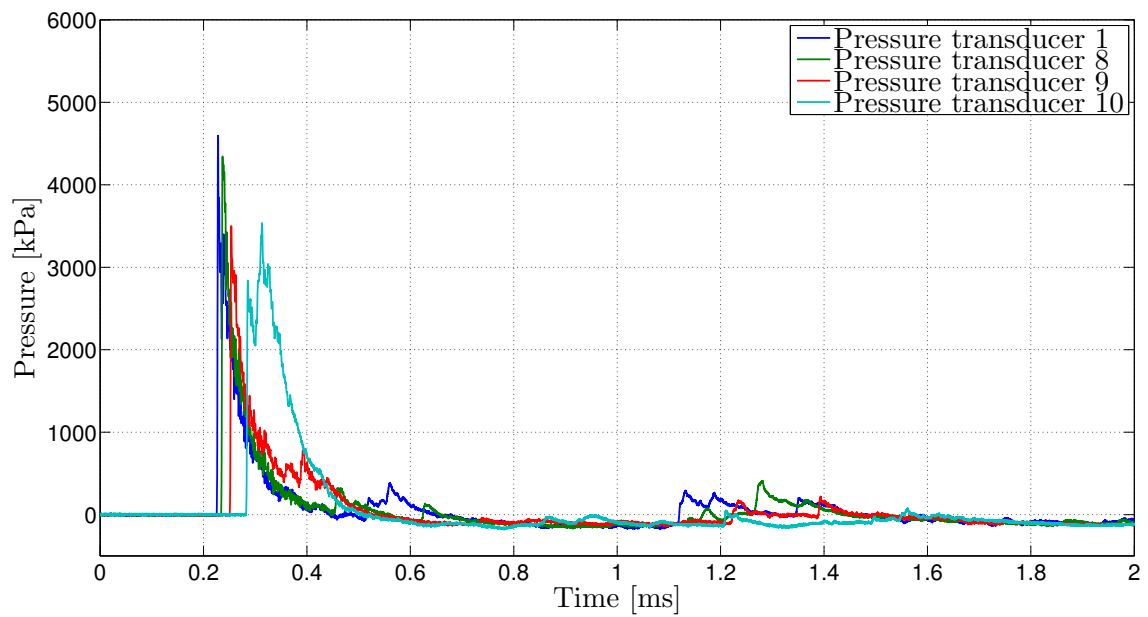
(b) Pressure transducers along the diagonal.
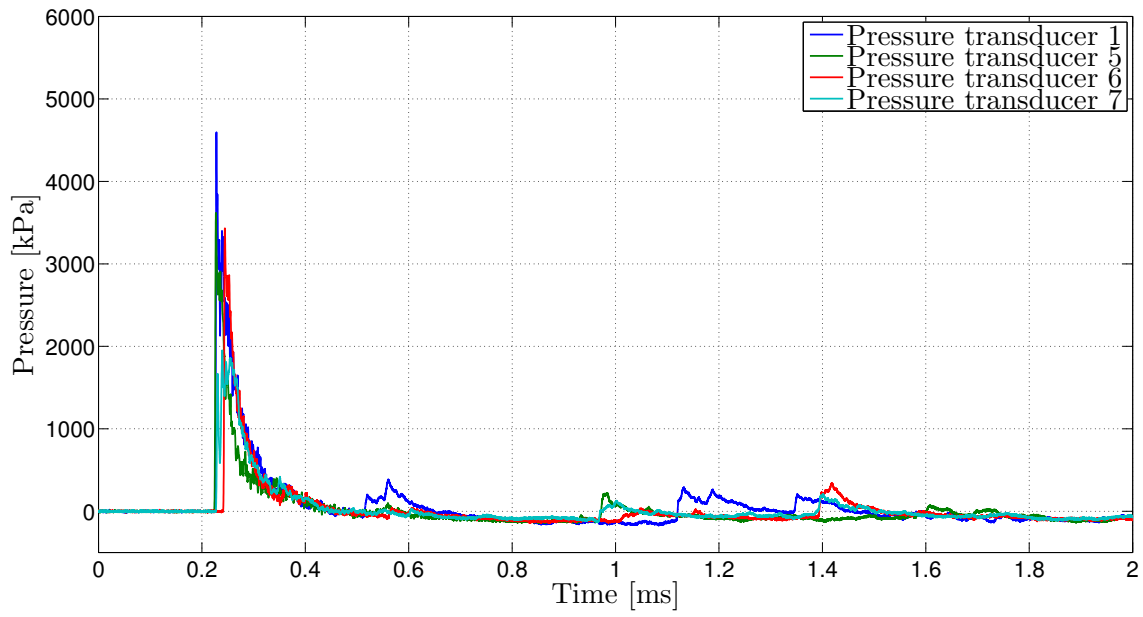
(c) Pressure transducers in the middle and in the clamping frame.

Figure A.5: Pressure in calibration test R22.
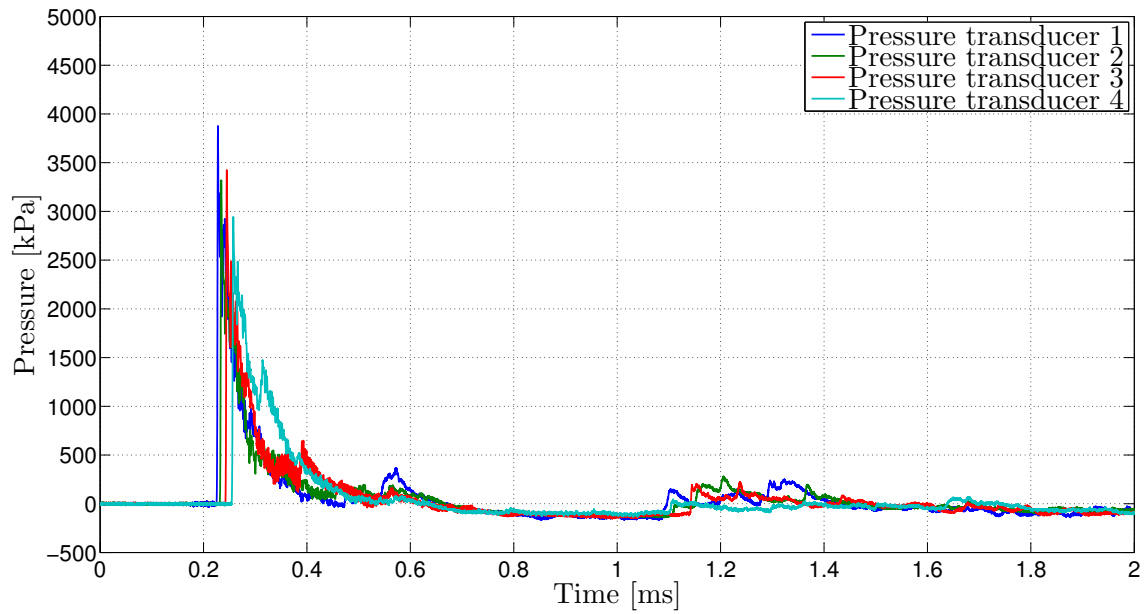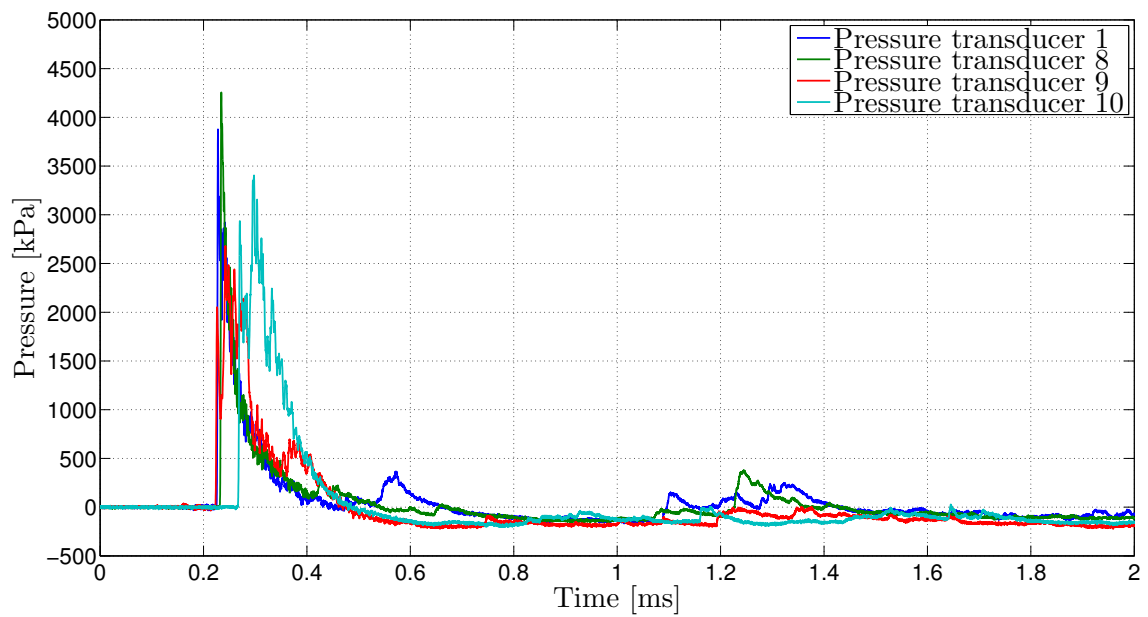
(a) Pressure transducers along the vertical.

(b) Pressure transducers along the diagonal.

A11
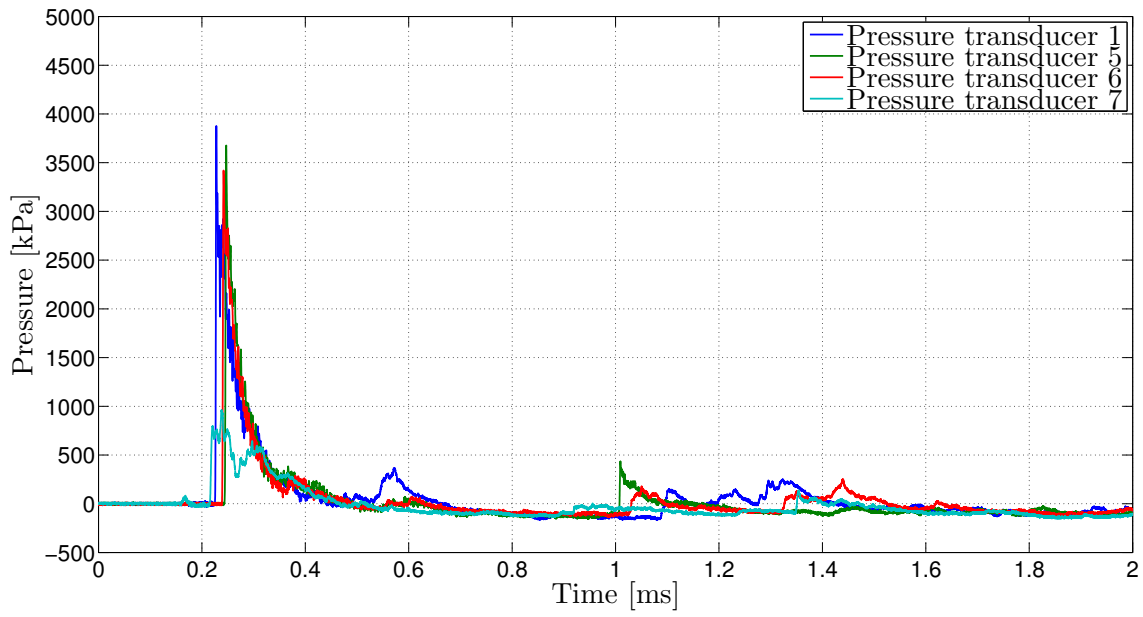
(c) Pressure transducers in the middle and in the clamping frame.

Figure A.6: Pressure in calibration test R23.
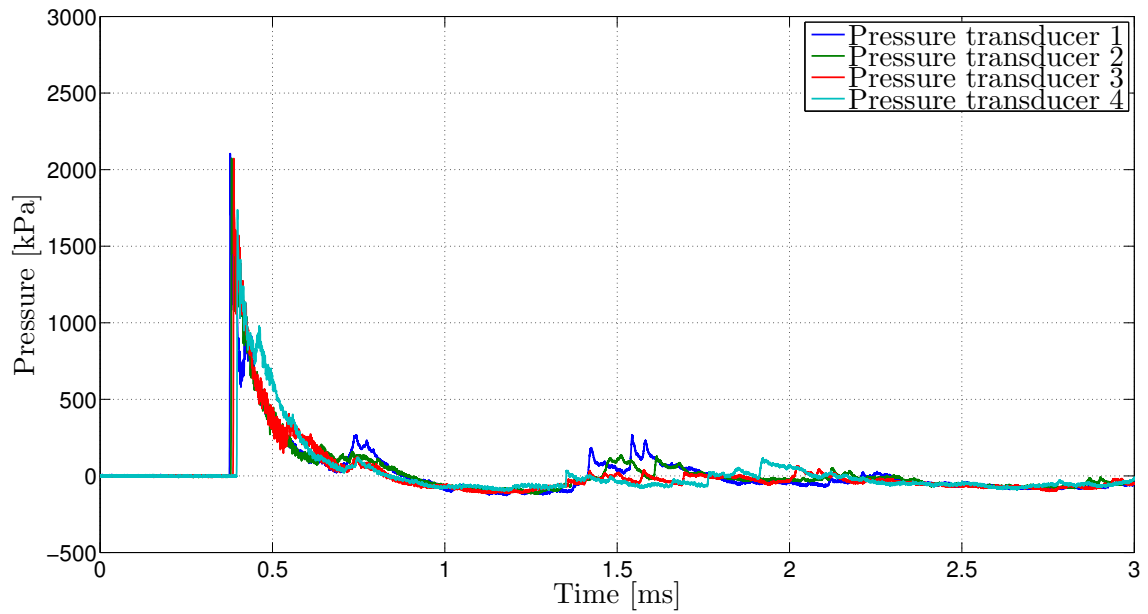
(a) Pressure transducers along the vertical.
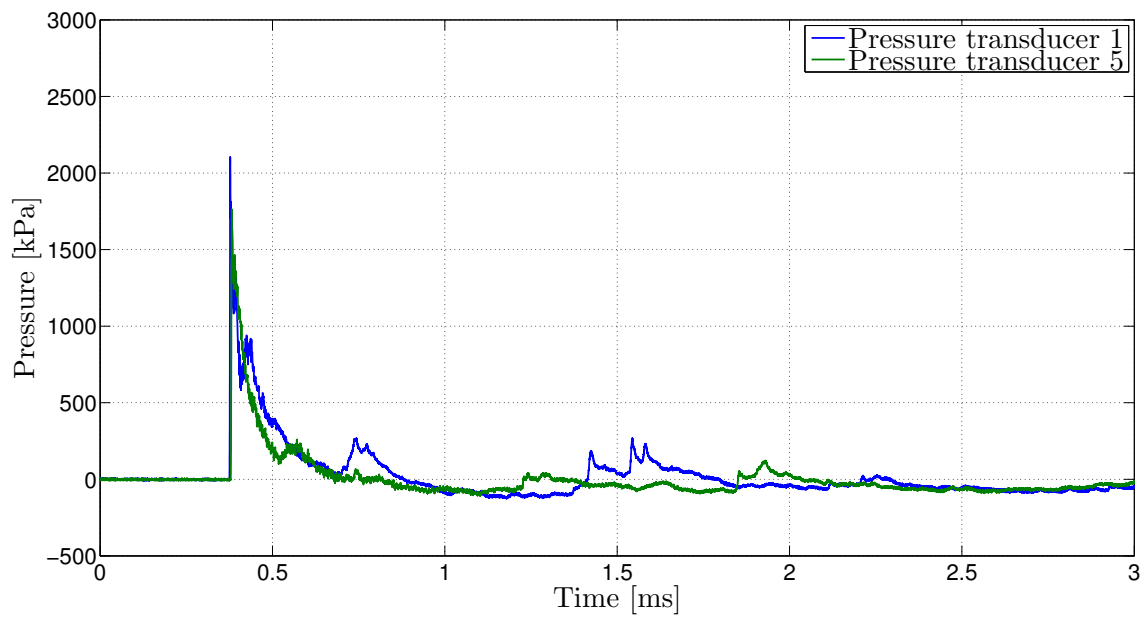
(b) Pressure transducers in the middle and in the clamping frame.

Figure A.7: Pressure in calibration test R31.
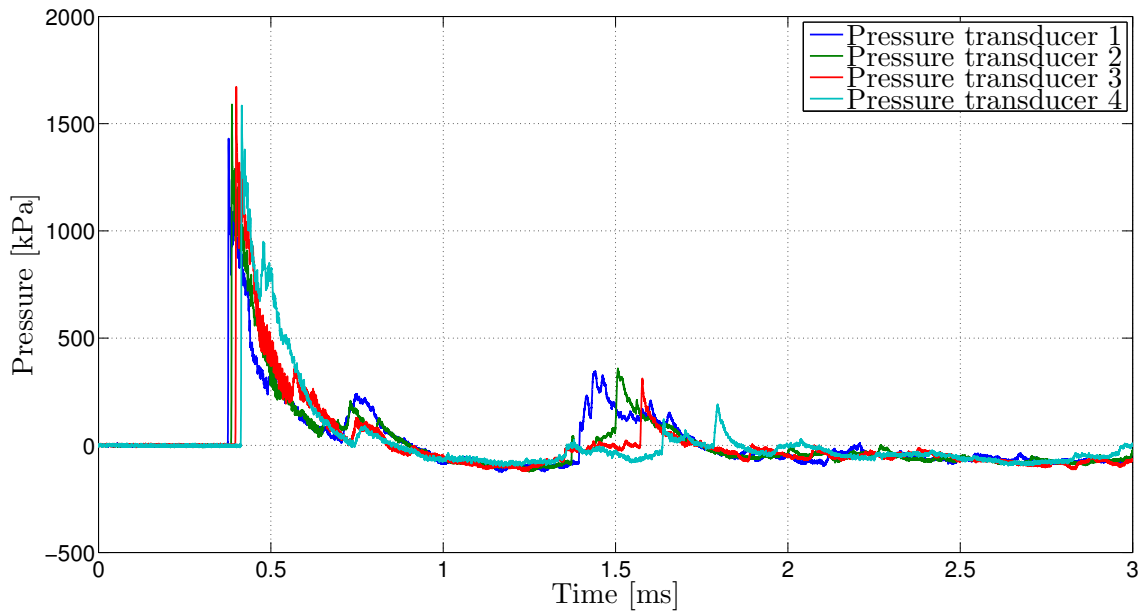
A13

(a) Pressure transducers along the vertical.
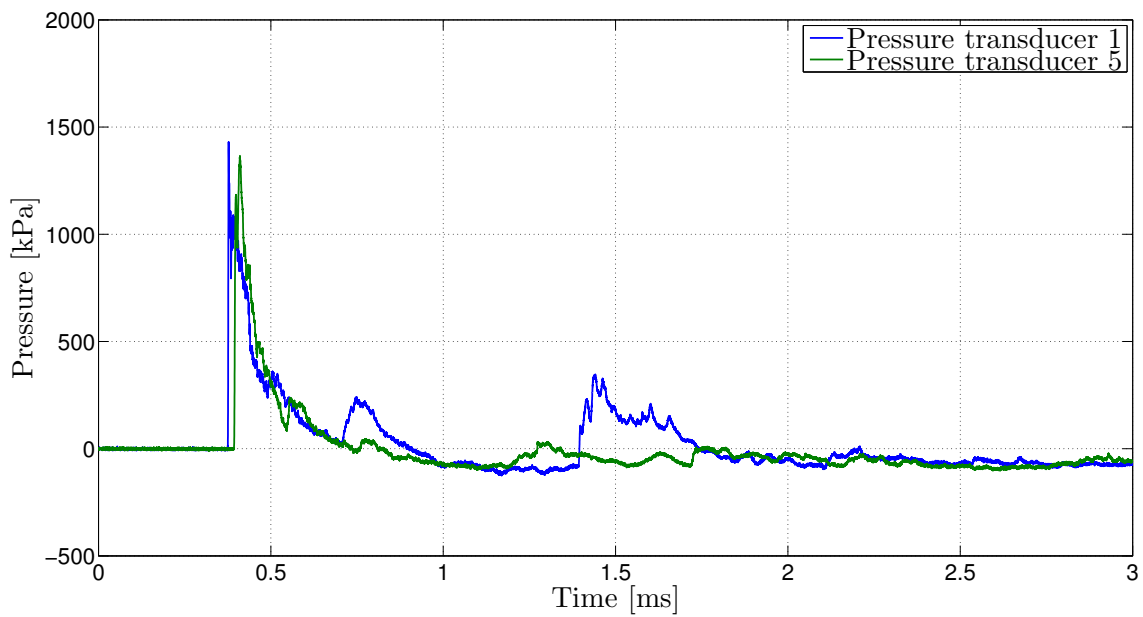
(b) Pressure transducers in the middle and in the clamping frame.

Figure A.8: Pressure in calibration test R32.
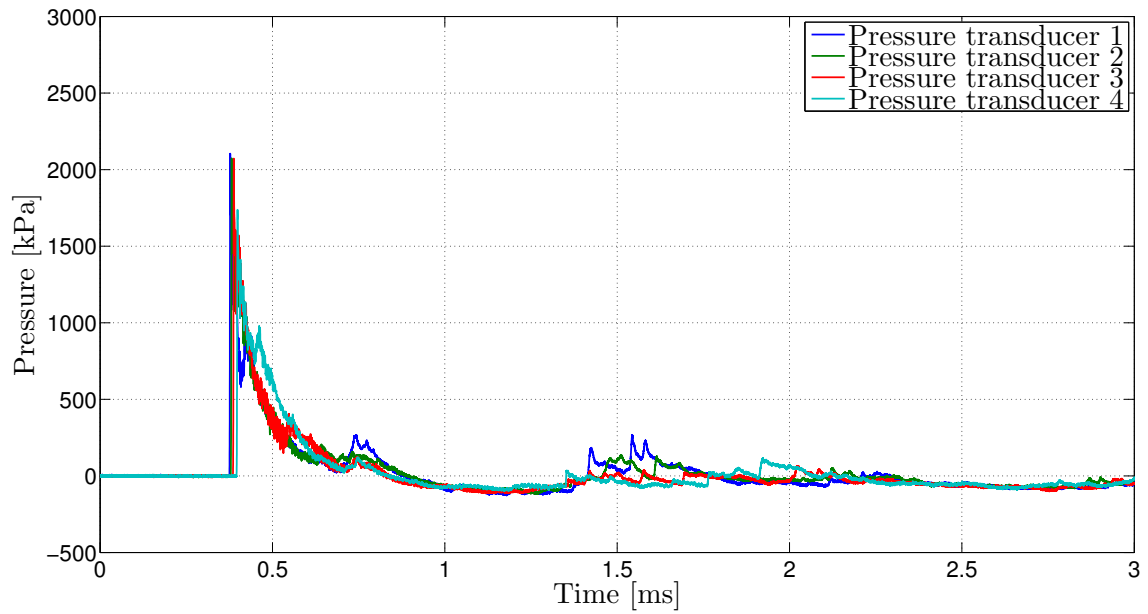
(a) Pressure transducers along the vertical.
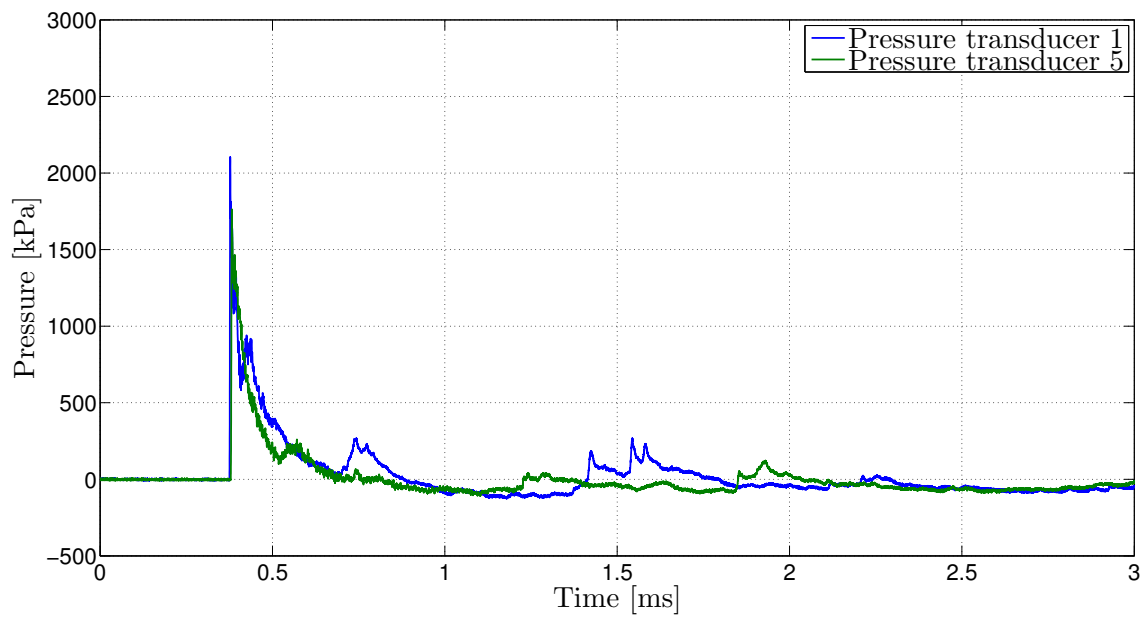
(b) Pressure transducers in the middle and in the clamping frame.

Figure A.9: Pressure in calibration test R33.
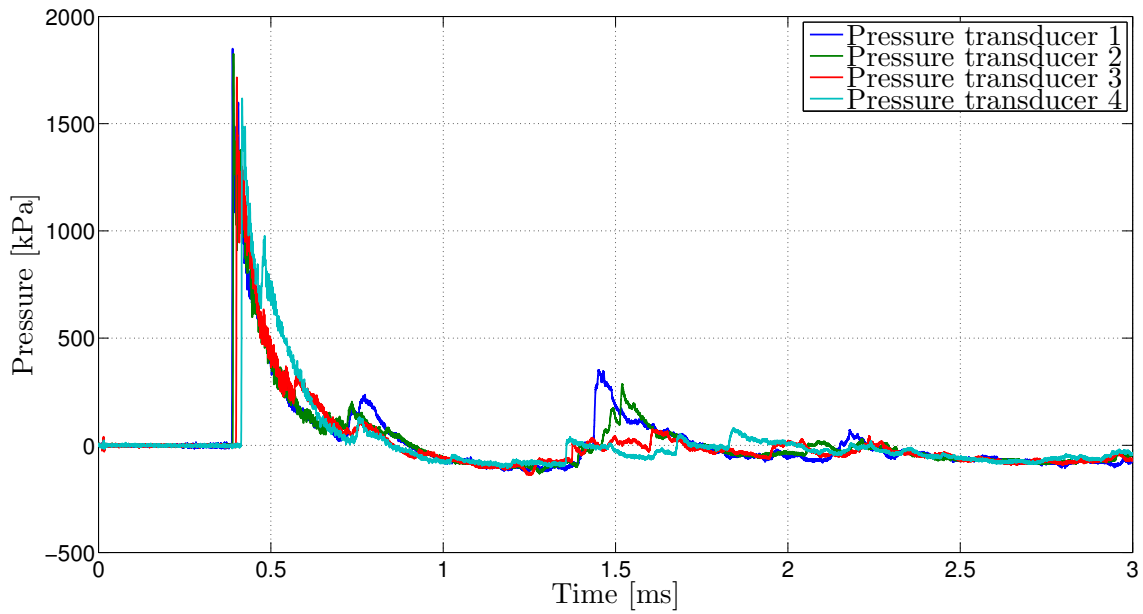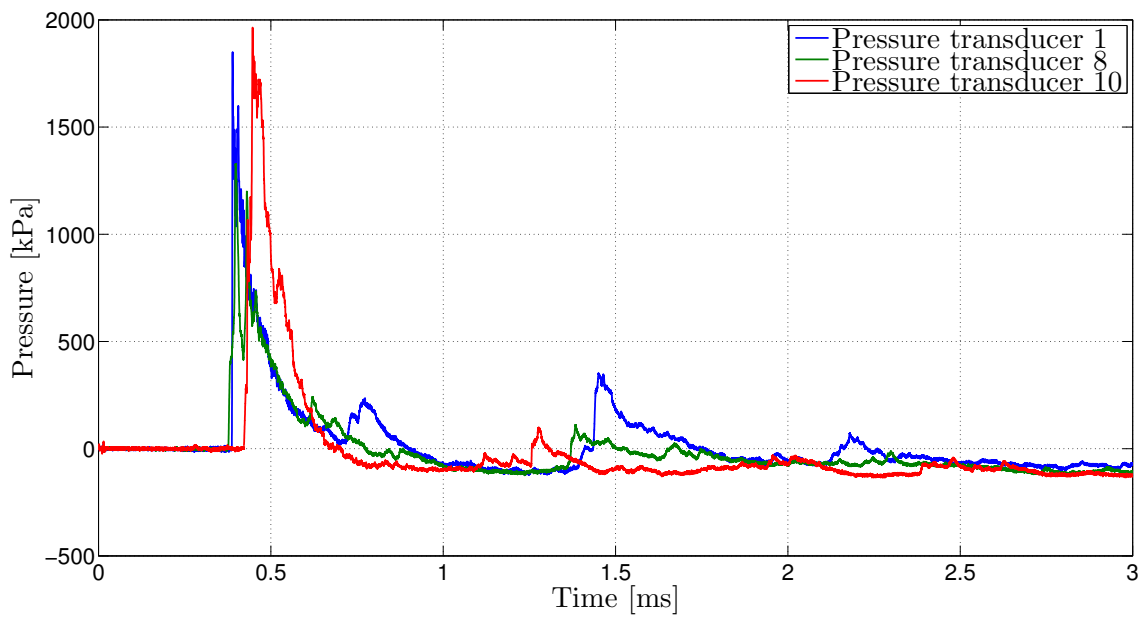
(a) Pressure transducers along the vertical.

(b) Pressure transducers along the diagonal.
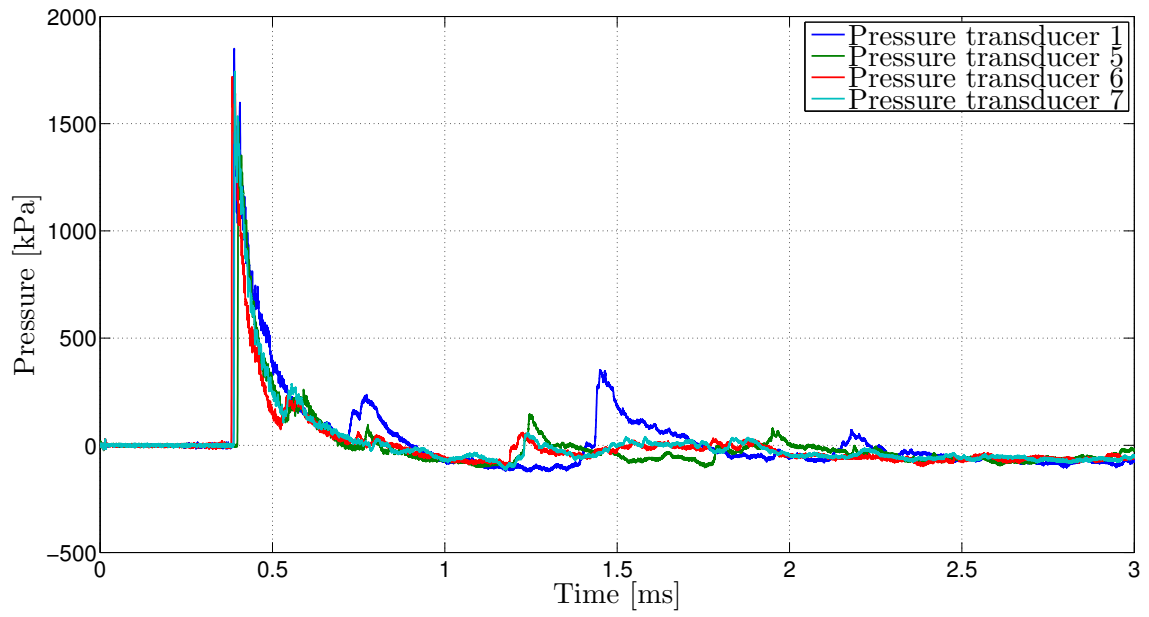
(c) Pressure transducers in the middle and in the clamping frame.

Figure A.10: Pressure in calibration test R31-2.
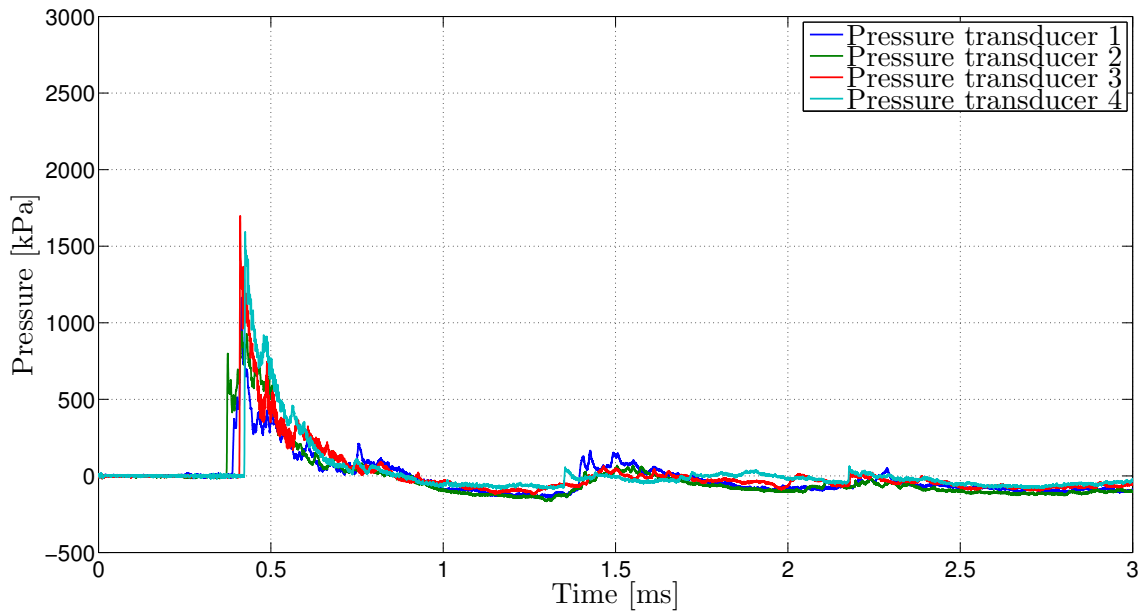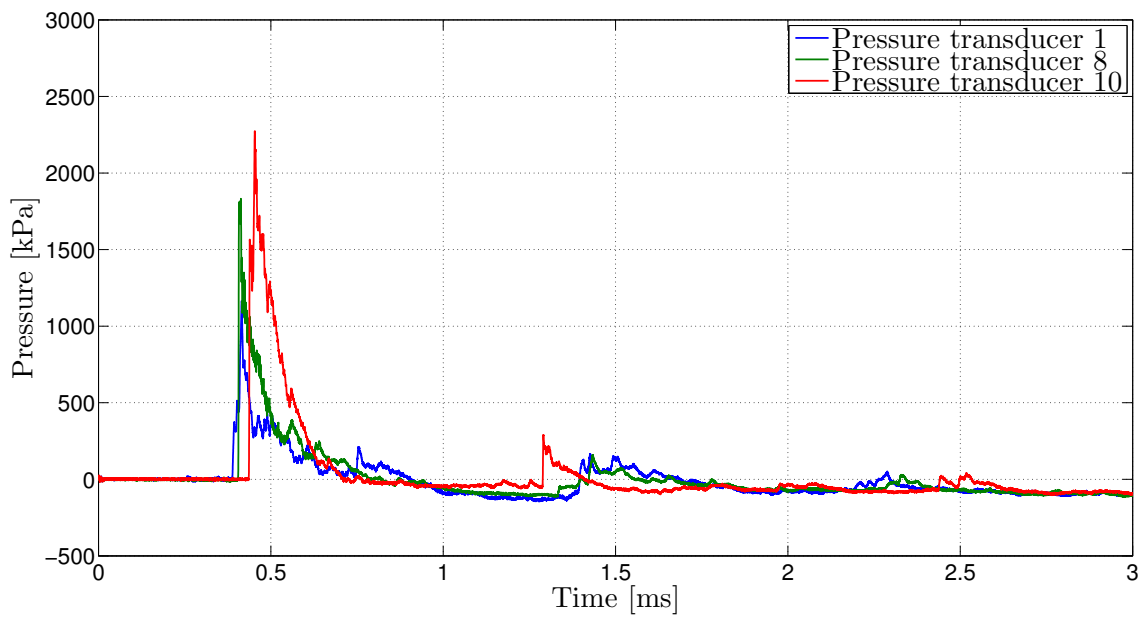
(a) Pressure transducers along the vertical.

(b) Pressure transducers along the diagonal.
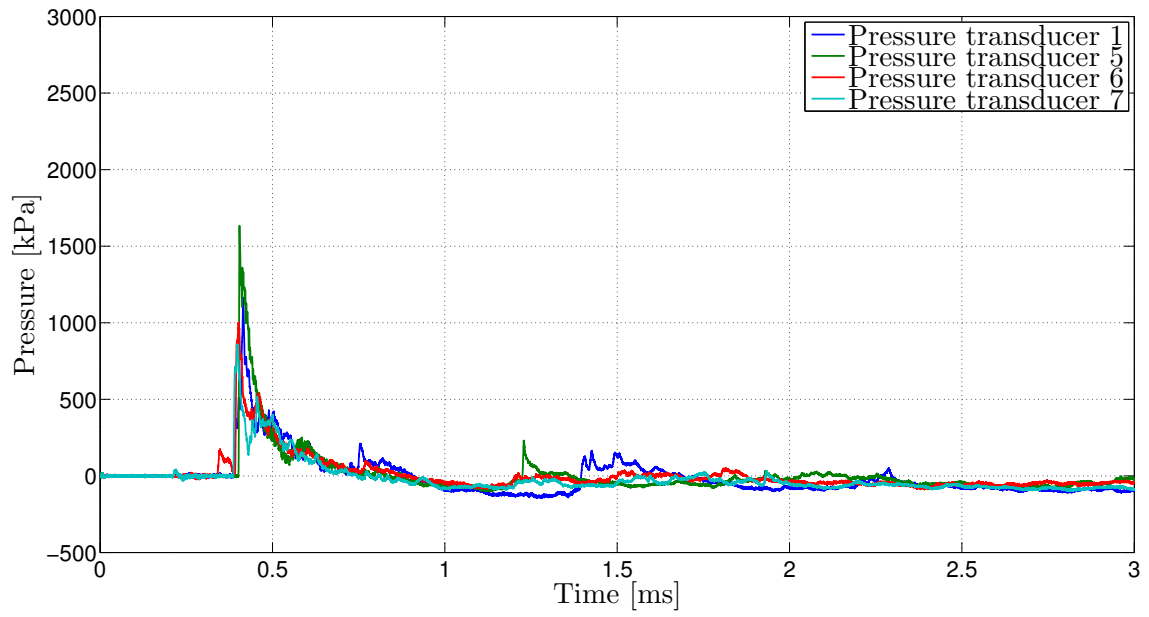
(c) Pressure transducers in the middle and in the clamping frame.

Figure A.11: Pressure in calibration test R32-2.
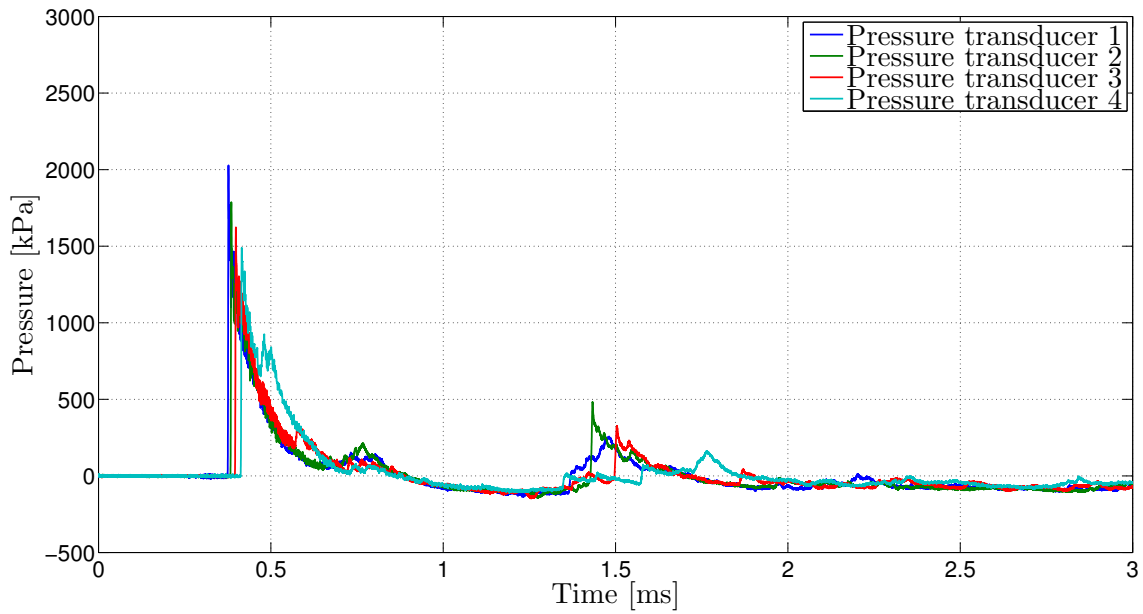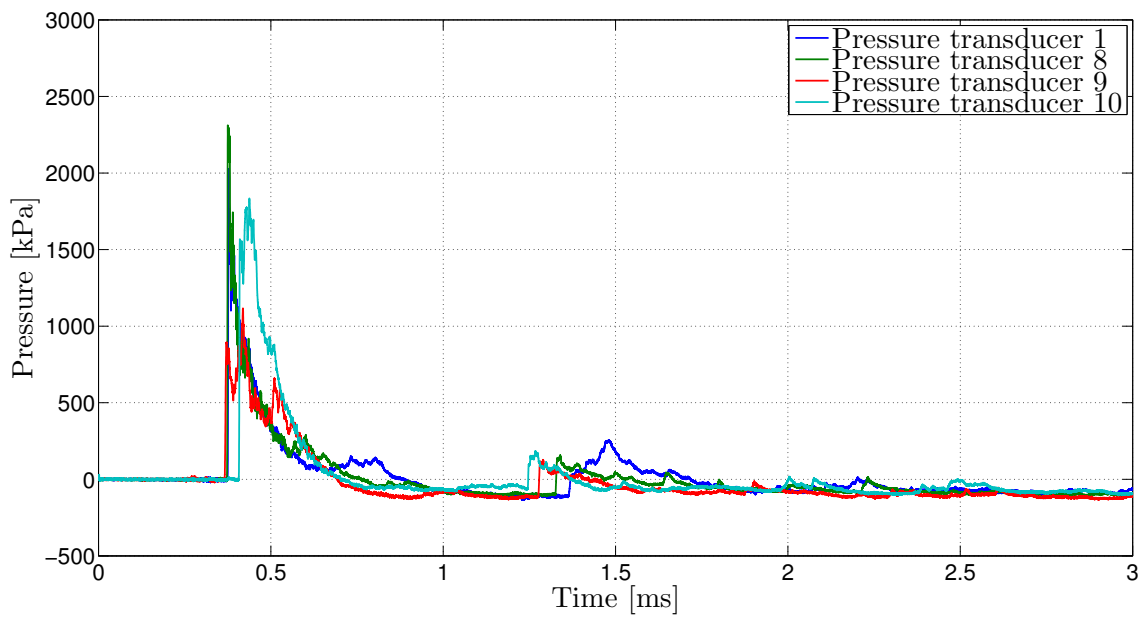
(a) Pressure transducers along the vertical.

(b) Pressure transducers along the diagonal.
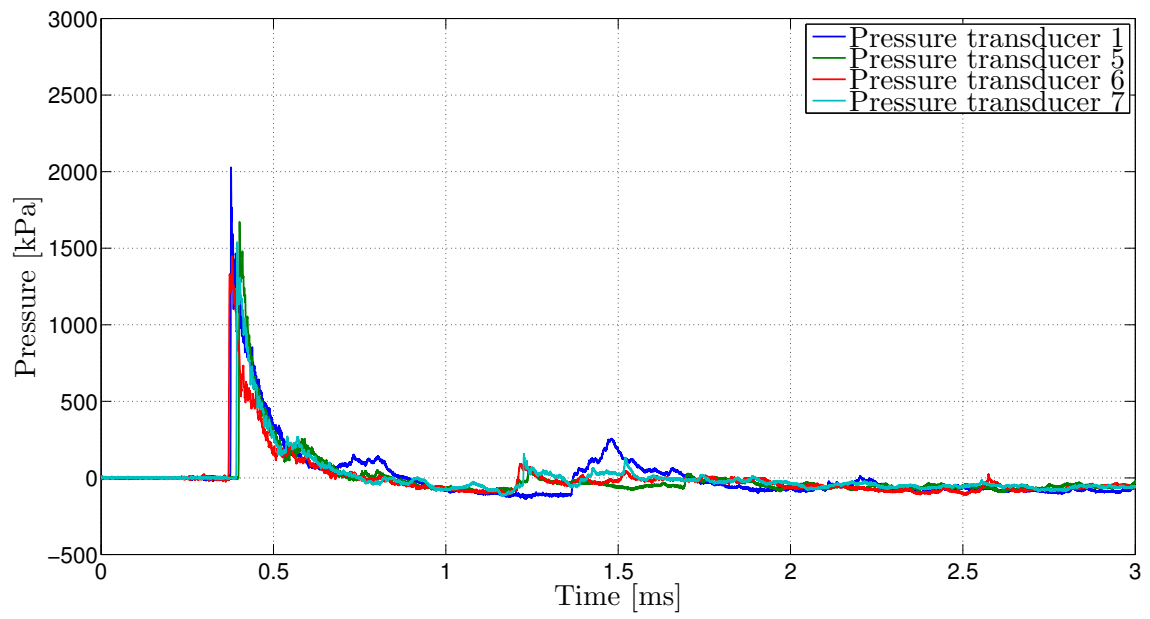
(c) Pressure transducers in the middle and in the clamping frame.

Figure A.12: Pressure in calibration test R33-2.

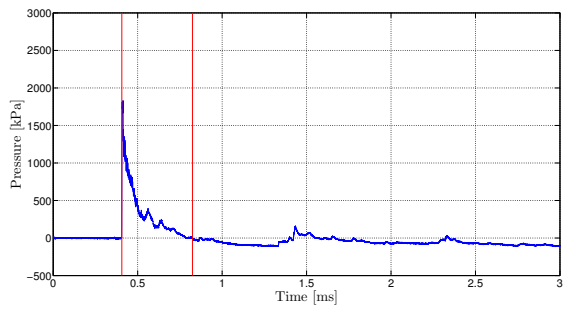## A.2 Pressure curves used for calculating positive impulse
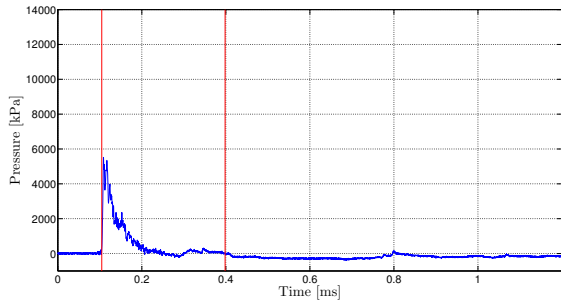
(a) Pressure transducer 1
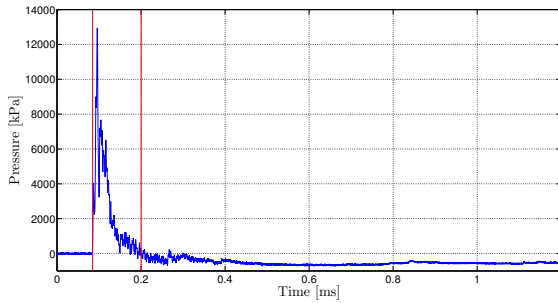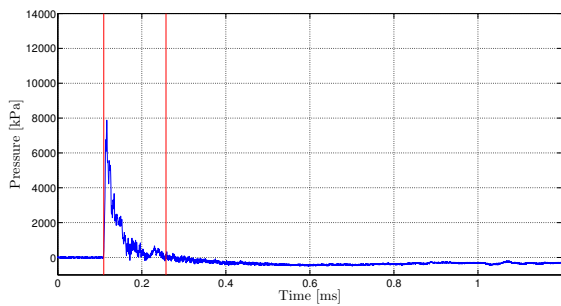
(b) Pressure transducer 2

(c) Pressure transducer 3

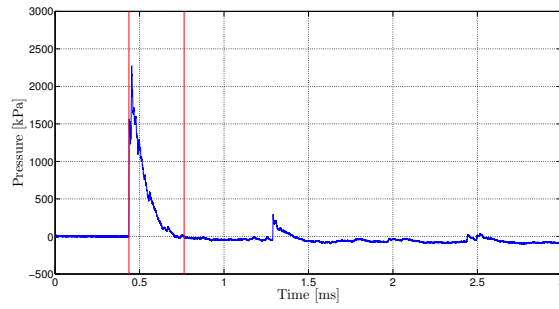(d) Pressure transducer 4

(e) Pressure transducer 5

(f) Pressure transducer 6

(g) Pressure transducer 7
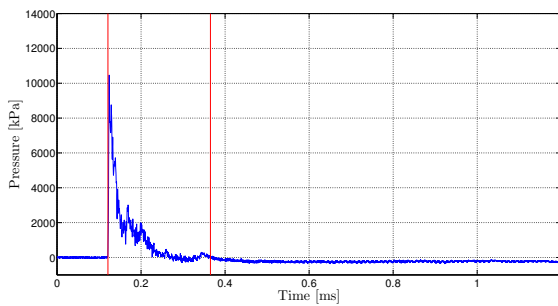
(h) Pressure transducer 8
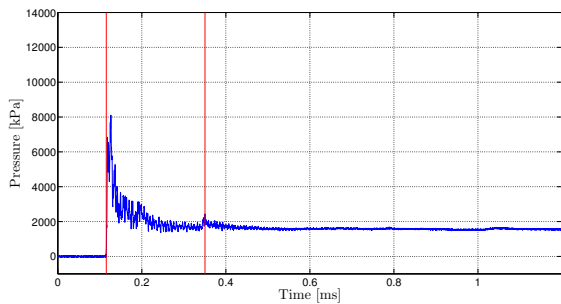
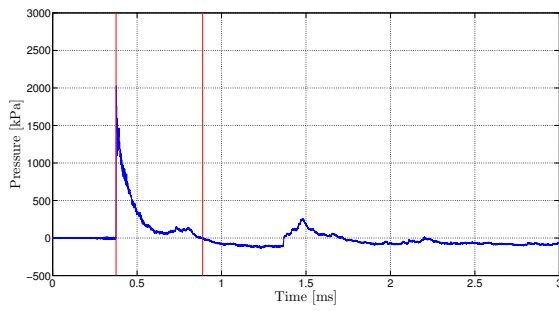(i) Pressure transducer 9
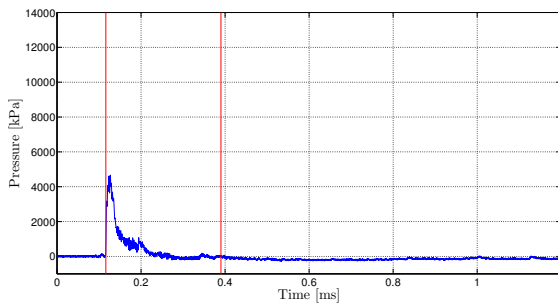
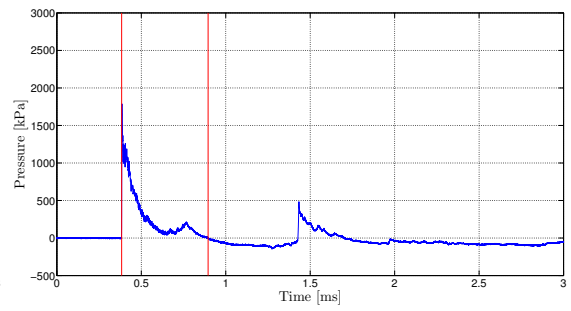(j) Pressure transducer 10
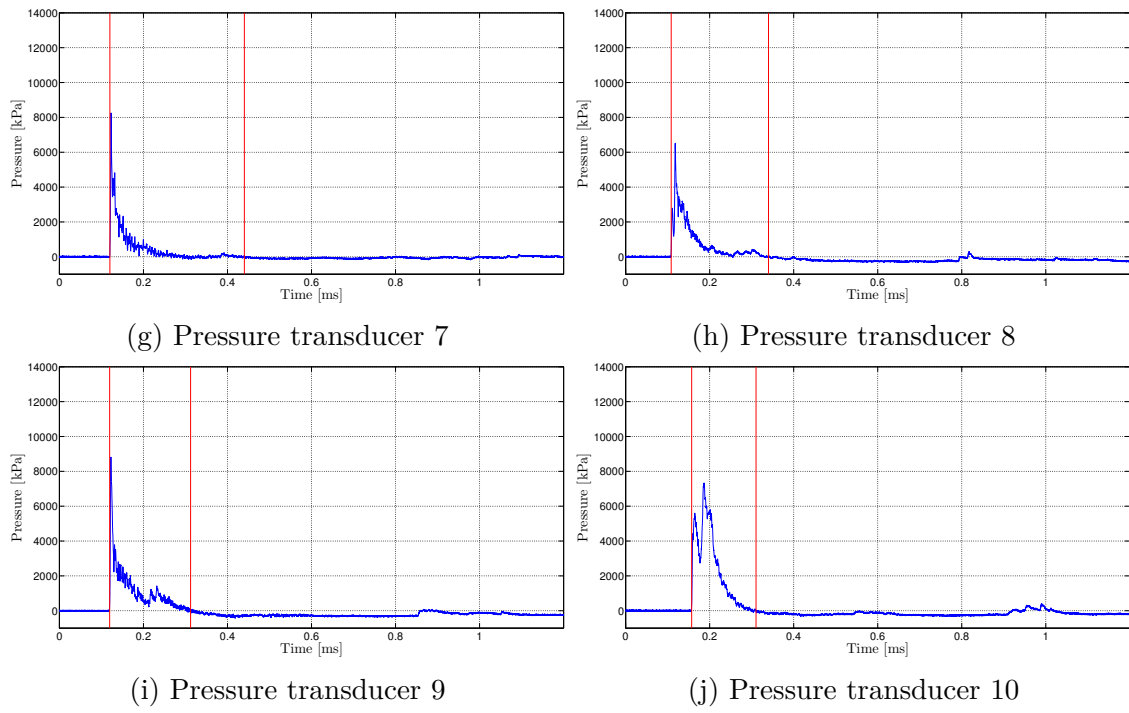
Figure A.13: Pressure from calibration test R11.
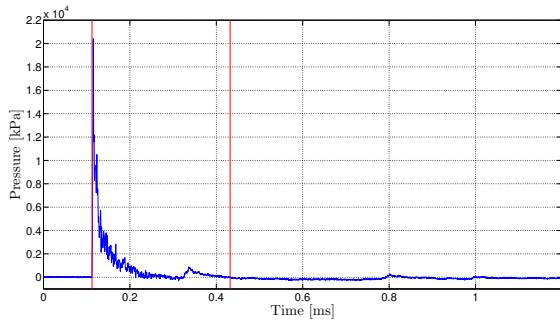
(a) Pressure transducer 1
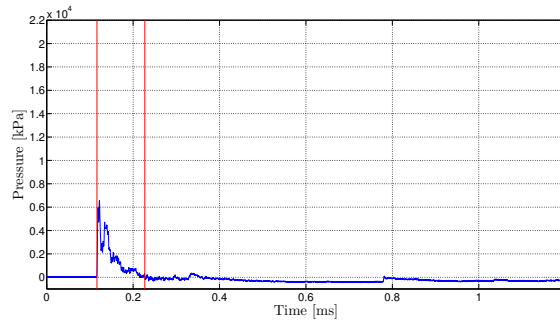
(b) Pressure transducer 2
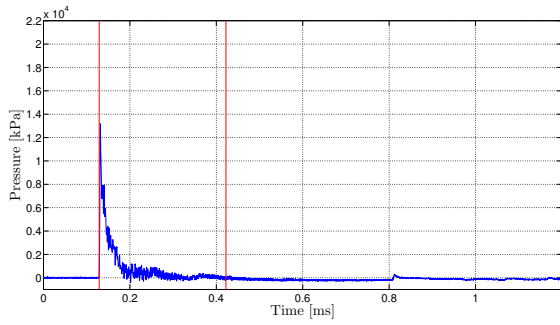
(c) Pressure transducer 3
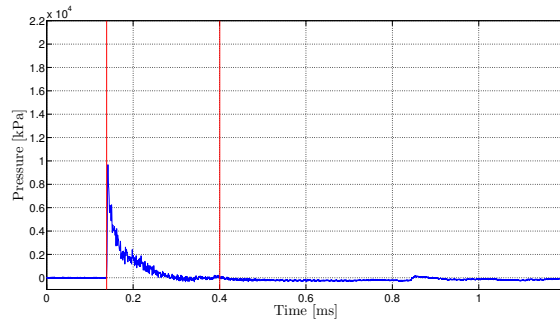
(d) Pressure transducer 4
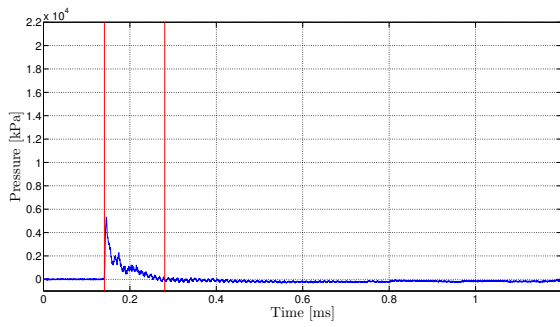
(e) Pressure transducer 5
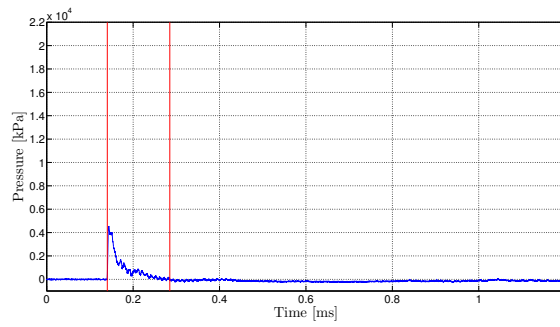
(f) Pressure transducer 6
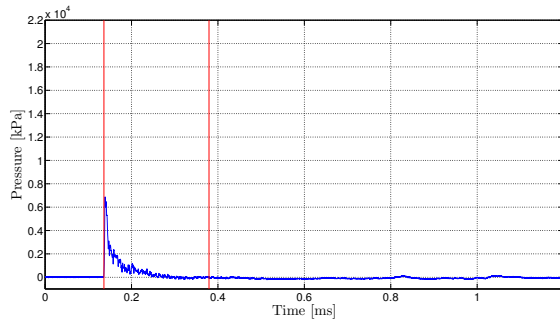
(g) Pressure transducer 7
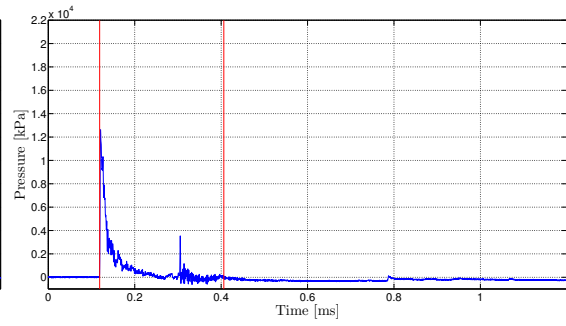
(h) Pressure transducer 8
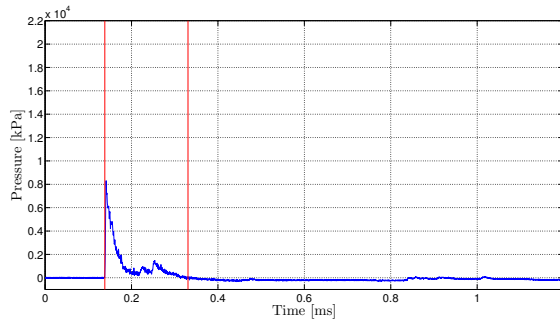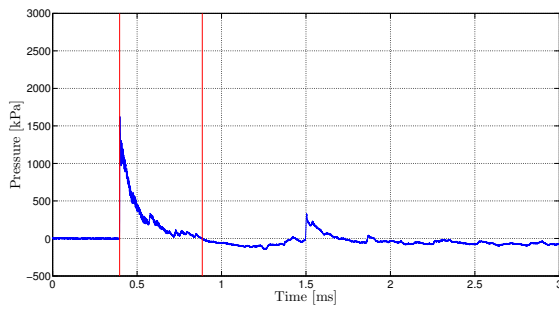
(i) Pressure transducer 9
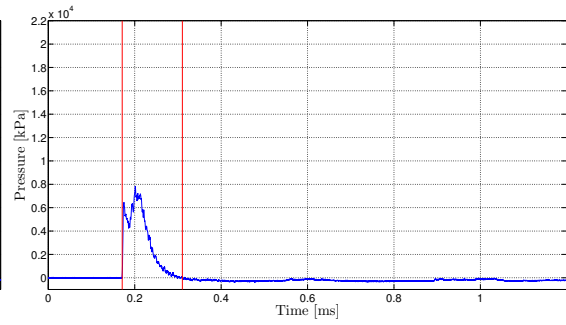
(j) Pressure transducer 10

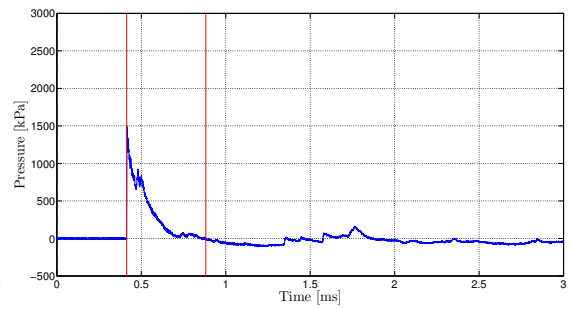Figure A.14: Pressure from calibration test R12.
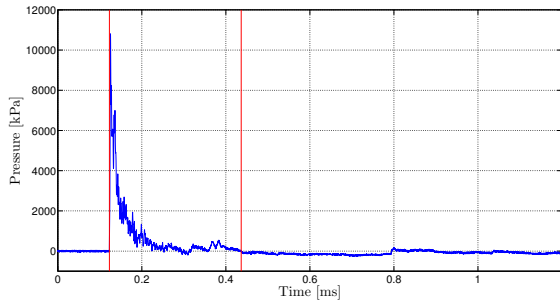
(a) Pressure transducer 1
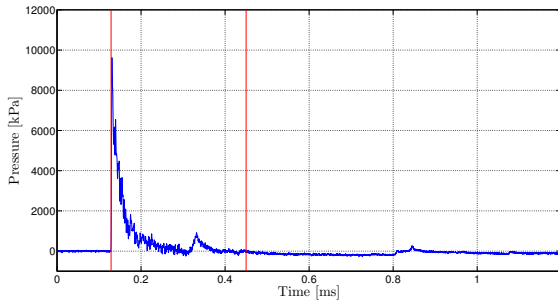
(b) Pressure transducer 2
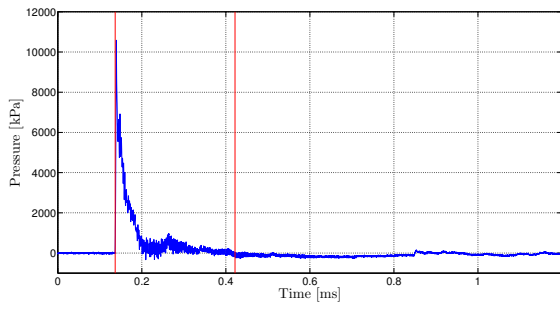
(c) Pressure transducer 3
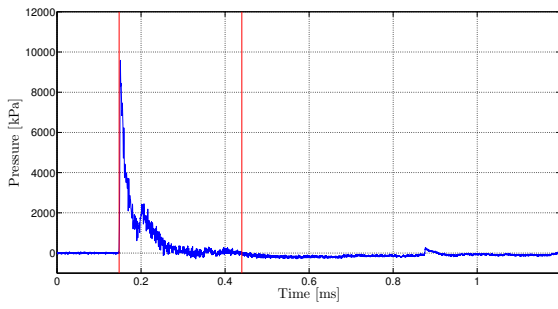
(d) Pressure transducer 4
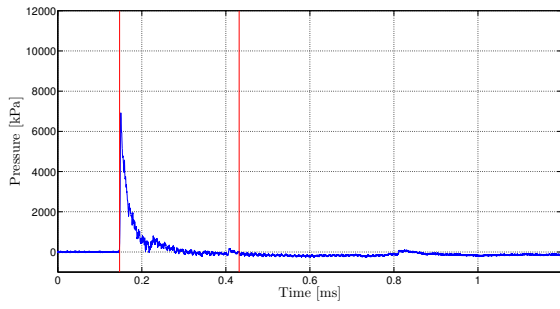
(e) Pressure transducer 5
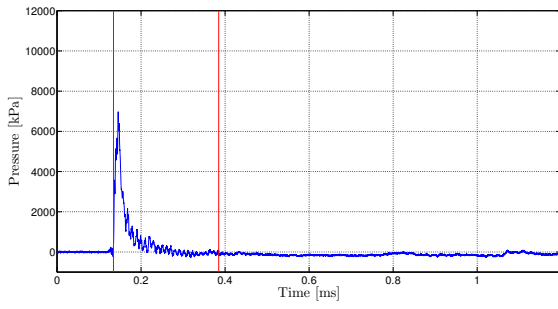
(f) Pressure transducer 6
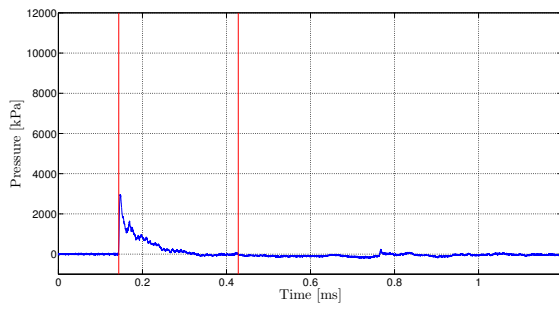
(g) Pressure transducer 7
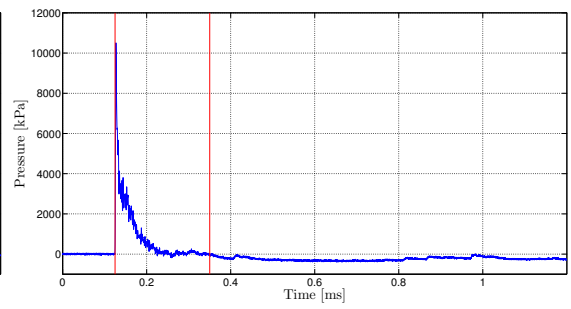
(h) Pressure transducer 8
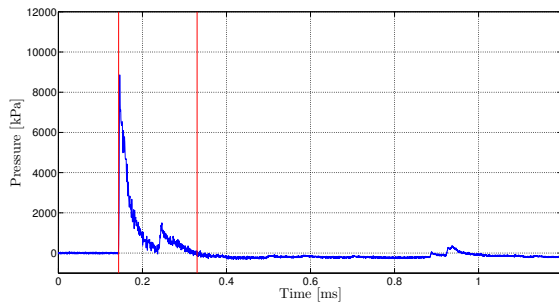
(i) Pressure transducer 9
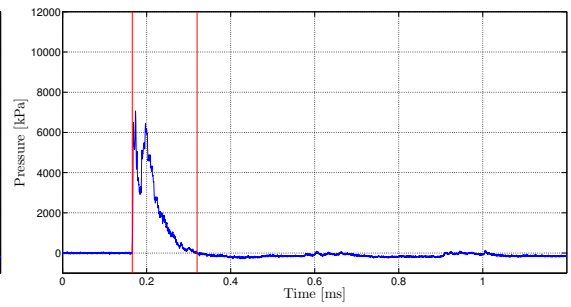
(j) Pressure transducer 10

Figure A.15: Pressure from calibration test R13.
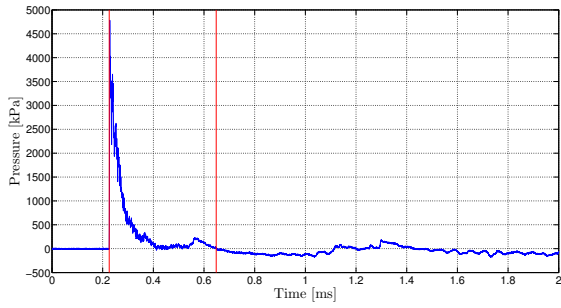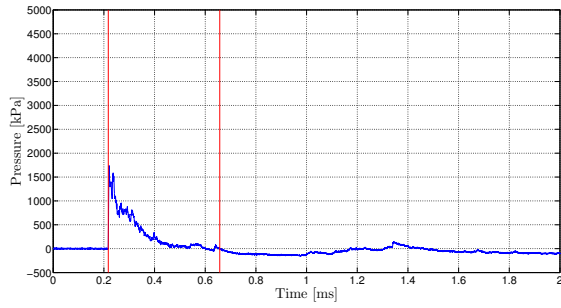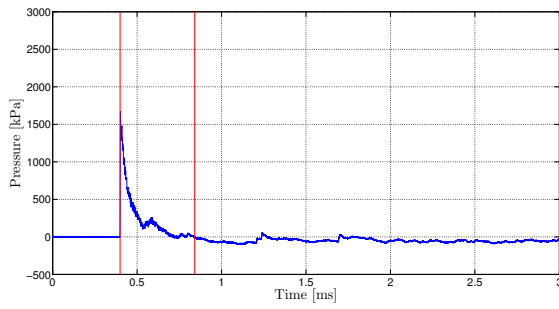
A27

(a) Pressure transducer 1
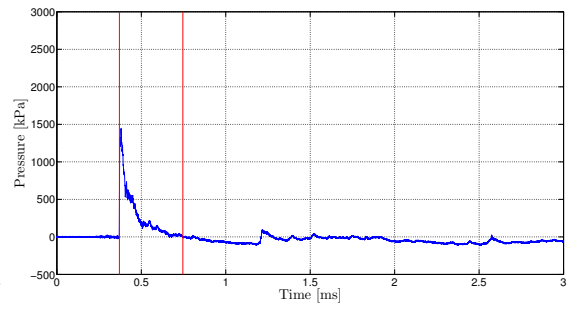

(b) Pressure transducer 2
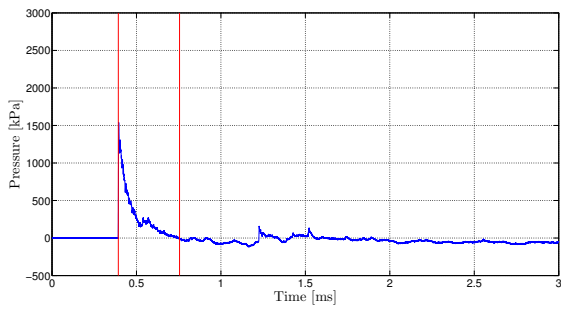

(c) Pressure transducer 3

(d) Pressure transducer 4

(e) Pressure transducer 5

(f) Pressure transducer 6
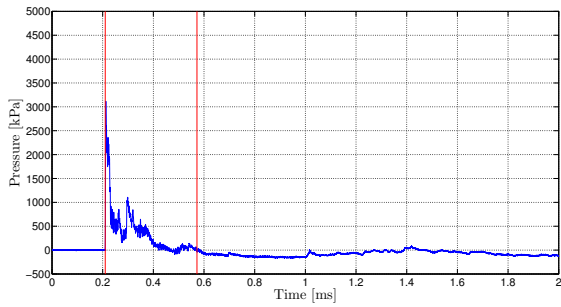
(g) Pressure transducer 7
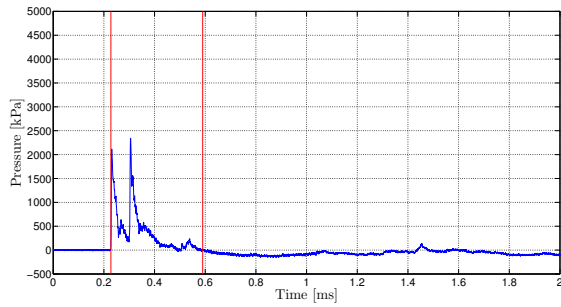
(h) Pressure transducer 8
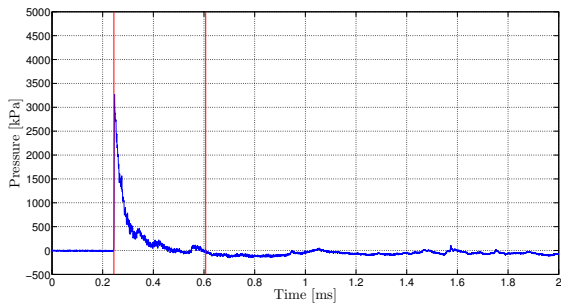
(i) Pressure transducer 9
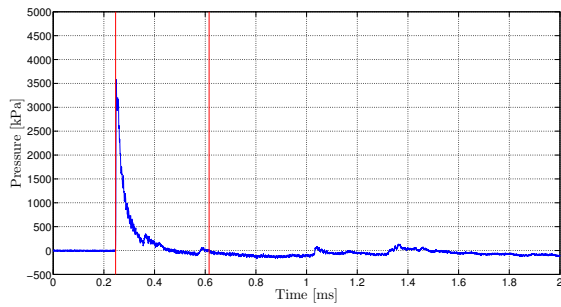
(j) Pressure transducer 10
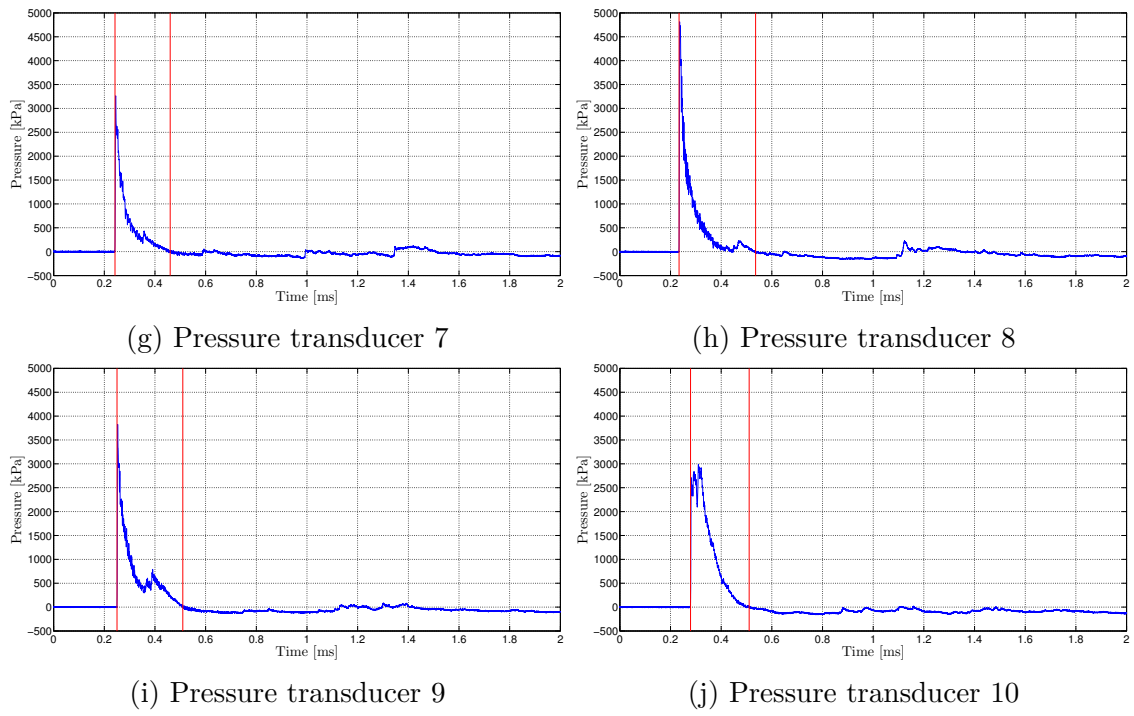
Figure A.16: Pressure from calibration test R21.
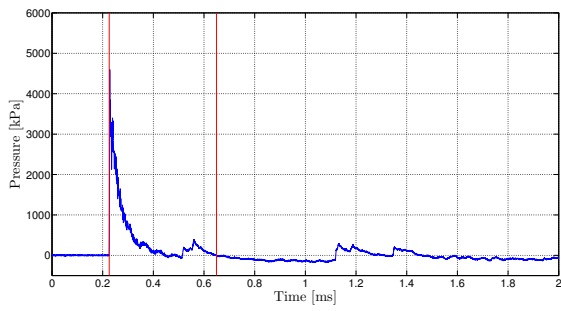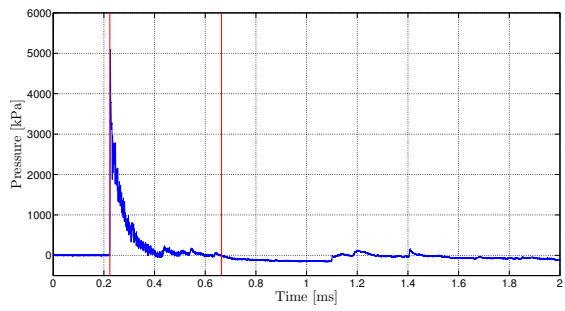
A29

(a) Pressure transducer 1

(b) Pressure transducer 2
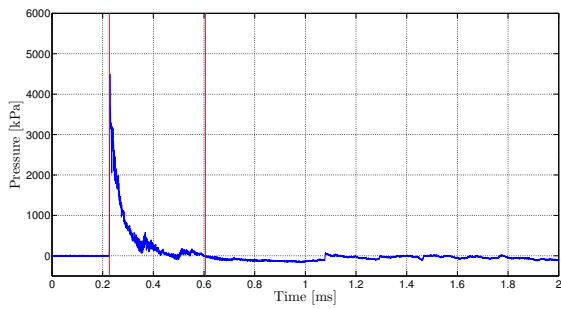
(c) Pressure transducer 3
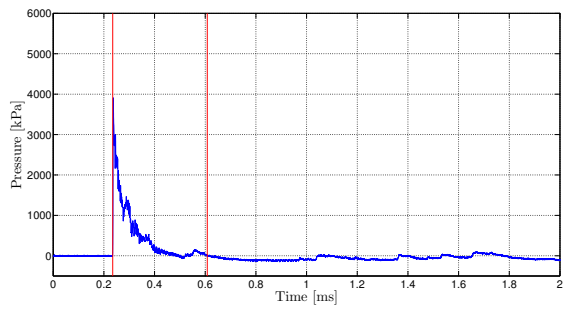
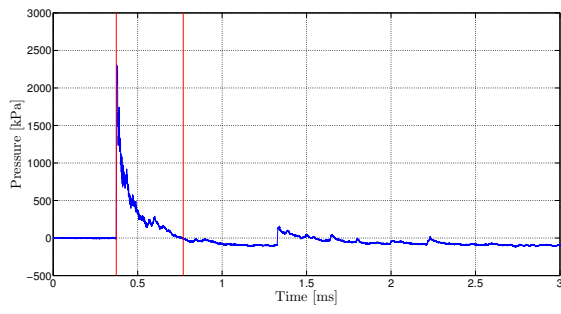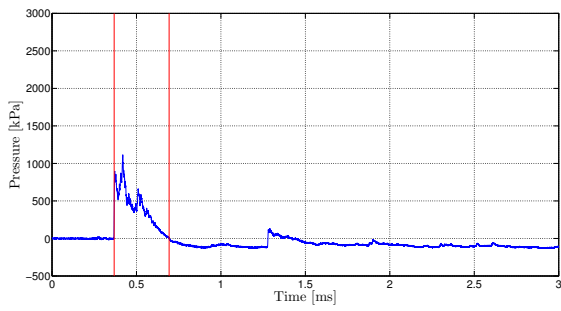(d) Pressure transducer 4
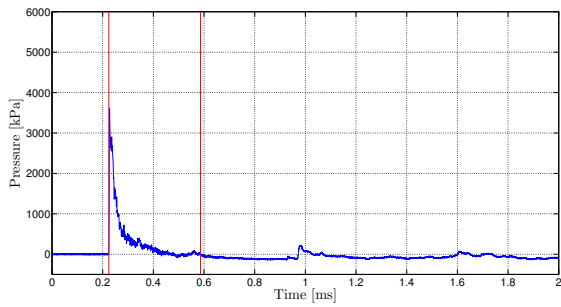
(e) Pressure transducer 5
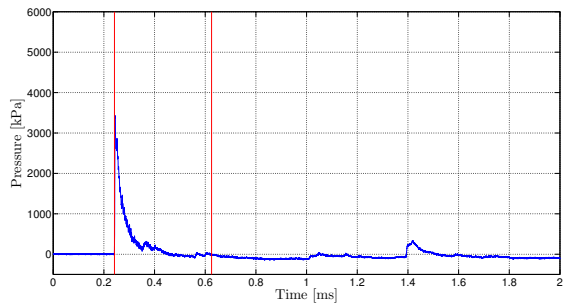
(f) Pressure transducer 6
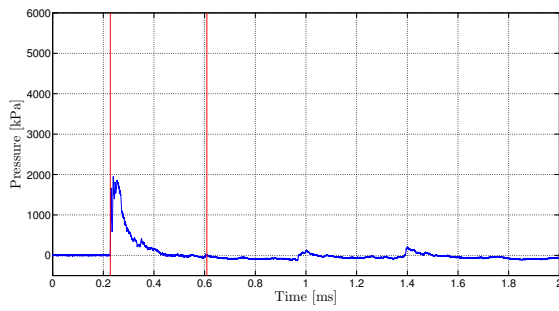
(g) Pressure transducer 7
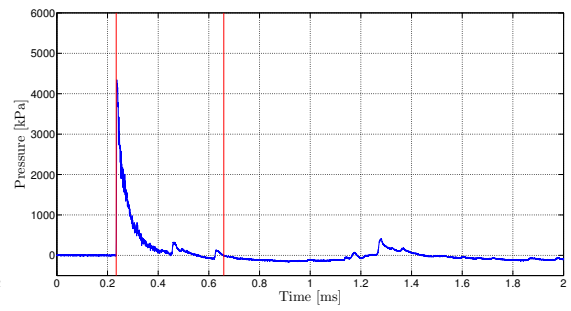
(h) Pressure transducer 8
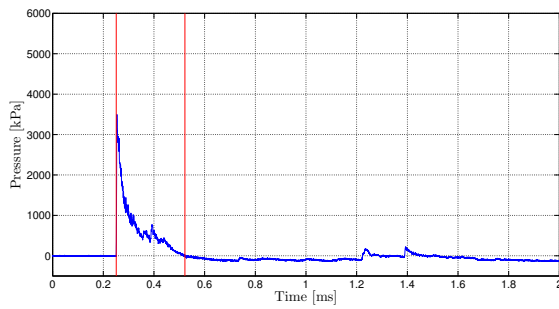
(i) Pressure transducer 9
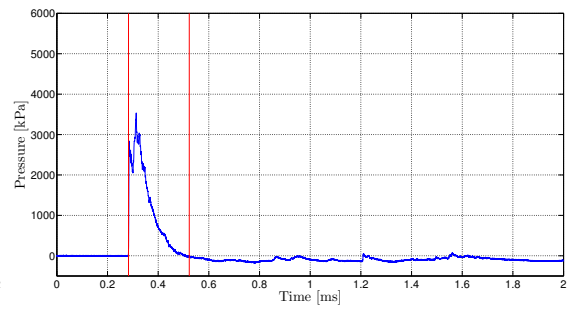
(j) Pressure transducer 10

Figure A.17: Pressure from calibration test R22.
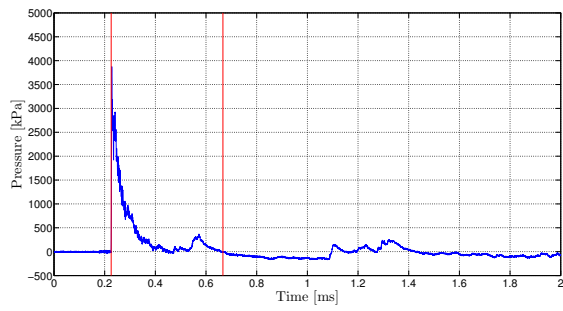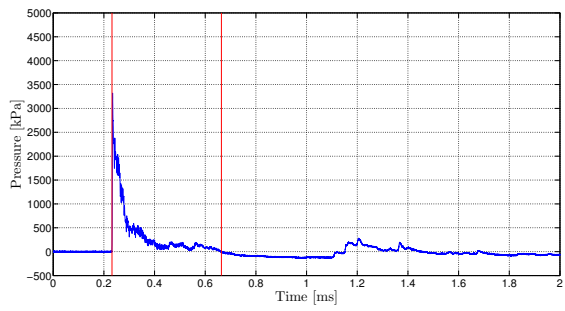
(a) Pressure transducer 1

(b) Pressure transducer 2
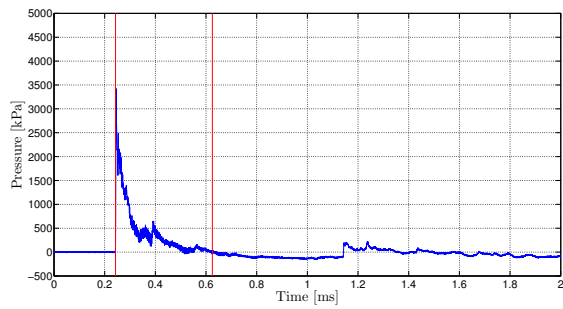
(c) Pressure transducer 3
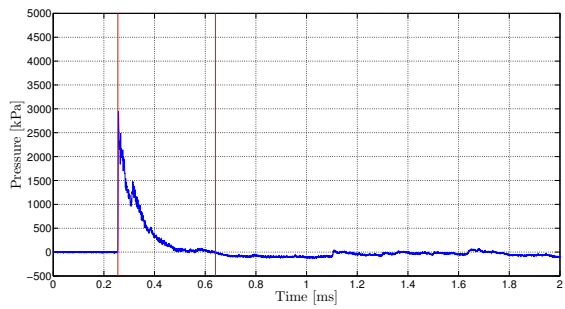
(d) Pressure transducer 4
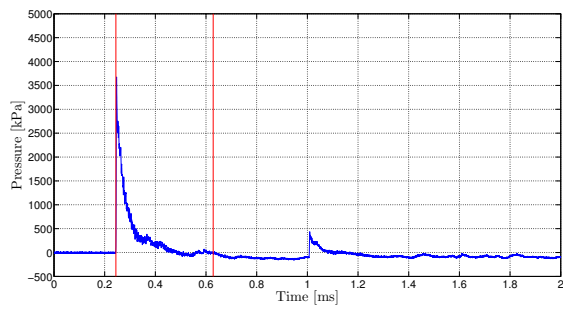
(e) Pressure transducer 5
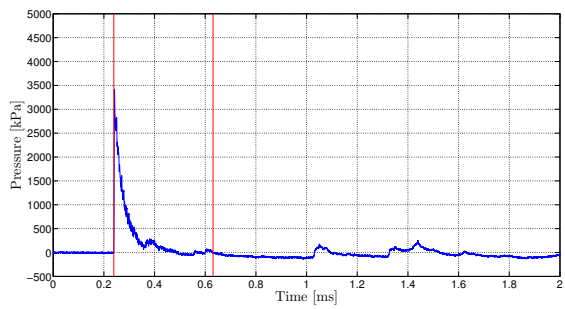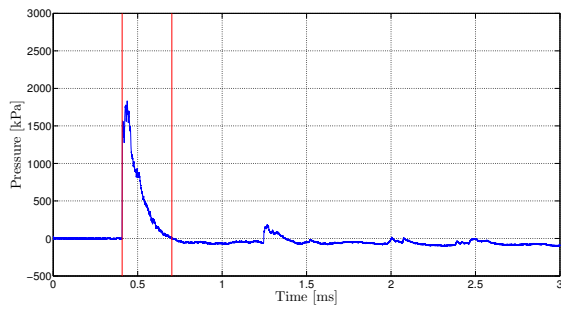

(f) Pressure transducer 6
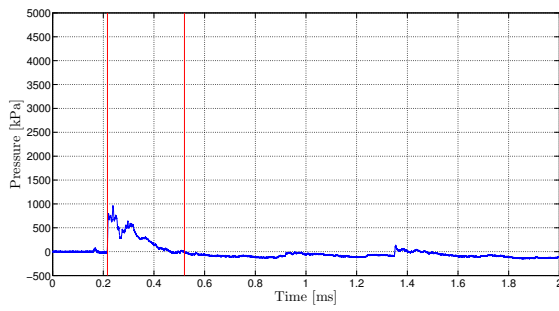
(g) Pressure transducer 7
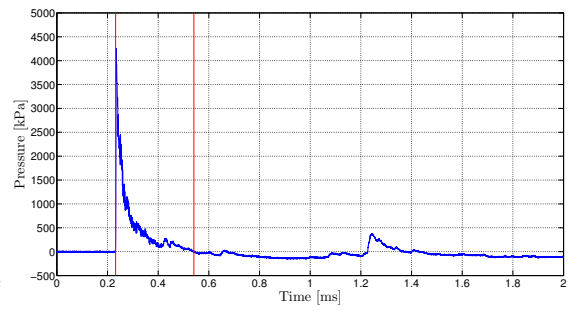
(h) Pressure transducer 8
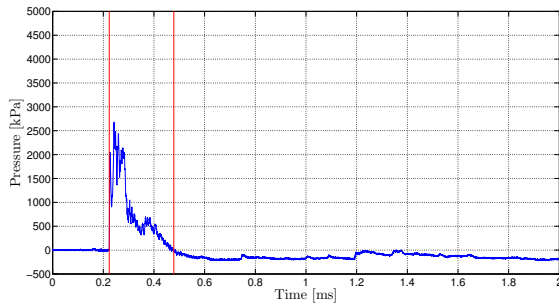
(i) Pressure transducer 9
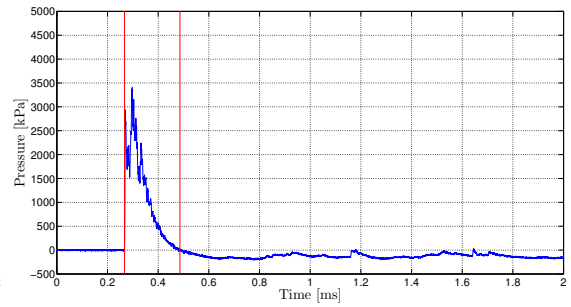
(j) Pressure transducer 10

Figure A.18: Pressure from calibration test R23.

(a) Pressure transducer 1

(b) Pressure transducer 2

(c) Pressure transducer 3

(d) Pressure transducer 4

(e) Pressure transducer 5
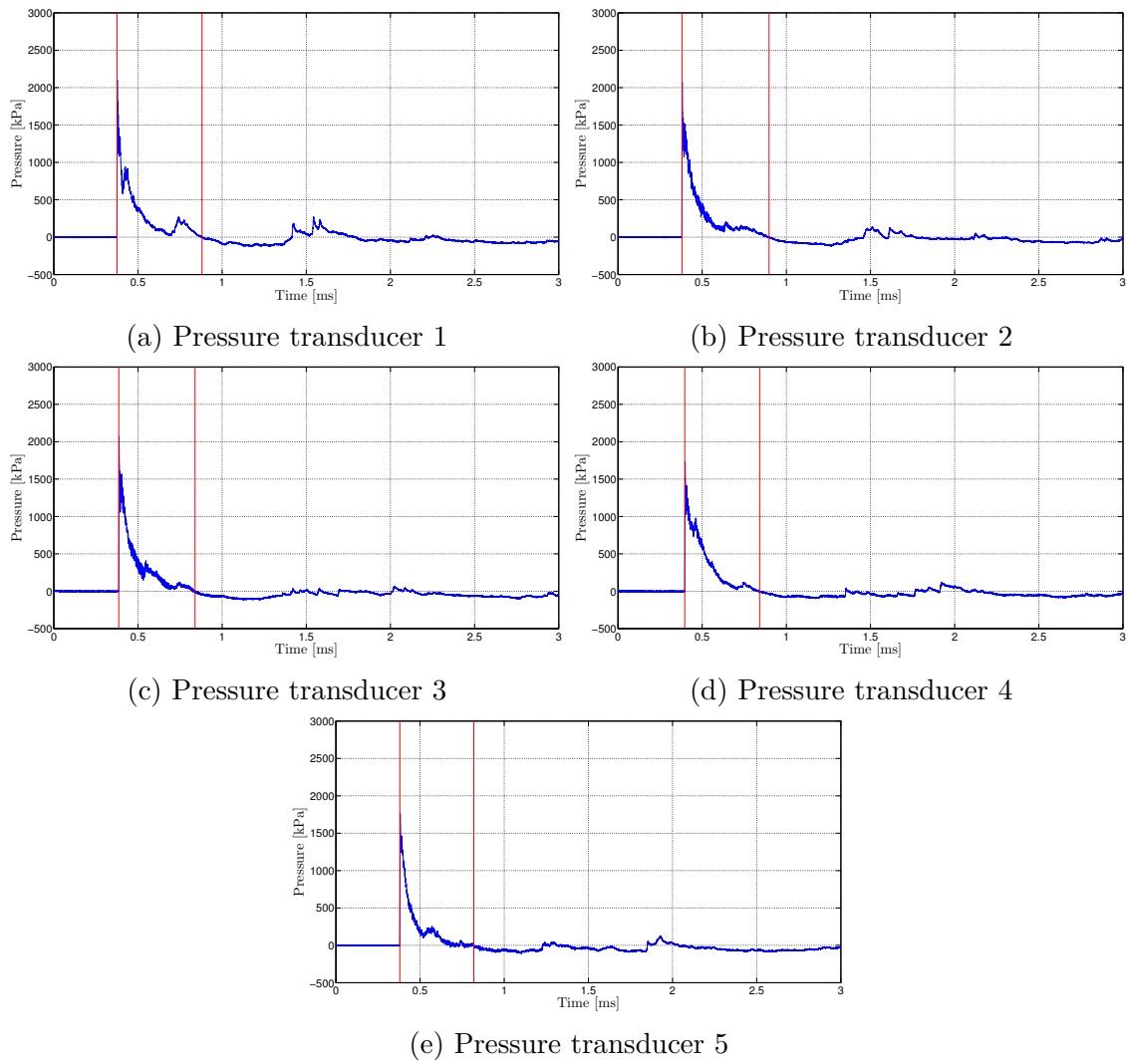
Figure A.19: Pressure from calibration test R31.

(a) Pressure transducer 1

(b) Pressure transducer 2

(c) Pressure transducer 3

(d) Pressure transducer 4

(e) Pressure transducer 5

Figure A.20: Pressure from calibration test R32.

(a) Pressure transducer 1

(b) Pressure transducer 2

(c) Pressure transducer 3

(d) Pressure transducer 4

(e) Pressure transducer 5

Figure A.21: Pressure from calibration test R33.
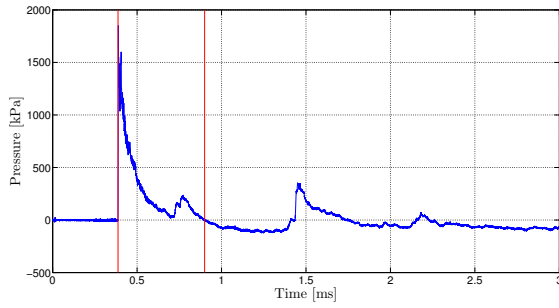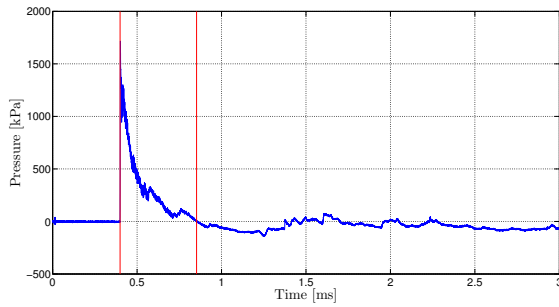
(a) Pressure transducer 1

(b) Pressure transducer 2

(c) Pressure transducer 3
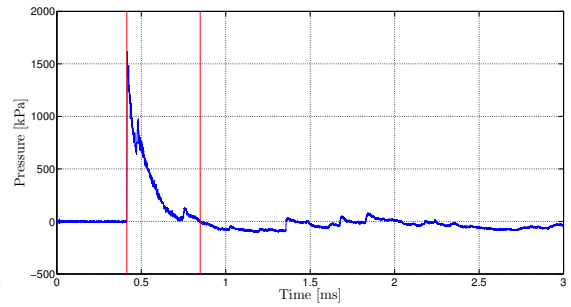
(d) Pressure transducer 4
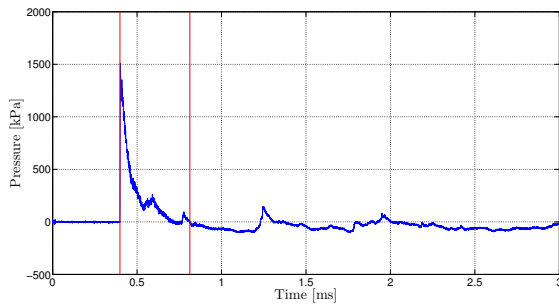
(e) Pressure transducer 5
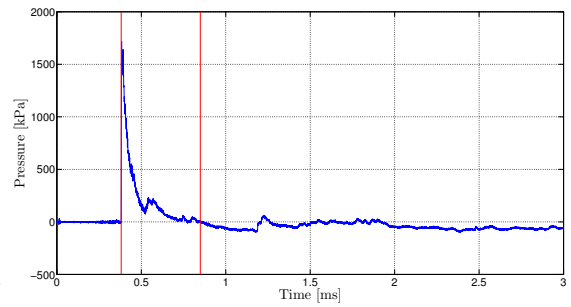
(f) Pressure transducer 6
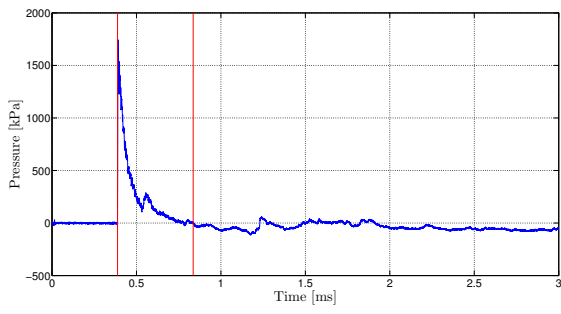
(g) Pressure transducer 7
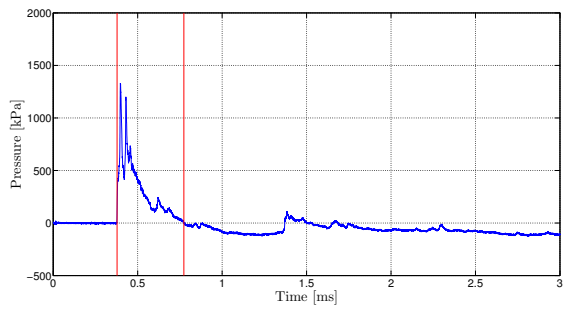
(h) Pressure transducer 8
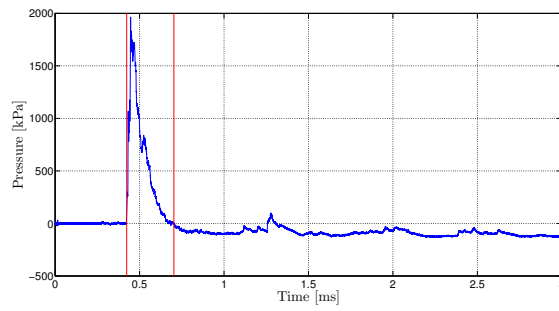
(i) Pressure transducer 10

Figure A.22: Pressure from calibration test R31-2.
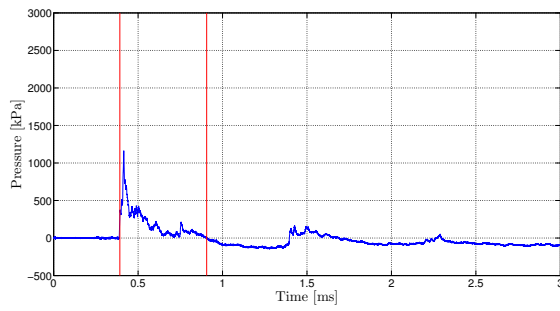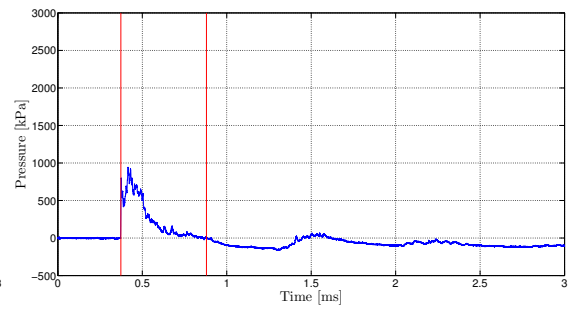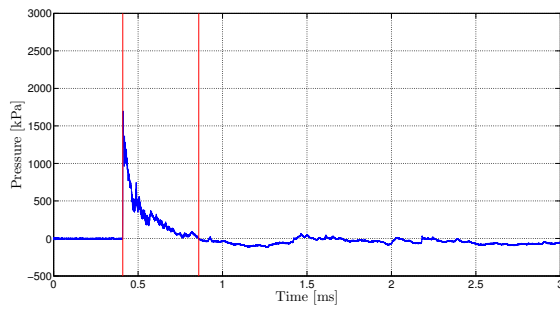
(a) Pressure transducer 1

(b) Pressure transducer 2

(c) Pressure transducer 3
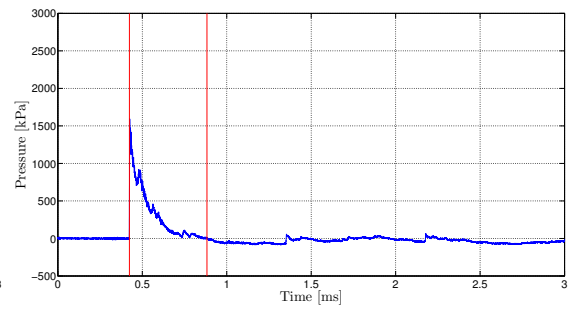
(d) Pressure transducer 4
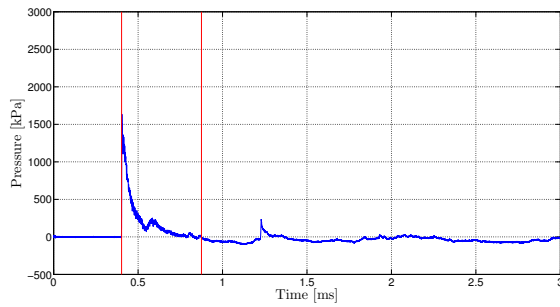
(e) Pressure transducer 5
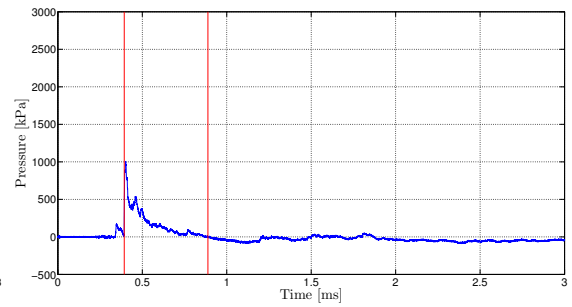
(f) Pressure transducer 6
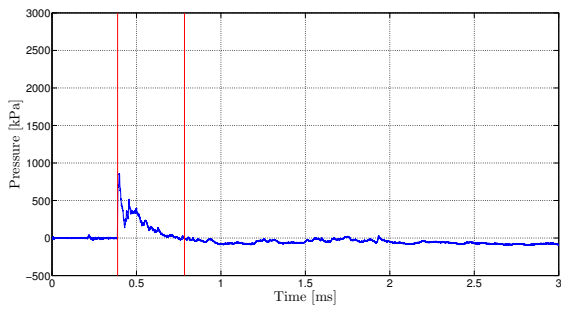
(g) Pressure transducer 7

(h) Pressure transducer 8

(i) Pressure transducer 10

Figure A.23: Pressure from calibration test R32-2.

(a) Pressure transducer 1

(b) Pressure transducer 2

(c) Pressure transducer 3

(d) Pressure transducer 4

(e) Pressure transducer 5

(f) Pressure transducer 6

(g) Pressure transducer 7

(h) Pressure transducer 8

(i) Pressure transducer 9

(j) Pressure transducer 10

Figure A.24: Pressure from calibration test R33-2.

A.3 Results from calibration tests

Table A.1: Calculated parameters from all pressure transducers.

Test	Pressure transducer	Time of arrival t_a [ms]	Max pressure p_{max} [kPa]	Positive impulse I_s^+ [kPa $\cdot$ms]	Positive phase duration t^+ [ms]
R11	1	0.10	5520	193.5	0.29
	2	0.08	12933	285.8	0.12
	3	0.11	7880	189.4	0.15
	4	0.12	10467	271.9	0.24
	5	0.12	8107	545.7	0.23
	6	0.12	4667	139.3	0.27
	7	0.12	8253	152.5	0.32
	8	0.11	6520	190.8	0.23
	9	0.12	8813	220.3	0.19
	10	0.16	7333	348.9	0.15
R12	1	0.11	20426	325.9	0.32
	2	0.12	6560	175.5	0.11
	3	0.13	13187	253.4	0.29
	4	0.14	9680	259.0	0.26
	5	0.14	5333	139.1	0.14
	6	0.14	4520	131.4	0.14
	7	0.14	6880	144.8	0.24
	8	0.12	12627	245.1	0.29
	9	0.14	8307	229.8	0.19
	10	0.17	7813	414.3	0.14
R13	1	0.12	10813	233.3	0.31
	2	0.13	9627	220.4	0.32
	3	0.14	10587	236.8	0.29
	4	0.15	9587	246.3	0.29
	5	0.15	6920	149.1	0.28
	6	0.13	6973	153.8	0.25
	7	0.14	2960	107.1	0.28
	8	0.12	10507	190.6	0.23
	9	0.14	8867	234.2	0.19
	10	0.17	7067	334.4	0.15

Test	Pressure transducer	Time of arrival t_a [ms]	Max pressure p_{max} [kPa]	Positive impulse I_s^+ [kPa ·ms]	Positive phase duration t^+ [ms]
R21	1	0.23	4783	182.9	0.42
	2	0.22	1740	137.1	0.44
	3	0.21	3117	130.5	0.36
	4	0.23	2343	133.7	0.36
	5	0.24	3267	121.7	0.36
	6	0.25	3580	124.0	0.37
	7	0.24	3263	119.7	0.22
	8	0.23	4813	176.4	0.30
	9	0.25	3827	181.0	0.26
	10	0.28	2987	247.8	0.23
R22	1	0.23	4596	185.2	0.42
	2	0.22	5100	174.8	0.44
	3	0.23	4496	177.0	0.38
	4	0.23	3912	175.3	0.37
	5	0.22	3624	121.7	0.36
	6	0.24	3432	115.2	0.38
	7	0.23	1952	119.1	0.38
	8	0.23	4344	175.7	0.42
	9	0.25	3500	182.6	0.27
	10	0.28	3536	259.8	0.24
R23	1	0.23	3876	170.9	0.44
	2	0.23	3320	156.4	0.43
	3	0.24	3424	159.6	0.38
	4	0.26	2944	178.7	0.39
	5	0.24	3676	129.4	0.38
	6	0.24	3420	127.5	0.39
	7	0.22	964	84.7	0.30
	8	0.23	4256	157.1	0.31
	9	0.22	2680	200.0	0.25
	10	0.27	3404	230.8	0.22

Test	Pressure transducer	Time of arrival t_a [ms]	Max pressure p_{max} [kPa]	Positive impulse I_s^+ [kPa ·ms]	Positive phase duration t^+ [ms]
R31	1	0.38	2104	146.9	0.50
	2	0.38	2074	148.9	0.52
	3	0.39	2072	143.3	0.45
	4	0.40	1738	148.0	0.44
	5	0.38	1762	102.0	0.44
	6	N/A	N/A	N/A	N/A
	7	N/A	N/A	N/A	N/A
	8	N/A	N/A	N/A	N/A
	9	N/A	N/A	N/A	N/A
	10	N/A	N/A	N/A	N/A
R32	1	0.38	1430	128.5	0.53
	2	0.39	1590	132.7	0.51
	3	0.40	1672	136.3	0.44
	4	0.41	1584	145.4	0.45
	5	0.39	1366	103.1	0.42
	6	N/A	N/A	N/A	N/A
	7	N/A	N/A	N/A	N/A
	8	N/A	N/A	N/A	N/A
	9	N/A	N/A	N/A	N/A
	10	N/A	N/A	N/A	N/A
R33	1	0.38	2104	146.9	0.50
	2	0.38	2074	148.9	0.52
	3	0.39	2072	143.3	0.45
	4	0.40	1738	148.0	0.44
	5	0.38	1762	102.0	0.44
	6	N/A	N/A	N/A	N/A
	7	N/A	N/A	N/A	N/A
	8	N/A	N/A	N/A	N/A
	9	N/A	N/A	N/A	N/A
	10	N/A	N/A	N/A	N/A

Test	Pressure transducer	Time of arrival t_a [ms]	Max pressure p_{max} [kPa]	Positive impulse I_s^+ [kPa ·ms]	Positive phase duration t^+ [ms]
R31-2	1	0.39	1850	146.0	0.51
	2	0.39	1826	141.5	0.52
	3	0.40	1716	139.3	0.45
	4	0.41	1618	146.0	0.43
	5	0.40	1510	97.1	0.41
	6	0.38	1718	102.2	0.47
	7	0.39	1744	111.2	0.45
	8	0.38	1328	119.0	0.40
	9	N/A	N/A	N/A	N/A
	10	0.42	1964	157.3	0.28
R32-2	1	0.39	1164	96.1	0.51
	2	0.37	944	124.6	0.51
	3	0.41	1698	128.8	0.45
	4	0.42	1592	136.4	0.46
	5	0.40	1634	98.4	0.47
	6	0.39	1004	87.9	0.50
	7	0.39	858	72.3	0.40
	8	0.41	1832	132.3	0.42
	9	N/A	N/A	N/A	N/A
	10	0.44	2274	173.1	0.33
R33-2	1	0.38	2028	142.8	0.51
	2	0.38	1788	139.0	0.51
	3	0.40	1622	133.9	0.49
	4	0.41	1490	142.4	0.47
	5	0.40	1672	101.9	0.44
	6	0.37	1448	98.2	0.38
	7	0.39	1540	101.5	0.36
	8	0.37	2312	142.6	0.40
	9	0.37	1116	128.8	0.33
	10	0.41	1834	176.1	0.29

Appendix B

Component Tests

B.1 Displacement Measurements

Table B.1: Displacements of deformed plates taken at Østøya.

Plate	Displacement at measure point [mm]									
	1	2	3	4	5	6	7	8	9	10
A11	22.2	N/A	39.1	N/A	16.2	15.9	N/A	39.1	N/A	17.7
A12	22.1	N/A	39.5	N/A	26.5	20.6	N/A	39.5	N/A	16.6
A13	27.4	N/A	43.3	N/A	19.0	20.3	N/A	43.3	N/A	19.5
A21	8.6	N/A	24.5	N/A	6.3	8.1	N/A	24.5	N/A	13.7
A22	19.6	N/A	30.8	N/A	13.3	10.0	N/A	30.8	N/A	13.8
A23	14.2	N/A	25.8	N/A	5.3	18.3	N/A	25.8	N/A	17.4
A31	-14.1	N/A	-15.9	N/A	-12.9	-12.5	N/A	-15.9	N/A	-14.6
A32	-15.2	N/A	-23.4	N/A	-14.5	-12.2	N/A	-23.4	N/A	-12.4
A33	-12.0	N/A	-23.7	N/A	-12.0	-10.1	N/A	-23.7	N/A	-10.1

Table B.2: Displacements of deformed plates taken at Gløshaugen.

Plate	Displacement at measure point [mm]									
	1	2	3	4	5	6	7	8	9	10
A11	21.9	33.5	37.9	26.3	14.4	17.8	30.8	38.4	29.1	15.9
A12	22.5	34.7	38.4	34.9	23.6	21.6	33.8	39.3	27.5	16.3
A13	24.5	24.5	43.3	32.3	19.0	23.2	34.7	43.2	35.7	14.7
A21	9.4	18.5	24.6	15.5	6.4	9.2	18.9	24.5	21.1	13.8
A22	19.7	25.3	28.5	23.5	12.8	9.7	21.3	29.8	24.1	16.3
A23	13.3	20.2	25.4	15.3	7.3	18.0	23.0	26.2	22.4	18.2
A31	-14.6	-16.5	-18.4	-18.3	-12.7	-13.4	-19.5	-16.8	-19.8	-14.2
A32	-15.6	-21.0	-22.5	-18.4	-13.4	-12.6	-18.8	-23.4	-18.9	-12.9
A33	-11.8	-20.2	-21.4	-15.5	-11.0	-11.3	-18.3	-23.6	-18.1	-12.3

B.2 Deformed plates
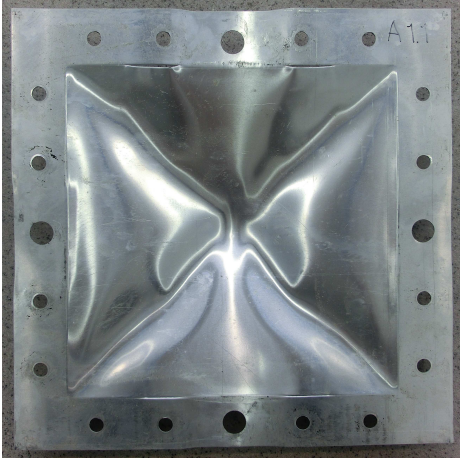
(a) A11
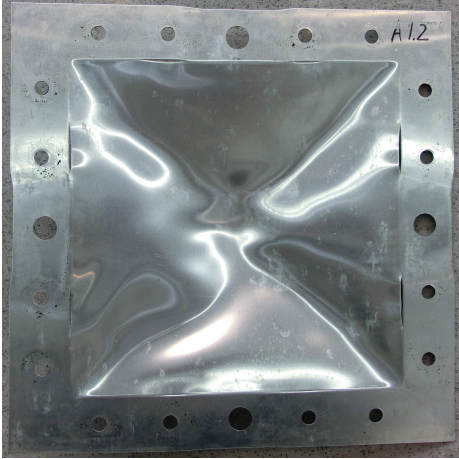
(b) A12
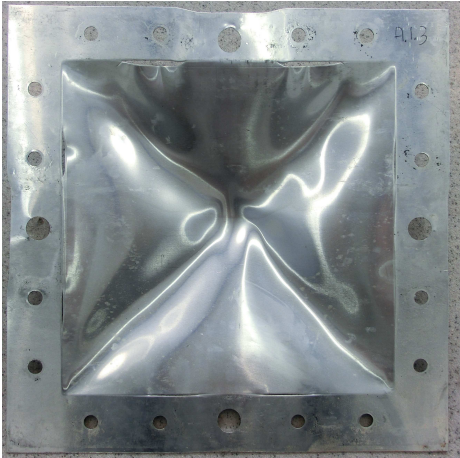
(c) A13
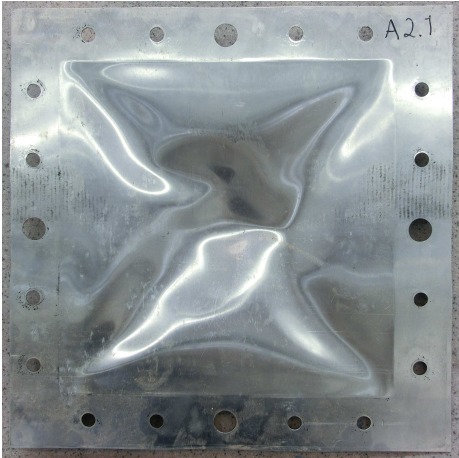
(d) A21
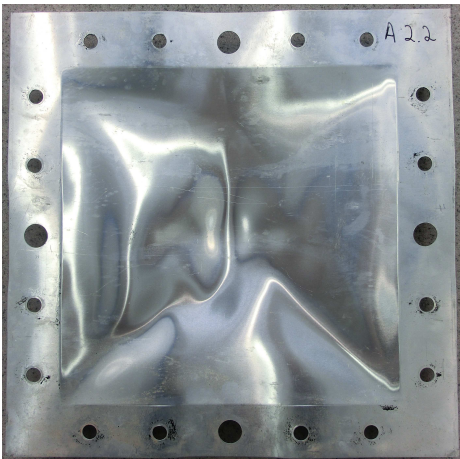
(e) A22
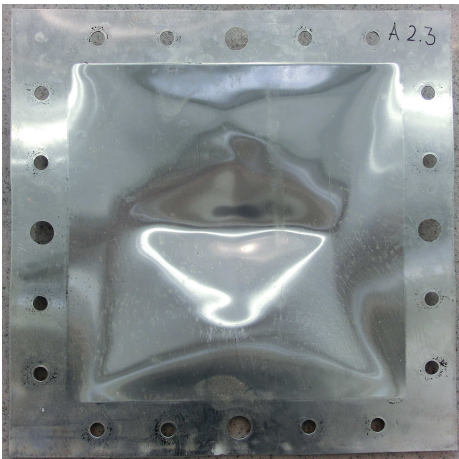
(f) A23

(g) A31
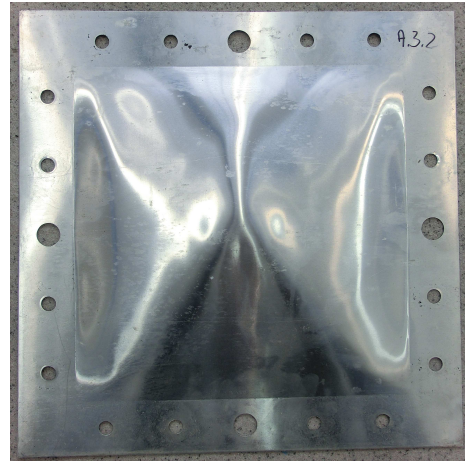
(h) A32
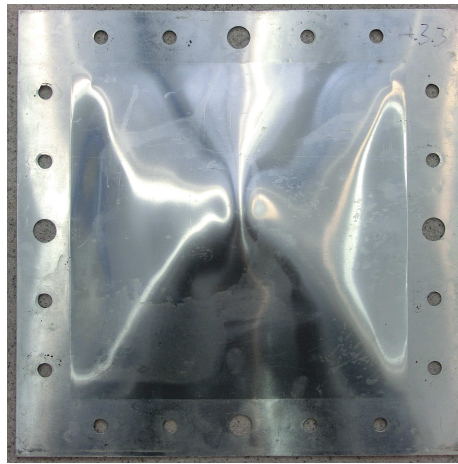
(i) A33

Figure B.1: Deformed plates after testing.

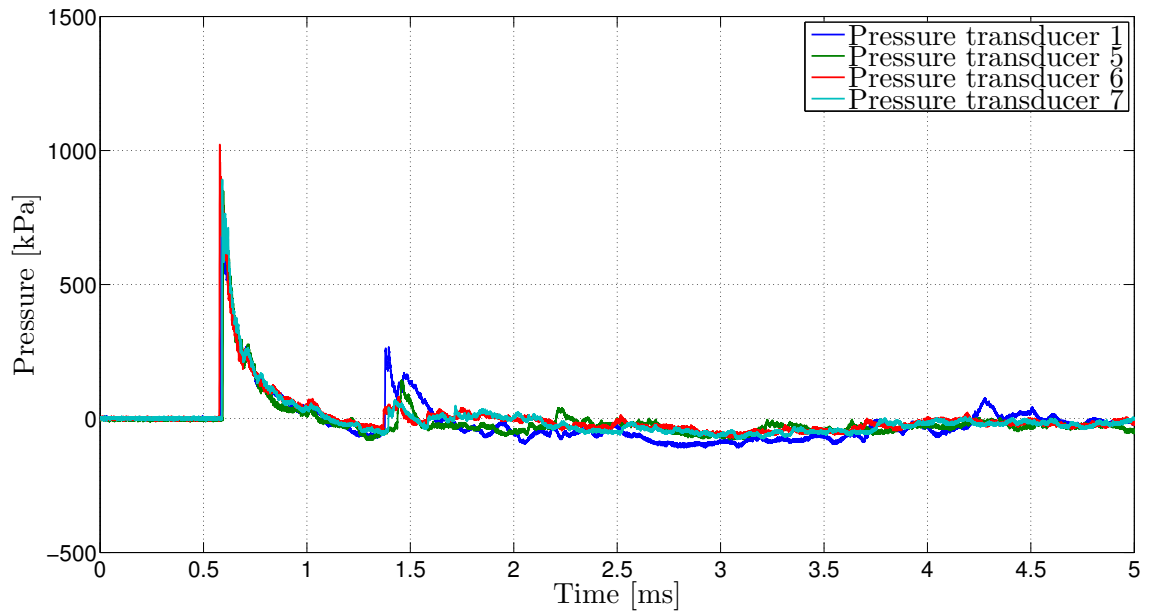# B.3   Comparison of pressure in transducers
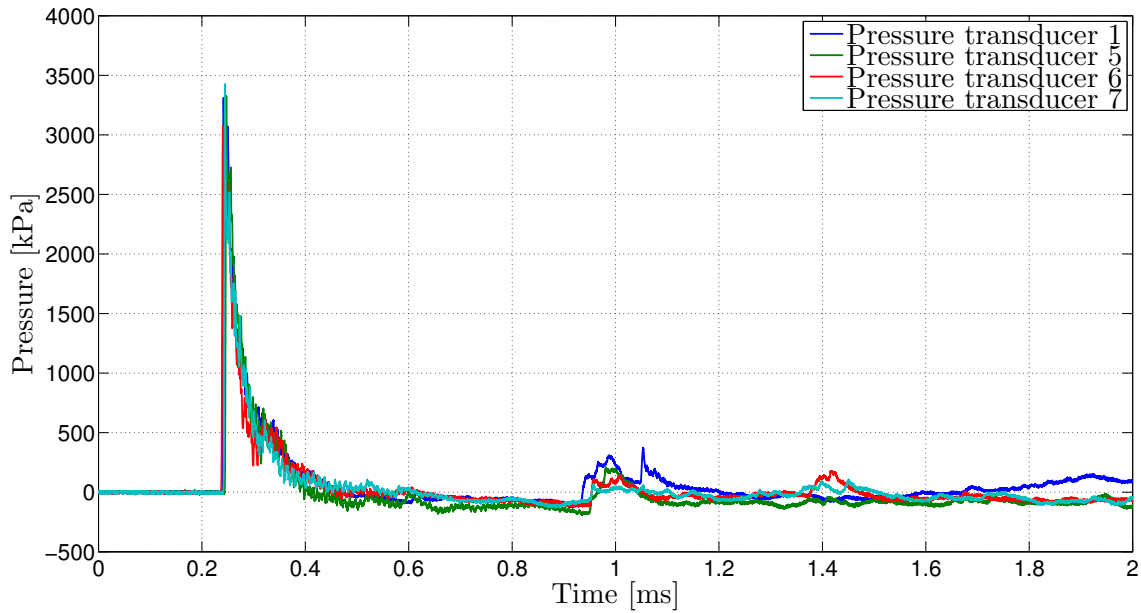
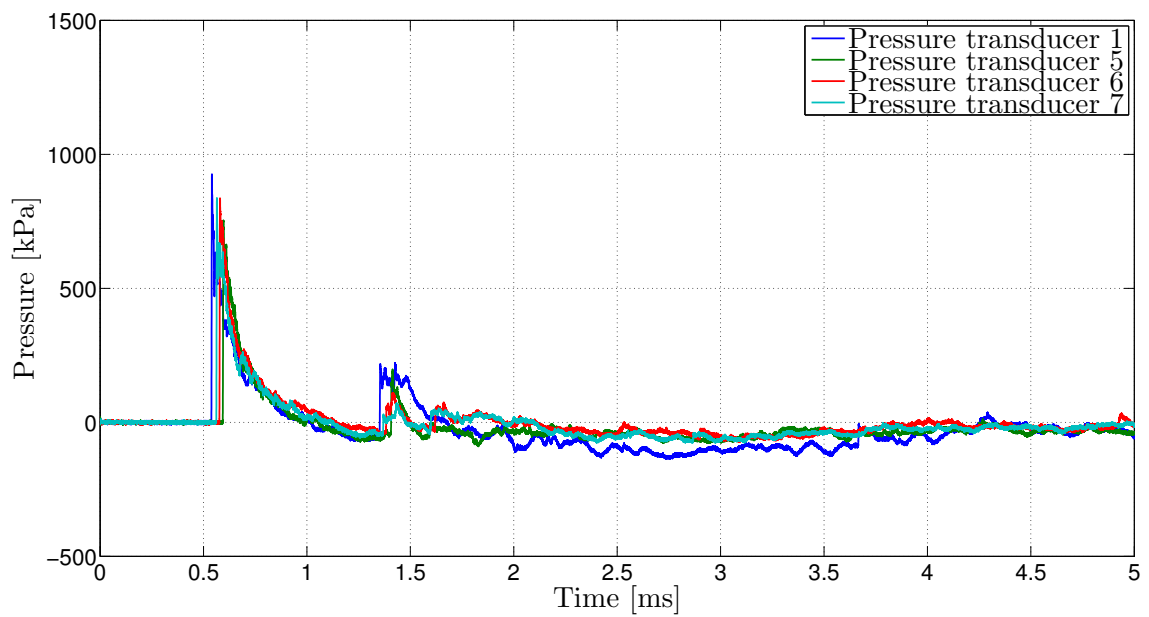Figure B.2: Pressure transducers in the clamping frame for test A11.
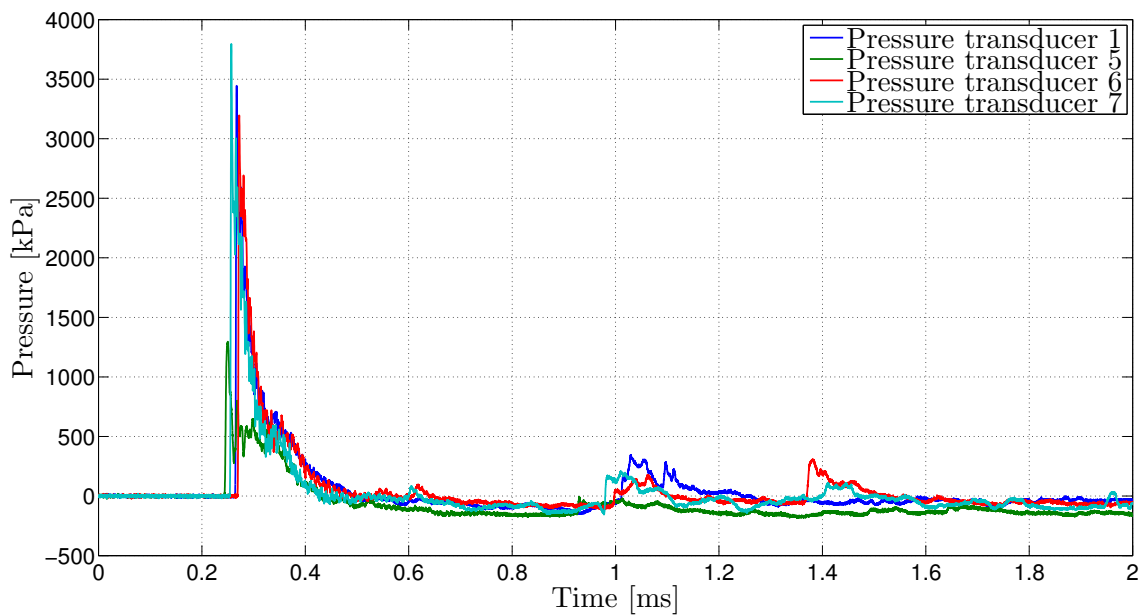
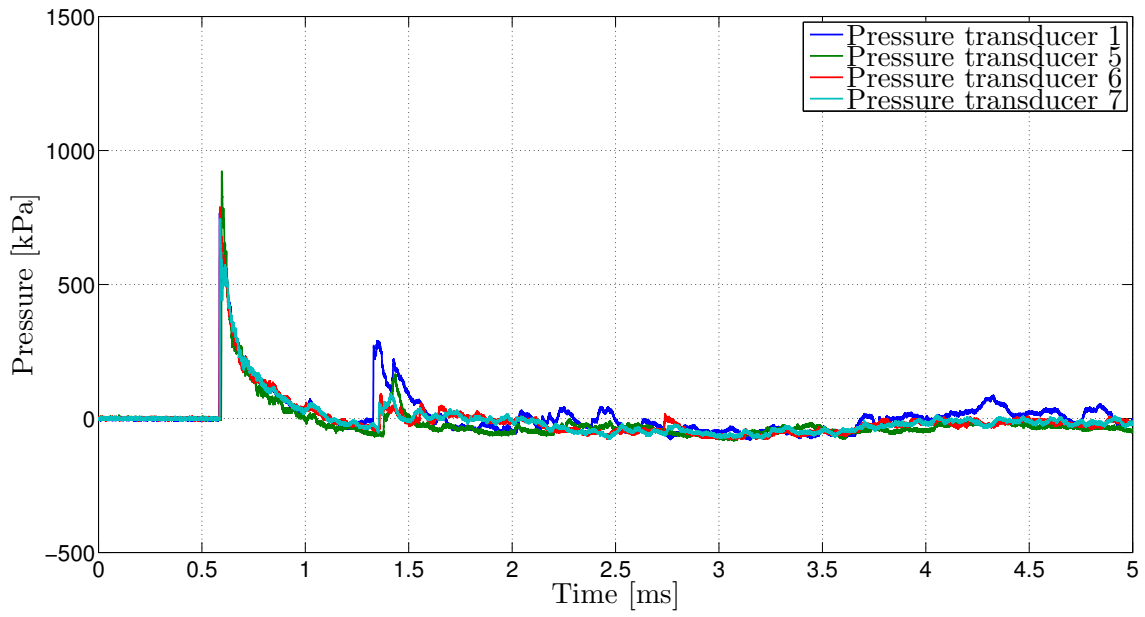
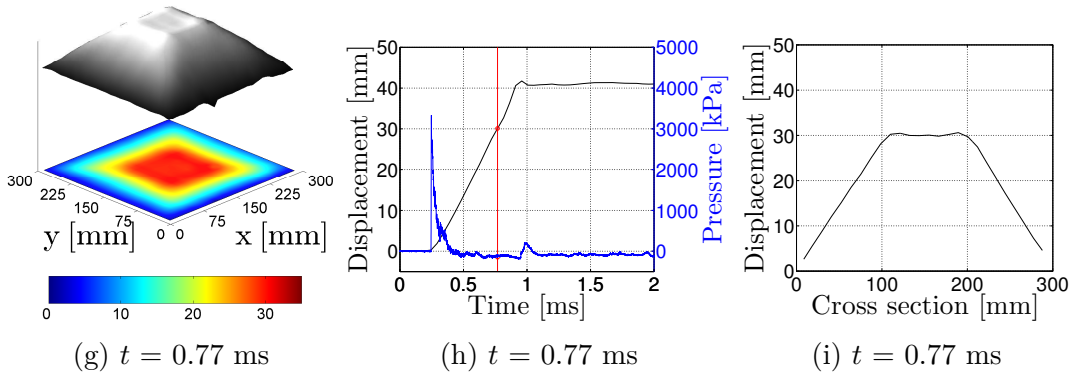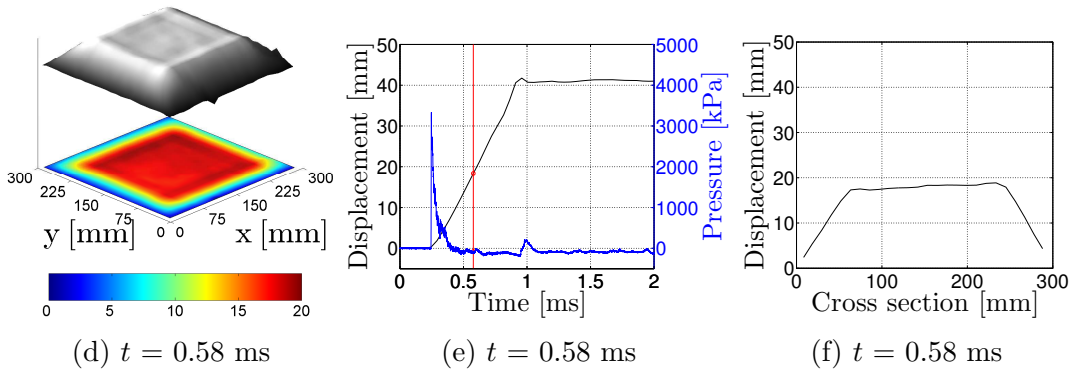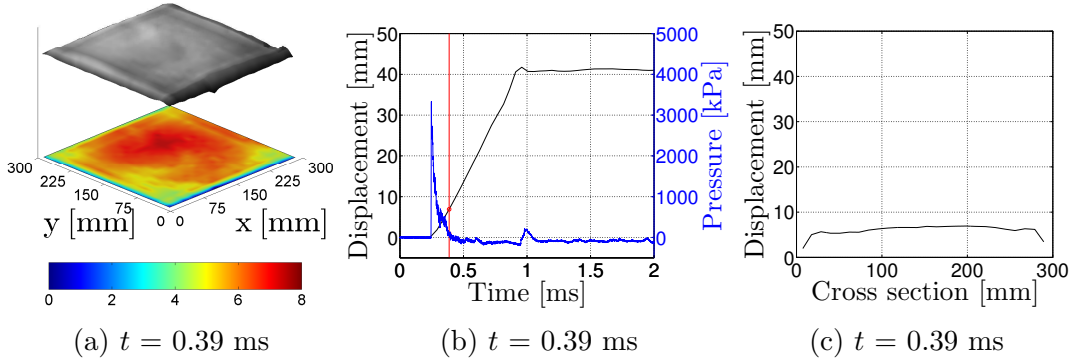Figure B.3: Pressure transducers in the clamping frame for test A12.
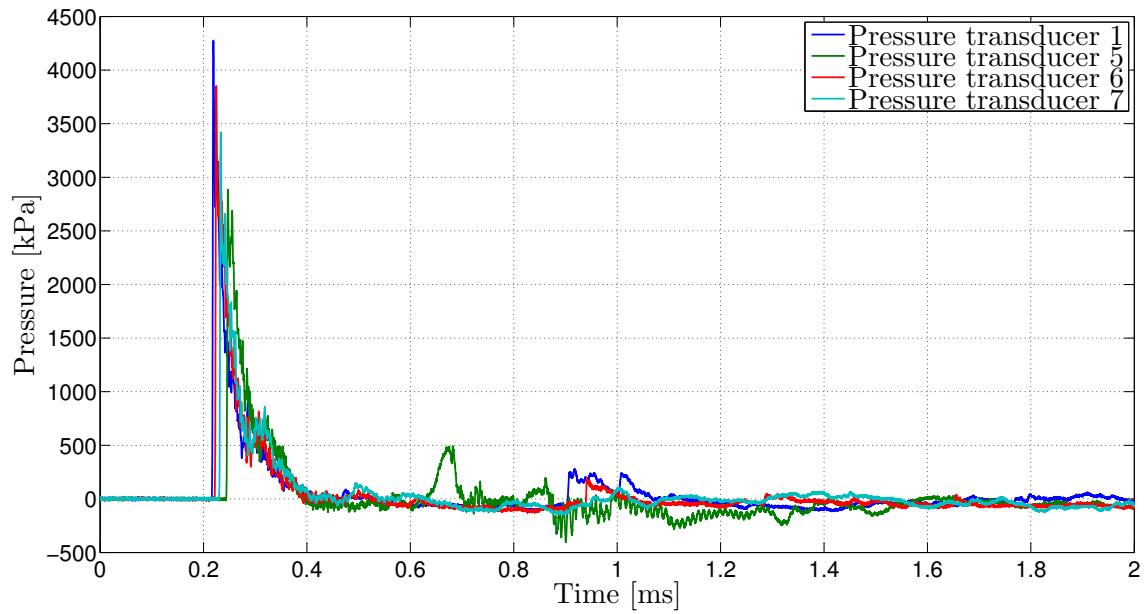
Figure B.4: Pressure transducers in the clamping frame for test A13.
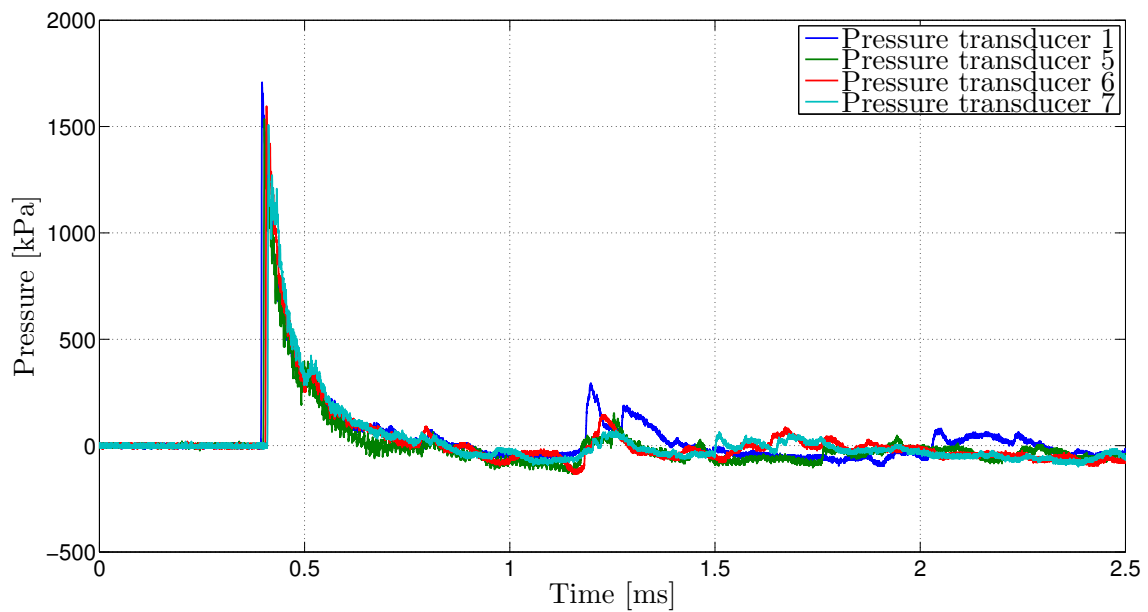
Figure B.5: Pressure transducers in the clamping frame for test A21.
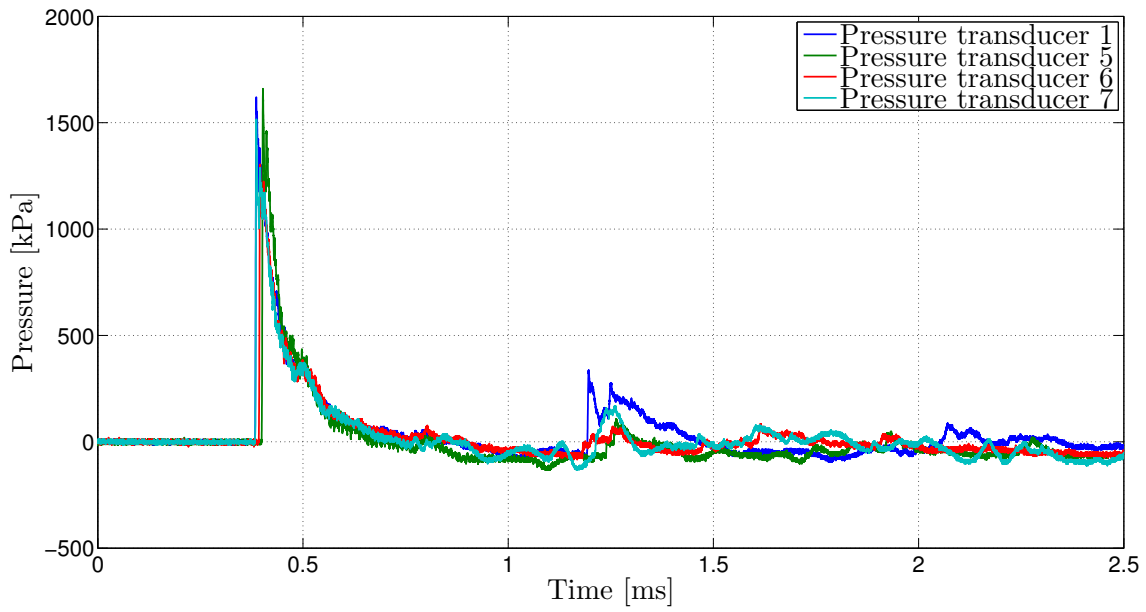
Figure B.6: Pressure transducers in the clamping frame for test A22.
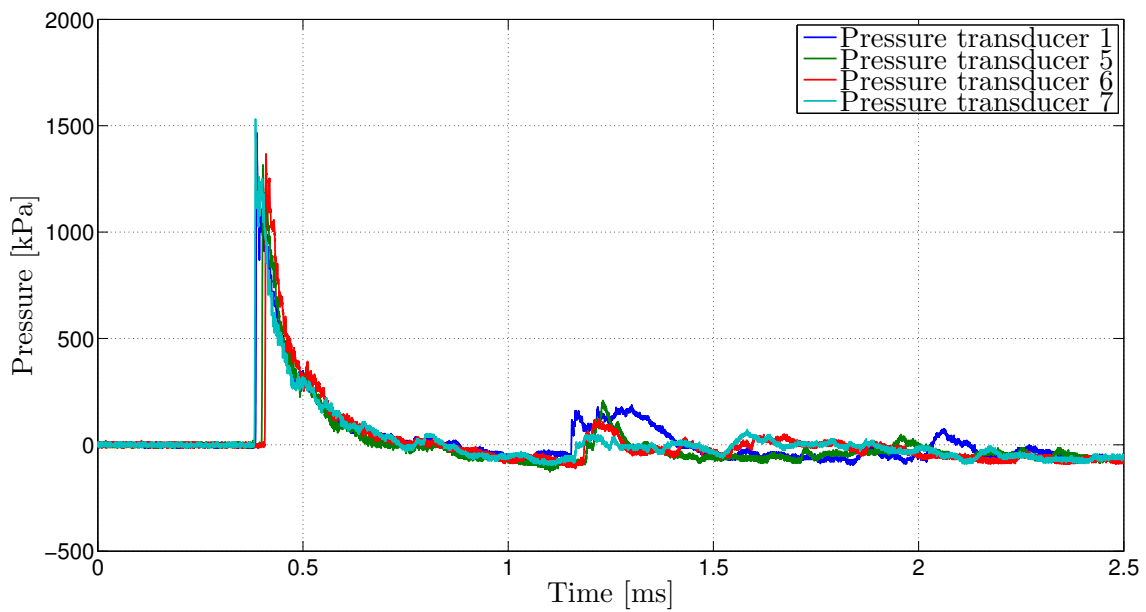
Figure B.7: Pressure transducers in the clamping frame for test A23.

Figure B.8: Pressure transducers in the clamping frame for test A31.

Figure B.9: Pressure transducers in the clamping frame for test A32.

Figure B.10: Pressure transducers in the clamping frame for test A33.

B.4   Deformation profiles at different timesteps

(a) $t = 0.39$ ms

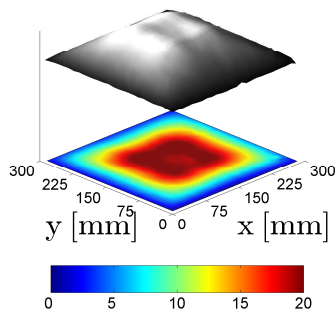

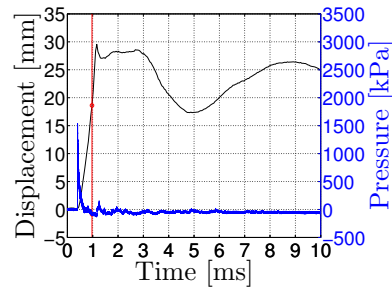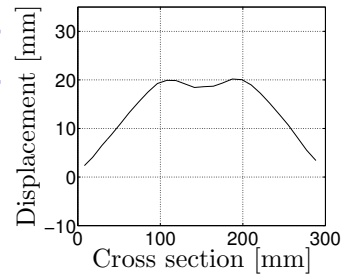(b) $t = 0.39$ ms

(c) $t = 0.39$ ms

(d) $t = 0.58$ ms

(e) $t = 0.58$ ms

(f) $t = 0.58$ ms

(g) $t = 0.77$ ms

(h) $t = 0.77$ ms

(i) $t = 0.77$ ms
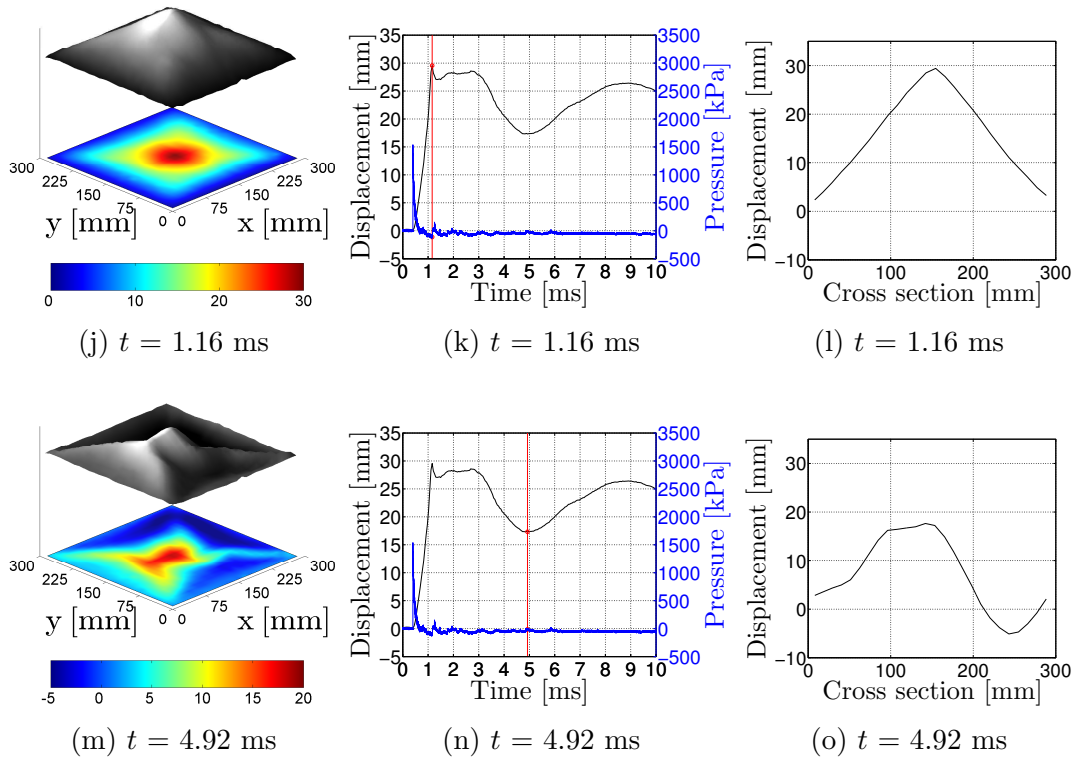
(j) $t = 0.96$ ms   (k) $t = 0.96$ ms   (l) $t = 0.96$ ms
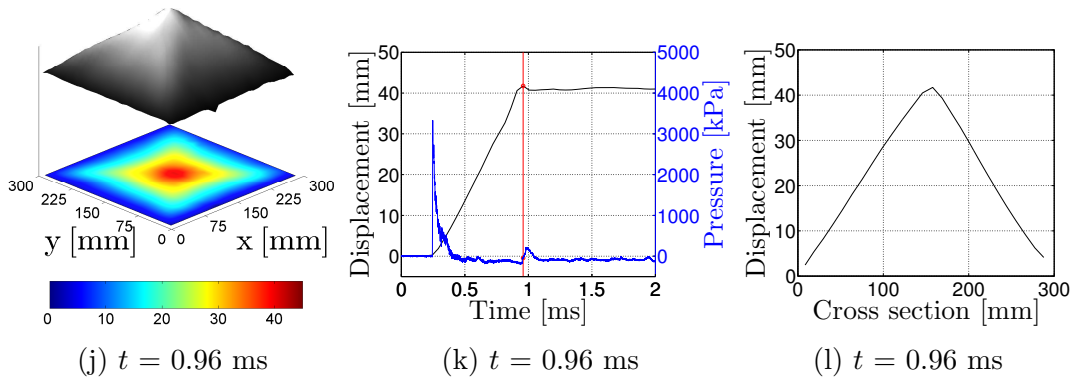
Figure B.11: Displacement of plate A11.

(a) $t = 0.39$ ms

(b) $t = 0.39$ ms

(c) $t = 0.39$ ms

(d) $t = 0.58$ ms

(e) $t = 0.58$ ms

(f) $t = 0.58$ ms

(g) $t = 0.77$ ms

(h) $t = 0.77$ ms

(i) $t = 0.77$ ms

(j) $t = 0.96$ ms

(k) $t = 0.96$ ms

(l) $t = 0.96$ ms
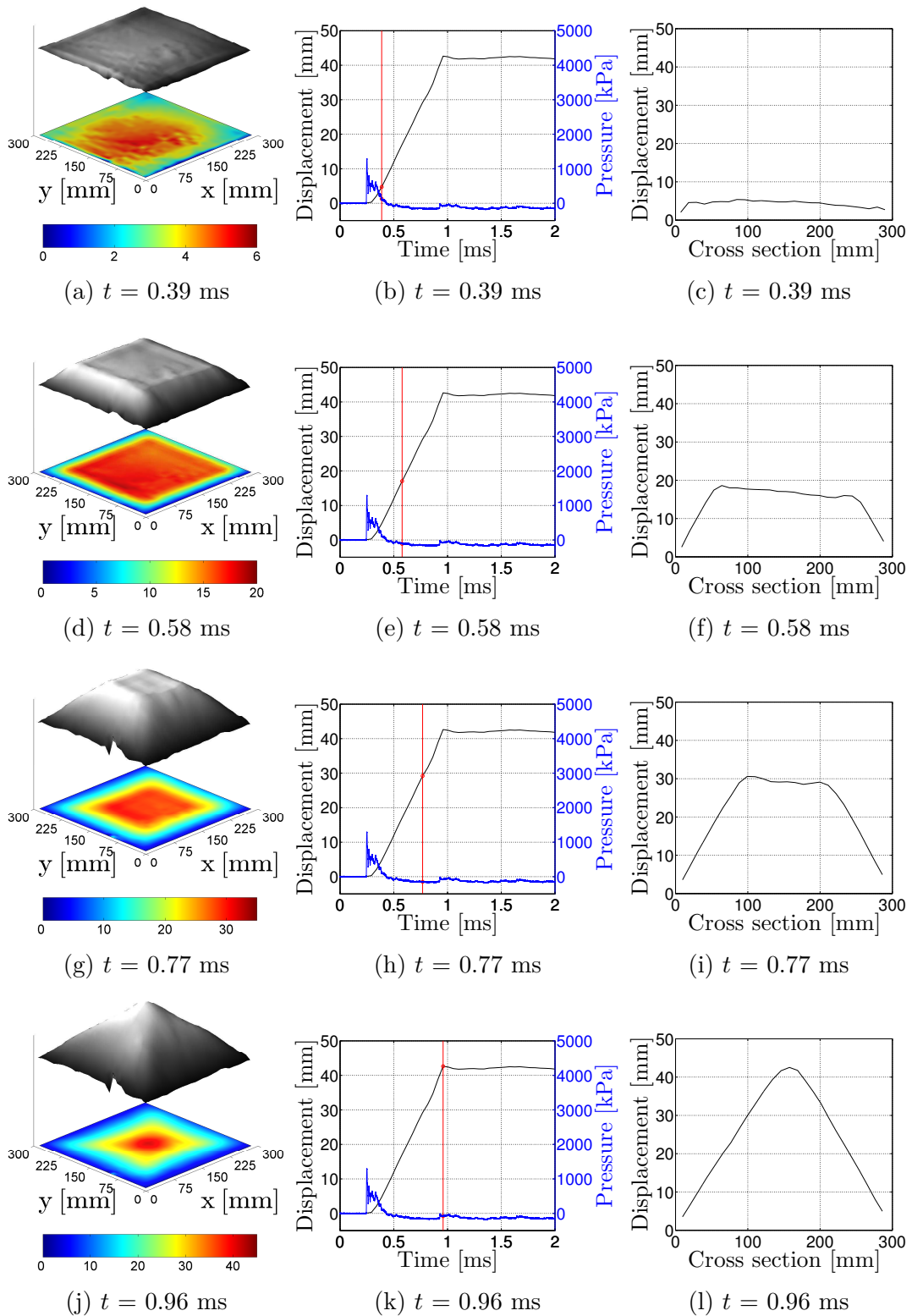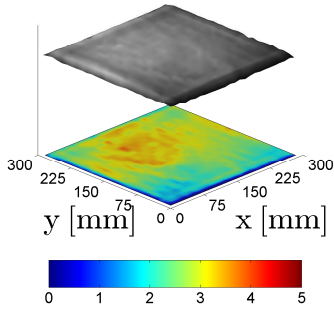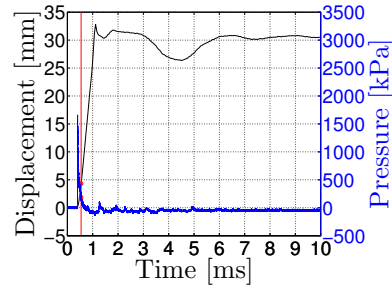
Figure B.12: Displacement of plate A12.

(a) $t = 0.39$ ms

(b) $t = 0.39$ ms

(c) $t = 0.39$ ms

(d) $t = 0.58$ ms

(e) $t = 0.58$ ms

(f) $t = 0.58$ ms

(g) $t = 0.77$ ms

(h) $t = 0.77$ ms

(i) $t = 0.77$ ms

(j) $t = 0.96$ ms

(k) $t = 0.96$ ms

(l) $t = 0.96$ ms
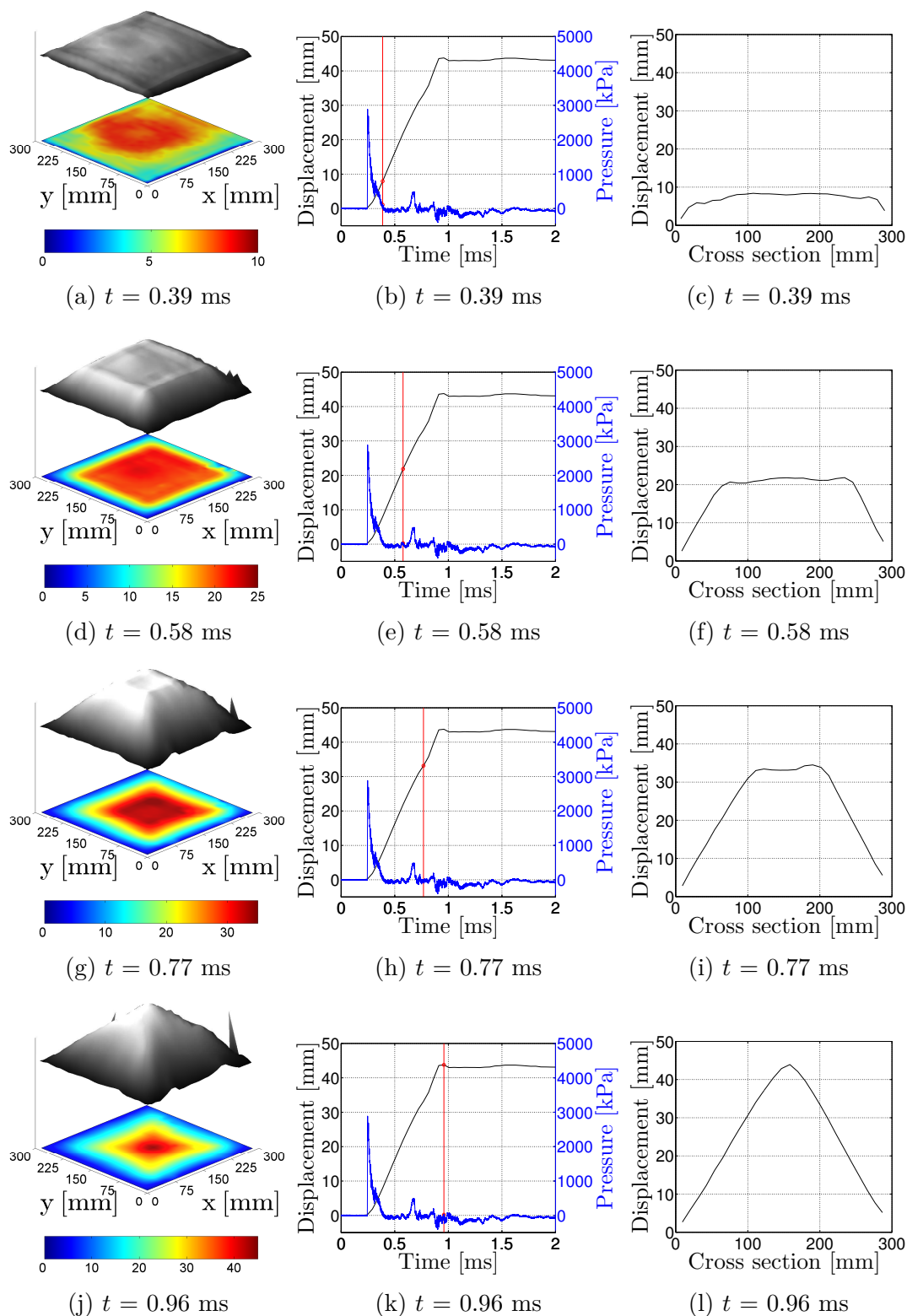
Figure B.13: Displacement of plate A13.
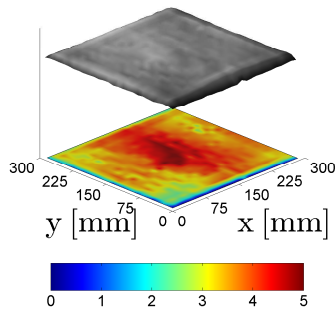
(a) $t = 0.59$ ms

(b) $t = 0.59$ ms

(c) $t = 0.59$ ms

(d) $t = 0.78$ ms

(e) $t = 0.78$ ms

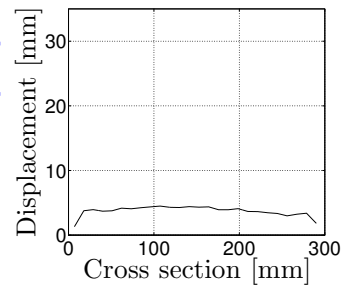(f) $t = 0.78$ ms

(g) $t = 0.97$ ms

(h) $t = 0.97$ ms

(i) $t = 0.97$ ms

B13

(j) $t = 1.16$ ms

(k) $t = 1.16$ ms

(l) $t = 1.16$ ms

(m) $t = 4.92$ ms

(n) $t = 4.92$ ms
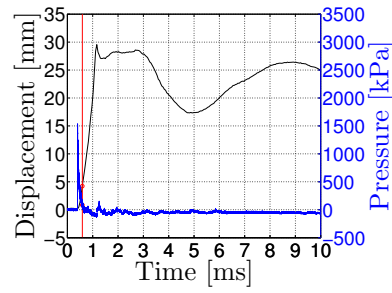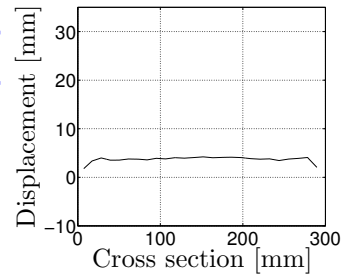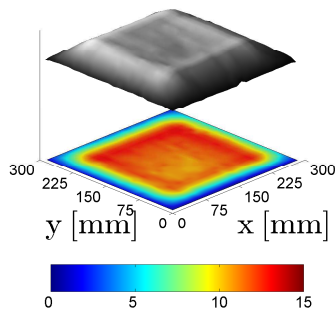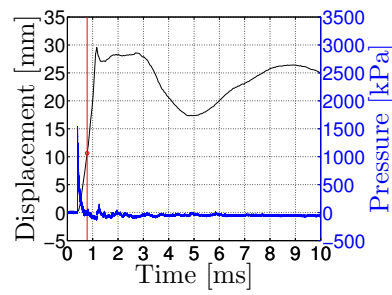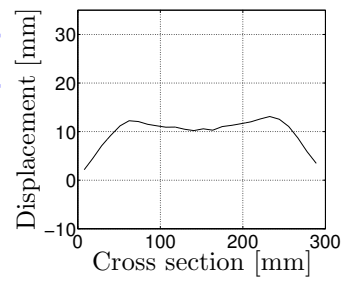
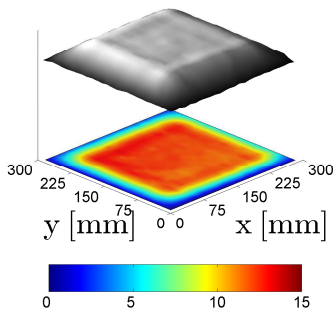(o) $t = 4.92$ ms
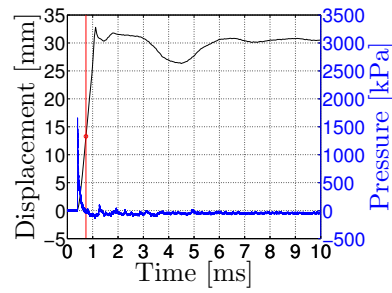
Figure B.14: Displacement of plate A21.
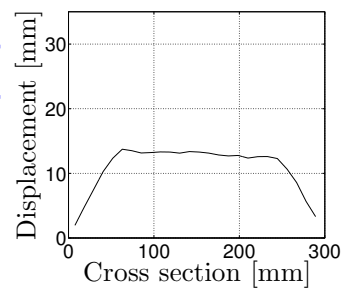
(a) $t = 0.54$ ms

(b) $t = 0.54$ ms

(c) $t = 0.54$ ms

(d) $t = 0.73$ ms

(e) $t = 0.73$ ms

(f) $t = 0.73$ ms

(g) $t = 0.92$ ms

(h) $t = 0.92$ ms

(i) $t = 0.92$ ms

B15

(j) $t = 1.11$ ms

(k) $t = 1.11$ ms

(l) $t = 1.11$ ms

(m) $t = 4.40$ ms

(n) $t = 4.40$ ms

(o) $t = 4.40$ ms
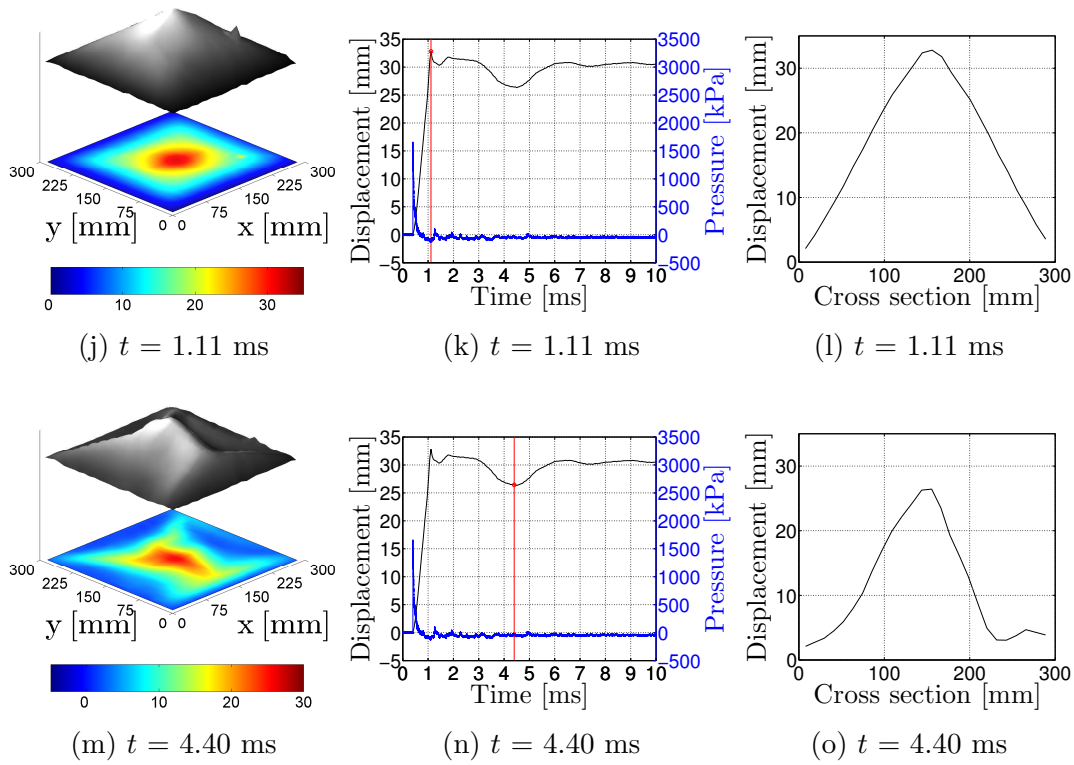
Figure B.15: Displacement of plate A22.

(a) $t = 0.54$ ms
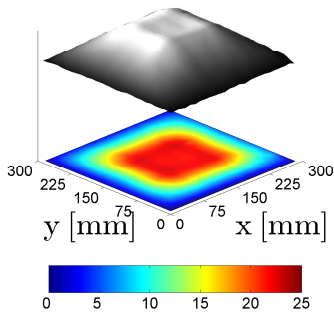
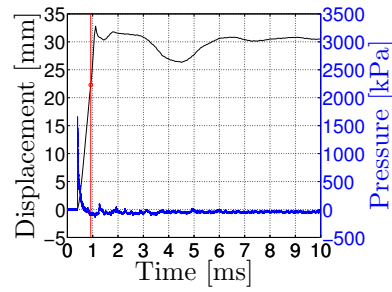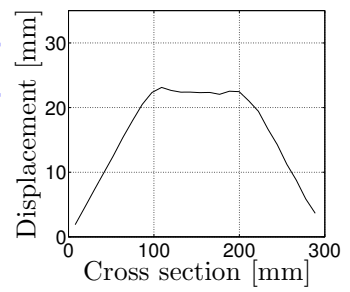(b) $t = 0.54$ ms

(c) $t = 0.54$ ms

(d) $t = 0.73$ ms

(e) $t = 0.73$ ms

(f) $t = 0.73$ ms

(g) $t = 0.92$ ms

(h) $t = 0.92$ ms

(i) $t = 0.92$ ms

(j) $t = 1.11$ ms

(k) $t = 1.11$ ms

(l) $t = 1.11$ ms
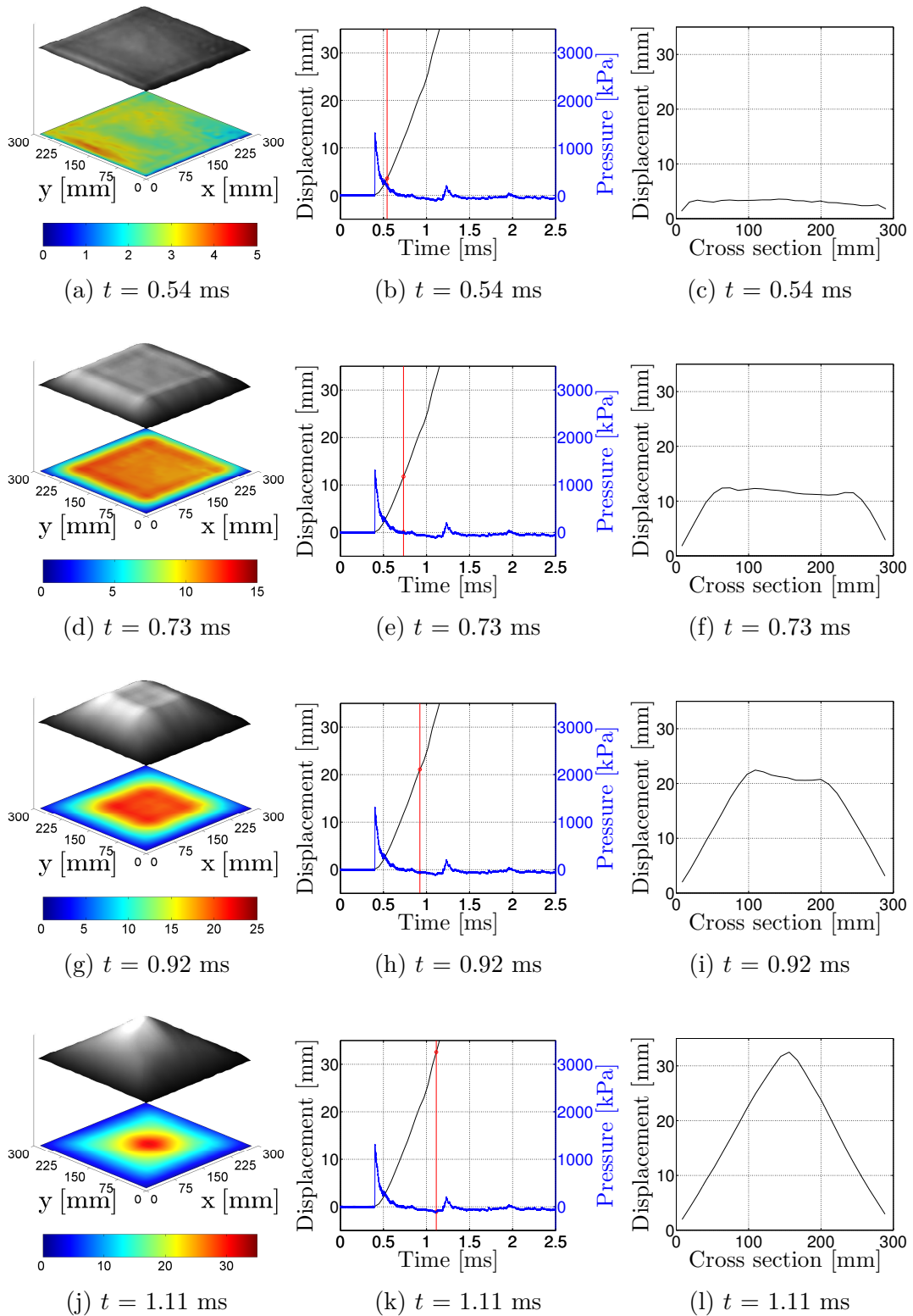
Figure B.16: Displacement of plate A23.

(a) $t = 0.78$ ms
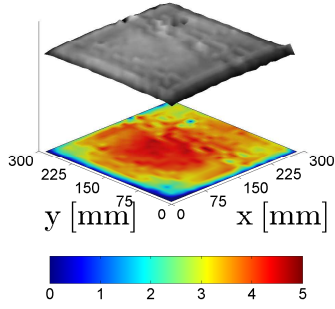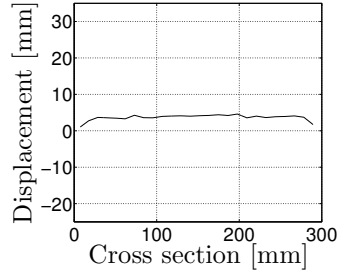
(b) $t = 0.78$ ms

(c) $t = 0.78$ ms

(d) $t = 0.97$ ms

(e) $t = 0.97$ ms

(f) $t = 0.97$ ms

(g) $t = 1.16$ ms

(h) $t = 1.16$ ms

(i) $t = 1.16$ ms

(j) $t = 1.36$ ms

(k) $t = 1.36$ ms

(l) $t = 1.36$ ms

B18

(m) $t = 3.88$ ms

(n) $t = 3.88$ ms

(o) $t = 3.88$ ms

(p) $t = 4.45$ ms

(q) $t = 4.45$ ms

(r) $t = 4.45$ ms

(s) $t = 4.83$ ms

(t) $t = 4.83$ ms

(u) $t = 4.83$ ms

(v) $t = 5.36$ ms

(w) $t = 5.36$ ms
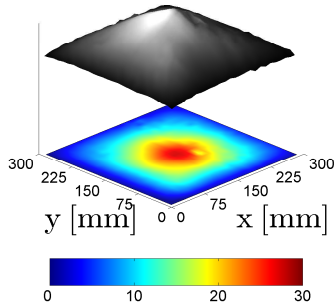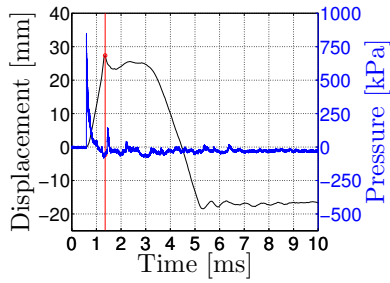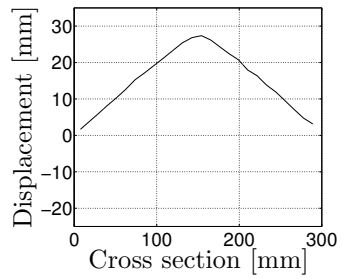
(x) $t = 5.36$ ms
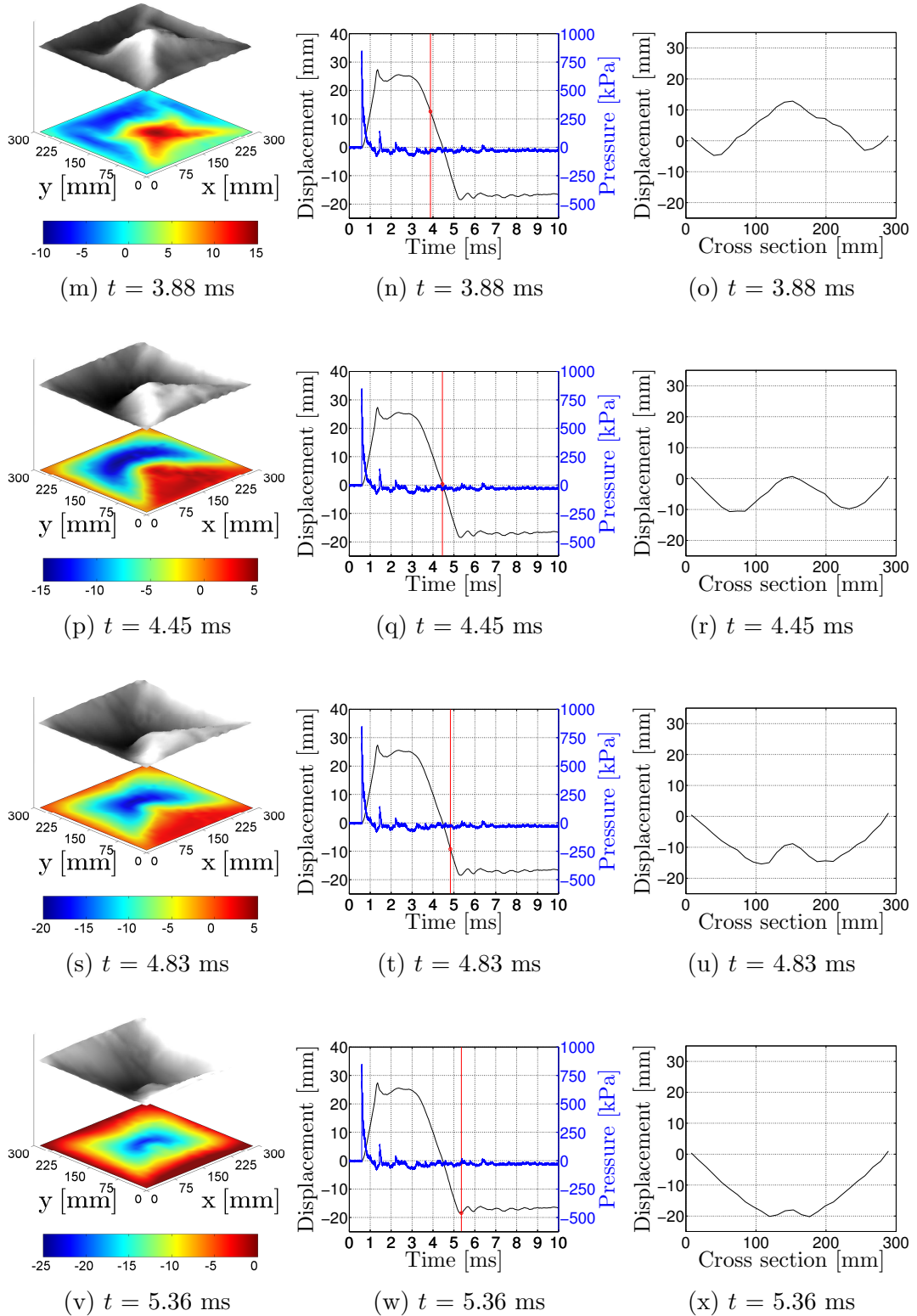
Figure B.17: Displacement of plate A31.

(a) $t = 0.74$ ms

(b) $t = 0.74$ ms

(c) $t = 0.74$ ms

(d) $t = 0.93$ ms

(e) $t = 0.93$ ms

(f) $t = 0.93$ ms

(g) $t = 1.12$ ms

(h) $t = 1.12$ ms

(i) $t = 1.12$ ms

(j) $t = 1.31$ ms

(k) $t = 1.31$ ms

(l) $t = 1.31$ ms
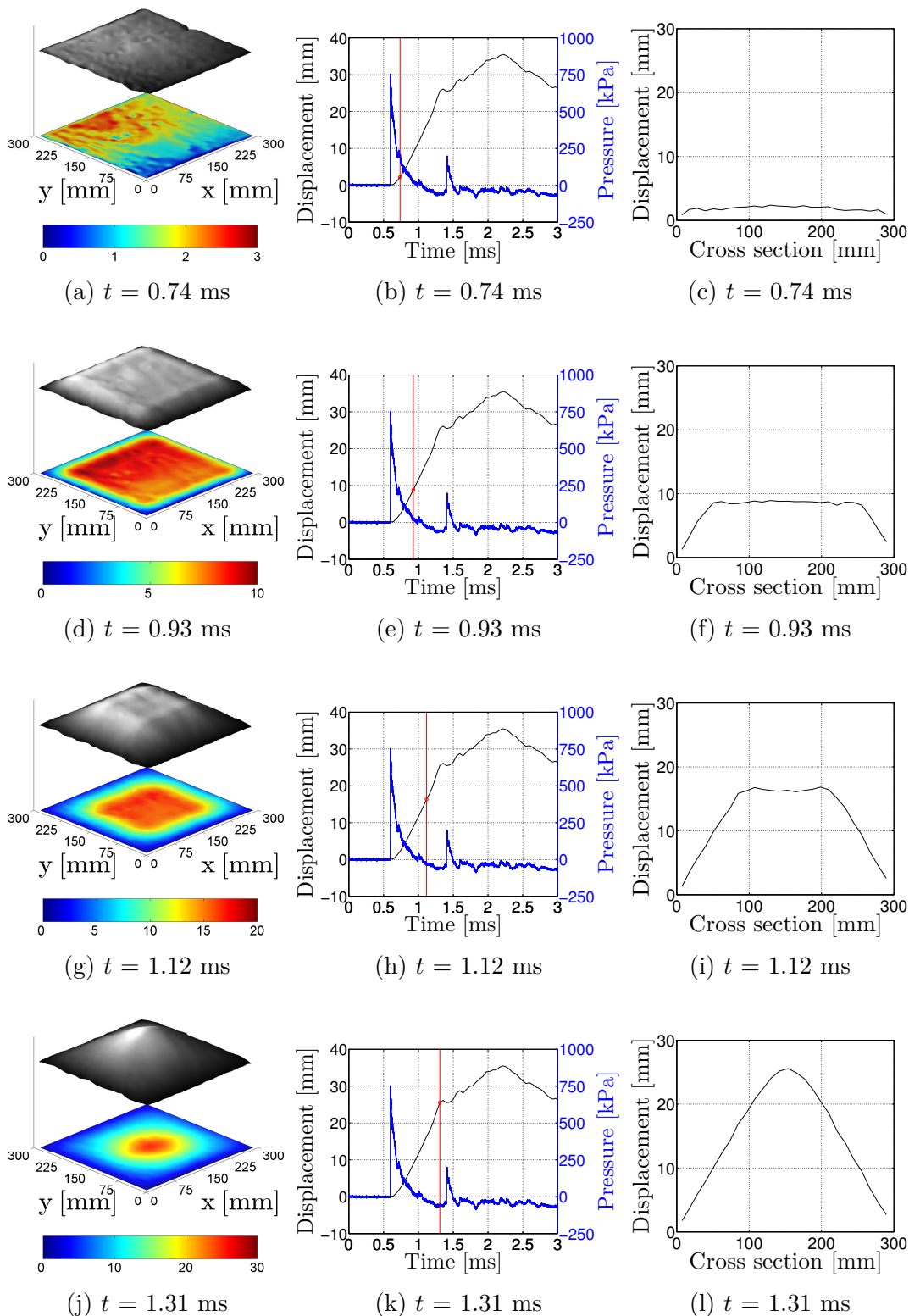
Figure B.18: Displacement of plate A32.
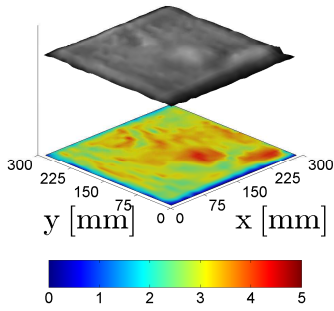
(a) $t = 0.78$ ms
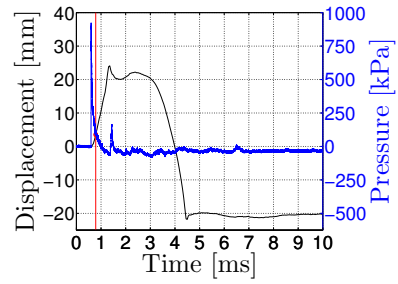
(b) $t = 0.78$ ms
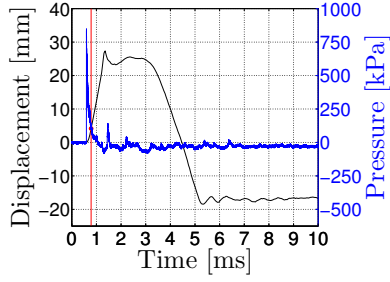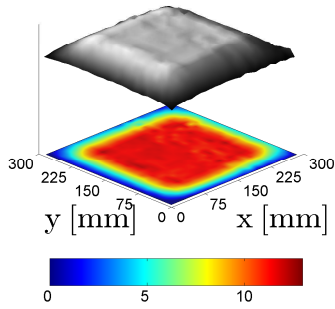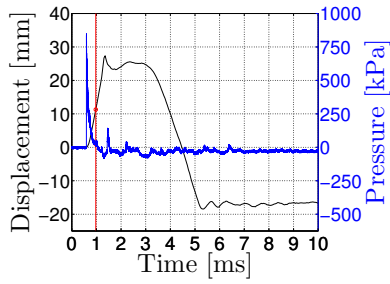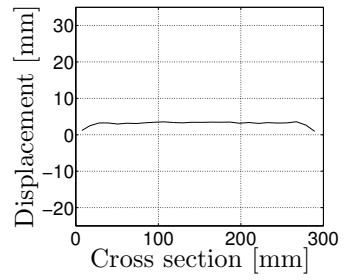
(c) $t = 0.78$ ms
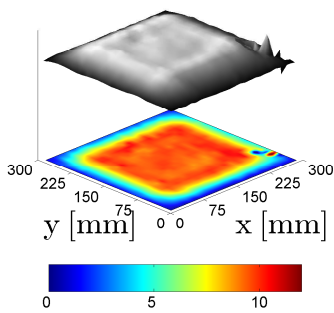
(d) $t = 0.97$ ms

(e) $t = 0.97$ ms

(f) $t = 0.97$ ms

(g) $t = 1.16$ ms

(h) $t = 1.16$ ms

(i) $t = 1.16$ ms

(j) $t = 1.36$ ms

(k) $t = 1.36$ ms

(l) $t = 1.36$ ms
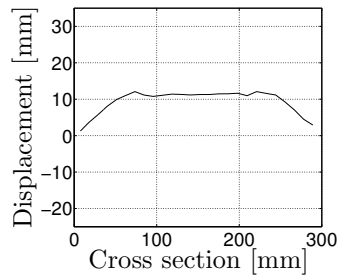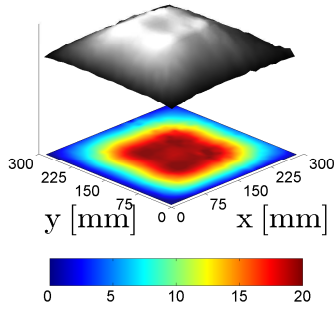
B21

(m) $t = 3.59$ ms

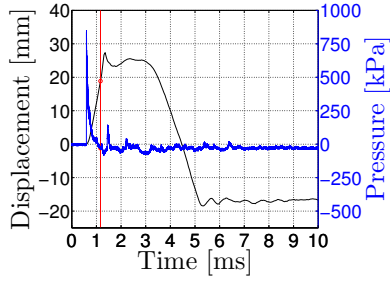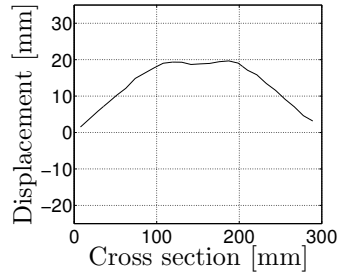(n) $t = 3.59$ ms

(o) $t = 3.59$ ms

(p) $t = 3.97$ ms

(q) $t = 3.97$ ms

(r) $t = 3.97$ ms

(s) $t = 4.26$ ms

(t) $t = 4.26$ ms

(u) $t = 4.26$ ms

(v) $t = 4.50$ ms

(w) $t = 4.50$ ms
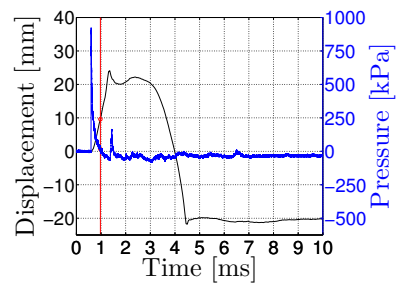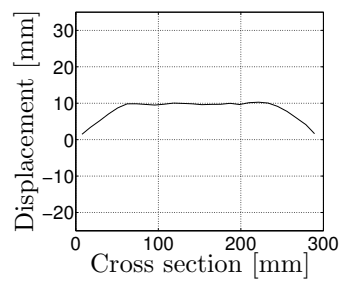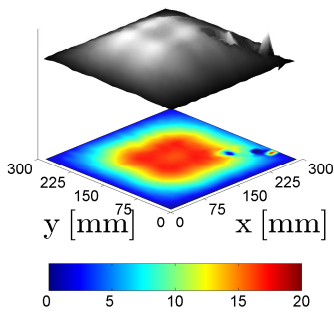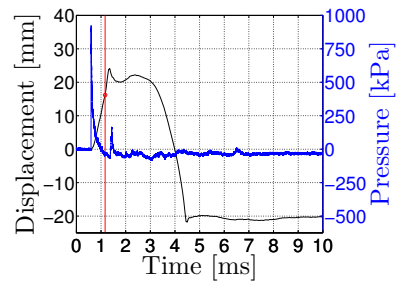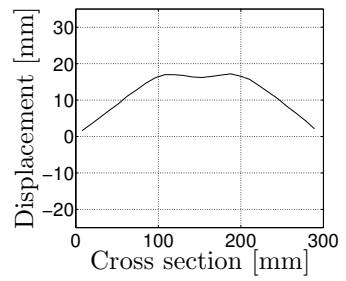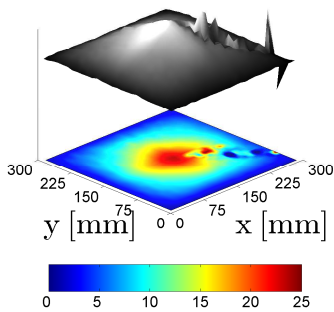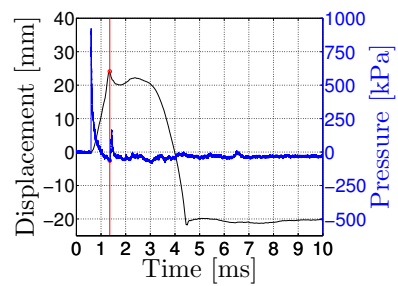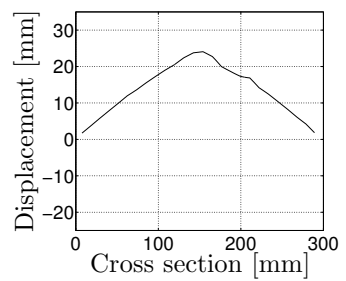
(x) $t = 4.50$ ms
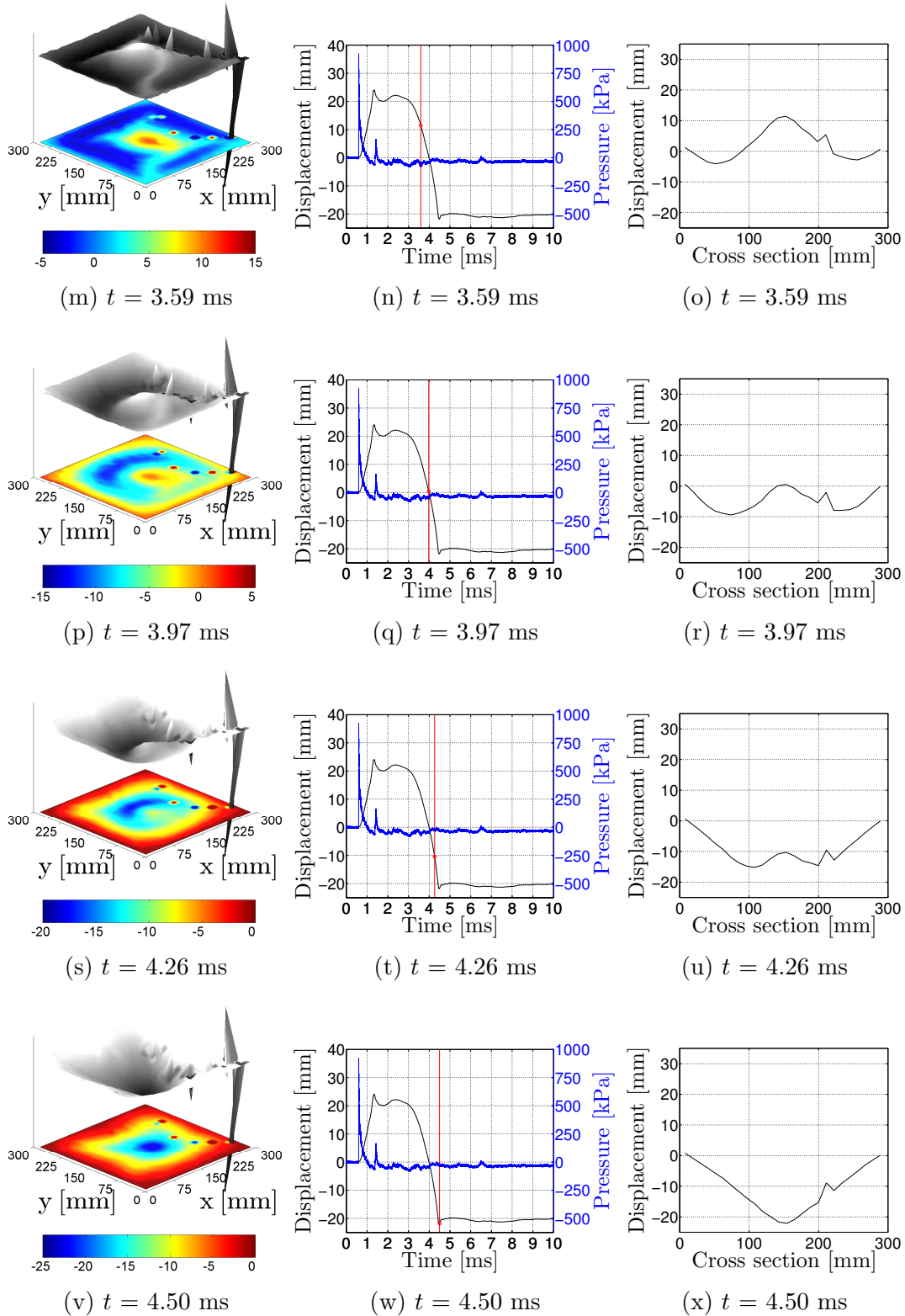
Figure B.19: Displacement of plate A33.

Appendix C

MATLAB-files

C.1 Script used to calculate results from calibration test R11

```matlab
% Script used to calculate results from calibration test R11

clear all
close all
clc

% Importing data from specific test

testdata=importdata('R11.csv');

t=testdata.data(:,1);
p=testdata.data(:,2:11)*10^2;        % Converting from bar to kPa
bw=testdata.data(:,12);

max_pressure=max(p);

% Converting time from s to ms

t=t*10^3;

% Pressure transducer specific values

% Approximate time at the end of positive impulse
t1pick=[3.982 2.002 2.575 3.651 3.503 3.901 4.401 3.400 3.121 3.103]*10^-1;

% Approximate time at the end of negative impulse
%t2pick=[7.97 20 20 20 20 10.005 20 8.001 8.581 9.198]*10^-1;

% Used when ignoring negative impulse
t2pick=[2.5 2.5 2.5 2.5 2.5 2.5 2.5 2.5 2.5 2.5];
```

```matlab
% Correcting curves according to time of detonation

top=bw(1);
count=1;

while top<=0.5
    count=count+1;
    top=bw(count);
end

figure(11);
plot(t,bw,'linewidth',1.6);
hold on;
grid on;

tbw=t(count);
bwline=[tbw tbw];
line=[-1000 1000]*10^2;
plot(bwline,line,'r','linewidth',1.6);
axis([0 20 -1 6]);
xlabel('Time [ms]','fontsize',26,'interpreter','latex');
ylabel('Response','fontsize',26,'interpreter','latex');
set(gca,'fontsize',20);

pause(0.01);
jFrame=get(handle(gcf),'JavaFrame');
set(jFrame,'maximized',true);
set(gcf,'PaperPositionMode','auto');

pause(0.001);
export_fig R11-bw.eps -eps -transparent

t=t(count:end);
t=t-t(1);
p=p(count:end,:);

ta=zeros(1,10);
t1=zeros(1,10);
t2=zeros(1,10);
impulse_pos=zeros(1,10);
impulse_neg=zeros(1,10);

for i=1:10
    % Find time of arrival
    top=p(1,i);
    count=1;

    while top<=300
        count=count+1;
        top=p(count,i);
    end
```

```matlab
        ta(i)=t(count);
        tacount=count;

        % Define time of positive impulse t1 and negative impulse t2
        count=1;

        while t(count)<=t1pick(i)
            count=count+1;
        end

        t1count=count;
        t1(i)=t(t1count);

        while t(count)<=t2pick(i)
            count=count+1;
        end

        t2count=count;
        t2(i)=t(t2count);

        tpos=t(tacount:t1count);
        ppos=p(tacount:t1count,i);

        tneg=t(t1count:t2count);
        pneg=p(t1count:t2count,i);

        impulse_pos(i)=trapz(tpos,ppos);
        impulse_neg(i)=trapz(tneg,pneg);

        taline=[ta(i) ta(i)];
        t1line=[t1(i) t1(i)];
        t2line=[t2(i) t2(i)];

        % Plotting pressure in individual pressure transducers

        figure(i);
        plot(t,p(:,i),'linewidth',1.6);
        hold on;
        grid on;
        plot(taline,line,'r','linewidth',1.6);
        plot(t1line,line,'r','linewidth',1.6);
        plot(t2line,line,'r','linewidth',1.6);
        axis([0 1.2 -10*10^2 140*10^2]);
        xlabel('Time [ms]','fontsize',26,'interpreter','latex');
        ylabel('Pressure [kPa]','fontsize',26,'interpreter','latex');
        set(gca,'fontsize',20);

        pause(0.01);
        jFrame=get(handle(gcf),'JavaFrame');
        set(jFrame,'maximized',true);
        set(gcf,'PaperPositionMode','auto');
end
```

```matlab
tplus=t1-ta;
tminus=t2-t1;

% Creating plots for comparing pressure in transducers

figure(12);
plot(t,p(:,1),t,p(:,2),t,p(:,3),t,p(:,4),'linewidth',1.6);
grid on;
axis([0 1.2 -10*10^2 140*10^2]);
xlabel('Time [ms]','fontsize',26,'interpreter','latex');
ylabel('Pressure [kPa]','fontsize',26,'interpreter','latex');
set(gca,'fontsize',20);
leg=legend('Pressure transducer 1','Pressure transducer 2', ...
    'Pressure transducer 3','Pressure transducer 4');
set(leg,'fontsize',26,'interpreter','latex');

pause(0.01);
jFrame=get(handle(gcf),'JavaFrame');
set(jFrame,'maximized',true);
set(gcf,'PaperPositionMode','auto');

pause(0.001);
export_fig R11-1-4.eps -eps -transparent

figure(13);
plot(t,p(:,1),t,p(:,8),t,p(:,9),t,p(:,10),'linewidth',1.6);
grid on;
axis([0 1.2 -10*10^2 140*10^2]);
xlabel('Time [ms]','fontsize',26,'interpreter','latex');
ylabel('Pressure [kPa]','fontsize',26,'interpreter','latex');
set(gca,'fontsize',20);
leg=legend('Pressure transducer 1','Pressure transducer 8', ...
    'Pressure transducer 9','Pressure transducer 10');
set(leg,'fontsize',26,'interpreter','latex');

pause(0.01);
jFrame=get(handle(gcf),'JavaFrame');
set(jFrame,'maximized',true);
set(gcf,'PaperPositionMode','auto');

pause(0.001);
export_fig R11-1+8-10.eps -eps -transparent

figure(14);
plot(t,p(:,1),t,p(:,5),t,p(:,6),t,p(:,7),'linewidth',1.6);
grid on;
axis([0 1.2 -10*10^2 140*10^2]);
xlabel('Time [ms]','fontsize',26,'interpreter','latex');
ylabel('Pressure [kPa]','fontsize',26,'interpreter','latex');
set(gca,'fontsize',20);
leg=legend('Pressure transducer 1','Pressure transducer 5', ...
    'Pressure transducer 6','Pressure transducer 7');
set(leg,'fontsize',26,'interpreter','latex');
```

```matlab
pause(0.1);
jFrame=get(handle(gcf),'JavaFrame');
set(jFrame,'maximized',true);
set(gcf,'PaperPositionMode','auto');

pause(0.01);
export_fig R11-1+5-7.eps -eps -transparent

figure(1);
pause(0.001);
export_fig R11-p1.eps -eps -transparent

figure(2);
pause(0.001);
export_fig R11-p2.eps -eps -transparent

figure(3);
pause(0.001);
export_fig R11-p3.eps -eps -transparent

figure(4);
pause(0.001);
export_fig R11-p4.eps -eps -transparent

figure(5);
pause(0.001);
export_fig R11-p5.eps -eps -transparent

figure(6);
pause(0.001);
export_fig R11-p6.eps -eps -transparent

figure(7);
pause(0.001);
export_fig R11-p7.eps -eps -transparent

figure(8);
pause(0.001);
export_fig R11-p8.eps -eps -transparent

figure(9);
pause(0.001);
export_fig R11-p9.eps -eps -transparent

figure(10);
pause(0.001);
export_fig R11-p10.eps -eps -transparent
```

C.2   Script used to calculate results from component test A11

```matlab
% Script used to calculate results from component test A11

clear all
close all
clc

% Importing data from specific test

testdata=importdata('A11.csv');

t=testdata.data(:,1)*10^3;      % Converting time from s to ms
p=testdata.data(:,2:5)*10^2;    % Converting pressure from bar to kPa
bw=testdata.data(:,6);
p1=p(:,1);
p5=p(:,2);
p6=p(:,3);
p7=p(:,4);

figure(1);
plot(t,p);
grid on;
xlabel('Time [ms]');
ylabel('Pressure [kPa]');

% Importing deformation profiles

defodata=importdata('A11 - deformation profiles.txt');

framedefo=[41 43 45 47 49 51 53 55 57 350]; % DIC frames used
nframes=length(framedefo);

position=defodata.data(:,1:2:2*nframes-1);
defoprofile=defodata.data(:,2:2:2*nframes)*-1;

for i=1:nframes
    position(:,i)=position(:,i)+(300-position(end,i))*7/17;
end

for i=1:nframes
    figure(framedefo(i));
    plot(position(:,i),defoprofile(:,i),'k','linewidth',1.6);
    grid on;
    xlabel('Cross section [mm]','fontsize',45,'interpreter','latex');
    ylabel('Displacement [mm]','fontsize',45,'interpreter','latex');
    set(gca,'fontsize',32);
    axis([0 300 0 50]);
    set(gca,'Position',[0.2 .18 .6 .79]);
    set(gcf,'units','normalized','outerposition',[0.2 0.1 0.6 0.8])
```

```matlab
    set(gcf,'PaperPositionMode','auto');
end

% Importing data from the log used in DIC

logdata=importdata('A11 - log.txt');

frame=logdata.data(:,1);
tlog=logdata.data(:,2);
plog=logdata.data(:,3:6)*10^2;
p5log=plog(:,2);
bp=logdata.data(:,7);
middefo=logdata.data(:,8)*-1;

figure(3);
plot(tlog,plog);
grid on;
xlabel('Time [ms]');
ylabel('Pressure [kPa]');

figure(4);
plot(tlog,p5log);
hold on;
scatter(tlog(framedefo),p5log(framedefo),'r');
grid on;
xlabel('Time [ms]');
ylabel('Pressure [kPa]');

% Time of arrival of pressure transducer 5 according to R23
ta=0.2443;

% Adjusting curves according to time for arrival

% Identifying arrival of log curve for p5
top=plog(1,2);
count=1;

while top<=1.5*10^2
    count=count+1;
    top=plog(count,2);
end

talog=tlog(count-1);
talogcount=count-1;

% Identifying arrival of full curve for p5
top=p(1,2);
count=1;

while top<=0.5*10^2
    count=count+1;
    top=p(count,2);
end
```

```matlab
tafull=t(count);
tafullcount=count;

% Connect frames from log series to complete pressure curve

fullpos=zeros(1,length(framedefo));

for i=1:length(framedefo)
    while t(count)-tafull<=tlog(framedefo(i))-talog
        count=count+1;
    end
    fullpos(i)=count;
end

% Correcting curve for time of detonation

tfullcorr=t-t(tafullcount)+ta;
tlogcorr=tlog-tlog(talogcount)+ta;

figure(5);
plot(tfullcorr,p5);
hold on;
scatter(tfullcorr(fullpos),p5(fullpos),'r');
grid on;
xlabel('Time [ms]');
ylabel('Pressure [kPa]');

% Creating plots for comparing pressure in pressure transducers

figure(6);
plot(tfullcorr,p,'linewidth',1.6);
grid on;
xlabel('Time [ms]','fontsize',26,'interpreter','latex');
ylabel('Pressure [kPa]','fontsize',26,'interpreter','latex');
leg=legend('Pressure transducer 1','Pressure transducer 5', ...
    'Pressure transducer 6','Pressure transducer 7');
set(leg,'fontsize',26,'interpreter','latex');
set(gca,'fontsize',20);
axis([0 2 -500 4000]);

pause(0.01);
jFrame=get(handle(gcf),'JavaFrame');
set(jFrame,'maximized',true);
set(gcf,'PaperPositionMode','auto');

export_fig A11-pressure.eps -eps -transparent

figure(7);
plot(tlogcorr,middefo,'linewidth',1.6);
hold on;
grid on;
xlabel('Time [ms]','fontsize',26','interpreter','latex');
```

```matlab
ylabel('Displacement at midpoint [mm]','fontsize',26', ...
    'interpreter','latex');
set(gca,'fontsize',20);
axis([0 10 0 45]);

pause(0.01);
jFrame=get(handle(gcf),'JavaFrame');
set(jFrame,'maximized',true);
set(gcf,'PaperPositionMode','auto');

export_fig A11-middefo.eps -eps -transparent

line=[-1000 1000];

% Creating plots that compare pressure and midpoint displacement at
% different timesteps.

for i=1:nframes-1
    figure(100+framedefo(i));
    [haxes,hline1,hline2]=plotyy(tlogcorr,middefo,tfullcorr,p5);
    ylabel(haxes(1),'Displacement [mm]','fontsize',45, ...
        'interpreter','latex');
    ylabel(haxes(2),'Pressure [kPa]','fontsize',45,'interpreter','latex');
    xlabel(haxes(2),'Time [ms]','fontsize',45,'interpreter','latex');
    set(haxes,'fontsize',32);
    set(hline1,'color','k','linewidth',1.6);
    set(hline2,'color','b','linewidth',1.6);
    set(haxes,{'ycolor'},{'k';'b'});
    hold on;
    scatter(tlogcorr(framedefo(i)),middefo(framedefo(i)),'r', ...
        'linewidth',1.6);
    scatter(tfullcorr(fullpos(i)),p5(fullpos(i))*10^-2,'r', ...
        'linewidth',1.6);
    grid(haxes(1),'on');
    axis([0 2 -5 50]);
    set(haxes(1),'ytick',[-10:10:50]);
    set(haxes(2),'ytick',[-1000:1000:5000]);
    set(haxes,'xtick',[0:0.5:2]);
    ylim(haxes(2),[-500 5000]);
    xlim(haxes(2),[0 2]);
    tpickline=[tfullcorr(fullpos(i)) tfullcorr(fullpos(i))];
    plot(tpickline,line,'r','linewidth',1.6);
    set(gca,'Position',[0.2 .18 .6 .79]);
    set(gcf,'units','normalized','outerposition',[0.2 0.1 0.6 0.8]);
    set(gcf,'PaperPositionMode','auto');
end

figure(45);
export_fig A11-2d-45.eps -eps -transparent

figure(49);
export_fig A11-2d-49.eps -eps -transparent
```

```
figure(53);
export_fig A11-2d-53.eps -eps -transparent

figure(57);
export_fig A11-2d-57.eps -eps -transparent

figure(145);
export_fig A11-plot-45.eps -eps -transparent

figure(149);
export_fig A11-plot-49.eps -eps -transparent

figure(153);
export_fig A11-plot-53.eps -eps -transparent

figure(157);
export_fig A11-plot-57.eps -eps -transparent
```

C.3 Script used to generate 3D-plot from component tests

```matlab
% Script for generating 3D-plots of DIC results

clear all
close all
clc

id = 57;        % Input picture number
cat = 'D:\Masteroppgave\2014_03_Ostoya\2014_03_13\A11\dic25\';
pre = 'A11_C1_';

name = '';
if(id < 10)
    name = ['000' num2str(id)];
elseif(id < 100)
    name = ['00' num2str(id)];
elseif(id < 1000)
    name = ['0' num2str(id)];
elseif(id < 10000)
    name = [num2str(id)];
end

if(~strcmp(cat(length(cat)-1),'\')) cat = [cat '\']; end
fpath = [cat pre name '.eco'];

dicmesh = ReadMeshBinary(fpath);
dicmesh = RigidBodyTransform(dicmesh, -0.60, -14.29, 0, 0, 0, -44.0);

corrX = 60;
corrY = 187;

dicmesh.nlocX(:,1) = dicmesh.nlocX(:,1) + corrX;
dicmesh.nlocX(:,2) = dicmesh.nlocX(:,2) + corrY;

if(~isempty(dicmesh.nlocX))
    [elmGrid, nodeGrid] = Mesh2ElementQ4Grid(dicmesh);
    ndX = dicmesh.nlocX + dicmesh.ndefX;
    X = zeros(size(nodeGrid)); Y = X; Z = X; dZ = X;
    for i = 1:length(nodeGrid(:,1))
        for j=1:length(nodeGrid(1,:))
            X(i,j) = ndX(nodeGrid(i,j), 1);
            Y(i,j) = ndX(nodeGrid(i,j), 2);
            Z(i,j) = ndX(nodeGrid(i,j), 3);
            dZ(i,j) = dicmesh.ndefX(nodeGrid(i,j), 3);
        end
    end

    % Plot 3D-surface
```

```
figure(1)
surf(X,Y,-Z,-dZ);
camlight left;
lighting phong
colormap gray
material dull
shading interp

axis([0 300 0 300 -60 20])
set(gca,'CLim',[0 45]);      % Adjust in order to get correct colorbar
cb=colorbar('Location','SouthOutside');

h = camlight;
set(h,'Position',[0 1200, 100])

scale = 20;
iLen = length(X(:,1))*scale;
jLen = length(X(1,:))*scale;
Xi = zeros(iLen,jLen);
Yi = zeros(iLen,jLen);

for i= 1:iLen,
    for j= 1:jLen,
        Xi(i,j) = j / scale;
        Yi(i,j) = i / scale;
    end
end

ZZ = interp2(Z,Xi,Yi);
XX = interp2(X,Xi,Yi);
YY = interp2(Y,Xi,Yi);

mini = 1;
for i = 1:length(ZZ(:,1))
    if(length(find(isnan(ZZ(i,:)))) < length(ZZ(i,:)))
        mini = i;
        break;
    end
end

minj = 1;

for i = 1:length(ZZ(1,:))
    if(length(find(isnan(ZZ(:,i)))) < length(ZZ(:,1)))
        minj = i;
        break;
    end
end

XX = XX(mini:length(XX(:,1)), minj:length(XX(1,:)));
YY = YY(mini:length(XX(:,1)), minj:length(XX(1,:)));
ZZ = ZZ(mini:length(XX(:,1)), minj:length(XX(1,:)));
```

```matlab
    % Generate color picture that displays displacements
    min_x = min(min(XX));
    min_y = min(min(YY));
    max_x = max(max(XX));
    max_y = max(max(YY));

    planeimg = -ZZ;

    imgzposition = -60;

    minplaneimg = 0;            % Adjust in order to get correct colorbar
    maxplaneimg = 45;           % Adjust in order to get correct colorbar
    scaledimg = (floor(((planeimg - minplaneimg) ./ ...
    (maxplaneimg - minplaneimg)) * 255));

    colorimg = mat2im(scaledimg,jet(256));

    hold on;

    % Plot image
    surf([min_x max_x],[min_y max_y],repmat(imgzposition, [2 2]),...
    colorimg,'facecolor','texture');

    view(-45,30);
    f3 = 22;
    set(gca,'XTick',0:75:300,'YTick',0:75:300,'ZTick',[],...
        'FontSize',f3);

    grid off;

    xlabel('x [mm]','fontsize',28,'interpreter','latex');
    ylabel('y [mm]','fontsize',28,'interpreter','latex');

    colormap(jet(256));
    cbfreeze(cb);
    colormap(gray);
    set(gca,'Position',[0.1 .35 .8 .55]);
    set(gcf,'units','normalized','outerposition',[0.3 0 0.4 1])
    set(gcf,'PaperPositionMode','auto');
end

pause(0.1);
print -depsc A11-3d-57.eps
```

Appendix D

Cast3M-files

D.1   File used to convert mesh from SALOME

```
OPTI ECHO 1;
OPTI REST FORM 'tt2d.sauv';
REST FORM;
LIST;
OPTI SAUV FORM 'tt2d.msh';
LIST (nbel allele);
mesh = allele;
TASS allele NOOP;
SAUV FORM allele;
FIN;
```

D.2   File used to generate mesh for FSI-model

```
OPTI ECHO 1;
OPTI DIME 3 ELEM QUA4;
OPTI TITR 'PLATE EXPLOSION FSI';
OPTI TRAC PSC FTRA 'expfsi11_mesh.ps';
opti SAUV FORM 'expfsi11.msh';

* Tolerance when merging nodes
tol = 0.001;

* xs is position of load along x-axis.
* xend is cuttoff length of model.
xend = 0.625;
xs = 0.500;

* Defining plate

den = 0.025;
n1 = 12;
n2 = 25;
DENS den;

p1 = 0 -0.15 -0.15;
p2 = 0 0.15 -0.15;
p3 = 0 0.15 0.15;
p4 = 0 -0.15 0.15;

cont1 = p1 d p2 d p3 d p4 d;

surf11 = SURF cont1 PLAN;
surf12 = surf11 PLUS (0 0 0);

surf1t = surf11 PLUS (0 0 0);

* Defining frame

p5 = 0 -0.5 -0.5;
p6 = 0 0.5 -0.5;
p7 = 0 0.5 0.5;
p8 = 0 -0.5 0.5;

cont2 = p5 d p6 d p7 d p8 d;

surf2 = SURF cont2 PLAN;

elim tol(surf2 et surf1t);

surf2t = surf2 PLUS (0 0 0);

surf31 = surf2 DIFF surf1t;
surf32 = surf31 PLUS (0 0 0);
```

```
* Defining air

p9 = 0 -0.7 -0.5;
p10 = 0 -0.7 0.7;
p11 = 0 0.7 0.7;
p12 = 0 0.7 -0.5;

cont4 = p9 d p10 d p11 d p12 d;

surf4 = SURF cont4 PLAN;

elim tol(surf4 et surf2t);

surf51 = surf4 DIFF surf2t;
surf52 = surf51 PLUS (0 0 0);

* Defining boundaries

p13 = -0.3 -0.7 -0.5;
p14 = xend -0.7 -0.5;
p15 = xend -0.7 0.7;
p16 = -0.3 -0.7 0.7;

p17 = -0.3 0.7 0.7;
p18 = -0.3 0.7 -0.5;
p19 = xend 0.7 0.7;
p20 = xend 0.7 -0.5;

* Top

contb1 = p15 d p16 d p17 d p19 d;
surfb1= SURF contb1 PLAN;

* Back

contb2 = p13 d p16 d p17 d p18 d;
surfb2 = SURF contb2 PLAN;

* Front

contb3 = p14 d p15 d p19 d p20 d;
surfb3 = SURF contb3 PLAN;

* Left

contb4 = p17 d p19 d p20 d p18 d;
surfb4 = SURF contb4 PLAN;

* Right

contb5 = p13 d p16 d p15 d p14 d;
surfb5 = SURF contb5 PLAN;
```

```
* Bottom

contb6 = p13 d p18 d p20 d p14 d;
surfb6 = SURF contb6 PLAN;


absorb = surfb1 et surfb2 et surfb3 et surfb4 et surfb5;
blockz = surfb6;


surfs = absorb et blockz;


* Definining physical plate

p1p = 0 -0.15 -0.15;
p2p = 0 0.15 -0.15;
p3p = 0 0.15 0.15;
p4p = 0 -0.15 0.15;


cont1p = p1p d p2p d p3p d p4p d;


plate = SURF cont1p PLAN;


bound = CHAN POI1 cont1p;


* Extrude mesh to form mesh of air

dt1 = -0.3 0 0;
dt2 = xend 0 0;


OPTI dime 3 elem CUB8;


v11 = surf11 VOLU TRANS n1 dt1;
v12 = surf12 VOLU TRANS n2 dt2;


V31 = surf31 VOLU TRANS n1 dt1;
V32 = surf32 VOLU TRANS n2 dt2;


V51 = surf51 VOLU TRANS n1 dt1;
V52 = surf52 VOLU TRANS n2 dt2;


* Make space to spherical charge

dtlb = 0.2;
* dtlb is 2 times lbsize
* dtlb is the length when extruding the large box


p1sc = (xs+0.1) -0.1 -0.1;
p2sc = (xs+0.1) 0.1 -0.1;
p3sc = (xs-0.1) 0.1 -0.1;
p4sc = (xs-0.1) -0.1 -0.1;
* Change the number 0.1 to another depending
* on the required size of the large box
contsc = p1sc d p2sc d p3sc d p4sc d;
```

```
scs = SURF contsc PLAN;
dt3 = 0. 0. dtlb;


nsc = 8;
* nsc is the number of elements along the extruded edge
* nsc is usually nsc = dtlb/den

cutout = scs VOLU TRANS nsc dt3;


elim tol (v12 et cutout);


v12c = v12 DIFF cutout;


* Build spherical charge

* Construction of a sphere from a cube
* Total bisections
nel0 = 4;
nel1 = 4;


* Side of the cube intermediate
r0 = 0.25;
* r0 is the ratio between half the length of the side
* of the inner cube and the radius of the circle
* r0 = elesize*n10/sizeex;

sizeex = 0.01725;
* sizeex is the radius of the circle

sizeai = 0.1;
* sizeai is half the length of the sides in the cube

width = 0.4;
height = 2.0;
dini = 3.141*sizeex/(4.*nel0);
dfin = 3.141*sizeai/(4.*nel0);

* Reference
o0 = 0. 0. 0.;
x0 = (sizeex) 0. 0.;
x01 = ((-1)*sizeex) 0. 0.;
y0 = 0. (sizeex) 0.;
z0 = 0. 0. (sizeex);
z01 = 0. 0. ((-1)*sizeex);
x1 = (sizeai) 0. 0.;
x11 = ((-1)*sizeai) 0. 0.;
y1 = 0. (sizeai) 0.;
z1 = 0. 0. (sizeai);
z11 = 0. 0. ((-1)*sizeai);
symp1 = (sizeex/2.) (sizeex/2.) (sizeex/2.);
symp11 = ((-1)*sizeex/2.) (sizeex/2.) (sizeex/2.);
symp12 = ((-1)*sizeex/2.) (sizeex/2.) ((-1)*sizeex/2.);
```

```
symp13 = (sizeex/2.) (sizeex/2.) ((-1)*sizeex/2.);
symp2 = (sizeai/2.) (sizeai/2.) (sizeai/2.);
symp21 = ((-1)*sizeai/2.) (sizeai/2.) (sizeai/2.);
symp22 = ((-1)*sizeai/2.) (sizeai/2.) ((-1)*sizeai/2.);
symp23 = (sizeai/2.) (sizeai/2.) ((-1)*sizeai/2.);

vol0 = o0 droi nel0 x0 tran nel0 z0 volu tran nel0 y0
*Inner cube of TNT
coul roug homo o0 r0;
vol01 = vol0 PLUS (((-1)*(r0)*sizeex) 0. 0.);
vol02 = vol0 PLUS (((-1)*(r0)*sizeex) 0. ((-1)*(r0)*sizeex));
vol03 = vol0 PLUS (0. 0. ((-1)*(r0)*sizeex));
vol10 = o0 droi nel0 x0 tran nel0 z0 volu tran nel0 y0
coul roug homo o0 0.2;
vol101 = o0 droi nel0 x01 tran nel0 z0 volu tran nel0 y0
coul roug homo o0 0.2;
vol102 = o0 droi nel0 x01 tran nel0 z01 volu tran nel0 y0
coul roug homo o0 0.2;
vol103 = o0 droi nel0 x0 tran nel0 z01 volu tran nel0 y0
coul roug homo o0 0.2;

* Building surfaces

cub0 = (o0 droi nel0 y0 tran nel0 x0)
et (o0 droi nel0 z0 tran nel0 y0) et
(o0 droi nel0 x0 tran nel0 z0)
syme 'POINT' symp1 homo o0 r0;

* Building the next half of the model
* with same procedure as first 1/8

cub01 = (o0 droi nel0 y0 tran nel0 x01)
et (o0 droi nel0 z0 tran nel0 y0) et
(o0 droi nel0 x01 tran nel0 z0)
syme 'POINT' symp11 homo o0 r0;
cub02 = (o0 droi nel0 y0 tran nel0 x01)
et (o0 droi nel0 z01 tran nel0 y0) et
(o0 droi nel0 x01 tran nel0 z01)
syme 'POINT' symp12 homo o0 r0;
cub03 = (o0 droi nel0 y0 tran nel0 x0)
et (o0 droi nel0 z01 tran nel0 y0) et
(o0 droi nel0 x0 tran nel0 z01)
syme 'POINT' symp13 homo o0 r0;
cub1 = (o0 droi nel0 y0 tran nel0 x0)
et (o0 droi nel0 z0 tran nel0 y0) et
(o0 droi nel0 x0 tran nel0 z0)
syme 'POINT' symp1;
cub11 = (o0 droi nel0 y0 tran nel0 x01)
et (o0 droi nel0 z0 tran nel0 y0) et
(o0 droi nel0 x01 tran nel0 z0)
syme 'POINT' symp11;
cub12 = (o0 droi nel0 y0 tran nel0 x01)
et (o0 droi nel0 z01 tran nel0 y0) et
```

```
(o0 droi nel0 x01 tran nel0 z01)
syme 'POINT' symp12;
cub13 = (o0 droi nel0 y0 tran nel0 x0)
et (o0 droi nel0 z01 tran nel0 y0) et
(o0 droi nel0 x0 tran nel0 z01)
syme 'POINT' symp13;
cub2 = (o0 droi nel0 y1 tran nel0 x1)
et (o0 droi nel0 z1 tran nel0 y1) et
(o0 droi nel0 x1 tran nel0 z1)
syme 'POINT' symp2;
cub21 = (o0 droi nel0 y1 tran nel0 x11)
et (o0 droi nel0 z1 tran nel0 y1) et
(o0 droi nel0 x11 tran nel0 z1)
syme 'POINT' symp21;
cub22 = (o0 droi nel0 y1 tran nel0 x11)
et (o0 droi nel0 z11 tran nel0 y1) et
(o0 droi nel0 x11 tran nel0 z11)
syme 'POINT' symp22;
cub23 = (o0 droi nel0 y1 tran nel0 x1)
et (o0 droi nel0 z11 tran nel0 y1) et
(o0 droi nel0 x1 tran nel0 z11)
syme 'POINT' symp23;

* Pojection on the sphere of unit radius

spe1 = cub0 proj 'CONI' o0 'SPHE' o0 x0;
spe11 = cub01 proj 'CONI' o0 'SPHE' o0 x01;
spe12 = cub02 proj 'CONI' o0 'SPHE' o0 x01;
spe13 = cub03 proj 'CONI' o0 'SPHE' o0 x0;
spe2 = cub2 proj 'CONI' o0 'SPHE' o0 x1;
spe21 = cub21 proj 'CONI' o0 'SPHE' o0 x11;
spe22 = cub22 proj 'CONI' o0 'SPHE' o0 x11;
spe23 = cub23 proj 'CONI' o0 'SPHE' o0 x1;

* Filling the open boxes with volumes

vol1 = cub0 volu nel1 spe1 coul roug;
vol11 = cub01 volu nel1 spe11 coul roug;
vol12 = cub02 volu nel1 spe12 coul roug;
vol13 = cub03 volu nel1 spe13 coul roug;
vol1 = vol1 et vol0;
vol11 = vol11 et vol01;
vol12 = vol12 et vol02;
vol13 = vol13 et vol03;
vol2 = spe1 volu 'DINI' dini 'DFIN' dfin cub2 coul turq;
vol21 = spe11 volu 'DINI' dini 'DFIN' dfin cub21 coul turq;
vol22 = spe12 volu 'DINI' dini 'DFIN' dfin cub22 coul turq;
vol23 = spe13 volu 'DINI' dini 'DFIN' dfin cub23 coul turq;

air = vol2 et vol21 et vol22 et vol23;
tnt = vol1 et vol11 et vol12 et vol13;

* Defining symmetry plane
```

D7

```
p1s = (sizeai) 0. 0.;
p2s = (sizeai) 0. (sizeai);
p3s = 0. 0. (sizeai);

* Coping half of the model by using symmetry plane

tnt2 = tnt SYME 'PLAN' p1s p2s p3s;
air2 = air SYME 'PLAN' p1s p2s p3s;

sphere = air et tnt et air2 et tnt2;
elim tol sphere;

* Translate sphere to given stand-off

sphere = sphere PLUS ((xs) 0. 0.);
tnt = tnt PLUS ((xs) 0. 0.);
tnt2 = tnt2 PLUS ((xs) 0. 0.);
air = air PLUS ((xs) 0. 0.);
air2 = air2 PLUS ((xs) 0. 0.);

elim tol (v12c ET sphere ET tnt ET tnt2 ET air ET air2);

elim tol(v11 et v12c);
elim tol(v51 et v52);
elim tol(v11 et v31);
elim tol(v31 et v51);
elim tol(v12c et v32);
elim tol(v32 et v52);

fluid = v11 ET v12c ET v31 ET v32 ET v51 ET v52;

elim tol(v51 ET v52 ET absorb ET blockz);
elim tol(v11 ET v31 ET absorb ET blockz);
elim tol(v12c ET v32 ET absorb ET blockz);

* Finishing touches

mesh = fluid et absorb et blockz et plate et sphere et tnt et tnt2
       et air et air2;

TASS mesh NOOP;
SAUV FORM mesh;
TRAC CACH QUAL mesh;

FIN;
```

Appendix E

EUROPLEXUS-files

E.1   Material tensile test

```
TENSION TEST
ECHO
!CONV win
CAST mesh
CPLA LAGR
GEOM Q42L mesh TERM
COMP EPAI 0.8e-3 LECT mesh TERM
     COUL TURQ LECT mesh TERM
     NGRO 1 'disp' LECT mesh TERM
                         COND BOX X0 0.043 Y0 -0.0001 Z0 -0.0001
                                  DX 0.002 DY 0.0002 DZ  0.0002
FONC 1 TABL 22
     0       0
     0.0025 0.0000129
     0.0050 0.0000514
     0.0075 0.0001144
     0.0100 0.0002005
     0.0125 0.0003075
     0.0150 0.0004328
     0.0175 0.0005733
     0.0200 0.0007255
     0.0225 0.0008857
     0.0250 0.0010500
     0.0275 0.0012143
     0.0300 0.0013745
     0.0325 0.0015267
     0.0350 0.0016672
     0.0375 0.0017925
     0.0400 0.0018995
     0.0425 0.0019856
     0.0450 0.0020486
     0.0475 0.0020871
```

```
      0.0500 0.0021000
      100.00 0.0021000
REGI 'force' RESU POIN LECT boundx TERM
MATE VMJC RO 2710 YOUN 7.1E10 NU 0.33 COA1 1.15E08
      COA2 0.57E08 CLB1 0.014 CLB2 0.26 SRRF 1.0
      LECT mesh TERM
LINK COUP
      VITE 1 1.0 FONC 1 LECT load TERM
      CONT SPLA NX -1 NY 0 LECT boundx TERM
      CONT SPLA NX 0 NY -1 LECT boundy TERM
ECRI DEPL VITE CONT ECRO TFREQ 0.04E-1
FICH SPLI ALIC TFRE 0.04E-1
OPTI NOTEST
      LOG 1
CALCUL TINI 0.0 NMAX 100000000 TEND 2.0
FIN
```

E.2   Explosion - Lagrangian approach

```
PLATE AIRBLAST EXPLOSION
ECHO
!CONV win
CAST mesh
TRID LAGR
DIME TERM
GEOM Q4GS allele CL3D load TERM
COMP COUL ROUG LECT allele TERM
     EPAI 0.8e-3 LECT allele TERM
MATE
     VMJC RO 2710 YOUN 7.1E10 NU 0.33 COA1 1.15E08
          COA2 0.57E08 CLB1 0.014 CLB2 0.26 SRRF 1.0
          LECT allele TERM
     IMPE AIRB X 0.500 Y 0.15 Z 0.15 CONF 1 MASS 0.04 TAUT
          LECT load TERM
LINK COUP
     BLOQ 123456 LECT bound TERM
ECRI DEPL VITE ECRO FAIL TFRE 0.5E-5
     FICH SPLI ALIC TFRE 0.5E-5
OPTI NOTE CSTA 0.9
     LOG 1
CALC TINI 0 TEND 10E-3
FIN
```

E.3   Explosion - Embedded FSI approach

```
EXPFSI
ECHO
!CONV win
CAST MESH
TRID ALE
DIME NALE 1 NBLE 1 TERM
GEOM
     CUVF fluid
     CUVF tnt tnt2 air air2
     Q4GS plate
     CL3D absorb
TERM
COMP GROU 2 'half' LECT fluid TERM COND YB GT 0.0
            'vcut' LECT fluid plate TERM COND YB GT 0
     COUL ROUG LECT tnt tnt2 TERM
          TURQ LECT fluid air air2 TERM
          ROSE LECT absorb TERM
          VERT LECT plate TERM
     EPAI 0.8e-3 LECT plate TERM
GRIL LAGR LECT plate TERM
     EULE LECT fluid TERM
MATE
     GAZP RO 588.1309 GAMM 1.4 PINI 2.0467E10
          PREF 1.E5 LECT tnt tnt2 TERM
     GAZP RO 1 GAMM 1.4 PINI 1.E5
          PREF 1.E5 LECT fluid air air2 TERM
     CLVF ABSO RO 1.
          LECT absorb TERM
     VMJC RO 2710 YOUN 7.1E10 NU 0.33 COA1 1.15E08
          COA2 0.57E08 CLB1 0.014 CLB2 0.26 SRRF 1.0
          LECT plate TERM
LINK COUP
     BLOQ 123456 LECT bound TERM
LINK DECO
     FLSW STRU LECT plate TERM
          FLUI LECT fluid TERM
          R 0.0219
          HGRI 0.0256
          DGRI
          FACE
          BFLU 1
          FSCP 1
ECRI VITE ECRO TFRE 10.5E-4
     ELEM LECT 1 TERM
     POIN LECT 1 TERM
     FICH SPLI ALIC TFRE 10.5E-6
OPTI PART NOTEST
     CSTA 0.125
     LOG 1
     VFCC FCON 6
```

```
        ORDR 2
        OTPS 1
        RECO 0
        FLSW 1
CALCUL TINI 0 TEND 10.5E-3
FIN
```

E.4 Explosion - ALE approach

```
EXPFSI
ECHO
!CONV win
CAST MESH
TRID ALE
DIME NALE 1 NBLE 1352 TERM
GEOM
     CUVF fluid
     Q4GS plate
     CL3D absorb
TERM
COMP GROU 4 'explo' LECT fluid TERM
                    COND BOX X0 0.35775 Y0 -0.01725 Z0 -0.01725
                             DX 0.0345  DY 0.0345   DZ 0.0345
              'half'  LECT fluid TERM COND YB GT 0.0
              'vcut'  LECT fluid plate TERM COND YB GT 0
              'rezo'  LECT fluid TERM
                      COND BOX X0 -0.1 Y0 -0.151 Z0 -0.151
                               DX 0.2  DY 0.302  DZ 0.302
     COUL ROUG LECT explo TERM
          TURQ LECT fluid DIFF explo TERM
          ROSE LECT absorb TERM
          VERT LECT plate TERM
          BLEU LECT rezo TERM
     EPAI 0.8e-3 LECT plate TERM
GRIL LAGR LECT plate TERM
     EULE LECT eule TERM
     AUTO NOEU LECT rezo DIFF eule plate TERM
MATE
     GAZP RO 171.3846 GAMM 1.4 PINI 1.7380E09
          PREF 1.E5 LECT explo TERM
     GAZP RO 1 GAMM 1.4 PINI 1.E5
          PREF 1.E5 LECT fluid DIFF explo TERM
     CLVF ABSO RO 1.
          LECT absorb TERM
     VMJC RO 2710 YOUN 7.1E10 NU 0.33 COA1 1.15E08
          COA2 0.57E08 CLB1 0.014 CLB2 0.26 SRRF 1.0
          LECT plate TERM
LINK COUP
     BLOQ 123456 LECT bound TERM
ECRI VITE ECRO TFRE 10.5E-4
     ELEM LECT 1 TERM
     POIN LECT 1 TERM
     FICH SPLI ALIC TFRE 10.5E-6
OPTI NOTEST
     CSTA 0.25
     LOG 1
     REZO LIAI MVRE MODU GAM0 0.5
     VFCC FCON 6
          ORDR 2
```

```
        OTPS 1
        RECO 0
CALCUL TINI 0 TEND 10.5E-3
FIN
```